POLYBENZOXAZINE BASED HIGH PERFORMANCE NANOFIBERS VIA ELECTROSPINNING

A DISSERTATION SUBMITTED TO

THE GRADUATE SCHOOL OF ENGINEERING AND SCIENCE

OF BILKENT UNIVERSITY

IN PARTIAL FULFILLMENT OF THE REQUIREMENTS FOR

THE DEGREE OF

DOCTOR OF PHILOSOPHY

IN

MATERIALS SCIENCE AND NANOTECHNOLOGY

By

YELDA ERTAŞ

August 2016

POLYBENZOXAZINE BASED HIGH PERFORMANCE NANOFIBERS VIA ELECTROSPINNING

By Yelda Ertaş

August 2016

We certify that we have read this dissertation and that in our opinion it is fully adequate, in scope and in quality, as a dissertation for the degree of Doctor of Philosophy.

Tamer Uyar (Advisor)

Jale Hacaloğlu

Dönüş Tuncel

Bilge Baytekin

Tuncer Çaykara

Approved for the Graduate School of Engineering and Science:

Levent Onural

Director of the Graduate School

ABSTRACT

POLYBENZOXAZINE BASED HIGH PERFORMANCE NANOFIBERS VIA ELECTROSPINNING

Yelda Ertaş

Ph.D. in Materials Science and Nanotechnology

Advisor: Tamer Uyar

August, 2016

Polybenzoxazines are newly developing phenolic type thermoset resins having fascinating properties which overcome the shortcomings of the traditional resins. In recent years, polybenzoxazines are attracting much interest because of their outstanding features, such as near-zero volumetric change upon curing, no by-products during curing, low water absorption, high glass transition temperature and high char yield. In addition, the molecular structure of polybenzoxazines facilitates immense design flexibility which enables tailoring the properties of the cured material for a wide range of application.

Electrospinning is a widely used simple and cost-effective technique to produce nanofibers from various polymers, polymer blends, inorganic materials, supramolecular structures and composites. In principle, a continuous filament is formed from polymer solution or melt under high electric field which resulted in fibers with diameters ranging from tens of nanometers to few microns. Nanofibers produced with electrospinning technique show unique physical/chemical properties due to their very high surface area and nanoporous structures.

In this thesis, we have produced polybenzoxazine based high performance nanofibrous materials *via* electrospinning by using two approaches. In the first approach, main-chain polybenzoxazines (MCPBz) were synthesized to produce bead free and uniform

nanofibers without using polymeric carrier matrix. However, it was observed that these nanofibers lost the fiber morphology at low temperatures and they formed film before cross-linking. Subsequently, novel photo/thermal curable MCPBz resins were designed and synthesized readily owing to the design flexibility of polybenzoxazines in order to enhance thermal stability of MCPBz nanofibers. Therefore, firstly photo curing was performed to improve the thermal stability of nanofibers and then, thermal curing was carried out at high temperatures to obtain cross-linked MCPBz nanofibers with good thermal and mechanical properties. In addition, it was shown that these cross-linked and highly porous MCPBz nanofibers are very stable in various organic solvents, highly concentrated acid solutions and at high temperatures which make these nanofibers quite useful for the certain filtration applications requiring high temperatures and harsh environmental conditions. In the second approach, we produced polybenzoxazine based composite nanofibers from both polymeric materials and non-polymeric systems (cyclodextrins) with enhanced thermal and mechanical properties. At the same time, PAHs, dye molecules and heavy metal ions removal experiments were performed with polybenzoxazine based composite nanofibers to demonstrate their potential application for the waste water treatment.

Keywords: benzoxazine, bio-benzoxazine, main-chain polybenzoxazine, curing, cross-linked, cellulose acetate, polycarbonate, modified cyclodextrin, nanofiber, electrospinning, thermal, mechanical, PAHs, dye molecules, metal ions, waste water.

ÖZET

ELEKTROEĞİRME YÖNTEMİ İLE ÜRETİLEN POLİBENZOKZAZİN BAZLI YÜKSEK PERFORMANSLI NANOLİFLER

Yelda Ertaş
Malzeme Bilimi ve Nanoteknoloji programı, Doktora
Tez Danışmanı: Tamer Uyar
Ağustos, 2016

Polibenzokzazinler yeni geliştirilen fenolik termoset rezinler olarak, geleneksel fenolik rezinlerin eksiklerini giderebilecek üstün özelliklere sahiptirler. Son yıllarda daha fazla ilgi çeken bu rezinler, tavlama için güçlü asitlere ihtiyaç duymama, tavlama sırasında toksik yan ürün oluşturmama, düşük su absopsiyonu, yüksek camsı geçiş sıcaklığı ve yüksek kömürleşme verimi gibi etkileyici özelliklere sahiptirler. Ayrıca, polibenzokzazinlerin molekül yapısı çok geniş tasarlanma esnekliğine sahip olduğu için, kullanım alanına uygun istenilen özelliklerde malzemelerin üretilebilmesini mümkün kılmaktadır.

Elektrospin tekniği, değişik polimerlerden, polimer karışımlarından, inorganik malzemelerden, supramoleküler yapılardan ve kompozitlerden nanolif üretmek için yaygın olarak kullanılan, kolay ve maliyeti düşük bir üretim tekniğidir. Prensip olarak, polimer solüsyonlarından yüksek elektrik alan altında sürekli bir jet oluşturularak çapları nanometre ile birkaç mikron arasında değişen lifler elde edilmektedir. Elektrospin tekniği ile elde edilen nanolifler, yüksek yüzey alanları ve nano boyuttaki gözenekli yapıları sayesinde sıra dışı fiziksel/kimyasal özellikler göstermektedirler ve özellikle filtrasyon uygulamaları için etkili malzemelerdir.

Bu tezde, elektrospin yöntemi kullanılarak iki farklı yaklaşımla polibenzokzazin bazlı yüksek performansa sahip nanogözenekli malzemeler üretilmiştir. İlk yaklaşımda, ana-zincir polibenzokzazinler (MCPBz'ler) sentezlenerek ilk kez bu rezinlerden taşıyıcı matriks kullanılmaksızın boncuksuz homojen dağılımlı nanolifler üretilmiştir. Ancak, bu nanoliflerin tavlama sıcaklığının altında, çapraz-bağlı yapılar oluşturamadan eriyek film haline dönüştüğü gözlemlenmiştir. Daha sonra, polybenzokzazinlerin istenilen özelliklerde tasarlanabilme esnekliği sayesinde, MCPBz nanoliflerinin termal karalılıklarını arttırabilmek için foto/termal yolla tavlanabilen yeni MCPBz rezinleri kolaylıkla tasarlanmış ve sentezlenmiştir. Böylece ilk basamakta foto tavlama uygulanarak nanoliflerin thermal karalılıkları arttırılmıştır, ikinci basamakta ise termal tavlama uygulanarak üstün termal ve mekanik özelliklere sahip MCPBz nanolifleri üretilmiştir. Ayrıca çapraz-bağlı ve yüksek gözenekli MCPBz nanoliflerinin çeşitli solventlerde, yüksek konsatrasyondaki asitlerde ve yüksek sıcaklıklarda oldukça kararlı olmaları, bu nanoliflerin yüksek sıcaklık ve şiddetli çevre koşulları gerektiren filtrasyon uygulamalarında kullanılabilecek oldukça etkili malzemeler olabilecekleri gösterilmiştir. İkinci yaklaşımda ise hem termoplastik polimerlerden hem de polimerik olmayan sistemlerden (siklodekstrinler) polibenzokzazin bazlı kompozit nanolifler üretilerek, polimerlerin ve siklodekstrinlerin thermal ve mekanik özellikleri geliştirilmiştir. Aynı zamanda, bu malzemelerin sulu çözeltilerdeki PAH'ları, boya moleküllerini ve ağır metalleri giderim deneyleri yapılarak elde edilen polibenokzazin bazlı kompozit nanoliflerinin atık su giderimlerinde potansiyel kullanım alanı gösterilmiştir.

Anahtar sözcükler: benzokzazin, biyo-benzokzazin, ana-zincir polibenzokzazin, tavlama, çapraz-bağlı, selüloz asetat, polikarbonat, modifiye siklodekstrin, nanolif, elektrospin, termal, mekanik, poliaromatik hidrokarbons, boya molekülleri, metal iyonları, atık su.

Sevgili Ailem...

ACKNOWLEDGEMENT

I would like to start acknowledgement part with my PhD supervisor Assoc. Prof. Tamer Uyar. He deserves the greatest appreciation with his encouragement, guidance, patience, understanding, and trust for me throughout my PhD studies. More importantly, He is an examplary supervisor teaching us how to be a good scientist and good person. I am proud of being a member of his research group.

I am sincerely grateful to my PhD progress committee members Prof. Jale Hacaloğlu and Assoc. Prof. Dönüş Tuncel for their valuable advices and fruitful discussions. And I would also like to express acknowledgements to my jury members Prof. Tuncer Çaykara and Assit. Prof. Bilge Baytekin for valuable contributions to my PhD thesis.

I have special thanks to Dr. Sesha Vempati for his fruitful colloborations and discussions and also for his advises, guidance, support and being a good example to us as a scientist. It was very good chance to work with him.

I owe a special thanks to Dr. Aslı Çelebioğlu not only collaborations and helpful discussions but also her endless support, everlasting help, understanding and valuable friendship. I am also so grateful to my dearest lab mates Dr. Fatma Kayacı, Dr. Nalan Oya San Keskin, Zeynep Aytaç, Zehra İrem Yıldız and Şefika Özcan not only creating such a nice ambiance in the laboratory which make easy and enjoyable to work but also being a great friend which reduce the stress and difficulties faced during last five years. I feel myself lucky to met and worked with them.

I would also like to acknowledge my previous and present lab members, Dr. Jagadeesh Veluru, Dr. Ali Demirci, Dr. Osman Arslan, Dr. Brabu Balusamy, Dr. Kugalur Shanmugam Ranjith, Dr. Amaresh Chandra Pradhan, Ömer Faruk Sarıoğlu, Ali Ekrem Deniz, and Ahmet Fatih Işık for their help, understanding and friendship.

I want to thank my present and past office friends Dr. İlke Şimşek Turan, Dr. Gözde Uzunallı, Dr. Gülcihan Gülseren, Dr. Göksu Çinar, Dr. Büşra Mammadov, Dr. Rashad Mammadov, Dr. Melis Şardan Ekiz, Dr. Ruslan Garifullin, Gülistan Tansık, Nuray Gündüz, Seylan Ayan, Hepi Susapto, Meryem Hatip, Aygül Zengin, Tuğçe Önür, Behide Saltepe, Begüm Dikeçoğlu, T. Gamze Ulusoy Ghobadi, Zeliha Soran Erdem, Talha Erdem and M. Aref Khalily for their friendship, help, support and understanding during my PhD in UNAM.

I am very grateful for having the opportunity to work with UNAM facilities, I would like to thank to everyone contributed to the foundation of UNAM. I also thank to Dr. Gökçe Çelik and Mrs. Zeynep Erdoğan for their technical contribution to my thesis.

I would like to acknowledge The Scientific and Technological Research Council of Turkey (TÜBİTAK BIDEB-2211C, TÜBİTAK project # 110M612 and # 213M185) for funding my PhD research and financially supporting me in one international conference (2224-A).

Finally, deepest thanks go to my beloved family for their endless support, great love, patience and understanding throughout of my life. I owe a lot to them.

TABLE OF CONTENT

ABSTRACT ..... **iii**
ÖZET ..... **v**
ACKNOWLEDGEMENT ..... **viii**
TABLE OF CONTENT ..... **x**
LIST OF ABBREVIATIONS ..... **xv**
LIST OF FIGURES ..... **xvii**
LIST OF TABLES ..... **xxvi**
1. INTRODUCTION **1**
1.1. Polybenzoxazines 1
1.2. Electrospinning 8
1.3. Polybenzoxazine based nanofibers 14
2. EXPERIMENTAL DETAILS **22**
2.1. Materials 22
2.2. Synthesis of benzoxazine monomers and main-chain polybenzoxazines 24
2.2.1. Synthesis of bisphenol-A and aniline based benzoxazine monomer (BA-a) 24
2.2.2. Synthesis of eugenol-based bio-benzoxazine monomers 24
2.2.3. Synthesis of thymol-based bio-benzoxazine monomers 26
2.2.4. Synthesis of fully bio-based benzoxazine monomer 28
2.2.5. Synthesis of main-chain polybenzoxazine resins 28
2.3. Preparation of the solutions and electrospinning of nanofibers 31
2.3.1. Preparation of PBA-ad6 and PBA-ad12 solutions and electrospinning of PBA-ad6 and PBA-ad12 nanofibers 31
2.3.2. Preparation of DHBP-ad6 and DHBP-ad12 solutions electrospinning of DHBP-ad6 and DHBP-ad12 nanofibers 32

2.3.3. Preparation of cellulose acetate and cellulose acetate/BA-a precursor solutions electrospinning of nanofibers 33
2.3.4. Preparation of polycarbonate and polycarbonate/BA-a precursor solutions and electrospinning of nanofibers 34
2.3.5. Preparation of modified cyclodextrin, modified cyclodextrin/BA-a precursor solutions and electrospinning of nanofibers 35
2.3.5. Preparation of HPβCD/E-f precursor solutions and electrospinning of nanofibers 36
2.4. Characterization and Measurement 37
2.5. Curing Studies 43
2.5.1. Curing studies of the bio-based benzoxazine monomers 43
2.5.2. Curing studies of PBA-ad6 and PBA-ad12 nanofibers 43
2.5.3. Curing studies of DHBP-ad6 and DHBP-ad12 nanofibers 44
2.5.3. Curing studies of CA/BA-a composite nanofibers 44
2.5.4. Curing studies of PC/BA-a composite nanofibers 45
2.5.5. Curing studies of modified CD/BA-a composite nanofibers 45
2.5.6. Curing studies of HPβCD/E-f composite nanofibers 45
2.6. Solubility and stability tests 46
2.6.1. Solubility and stability test of cross-linked DHBP-ad6 and DHBP-ad12 nanofibers 46
2.6.2. Solubility test of HPβCD/PBA-a composite nanofibers 46
2.7. Adsorption experiments 48
2.7.1. Molecular entrapment of dye molecules from liquid environment by HPβCD/PBA-a composite nanofibers 48
2.7.2. Molecular entrapment of polyaromatic hydrocarbons from liquid environment by HPβCD/PBA-a composite nanofibers 48
2.7.3. Molecular entrapment of PAHs from liquid environment by CA/PBA-a composite nanofibers 50

3. RESULTS and DISCUSSIONS 52
Chapter 1: Bio-based benzoxazine monomers 53
3.1. Eugenol-based bio-benzoxazine monomers 54
3.1.1. Synthesis and structural characterization of the eugenol-based bio-benzoxazine monomers 55
3.1.2. Polymerization of the eugenol-based bio-benzoxazine monomers by thermal curing; their structural and thermal characterizations 63
3.2. Thymol-based bio-benzoxazine monomers 71
3.2.1. Synthesis and structural characterization of the thymol-based bio-benzoxazine monomers 71
3.2.2. Polymerization of the thymol-based benzoxazine monomers by thermal curing; their structural and thermal characterizations 80
Chapter 2: Main-chain polybenzoxazine nanofibers 87
3.3. Bisphenol-A based main-chain polybenzoxazine nanofibers 88
3.3.1. Synthesis and structural characterization of the bisphenol-A based main-chain polybenzoxazines; PBA-ad6 and PBA-ad12 89
3.3.2. Electrospinning of PBA-ad6 nanofibers 93
3.3.3. Electrospinning of PBA-ad12 nanofibers 97
3.3.4. Curing studies of PBA-ad6 and PBA-ad12 nanofibrous mats 100
3.4. Cross-linked main-chain polybenzoxazine nanofibers by photo and thermal curing 110
3.4.1. Structural characterization of DHBP-ad6 and DHBP-ad12 resins 111
3.4.2. Electrospinning of DHBP-ad6 and DHBP-ad12 nanofibers 116
3.4.3. Curing studies of DHBP-ad6 and DHBP-ad12 nanofibers 119
3.4.5. Solubility and stability test of cross-linked DHBP-ad6 and DHBP-ad12 nanofibers 132
Chapter 3: Polymer/polybenzoxazine composite nanofibers 136
3.5. Cellulose acetate/BA-a composite nanofibers 137

3.5.1. Structural characterization of BA-a 138
3.5.2. Electrospinning of cellulose acetate and cellulose acetate/BA-a composite nanofibers 140
3.5.3. Structural and morphological characterization of the CA/BA-a composite nanofibers after thermal curing 142
3.5.4. Thermal and mechanical Properties of CA and CA10/PBA-a5/CTR1 composite nanofibers 148
3.5.5. Molecular entrapment efficiency of CA/PBA-a composite nanofibers with polyaromatic hydrocarbons 152
3.6. Polycarbonate/BA-a composite nanofibers 156
3.6.1. Electrospinning of Polycarbonate and Polycarbonate/BA-a composite nanofibers 157
3.6.2. Structural and morphological characterizations of the cross-linked PC20/PBA-a5/CTR2 composite nanofibers 158
3.6.3. Thermal and thermomechanical properties of PC and PC20/PBA-a5/CTR2 composite nanofibers 162
Chapter 4: Cyclodextrin/polybenzoxazine composite nanofibers 166
3.7. Water insoluable cyclodextrin nanofibers by using BA-a as a cross-linking agent 167
3.7.1. Electrospinning of modified cyclodextrin/BA-a composite nanofibers 169
3.7.2. Structural and morphological and thermal characterization of the modified CD/PBA-a composite nanofibers after thermal curing 172
3.7.3. Polyaromatic hydrocarbons entrapment efficiency of HPβCD100/PBA-a25/CTR15 composite nanofibers 180
3.7.4. Dye molecules entrapment efficiency of HPβCD100/PBA-a25/CTR15 composite nanofibers 184
3.7.5. Heavy metal removal performance of HPβCD100/PBA-a25/CTR15 composite nanofibers 189

3.8. Water insoluable HPβCD nanofibers by fully bio-based benzoxazine 192
3.8.1. Structural characterization of the eugenol and furfurylamine based fully bio-benzoxazine monomer (E-f) 192
3.8.2. Electrospinning of HPβCD/E-f composite nanofibers 195
3.8.3. Morphological characterization of the HPβCD/E-f composite nanofibers after thermal curing 196
3.8.4. Heavy metal removal performance of HPβCD100/E-f-20/CTR15 composite nanofibers 197
4. CONCLUSION AND FUTURE PROSPECTS 200
LIST OF PUBLICATINS 210
BIBLIOGRAPHY 212

LIST OF ABBREVIATIONS

^{1}H NMR	:	Proton nuclear magnetic resonance
ACN	:	Acetonitrile
AFD	:	Average fiber diameter
BA-a	:	Bisphenol-A and aniline based benzoxazine monomer
CA	:	Cellulose Acetate
CD	:	Cyclodextrin
CDCl3	:	Deuterated chloroform
CTR	:	Citric acid
DCM	:	Dichloromethane
DHPB	:	4,4-Dihydroxybenzophenone
DMA	:	Dynamic mechanical analyzer
DMAc	:	Dimethylacetamide
DMF	:	N,N Dimethylformamide
DMSO-d6	:	Deuterated dimethylsulfoxide
DSC	:	Differential scanning calorimeter
FTIR	:	Fourier transform infrared
GC-MS	:	Gas chromatography-mass spectrometry
HPLC	:	High performance liquid chromatography
HPβCD	:	Hydroxypropyl-β-cyclodextrin

HPγCD	:	Hydroxypropyl-γ-cyclodextrin
ICP-MS	:	Inductively coupled plasma-mass spectroscopy
MB	:	Methylene blue
MCPBz	:	Main-chain polybenzoxazine
MO	:	Methyl orange
MβCD	:	Methyl-β-cyclodextrin
PAHs	:	Polyaromatic hydrocarbons
PAN	:	Poly(acrylonitrile)
PC	:	Polycarbonate
SEM	:	Scanning electron microscope
TGA	:	Thermogravimetric analyzer

LIST OF FIGURES

Figure 1. Photograph of a typical benzoxazine resin. 3

Figure 2. Synthesis of benzoxazine monomer. 3

Figure 3. Molecular structures of the (a) mono-functional, (b) di-functional benzoxazine monomers and (c) main-chain polybenzoxazine. 5

Figure 4. Polymerization of benzoxazine monomers by thermally activated ring-opening reactions. 6

Figure 5. Electrospinning set-up at UNAM. 9

Figure 6. Schematic representations of electrospinning set-up and nanofiber formation. 10

Figure 7. SEM images of MCPBz nanofibers electrospun from (a) 30%, (b) 35%, and (c) 40% solution concentration. 11

Figure 8. SEM images of Nylon-6,6 nanofibers on the single human hair. 13

Figure 9. Synthesis of eugenol-based bio-benzoxazine monomers. 56

Figure 10. The proposed chemical structures and ^{1}H NMR spectra of (a) E-ea, (b) E-a and (c) E-dh in d*6*-DMSO. 58

Figure 11. FTIR spectra of (a) E-ea, (b) E-a and (c) E-dh, (i) in the range of 4000-400cm^{-1} and (ii) in the range of 2000-400cm^{-1}. 61

Figure 12. Mass spectra of (a) E-ea; $[M+H]^+$ (calculated): 234.1489, $[M+H]^+$ (observed): 234.1477, (b) E-a; $[M+H]^+$ (calculated): 282.1489, $[M+H]^+$ (observed): 282.1463, and (c) E-dh; $[M+H]^+$ (calculated): 493.3061, $[M+H]^+$ (observed): 493.3046. 62

Figure 13. Polymerization of eugenol-based bio-benzoxazines with thermally initiated ring-openning reaction. 65

Figure 14. FTIR spectra of (a) E-ea, (b) E-a and (c) E-dh; before and after each thermal curing step (i) in the range of 4000-400cm^{-1} and (ii) in the range of 2000-400cm^{-1}. 67

Figure 15. TGA thermograms of (a) E-ea and ET-ea (b) E-a and PE-a (c) E-dh and PE-dh. 69

Figure 16. Synthesis of thymol-based bio-benzoxazine monomers. 72

Figure 17. The proposed chemical structures and ^{1}H NMR spectra of a) T-ea, b) T-a and c) T-dh in DMSO-*d*6. 74

Figure 18. FTIR spectra of (a) T-ea, (b) T-a and (c) T-dh, (i) in the range of 4000-400cm^{-1} and (ii) in the range of 2000-400cm^{-1}. 77

Figure 19. Mass spectra of (a) T-ea; $[M+H]^+$ (calculated): 220.1695, $[M+H]^+$ (observed): 220.1705, (b) T-a; $[M+H]^+$ (calculated): 268.1695, $[M+H]^+$ (observed): 268.1700, and (c) T-dh; $[M+H]^+$ (calculated): 465.3475, $[M+H]^+$ (observed): 465.3479. 78

Figure 20. Polymerization of thymol-based bio-benzoxazines with thermally initiated ring-opening reaction. 81

Figure 21. FTIR spectra of (a) T-ea, (b) T-a and (c) T-dh after each thermal curing step (i) in the range of 4000-400cm^{-1} and (ii) in the range of 2000-400cm^{-1}. 83

Figure 22. TGA thermograms of (a) T-ea and PT-ea (b) T-a and PT-a (c) T-dh and PT-dh. 85

Figure 23. Synthesis of the PBA-ad6 and PBA-ad12 resins. 90

Figure 24. ^{1}H NMR spectra of (a) PBA-ad6 and (b) PBA-ad12 in $CDCl_3$ (c* corresponds to methylene protons attached to N; e* corresponds to aliphatic protons of

diamine). (Copyright © 2014, Reprinted from Ref. [191] with permission from Elsevier) 91

Figure 25. FTIR spectra and magnified region between 1800 and 500 cm^{-1} of (a) PBA-ad6 and (b) PBA-ad12. (Copyright © 2014, Reprinted from Ref. [191] with permission from Elsevier) 93

Figure 26. SEM images and corresponding fiber diameter distributions of the electrospun nanofibers obtained from solutions of PBA-ad6 (a, b) 30%, (c, d) 35%, (d, e) 40% and (g, h) 45%. Inset shows magnified view of a typical region. (Copyright © 2013, Reprinted from Ref. [191] with permission from Elsevier).....96

Figure 27. SEM images and corresponding fiber diameter distributions of the electrospun nanofibers obtained from solutions of PBA-ad12 (a, b) 15%, (c, d) 18% and (d,e) 20%. Inset depicts magnified view of a typical region. (Copyright © 2014, Reprinted from Ref. [191] with permission from Elsevier).....99

Figure 28. Photographs of the electrospun nanowebs from (a) 40% PBA-ad6, (b) 18% PBA-ad12 and after curing (c) PBA-ad6, (d) PBA-ad12 step by step at 75°C; 1h, 90 °C; 1h, 120 °C; 1h, 150°C;1h , 180°C; 1h and 220 °C; 1h. (Copyright © 2014, Reprinted from Ref. [191] with permission from Elsevier) 100

Figure 29. DSC thermograms of (a) PBA-ad6 and (b) PBA-ad12 nanofibers. (Copyright © 2014, Reprinted from Ref. [191] with permission from Elsevier).....102

Figure 30. SEM images of the electrospun nanofibers before and after thermal treatment; (a) 40% PBA-ad6, (b) 75°C; 1h, (c) 90°C; 1h, (d) 100°C; 1h, (e) 120°C; 1h. (Copyright © 2014, Reproduced from Ref. [191] with permission from Elsevier).....103

Figure 31. SEM images of the electrospun nanofibers before and after thermal treatment; (a) 18% PBA-ad12, (b) 50°C ;1h, (c) 60°C ;1h (d) 75°C; 1h and (e) 120 °C; 1h. (Copyright © 2014, Reproduced from Ref. [191] with permission from Elsevier).104

Figure 32. FTIR spectra and magnified region between 1800 and 400 cm^{-1} of (a) PBA-ad6 and (b) PBA-ad12 nanofibers before and after step cured at 75°C; 1h, 90°C; 1h, 120°C; 1h, 150°C;1h , 180°C; 1h and 220°C; 1h. (Copyright © 2014, Reprinted from Ref. [191] with permission from Elsevier) 106

Figure 33. TGA thermograms and derivative weight losses of (a) PBA-ad6 and (b) PBA-ad12 nanofibers after step cured at 75°C; 1h, 90°C; 1h, 120°C; 1h, 150°C;1h, 180°C; 1h and 220°C; 1h. (Copyright © 2014, Reprinted from Ref. [191] with permission from Elsevier) 108

Figure 34. Synthesis of the DHBP-ad6 and DHBP-ad12 main-chain polybenzoxazine resins. (Copyright © 2016, Reproduced from Ref. [228] with permission from Elsevier) 112

Figure 35. The proposed chemical structures and ^{1}H NMR spectra of a) DHBP-ad6 and b) DHBP-ad12 resins in $CDCl_3$. (Copyright © 2016, Reprinted from Ref. [228] with permission from Elsevier) 113

Figure 36. FTIR spectra of DHBP-ad6 and DHBP-ad12 resins. (Copyright © 2016, Reprinted from Ref. [228] with permission from Elsevier) 114

Figure 37. UV-vis spectra of DHBP, DHBP-ad6 and DHBP-ad12 resins. (Copyright © 2016, Reprinted from Ref. [228] with permission from Elsevier) 115

Figure 38. SEM images of the electrospun nanofibers obtained from solutions of DHBP-ad6 a) 25%, b) 30%, c) 35% and DHBP-ad12 d) 15%, e) 20%, f) 25%. (Copyright © 2016, Reprinted from Ref. [228] with permission from Elsevier) 118

Figure 39. SEM images of a) DHBP-ad6 nanofibers, b) directly thermal-cured DHBP-ad6 nanofibers, c) photo-cured DHBP-ad6 nanofibers, d) photo and thermal-cured DHBP-ad6 nanofibers, e) DHBP-ad12 nanofibers, f) directly thermal-cured DHBP-ad12 nanofibers, g) photo- cured DHBP-ad12 nanofibers, h) photo and thermal-cured DHBP-

ad12 nanofibers. (Copyright © 2016, Reproduced from Ref. [228] with permission from Elsevier) 122

Figure 40. DSC thermograms of a) DHBP-ad6 and b) DHBP-ad12 nanofibers. (Copyright © 2016, Reproduced from Ref. [228] with permission from Elsevier)..... 123

Figure 41. FTIR spectra of a) DHBP-ad6 and b) DHBP-ad12 nanofibers. (Copyright © 2016, Reproduced from Ref. [228] with permission from Elsevier) 125

Figure 42. Photographs of (a) as-electrospun DHBP-ad6 nanofibers, (b) photo-cured DHBP-ad6 nanofibrous mat, (c) photo and thermal-cured DHBP-ad6 nanofibrous mat, (d) as-electrospun DHBP-ad12 nanofibrous mat, (e) photo-cured DHBP-ad12 nanofibers and (f) photo and thermal cured DHBP-ad12 nanofibers. (Copyright © 2016, Reproduced from Ref. [228] with permission from Elsevier) 127

Figure 43. Representative stress-strain curves of the photo and thermal-cured DHBP-ad6 and DHBP-ad12 nanofibrous mats. (Copyright © 2016, Repriented from Ref. [228] with permission from Elsevier)..... 129

Figure 44. TGA thermograms of a) DHBP-ad6 and b) DHBP-ad12 nanofibers. (Copyright © 2016, Repriented from Ref. [228] with permission from Elsevier) 131

Figure 45. SEM images of cross-linked DHBP-ad6 and DHBP-ad12 nanofibers after immersing 24 hours in chloroform, DMF, 1,4-dioxane, DMAc and THF. (Copyright © 2016, Reproduced from Ref. [228] with permission from Elsevier) 133

Figure 46. SEM images of the cross-linked DHBP-ad6 and DHBP-ad12 nanofibers after treating different temperatures in high temperature tube furnace at open air. (Copyright © 2016, Reproduced from Ref. [228] with permission from Elsevier) 134

Figure 47. SEM images of cross-linked DHBP-ad6 and DHBP-ad12 nanofibers after immersing 24 hours in 5M HCl, HNO_3 and H_2SO_4 solutions. (Copyright © 2014, Reproduced from Ref. [228] with permission from Elsevier) 135

Figure 48. Synthesis of BA-a. 139

Figure 49. The proposed chemical structure and 1H NMR spectrum of BA-a in CDCl3. 139

Figure 50. The FTIR spectrum of BA-a. 140

Figure 51. SEM images of (a) CA nanofibers, (b) CA10/BA-a2, (c) CA10/BA-a5 and (d) CA12/BA-a2 composite nanofibers. 142

Figure 52. SEM images of (a) CA10/BA-a2, (b) CA10/BA-a5 and (c) CA12/BA-a2 composite nanofibers cured step-wise at 150, 175, 200 and 225ºC. 143

Figure 53. SEM images of (a) CA nanofibers and (b) CA10/PBA-a5/CTR1 composite nanofibers cured step-wise at 150, 175, 200 and 225ºC. 144

Figure 54. FTIR spectra of BA-a, CA nanofibers, CA10/BA-a5/CTR1 and CA10/PBA-a5/CTR1 composite nanofibers cured step-wise at 150, 175, 200 and 225°C. 147

Figure 55. Photograps of (a) CA nanofibers and (b) CA10/PBA-a5/CTR1 composite nanofibers. 148

Figure 56. TGA thermograms of the (a) CA10/BA-a5/CTR1 and (b) CA10/PBA-a5/CTR1 composite nanofibers. 149

Figure 57. DMA curves of CA nanofibers, CA10/BA-a5/CTR1 and CA10/PBA-a5/CTR1 composite nanofibers. 151

Figure 58. Photograph of the CA nanofibers after DMA measuement. 151

Figure 59. The time dependent phenanthrene removal efficiency CA nanofibers and CA10/PBA-a5/CTR1 composite nanofibers. 153

Figure 60. Cross-linking of BA-a monomer with thermally induced ring-openning reaction. 154

Figure 61. Photographs and SEM images of (a,c) CA nanofibers, (b,d) CA10/PBA-a5/CTR1 composite nanofibers after the filtration test. 155

Figure 62. SEM images of the (a) PC nanofibers, (b) PC18/BA-a5, (c) PC18/BA-a7, (d) PC20/BA-a3, (e) PC20/BA-a5 and (f) PC20/BA-a5/CTR2 composite nanofibers. 158

Figure 63. SEM images of the PC20/BA-a5/CTR2 composite nanofibers cured step-wised at (a) 100°C , (b) +120°C, (c) +140°C and (d) +160°C ('+' is used to show additional 1 hour heat treatment). 160

Figure 64. FTIR spectra of BA-a, PC nanofibers, PC20/ BA-a5/CTR2 composite nanofibers and PC20/ PBA-a5/CTR2 composite nanofibers cured step-wise at 100, 120 and 140°C. 162

Figure 65. TGA thermograms of the PC nanofibers and PC20/PBA-a5/CTR2 composite nanofibers cured step-wise at 100, 120 and 140°C. 163

Figure 66. DMA curves of the PC20/ PBA-a5/CTR2 composite nanofibers before and afer cured step-wise at different temperatures. 165

Figure 67. Schematic view and (b) chemical structures of modified HPβCD, HPγCD and MβCD and (c) SEM images of the electrospun nanofibers obtained from the highly concentrated solutions of modified HPβCD, HPγCD and MβCD. 168

Figure 68. SEM images of the nanofibers obtained from different compositions of CD/BA-a solutions. 171

Figure 69. SEM images of the (a) HPβCD100/BA-a25, (b) HPγCD100/BA-a25 and MβCD125/BA-a25 composite nanofibers after step-wise curing at 150, 175, and 200ºC. 172

Figure 70. SEM images of (a) HPβCD100/BA-a25, (b) HPβCD100/CTR15, (c) HPβCD100/BA-a25/CTR5 and (d) HPβCD100/BA-a25/CTR15; (i) as-electrospun nanofibers and (ii) after step-wise curing at 150, 175, 200 and 225ºC 174

Figure 71. FTIR spectra of (a) HPβCD100/PBA-a25, (b) HPβCD100/CTR15, (c) HPβCD100/PBA-a25/CTR5 and (d) HPβCD100/PBA-a25/CTR15 composite nanofibers obtained at each step of thermal curing. 176

Figure 72. FTIR spectra of (a) HPβCD100/PBA-a25, (b) HPβCD100/CTR15, (c) HPβCD100/PBA-a25/CTR5 and (d) HPβCD100/PBA-a25/CTR15 composite nanofibers obtained at each step of curing.....177

Figure 73. SEM images of the HPβCD100/PBA-a25/CTR15 composite nanofibers after overnight immersing in different solvents. 179

Figure 74. (a) Molecular structure of the PAHs used in the removal experiments and (b) schematic representation of the inclusion complex formation between PAHs and HPβCD. 180

Figure 75. (a) Time and (b) concentration dependent removal efficiency of the HPβCD100/PBA-a25/CTR15 composite nanofibers from the PAHs mixture solution and (c) removal efficiency of the activated charcoal from the PAHs mixture solution. 183

Figure 76. (a) Molecular structure of the dye molecules used in the removal experiments and (b) schematic representation of the inclusion complex formation between MB molecules and HPβCD. 184

Figure 77. (a) Photographs and (b) UV-vis spectra of 20 ppm MO, MB and MO/MB mixture solution. 185

Figure 78. (a) Photographs of the MO/MB mixture solutions after the removal experiment performed at certain time intervals and (b) UV-Vis Spectra of MO/MB dye mixture solution before and after 6 hours removal experiment. 187

Figure 79. (a) The removal efficiency of HPβCD100/PBA-a25/CTR15 composite nanofibers in different concentration of MO/MB dye mixture solutions after 6 hours

removal experiment, Photograps of different concentration MO/MB dye mixture solutions (b) before and (c) after the removal experiment. 189

Figure 80. Heavy metal removal efficiency of the HPβCD100/PBA-a25/CTR15 composite nanofibers in (a) mixture metal ion solution and (b) separate solution of each metal ion. 190

Figure 81. Synthesis of E-f. 193

Figure 82. ^{1}H NMR spectra of (a) eugenol in d*6*-DMSO and (b) E-f in $CDCl_3$. 194

Figure 83. SEM images of (a) HPβCD100/E-f-20/CTR10, (b) HPβCD100/E-f-20/CTR15 and (c) HPβCD100/E-f-25/CTR10 composite nanofibers. 195

Figure 84. SEM images of (a) HPβCD100/PE-f-20/CTR10, (b) HPβCD100/PE-f-20/CTR15 and (c) HPβCD100/PE-f-25/CTR10 composite nanofibers cured step-wise at 140, 160, 180, 200 and 220°C. 196

Figure 85. Heavy metal removal efficiency of the HPβCD100/E-f-20/CTR15 composite nanofibers in (a) mixture metal ion solution and (b) separate solution of each metal ion. 198

LIST OF TABLES

Table 1. Atomic weight percentages of elements in eugenol-based bio-benzoxazines. . 63

Table 2. Thermal properties of the eugenol-based bio-benzoxazines before and after thermal curing. 70

Table 3. Atomic weight percentages of elements in synthesized thymol based bio-benzoxazines. 79

Table 4. Thermal properties of the thymol-based bio-benzoxazines before and after thermal curing. 86

Table 5. The characteristics of the PBA-ad6, PBA-ad12 solutions and their electrospun fibers. (Copyright © 2014, Reprinted from Ref. [191] with permission from Elsevier) . 97

Table 6. The characteristics of the electrospun DHBP-ad6 and DHBP-ad12 nanofibers. (Copyright © 2016, Reprinted from Ref. [228] with permission from Elsevier) 117

Table 7. Mechanical properties of the DHBP-ad6 and DHBP-ad12 nanofibers after photo and thermal curing. (Copyright © 2016, Repriented from Ref. [228] with permission from Elsevier) 129

Table 8. The decomposition temperatures (Td) and char yield of the DHBP-ad6 and DHBP-ad12 nanofibers. (Copyright © 2016, Repriented from Ref. [228] with permission from Elsevier) 132

Table 9. Data obtained from the DMA curves of CA10/BA-a5/CTR1 and CA10/PBA-a5/CTR1 composite nanofibers. 152

Table 10. Heavy metal ion removal efficiency of the HPβCD100/PBA-a25/CTR15 composite nanofibers in the mixture and separate solutions of metal ions. 191

Table 11. Heavy metal ion removal efficiency of the HPβCD100/E-f-20/CTR15 composite nanofibers in mixture and separate solutions of metal ions. 199

1. INTRODUCTION

1.1. Polybenzoxazines

Phenolic resins as a synthetic thermo-setting resin have been used widely in many areas including construction, appliance, electronic and aerospace industries [1]. Although these resins have many desirable properties such as dimensional stability, chemical resistance, flame retardancy, low smoke generation, good electrical and mechanical properties, they have still various drawbacks related with the fundamental polymerization process. Especially, the use of strong acid or base as acatalyst during the synthesis may causes the corrosion of processing equipment, and the release of volatiles during the curing results in internal micro voids as structural defects [2, 3]. Therefore, several attempts have been made to develop novel materials which can overcome the shortcomings of traditional phenolic resins while maintaining their physical and mechanical properties. After various effort, polybenzoxazines have been developed as a new type of phenolic resin with comparable or even superior physical and mechanical properties than conventional phenolic, epoxy, bismaleimide and polyimide resins.

Benzoxazine monomers were first synthesized by Holly and Cope through Mannich condensation reactions of phenols with formaldehyde and amines in solvent [3]. Afterwards, Burke et al. provided significant contribution to the fundamental understanding of benzoxazine chemistry by preparing a variety of small molecular weight benzoxazine monomers [4-10]. Later, Higginbottom first produced cross-linked

polybenzoxazine resins from multifunctional benzoxazine monomers to develop a coating materials, yet properties of the obtained polybenzoxazines were not discussed [11-13]. Subsequently, Reiss et al. investigated the reaction kinetics of benzoxazine oligomer formation from monofunctional benzoxazines and demonstrated that it is not possible to obtain high molecular weight linear polybenzoxazines by using monofunctional benzoxazines [14]. Further, Turpin and Thrane produced self-curable benzoxazine functional cathodic electrocoat resin by using small molecular weight benzoxazine resins synthesized from both multifunctional phenols and amines [15]. In the early 90's, firstly Ning and Ishida reported the mechanical and thermal properties of the polybenzoxazines obtained by the ring- opening reactions of the benzoxazine monomers [2] .

Benzoxazines are molecules in which N and O containing heterocyclic ring is attached to the benzene ring. Conventionally, they are synthesized from a phenolic derivative, a primary amine and formaldehyde by Mannich condensation reaction (Figure 1) [3]. The mechanism for the formation of the benzoxazine ring structure was suggested as, amine reacts with formaldehyde at lower temperatures forming intermediate product N,N-dihydroxymethylamine, subsequently it reacts with the labile hydrogen of the hydroxyl group and ortho position of the phenol at the elevated temperatures to form the oxazine ring (Figure 2) [4].

Figure 1. Photograph of a typical benzoxazine resin. (Photo:Business Wire)

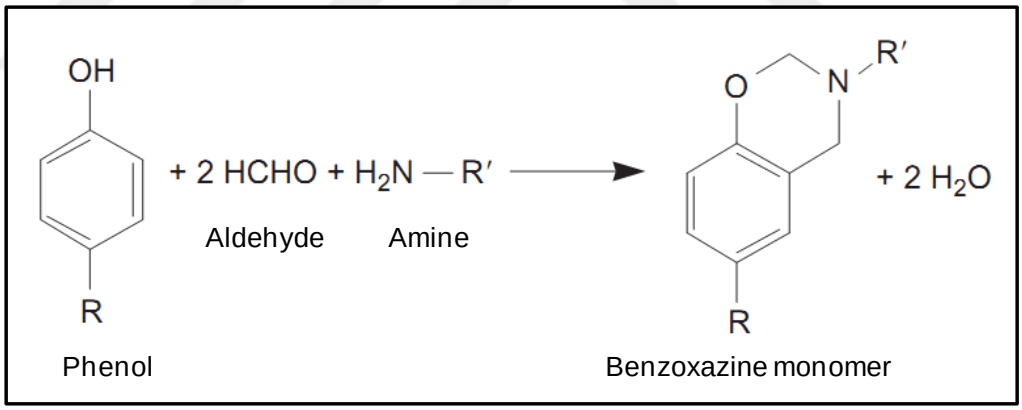

Figure 2. Synthesis of benzoxazine monomer.

Basically, benzoxazines are synthesized from both mono-functional phenols and amines with different substitutional groups and mono-functional benzoxazines are obtained. This type of benzoxazines posses only one oxazine ring for the polymerization through ring-opening and cross-linking reactions. Generally, this type of benzoxazines have

small molecular weight. On the other hand, combination of a difunctional phenol and mono-functional amine and similarly, combination of diamine and mono-functional phenol result with the formation of di-functional benzoxazine monomers having two oxazine rings for the polymerization through ring-opening reactions [1]. This types of benzoxazines are also small molecular weight compounds and polybenzoxazines obtained from mono and di-functional benzoxazines have highly cross-linked structure with branches instead of long linear chain structure. However, a more recent concept of benzoxazine resins involves the use of a difunctional phenolic derivative and a diamine, producing a linear polymer having oxazine ring in the main-chain called as main-chain polybenzoxazine (MCPBz) [16]. Basic structures of these three types of benzoxazines are shown in Figure 3. As MCPBz can be obtained by using difunctional amines and phenolic derivative, and they can also be synthesized as repeating unit of a polymer chain, block copolymer or as a side chain as well [16-33]. The thermal and mechanical performance of polybenzoxazine thermosets obtained from MCPBz are affirmed to be better than those obtained from the benzoxazine monomers [25]. In other words, some of the characteristics; for instance easy processibility, flexibility, high density of crosslink after curing and lower fragility for cured end-structures were achieved for polybenzoxazines. In one respect, MCPBz have potentials as an easy processable and crosslinkable thermoplastic, which become thermosets at ~200°C *via* opening of oxazine ring by thermal activation [34, 35].

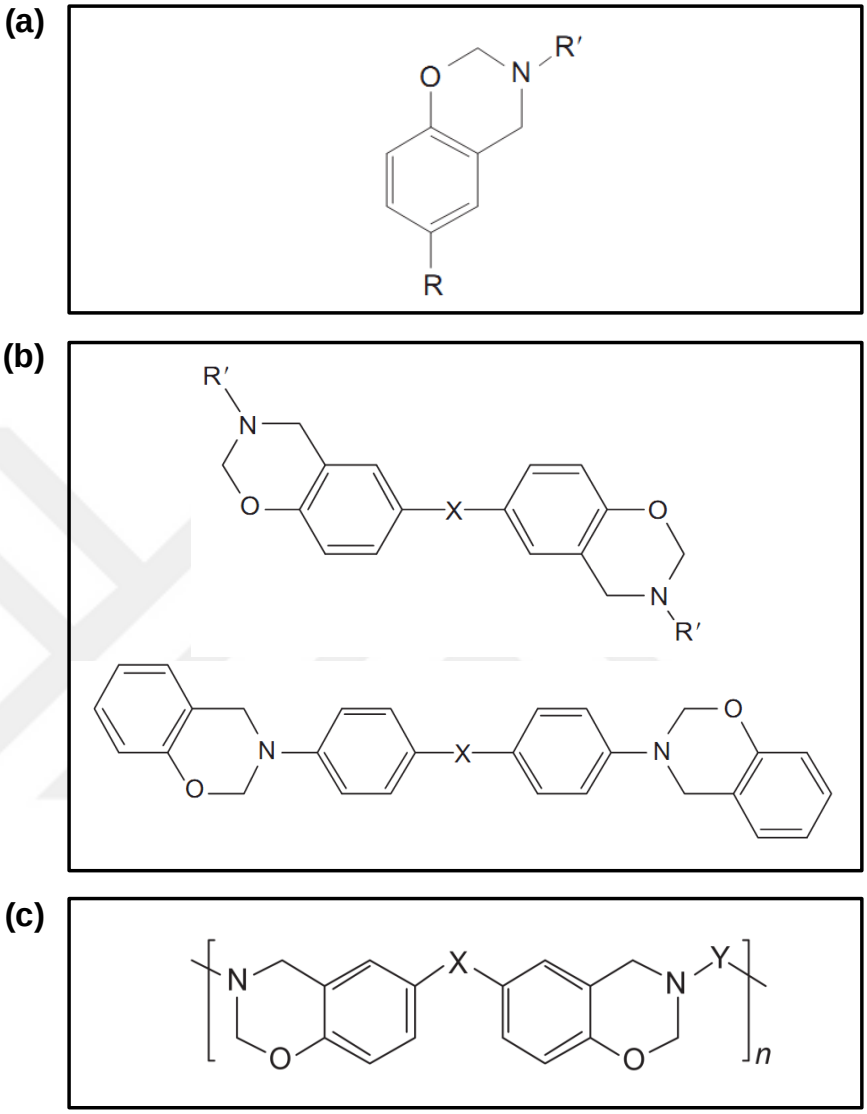

Figure 3. Molecular structures of the (a) mono-functional, (b) di-functional benzoxazine monomers and (c) main-chain polybenzoxazine.

Generally, polybenzoxazines are obtained by polymerization of the benzoxazine monomers through thermally initiated ring-opening reaction with or without initiator and/or catalyst. When the activation takes place with a labile proton initiator, such as

phenol, it yields phenolic polymer namely polybenzoxazine. However, if a nonlabile proton initiator, such as Lewis acid, is used for the relatively low temperature polymerizations, it could lead intermediate arylether structure which is thermally unstable and can transform to the phenolic structure at elevated temperatures [16] (Figure 4).

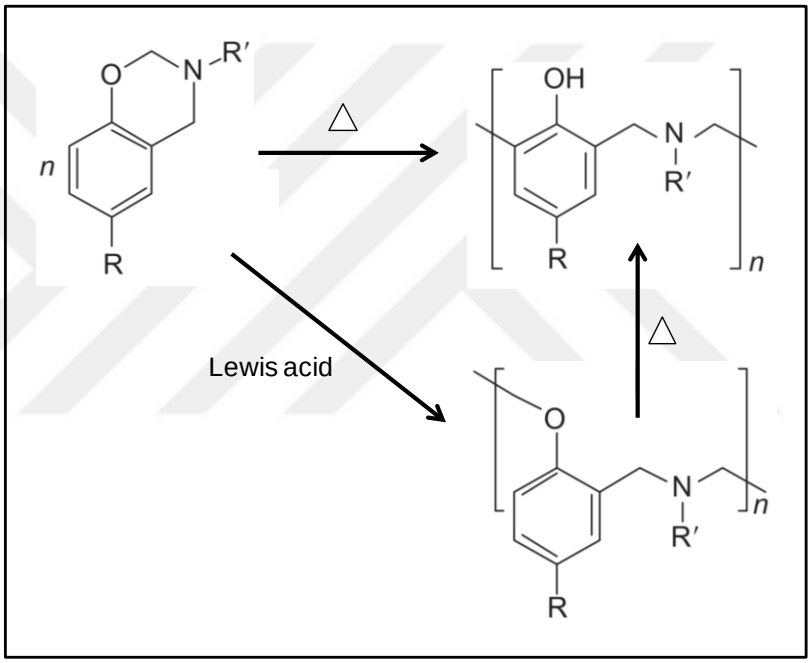

Figure 4. Polymerization of benzoxazine monomers by thermally activated ring-opening reactions.

The polymerization occurs by simple heating because the monomer generally contains a small amount of a cationic initiator, such as phenolic precursors and benzoxazine oligomers, as an impurity. Conventionally, unpurified monomers are polymerized easily by ring-opening reactions by heating the temperature range between 160 and 220ºC [36],

and gelation occurs in one to ten minutes at this temperature range, If there is no initiators and/or catalysts are added. On the other hand, purity of the benzoxazine monomer affects the polymerization rate, hence the final temperature complete the polymerization reaction because high purity benzoxazines require higher temperatures for the polymerization.

Polybenzoxazines as a new member of thermosetting phenolic resins are of great interest for various scientific and industrial fields owing to their superior physical and thermal properties. First of all, the sythesis of benzoxazine monomers or polymerization process do not need any acid or base catalyst. Secondly, benzoxazine resins do not produce any condensation by products and almost no volumetric shrinkage occurs during the polymerization achieved by thermal curing. The other appealing features of benzoxazine resins include, low melt viscosity, ease of processing, good mechanical and electrical properties [11-16]. Because of its outstanding advantages, many studies were done in mainly two fields; first one is to describe the fundamental relationship between its molecular structure and its attractive characteristics, second one is to enhance the existing properties of material for individual applications by incorporating new funtional groups to the molecular structure of benzoxazine monomer or blending such functional group containing molecules with benzoxazine monomer to obtain high performance materials.

Unlike traditional phenolics, the benzoxazine chemistry provides immense molecular design flexibility by using several types of phenols and amines having different

substitution groups. As a result, by designing the molecular structure of the benzoxazines, materials with desired properties such flame-retardant [37-47], high char yield [48-53], low dielectric constant [29, 54-63], low viscosity [54, 64-66], initiator or catalyst containing [67-71], very low surface energy [72-80], photoconductive [81, 82] and tough [83-85] can be obtained. Their wide range of molecular design flexibility which enables the tailoring the properties of the final product for specific applications make them much more attractive in different application areas including electronic packaging, composites, high performance adhesives, non-flammable materials, transportation and aerospace industries [16].

1.2. Electrospinning

Electrospinning is a widely used technique to produce multifunctional nanofibers from remarkable range of organic and inorganic materials including polymers, polymer blends, composites, sol-gels, ceramics and so on [86, 87]. It has many advantages such as low cost, simplicity of set-up, relatively high production rate and reproducibility which make this technique superior to other fiber production methods as melt drawing, template synthesis, phase separation and self-assembly [88-96].

Electrospinning unit at UNAM is given in Figure 5. Basically, it is composed of three main parts; high voltage power supply, syringe pump and collector which is schematically shown in Figure 6. In principle, electrospining solution in a syringe is pumped at a constant rate and high voltage is applied to solution through a thin nozzle

by inducing free charges inside the solution. When repulsive force induced by these charges overcomes the surface tension of the drop formed at the tip of the nozzle, a fluid jet ejects from the droplet by forming conical shape called as Taylor cone [90, 97] (Figure 6). While jet travels through the collector, solvent evaporates and dry nanofibers deposited on the collector randomly. As a result, fibers with diameter ranging from tens of nanometers to few microns can be obtained as a mat on the collector [90, 97].

Figure 5. Electrospinning set-up at UNAM.

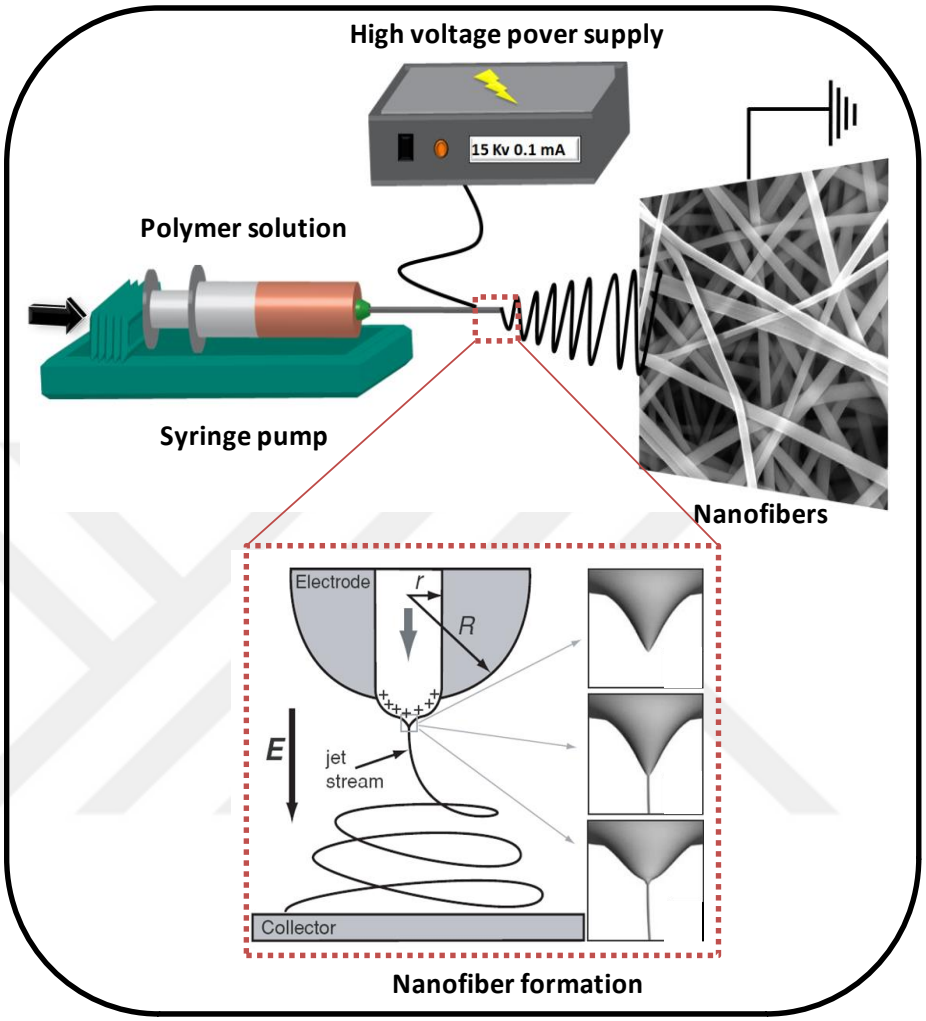

Figure 6. Schematic representations of electrospinning set-up and nanofiber formation.

In the electrospinning process, the morphological characteristics and the diameter of the electrospun nanofibers are governed by process parameters such as applied voltage, tip-to-collector distance, flow rate of the polymer solution and nozzle diameter; on the other hand, polymer/solution parameters such as polymer type, molecular weight, solvent, concentration, surface tension and conductivity of the polymer solution and fluid elasticity have shown a great influence. Notably, ambient conditions such as humidity

and temperature also play a crucial role [90, 97, 100-108]. It is possible to fabricate nanofibers with various morphology (beaded fibers, bead-free fibers) and different fiber diameters by varying these parameters. All these parameters should be examined to obtain optimum conditions for the production of bead free and uniform nanofibers. Unlike the process parameters and ambient conditions, polymer/solution parametrs posses higher effect on the morphology of nanofibers. For the polymeric systems, molecular weight of the polymer as a result polymer solution concentration greatly affect the viscosity of the electrospinning solution [90]. Therefore, required chain entenglement for the formation of nanofibers can be provided by adequate concentration of each polymer with specific molecular weight. The optimum level of entanglement and overlapping are crucial to maintain the continuity of the jet during the electrospinning. If It is not achieved, jets break up and electrospraying takes place resulting beads instead of continuous uniform fibers [90]. Figure 7 represents the effect of the solution concentration on the morphology of MCPBz nanofibers.

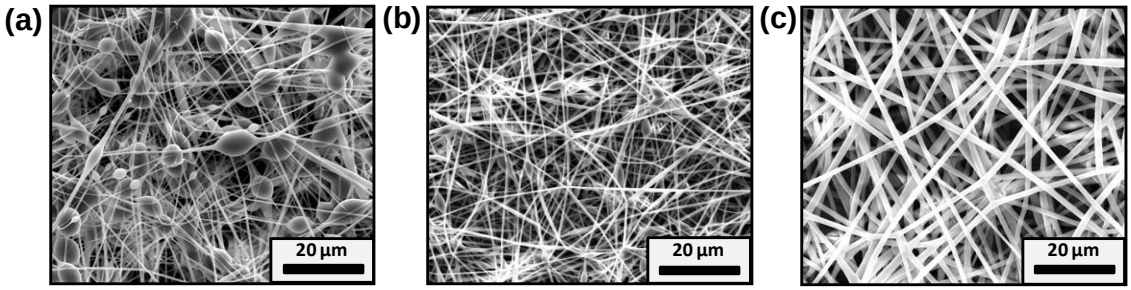

Figure 7. SEM images of MCPBz nanofibers electrospun from (a) 30%, (b) 35%, and (c) 40% solution concentration.

At lower concentrations, it is common to observe beads along with the fibers because of the higher amount of solvent and fewer chain entanglements causing a prevailing effect during electrospinning [86, 106]. As the polymer concentration increased, the number of beads decreases dramatically and elongated beaded nanofibers areproduced due to the relatively low viscosity which resultes in destabilization of the electrified jet during the electrospinning process and thus caused the formation of elongated beads instead of uniform fibers. When the polymer concentration reaches to optimum level in solution, transformation from beaded nanofibers to bead free nanofibers is achieved. The effect of concentration on the diameter of PBA-ad6 nanofibers clearly observed in Figure 7. The diameter of the fibers increased from nanometer to micron scale when the concentration of the polymer solution increased. The reason for increase in fiber diameter is the greater resistance of the solution to be stretched because of the more chain entanglements at higher polymer concentration [86].

Because of the nano-scale fiber diameters which is about one thousand times thinner a single human hair (Figure 8), electrospun nanofibers/nanowebs possess several appreciable features such as extremely high surface area, very light-weight, nano-porous features and distinctive physical and mechanical properties [90, 91, 98, 99]. Also, for the production of multifunctional nanofibers, electrospinning process allows the control of the fiber surface morphology, fiber orientation and cross sectional configuration, and offers flexibility for physical/chemical modification both during electrospinning and post-processing. Thus, it is possible to enhance the properties of nanofibers by simply

adding functional additives and/or nanoparticles into the fiber matrix and/or onto fiber surface [89-91, 108-116]. Owing to their distinctive properties, it has been shown that electrospun nanofibers/nanowebs have potentials for various applications in the field of food and agriculture [117-124], biomedical (wound dressing, tissue engineering, drug delivery) [125-134], functional textiles [91], filter/membrane (separation and affinity membrane, molecular filtration, liquid and gas filtration) [135-145], energy (solar cells, fuel cells, supercapacitors, hydrogen storage, optoelectronics, transistors) [146-150], sensor [151-156], catalysts/enzymes [157-164] and nanocomposite [90, 91, 97, 138, 165, 166].

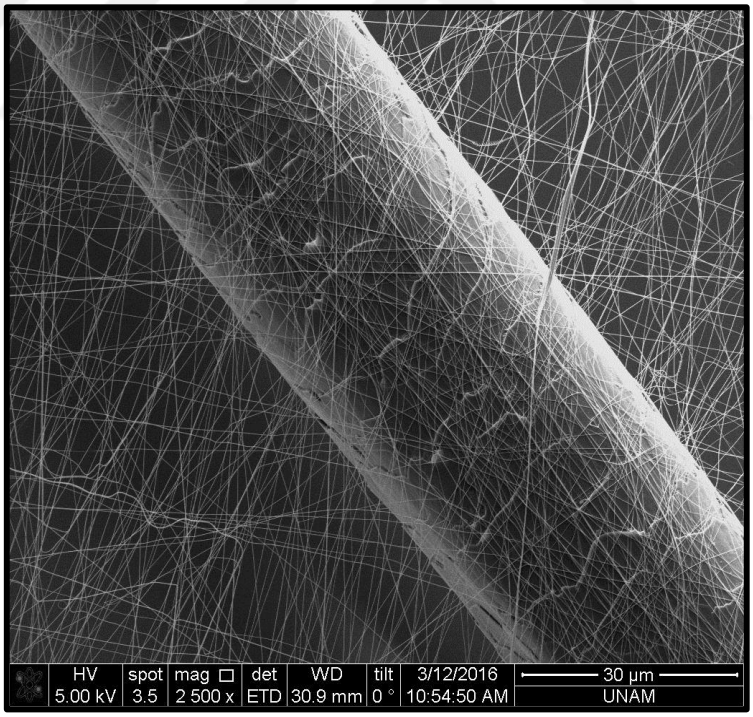

Figure 8. SEM images of Nylon-6,6 nanofibers on the single human hair.

1.3. Polybenzoxazine based nanofibers

The benzoxazine monomers could readily form thermosetting polybenzoxazines by *in situ* thermally initiated ring-opening polymerization, hence, they are promising materials for both the surface modification of polymeric nanofibrous mats and the production of polybenzoxazine based nanofibers. Electrospinning is a widely used technique to produce multifunctional nanofibers from remarkable range of organic and inorganic materials and nanofibers produced by this technique have distinctive chemical, physical and mechanical properties when compared to their bulk or film forms. Polybenzoxazines are extensively studied in the literature with their different forms such as bulk [67, 167-170], film [61, 72, 171-182], aerogel [183-188], porous membrane [189, 190], etc. for various applications. On the other hand, electrospinning of nanofibers from polybenzoxazine resins is a new concept.

Until now, various approaches such as plasma treatment, chemical deposition, colloidal assembly, lithography and template-based techniques have been employed to produce superhydrophobic membranes [192-195]. However, they have still some limitations for large-scale fabrication of such functional membranes and for practical applications due to costly and complicated fabrication procedures, harsh practical conditions, low stability and flexibility, as well as poor selectivity and recyclability. On the other hand, electrospinning is a simple but powerful technique for the preparation of functional fibrous membranes with nano- and microscale levels from variety of polymers, polymer

blends, sol–gels, composites and ceramics [86, 87]. Moreover, nanofibers produced by electrospinning have several appreciable features such as a very large surface area to volume ratio and nanoscale pores. In addition, materials having nanofibrous structure exhibit distinctive chemical, physical and mechanical properties when compared to their bulk or film forms. Surface modification of such functional membranes with hierarchical rough surface and controlled wettability provides the fabrication of superhydrophobic membranes [193, 196]. It is well known that polybenzoxazine is addition polymerized phenolic system with low surface energy and it could induce the hydrophobicity and oleophilicity along with a wide range of interesting features including near-zero volumetric change upon curing, chemical resistance, low water absorption, and high glass-transition temperature, which make it a promising component for functional membranes with special wettability [197-199]. Although it has been known for some time that superhydrophobic spin coating could be prepared from polybenzoxazine [78, 199], just recently, very few studies reported about the development of flexible polybenzoxazine modified nanofibrous membranes especially for oil-water separation [147, 200, 201].

Selective adsorption of the oil from oil–water mixtures generally depends on the hydrophobicity and oleophilicity of the membrane surface. Conventionally, the wettability of solid surfaces is controlled by the surface chemistry and the geometrical roughness [202-204]. Therefore production of poybenzoxazine based nanofibrous membranes is a promising approach to obtain hydrophobic surface membrane due to the

high surface area and roughness provided by nanofibers along with the hydrophobic characteristic of cross-linked molecular structure of the polybenzoxazines. Additionally, the introduction of a proper roughness could make a smooth hydrophobic surface to be more hydrophobic or even superhydrophobic due to the air to be entrapped under the water droplet as a cushion, on the other hand, an oleophilic surface becomes more oleophilic or even superoleophilic due to the capillary effect [205-208]. Since benzoxazine chemistry allows the incorporation of other nanoparticles such as SiO_2 [147, 200, 201], Al_2O_3 [209], and TiO_2 [210] during the process, superhydrophobic surfaces can be obtained easily by using benzoxazine as a precursor for the production of superhydrophobic membranes for oil-water separation purposess.

Generally, it is difficult to obtain nanofibers from monomers or small molecules since chain entanglement and overlapping is the key factor for the formation of nanofibers during the electrospinning. Kao and coworkers demonstrated a facile fabrication of non-fluorine and non-silicon low-surface-free energy fibers from the electrospinning of polyacrylonitrile (PAN) and phenol-aniline based benzoxazine (P-a) blend solution [211]. PAN which is an ideal blend material due to its high melting temperature and good missibility with the P-a monomer was used as carrier matrix and it was aimed to improve the practical application of polybenzoxazine as superhydrophobic fibrous mats. Thermally activated ring-opening of P-a affords the poly(P-a) networks which bear a great amount of phenolic hydroxyl groups providing hydrophobic feature to the PAN nanofibrous membrane.

Li and Liu fabricated the polyelectrolyte composite membranes from polybenzoxazine modified polybenzimidazole (PBI) nanofibers for proton exchange membrane fuel cells [212]. Composite nanofibers were produced by adding benzoxazine-containing polymer as a crosslinking agent to the electrospinning PBI solutions. The nanofibers were cross-linked through thermally initiatd ring-opening and cross-linking reactions of the benzoxazine groups. After thermal curing, mechanical strength and solvent resistance of PBI nanofibers were enhanced owing to the cross-linking. In addition remarkable improvement was achieved in mechanical properties, acid uptakes, and dimensional stability upon acid doping.

Another interesting application of the polybenzoxazine is the use as a precursor for the production of magnetic carbon nanofibers (MCNFs). Traditionally, synthetic approaches such as substrate method, spraying method, vapor growth method and plasma-enhanced chemical vapor deposition method are used for the fabrication of CNFs. However, these methods are not only complicated and costly, but also not suitable for the production of Fe_3O_4 nanoparticle embedded porous MCNFs since it is dificult to increase pore volume and mass fraction of Fe_3O_4 [213]. On the other hand, electrospinning is a simple and inexpensive method for the fabrication of nano- and mesoscale 1D composite nanofibers from the combination of both organic and inorganic precursors [155, 195]. By the calcination of these electrospun precursor nanofibers, MCNFs can be produced [214]. As a principle, the natures of the precursor nanofibers strongly effect the structural properties of electrospun MCNFs, since internal and surface defects of the precursor

nanofibers may be easily transferred into the obtained MCNFs causing the performance deterioration [215]. Polyacrilonitrile is the most commonly used precursor polymer for the production of electrospun CNFs [216]. Beside this, pitch, poly (vinyl alcohol), poly (vinylidene fluoride), poly (methyl methacrylate), poly (vinyl pyrrolidone) and poly (p-xylene tetrahydrothiophenium chloride), have also been reported [213, 217-219]. However, in order to prevent fibers fusing together during carbonization, these thermoplastic polymers require time consuming and expensive stabilization process converting into highly condensed thermosetting fibers by complex chemical and physical reactions, which limites the practical use of these electrospun CNFs [213]. On the other hand, polybenzoxazine owing to the interesting features such as near-zero volumetric change upon curing, high glass-transition temperature and high char yield [197, 199, 220], are promising precursor for high-performance CNFs.

Since chain entanglement and overlapping play a vital role for the formation of nanofibers during the electrospinning, main-chain polybenzoxazines are good materials for the production of nanofibers from benzoxazines. By combining the facinating properties of polybenzoxazines and interesting features of the electrospun nanofibers, after curing highly cross-linked thermoset polybenzoxazine nanofibers which have good mechanical/thermal properties and high stability at harsh enviromental conditions can be obtained. In addition, because of the cross-linked structure and roughness by nanoscale fibrous structure, these materials possess inherently hydrophobic characteristic without

further surface modification. Therefore, these materials are quite useful for the filtration applications which require high temperatures and harsh enviromental conditions.

First study that accomplished to produce bead-free and uniform polybenzoxazine nanofibers from MCPBz without using any carrier polymeric matrices reported by our group [191]. Briefly, two different types of MCPBz, DHBP-ad6 and DHBP-ad12 were synthesized by using two types of difunctional amine (1, 6-diaminohexane and 1, 12-diaminododecane), bisphenol-A, and paraformaldehyde as starting materials through a Mannich reaction. Highly concentrated homogeneous solutions of both MCPBz were prepared and bead free nanofibers were produced after optimization of the electrospinning parameters. DHBP-ad6 and DHBP-ad12 nanofibrous mats were obtained as free-standing, yet, DHBP-ad12 nanofibers was more flexible than DHBP-ad6 nanofibers which was possibly resulted from the longer diamine chain length and higher molecular weight of DHBP-ad12. Furthermore, curing studies on these nanofibrous mats provide us good starting point of crosslinking of MCPBz nanofibers. Although, the fibrous structure could not be preserved during the thermal curing of DHBP-ad6 and DHBP-ad12 nanofibrous mats due to the low melting point of these MCPBz, flexible and free-standing cross-linked films were obtained.

Generally, polymerization/cross-linking of benzoxazines can be achieved by thermal curing which is a thermally induced ring opening reaction of benzoxazines and MCPBz occur at around 200°C [16]. First successful study for the cross-linking of MCPBz nanofibers by thermal curing was reported by Li et al. [221]. They synthesized the

MCPBz by using 4,4-diaminophenylether, bisphenol-A, and formaldehyde as starting materials and they produced MCPBz nanofibers which are mechanically robust and stable under harsh environmental conditions. Since the melting point of the nanofibers were higher than their curing temperatures, they achieved to obtain cross-linked MCPBz nanofibers by thermal curing. However, in our previous study we were not able to produce cross-linked nanofibers from long linear aliphatic diamine based MCPBz nanofibers by directly thermal curing because of the very low melting points of PBA-ad6 and PBA-ad12 nanofibers (73 and 42ºC) which are quite lower than their curing temperatures (203 and 205ºC). In the following study we focus on two step curing procedure including the photo and thermal curing for the cross-linking of this type of MCPBz nanofibers. Photo-curing is another method that can be used to obtain cross-linked materials from benzoxazines having photo active group or part in their structure. Although, thermal curing is very common basic method to polymerize or cross-link benzoxazines and MCPBz, there are few studies that uses photo-curing for the polymerization of benzoxazines [222, 223]. In addition, benzophenone based benzoxazine monomers were synthesized and used as photoinitiator for the photopolymerization of acrylate monomers [224-227]. Besides, photopolymerization as a preliminary step and thermally activated polymerization for the ring-opening and cross-linking of methacryloyl functional benzoxazines were studied [24]. All these research works provide us useful information on designing new kind of benzoxazine resins to improve the curing procedure of MCPBz nanofibers in order to achieve cross-

linking without deteriorating the fiber structure. For this purpose, two novel MCPBz (DHBP-ad6 and DHBP-ad12) which consist of a benzophenone unit in the polymer main-chain were synthesized [228]. Due to the presence of benzophenone unit in the main-chain, DHBP-ad6 and DHBP-ad12 nanofibers are able to crosslink by UV-light initiated free radical polymerization. Therefore, by synthesizing benzophenone containing MCPBz, we aimed to provide preliminary cross-linking through photo curing to enhance the thermal stability of nanofibers for thermal curing in which ring-opening and almost complete cross-linking can be achieved as maintaining the nanofibrous structure.

2. EXPERIMENTAL DETAILS

2.1. Materials

Paraformaldehyde (Sigma-Aldrich, 95%), bisphenol-A (Sigma-Aldrich, 97%), 1,4-dihydroxybenzophenone (DHBP, Alfa-easer, 98%), thymol (Alfa Aesar, ≥%98), eugenol (Sigma-Aldrich, 99%), 1,6-diaminohexane (Aldrich, 98%), 1,12-diaminododecane (Aldrich, 98%), ethylamine (Fluka, 70 wt % in water), aniline (Sigma-Aldrich, 99.5%), furfurylamine (Aldrich), cellulose acetate (CA, Mw: 30000, 39.8 wt. % acetyl), poly (bisphenol-a carbonate) (PC, Aldrich), hydroxypropyl-β-cyclodextrin (HPβCD, molar substitution:~ 0.6), hydroxypropyl-γ-cyclodextrin (HPγCD, molar substitution:~ 0.6), methyl-β-cyclodextrin (MβCD, molar substitution:1.6-1.9), fluoranthene (FLT, Aldrich, 98%), pyrene (PYR, Aldrich, 98%), methylene blue (Sigma-Aldrich) , methyl orange (Fisher Scientific Com), zinc acetate dihydrate (Sigma-Aldrich, 98%), lead (II) nitrate (Sigma-Aldrich, 99.0%), manganese (II) acetate tetrahydrate (Sigma-Aldrich, 99%) and nickel (II) acetate tetrahydrate (Sigma-Aldrich, 99.0%), cadmium nitrate tetrahydrate (Fluka, ≥99%), activated charcoal (Sigma-Aldrich, untreated, granular, 8-20 mesh), citric acid (CTR, Sigma), sodium hydroxide (NaOH) (Fluka, P98%, small beads), chloroform (Sigma-Aldrich, 99-99.4%), N,N-dimethylformamide (DMF, Fluka, 98%), acetone (Sigma-Aldrich, ≥99%), ethanol (Sigma-Aldrich ≥99.8%), methanol (Sigma-Aldrich, ≥99.7%), tetrahydrofuran (THF, Merck, 99.7%), 1,4-dioxane (Sigma-Aldrich, 99%), dimethylacetamide (DMAc, Sigma-Aldrich, 99%), acetonitrile (ACN,

Chromasolv, HPLC ≥99.9%), dimethyl sulfoxide (DMSO) (Sigma-Aldrich, 99.9%), hydrochloric acid (HCl, Sigma-Riedel, 37%), sulfuric acid (H_2SO_4, Sigma-Riedel, 95%), nitric acid (HNO_3, Sigma-Riedel, 65%), deuterated chloroform ($CDCl_3$, deuteration degree min. 99.8% for NMR spectroscopy, Merck), deuterated dimethylsulfoxide (*d6*-DMSO, deuteration degree min. 99.8% for NMR spectroscopy, Merck) and potassium bromide (KBr, 99%, FTIR grade, Sigma-Aldrich) were obtained commercially. The water used was from a Millipore Milli-Q Ultrapure Water System. All the materials were used without any purification.

2.2. Synthesis of benzoxazine monomers and main-chain polybenzoxazines

2.2.1. Synthesis of bisphenol-A and aniline based benzoxazine monomer (BA-a)

Benzoxazine monomer was synthesized from bisphenol-A (0.05 mol), aniline (0.1 mol) and paraformaldehyde (0.2 mol) by employing solventless method. All the reactants were mixed in 50 ml vial and reaction mixture was stirred for 1hour at 110ºC in open atmosphere. Benzoxazine monomer (BA-a) was produced as yellow highly dense viscous liquid. Then, it kept at room temperature to cool down and transformed the solid form. Product was dissolved in chloroform and then chloroform was removed completely by using rotary evaporator system. Product was washed with 3M NaOH and residual reactants were removed. Final product was dried in vacuum oven over night and yellow powder was obtained.

2.2.2. Synthesis of eugenol-based bio-benzoxazine monomers

Eugenol as a phenolic derivative and three primary amine with different functionalities, aniline (aromatic), ethylamine (aliphatic) and 1,6-diaminohexane (difunctional) were used as starting materials. Synthesis process of the eugenol-based benzoxazine monomers and results for the novel bio-benzoxazine monomers are as follow;

Ethylamine (2.58 g, 40 mmol), paraformaldehyde (2.52 g, 80 mmol) and eugenol (6.14 ml, 40 mmol) were mixed and stirred at room temperature until the solids were

dissolved. The mixture was heated at 110°C for 2 hours and then cooled to room temperature. Yield = 89%; ^{1}H NMR (*d6*-DMSO, ppm) 6.59 (d, 2H), 5.92 (m, 1H), 5.03 (d, 2H), 4.79 (s, 2H), 3.88 (s, 2H), 3.71 (s, 3H), 3.24 (d, 2H), 2.67 (m, 2H) and 1.07 (t, 3H); FTIR (KBr, cm^{-1}) 3070, 2968, 2932, 2897, 2834, 1594, 1495, 1464, 1366, 1322, 1229, 1147, 1093, 1036, 997, 917, 844, 742, 629, 604 Calculated values of elemental composition of E-ea (C14H19NO2) are % C: 72.07, % H: 8.21, % N: 6.01 and observed percentages of C, H and N for E-ea were 71.28, 7.90 and 5.21, respectively. Mass spectroscopy results are $(M+H)^{+}$ calculated: 234.1489; observed: 234.1477.

Aniline (3.64 ml, 40 mmol), paraformaldehyde (2.52 g, 80 mmol) and eugenol (6.14 ml, 40 mmol) were mixed and stirred at room temperature until the solids were dissolved. The mixture was heated at 110°C for 2 hours and then cooled to room temperature. Yield = 79%; ^{1}H NMR (*d6*-DMSO, ppm) 7.23-7.12 (m, 2H), 6.89–6.51 (m, %H), 5.93 (m, 1H), 5.41 (s, 2H) , 4.59 (s, 2H), 3.74 (s, 3H) and 3.24 (d, 2H); FTIR (KBr, cm^{-1}) 3058, 3010, 2947, 2895, 2834, 2824, 1594, 1494, 1460, 1366, 1329, 1229, 1139, 1078, 974, 940, 919, 771, 698, 600. Calculated values of elemental composition of E-a (C18H19NO2) are % C: 76.84, % H: 6.81, % N: 4.98 and observed percentages of C, H and N for E-a were 74.97, 6.78 and 5.13, respectively. Mass spectroscopy results are $(M+H)^{+}$ calculated: 282.1489; observed: 282.1463.

Hexamethylenediamine (2.37 g, 20 mmol), paraformaldehyde (2.52 g, 80 mmol) and eugenol (6.14 ml, 40 mmol) were mixed and stirred at room temperature until the solids were dissolved. The mixture was heated at 110°C for 2 hours and then cooled to room

temperature. Yield = 91%; ^{1}H NMR (*d6*-DMSO, ppm) 6.71 (m, 4H), 5.92 (m, 2H), 5.02 (m, 4H), 4.76 (s, 4H), 3.85 (s, 4H), 3.69 (s, 6H), 3.22 (d, 4H), 2.58 (m, 4H) and 1.28 (m, 8H); FTIR (KBr, cm^{-1}) 3072, 2997, 2930, 2849, 1592, 1498, 1462, 1320, 1272, 1226, 1147, 1097, 922, 840, 692, 602. Calculated values of elemental composition of E-dh (C30H40N2O4) are % C: 71.15, % H: 8.18, % N: 5.84 and observed percentages of C, H and N for E-dh were 73.14, 8.18 and 5.69, respectively. Mass spectroscopy results are $(M+H)^{+}$ calculated: 493.3061; observed: 493.3046.

2.2.3. Synthesis of thymol-based bio-benzoxazine monomers

Thymol as a phenolic derivative and three primary amine with different functionalities, aniline (aromatic), ethylamine (aliphatic) and 1,6-diaminohexane (difunctional) were used as starting materials. Synthesis process of the thymol-based benzoxazine monomers and results for the novel bio-benzoxazine monomers are as follow;

Ethylamine (2.58g, 40 mmol), paraformaldehyde (2.52 g, 80 mmol) and thymol (6.12 g, 40 mmol) were mixed and stirred at room temperature until the solids were dissolved. The mixture was heated at 110°C for 2 hours and then cooled to room temperature. Yield = 92%; ^{1}H NMR (*d6*-DMSO, ppm): 6.88–6.64 (d,2H), 4.76 (s, 2H), 3.80 (s, 2H), 3.13 (m, 1H), 2.67 (t, 3H), 2.07 (s, 3H) and 1.10 (m, 9H); FTIR (KBr, cm^{-1}): 2961, 2872, 1609, 1582, 1492, 1455, 1384, 1349, 1253, 1222, 1149, 1028, 966, 945, 805, 753, 692 cm^{-1}. Calculated values of elemental composition of T-ea (C14H21NO) are % C: 76.67, % H: 9.64, % N: 6.38 and observed percentages of C, H and N for T-ea were 75.29, 8.82

and 6.31, respectively. Mass spectroscopy results are $(M+H)^+$ calculated: 220.1695; observed: 220.1705.

Aniline (3.64 ml, 40 mmol), paraformaldehyde (2.52 g, 80 mmol) and thymol (6.12 g, 40 mmol) were mixed and stirred at room temperature until the solids were dissolved. The mixture was heated at 110°C for 2 h and then cooled to room temperature. Yield = 83%; ^{1}H NMR (*d6*-DMSO, ppm): 7.24-7.16 (m, 5H), 6.93–6.68 (m, 2H), 5.39 (s, 2H), 4.51 (s, 2H), 3.13 (m, 1H), 2.17 (s, 3H) and 1.10 (m, 9H); FTIR (KBr, cm^{-1}): 2960, 2868, 1601, 1496, 1455, 1375, 1250, 1223, 1168, 1046, 972, 943, 811, 753, 692 cm^{-1}. Calculated values of elemental composition of T-a (C18H21NO) are % C: 80.86, % H: 7.91, % N: 5.23 and observed percentages of C, H and N for T-a were 80.45, 7.94 and 5.39, respectively. Mass spectroscopy results are $(M+H)^+$ calculated: 268.1695; observed: 268.1700.

Hexamethylenediamine (2.37g, 20 mmol), paraformaldehyde (2.52 g, 80 mmol) and thymol (6.12 g, 40 mmol) were mixed and stirred at room temperature until the solids were dissolved. The mixture was heated at 110°C for 2 hours and then cooled to room temperature. Yield = 92%; ^{1}H NMR (*d6*-DMSO, ppm): 7.06-6.76 (m, 4H), 4.89 (s, 4H), 3.81 (s, 4H), 3.13 (m, 2H), 2.80 (m, 4H), 2.20 (s, 6H), 1.45 (m, 8H) and 1.10 (m, 9H); FTIR (KBr, cm^{-1}): 2953, 2864, 1613, 1580, 1490, 1457, 1359, 1251, 1226, 1147, 1112, 1051, 966, 947, 805, 753 cm^{-1}. Calculated values of elemental composition of T-dh (C30H44N2O2) are % C: 77.54, % H: 9.54, % N: 6.03 and observed percentages of C,

H and N for T-dh were 75.87, 8.76 and 6.18, respectively. Mass spectroscopy results are $(M+H)^+$ calculated: 465.3475; observed: 465.3479.

2.2.4. Synthesis of fully bio-based benzoxazine monomer

Fully bio-based benzoxazine monomer (E-f) synthesized from naturally occuring compounds eugenol and furfurylamine. Furfurylamine (3.88 g, 40 mmol), paraformaldehyde (2.52 g, 80 mmol) and eugenol (6.57 g, 40 mmol) were mixed and stirred at room temperature until the solids were dissolved. The mixture was heated at 110°C for 3 hours and then cooled to room temperature. Yield: 91%, FTIR (KBr, cm^{-1}): 2906, 2837, 1586, 1493, 1455, 1292, 1225, 1143, 1010, 921, 832, 730. ^{1}H NMR ($CDCl_3$, ppm): 7.42 (d, 1H), 6.27−6.88 (m, 4H), 5.96 (m, 1H), 5.10 (d, 2h), 4.97 (s, 2H), 4.01 (s, 2H), 3.94 (s, 2H), 3.89 (s, 3H) and 3.31 (d, 2H).

2.2.5. Synthesis of main-chain polybenzoxazine resins

Two different types of main-chain polybenzoxazine (MCPBz) resin were synthesized from two different difunctional amines (1,6-diaminohexane and 1,12-diaminododecane), bisphenol-A and paraformaldehyde as starting materials by using solvent method. The MCPBz named as PBA-ad6 was synthesized from 1,6-diaminohexane (25 mmol), bisphenol-A (25 mmol) and paraformaldehyde (100 mmol) in a 1:1:4 M ratio. Reactants were taken in a 500-ml round-bottom flask and 250 ml of chloroform was added to the reaction mixture. Then, the solution mixture was refluxed for 7 hours at 60ºC. Afterwards, chloroform was evaporated completely by using rotary-evaporator system

and the product was dried under vacuum at 45ºC for 24 hours. In order to remove any residual reactants, PBA-ad6 was purified by washing through with cold methanol several times and then dried under vacuum at 45ºC for 24 hours. Yield of the synthesized PBA-ad6 was 83%. According to the GPC measurements, weight average molecular weight (Mw) and polydispersity index (PDI) of this sample were calculated as ~11,500 and 4.7, respectively. Same procedure was followed for the synthesis of PBA-ad12; 1,12-diaminododecane (25 mmol), bisphenol-A (25 mmol) and paraformaldehyde (100 mmol) were put in a 500-ml round-bottom flask and 250 ml of chloroform was added to the reaction mixture. In this case, the solution was refluxed for 10 hours at 60ºC. For PBA-ad12, the drying and purification steps were same as PBA-ad6. Yield of the synthesized PBAad12 was 71%. According to the GPC measurements, Mw and PDI of this sample was calculated as ~17,000 and 5.3, respectively.

Two novel MCPBz were synthesized by using two different amines (1, 6-diaminohexane and 1,12-diaminododecane), phenolic derivative (1,4-dihydroxybenzophenone) and paraformaldehyde as starting materials. For the synthesis of first MCPBz named as DHBPad6, 1,6-diaminohexane (10 mmol), 1,4-dihydroxybenzophenone (10 mmol) and paraformaldehyde (40 mmol) were dissolved in 200 ml chloroform and refluxed at 60 ºC for 30 hours. For the synthesis of second MCPBz named as DHBP-ad12, 1,12-diaminododecane (10 mmol), 1,4-dihydroxybenzophenone (10 mmol) and paraformaldehyde (40 mmol) were dissolved in 200 ml chloroform and refluxed at 60 ºC for 36 hours. Reaction mixtures were kept in the fume hood to cool down room

temperature, then chloroform was evaporated completely from the reaction mixture by using rotary evaporator system and the product was dried under vacuum at 35ºC for 24 hours. In order to remove any residual reactant, DHBP-ad6 was purified by washing through with cold methanol several times and then dried over night under vacuum at 35 ºC. yield of the synthesized DHBP-ad6 and DHBP-ad12 were 76% and 87%, respectively. According to the GPC measurements, Mw of DHBPad6 and DHBP-ad12 were calculated as ~10,000 (PDI:2.5) and ~15,000 (PDI:2.8), respectively.

2.3. Preparation of the solutions and electrospinning of nanofibers

2.3.1. Preparation of PBA-ad6 and PBA-ad12 solutions and electrospinning of PBA-ad6 and PBA-ad12 nanofibers

The homogenous solutions of PBA-ad6 and PBA-ad12 were prepared in binary chloroform/DMF mixture solvent system (chloroform:DMF; 4:1, v/v). For the electrospinning of PBA-ad6 nanofibers, solution concentration was varied from 30% to 45% (w/v) and clear light yellow solutions were obtained after stirring for 3 hours at room temperature. For the electrospinning of PBA-ad12 nanofibers, 15, 18 and 20% (w/v) solutions were prepared and solutions were stirred for 6 hours to obtain a clear and homogenous solutions. The solutions were taken in 1 ml syringes with metallic needle of 0.6 mm outer diameter. The syringe was positioned horizontally on the syringe pump (KD Scientific, KDS 101) and the positive electrode of the high voltage power supply (Matsusada Precision, AU Series) was clamped to the metal needle (Fig. 1). In order to optimize the electrospinning parameters, flow rate of the polymer solution (0.5-1.5 ml/h), applied voltage (10-20 kV) and tip-to collector distance (10-20 cm) were varied within the ranges given in the parenthesis. The most favorable results were obtained when the electrospinning parameters are 0.5 ml/h, 12.5 kV, 10 cm for the electrospinning of PAB-ad6 nanofibers and 1 ml/h, 15 kV, 15 cm for the electrospinning of PAB-ad12 nanofibers. In all cases, the electrospinning was carried out in a horizontal

position at 24ºC and 18% relative humidity in a completely enclosed plexiglas box. Electrospun nanofibers were collected on a grounded stationary cylindrical metal collector covered by a piece of aluminum foil. After the electrospinning, the collected nanofibrous mats were dried over night at 25ºC under vacuum in order to remove any residual solvent.

2.3.2. Preparation of DHBP-ad6 and DHBP-ad12 solutions electrospinning of DHBP-ad6 and DHBP-ad12 nanofibers

The homogenous solutions of DHBP-ad6 and DHBP-ad12 were prepared in chloroform/DMF mixture solvent system (chloroform:DMF; 4:1, v/v) and solution concentrations were varied from 20% to 35% (w/v) and from 15% to 25% (w/v), respectively. Homogenous and clear solutions were obtained after 3 hours stirring. The solutions were taken in 3 ml syringes with metallic needle of 0.4 mm outer diameter and the syringe was positioned horizontally on the syringe pump (KD Scientific, KDS 101). Then the positive electrode of the high voltage power supply (Spellman, SL60) was clamped to the metal needle. Metal plate collector covered by a piece of aluminum foil was placed across the horizontally positioned syringe to collect nanofibers. In order to optimize the electrospinning parameters,flow rate of the polymer solution (0.5-1.5 ml/h), applied voltage (10-20 kV) and tip-to-collector distance (10-20 cm) were varied within the ranges given in the parenthesis. For both of the MCPBz, the most favorable results were obtained when the flow rate of the polymer solution was 0.75 ml/h, applied voltage was 15 kV and tip-to-collector distance was 10 cm. Electrospinning was performed in

the completely enclosed Plexiglas box and the inside temperature and relative humidity were 22ºC and 18%, respectively. After the electrospinning, the collected nanofibers were dried over night at room temperature inside the fume hood in order to remove any residual solvent.

2.3.3. Preparation of cellulose acetate and cellulose acetate/BA-a precursor solutions electrospinning of nanofibers

The homogenous solutions of cellulose acetate (CA) and CA/BA-a were prepared in DCM/methanol mixture solvent system (DCM: methanol; 4:1, v/v). Concentration of the CA solution was determined to be 12% and precursor solutions of the CA/BA-a were prepared by using the different amount of the BA-a (2 and 5% w/v), CA (10 and 12% w/v) and citric acid (1 and 2% w/v). Homogenous and clear solutions were obtained after 2 hours stirring. The solutions were taken in 3 ml syringes with metallic needle of 0.4 mm outer diameter and the syringe was positioned horizontally on the syringe pump (KD Scientific, KDS 101). Then the positive electrode of the high voltage power supply (Spellman, SL60) was clamped to the metal needle. Metal plate collector covered by a piece of aluminum foil was placed across the horizontally positioned syringe to collect nanofibers. Electrospinning was performed by applying 15 kV voltage, 1 ml/h flow rate and 10 cm distance from the collector in the completely enclosed plexiglas box and the inside temperature and relative humidity were around 24°C and 18%, respectively. After the electrospinning, the collected nanofibers were dried over night at room temperature inside the fume hood in order to remove any residual solvent.

2.3.4. Preparation of polycarbonate and polycarbonate/BA-a precursor solutions and electrospinning of nanofibers

The homogenous solutions of polycarbonate (PC) and PC/BA-a were prepared in THF/DMF binary solvent system (THF: DMF; 1:1, v/v). Concentration of the PC solution was determined to be 25% and precursor solutions of the PC/BA-a were prepared by using the different amount of the BA-a (3, 5 and 7% w/v), PC (15, 18 and 20% w/v) and citric acid (1 and 2 % w/v). Homogenous and clear solutions were obtained after 2 hours stirring. The solutions were taken in 3 ml syringes with metallic needle of 0.6 mm outer diameter and the syringe was positioned horizontally on the syringe pump (KD Scientific, KDS 101). Then the positive electrode of the high voltage power supply (Spellman, SL60) was clamped to the metal needle. Metal plate collector covered by a piece of aluminum foil was placed across the horizontally positioned syringe to collect nanofibers. Electrospinning was performed by applying 14 kV voltage, 1 ml/h flow rate and 8 cm distance from the collector in the completely enclosed plexiglas box and the inside temperature and relative humidity were around 25°C and 24%, respectively. After the electrospinning, the collected nanofibers were dried over night at room temperature inside the fume hood in order to remove any residual solvent.

2.3.5. Preparation of modified cyclodextrin, modified cyclodextrin/BA-a precursor solutions and electrospinning of nanofibers

The solutions of hydroxypropyl-β-cyclodextrin (HPβCD), hydroxypropyl-γ-cyclodextrin (HPγCD) and methyl-β-cyclodextrin (MβCD) were prepared in various concentrations (100% (w/v) to 160% (w/v)) by using DMF as a solvent. The clear and homogeneous CD solutions were obtained after stirring for 1 hour at 50ºC and additional stirring for 30 minutes at room temperature. CD/BA-a mixture solutions were prepared by varying the ratio of CD and BA-a (CD: BA-a) as follow; 75:50, 75:75 and 120:25 (w:w/v). Initially BA-a dissolved in DMF by stirring at room temperature about 10 minutes and then CDs were added in to BA-a solutions. In order to provide complete cross-linking while preserving the fiber morphology during the thermal curing, CTR (5% and 15% w/v) was added to CD/BA-a solution as crosslinker at the second step. Also different control groups as CD/BA-a, CD/CTR, CD/BA-a/CTR solutions were prepared to investigate the effect of CTR and BA-a in the curing process of nanofibers. The solutions were taken in 1 ml syringes with metallic needle of 0.4 mm outer diameter and the syringe was positioned horizontally on the syringe pump (KD Scientific, KDS 101). Then the positive electrode of the high voltage power supply (Spellman, SL60) was clamped to the metal needle. Metal plate collector covered by a piece of aluminum foil was placed across the horizontally positioned syringe to collect nanofibers. Electrospinning was performed by applying 15 kV voltage, 1 ml/h flow rate and 10 cm distance from the collector in the completely enclosed plexiglas box and the inside temperature and

relative humudity were around 24°C and 18%, respectively. After the electrospinning, the collected nanofibers were dried over night at room temperature inside the fume hood in order to remove any residual solvent.

2.3.5. Preparation of HPβCD/E-f precursor solutions and electrospinning of nanofibers

The solutions of HPβCD/E-f mixture were prepared by using 120%HPβCD and varying the concentration of E-f (20 and 25 % w/v) and CTR (10 and 15% w/v) in DMF. First CTR was dissolved in DMF, then E-f was added in to the CTR solution. After 10 minutes stirring HPβCD was added to the mixture solution. The clear and homogeneous solutions were obtained after stirring for 2 hours at 50ºC and additional stirring for 30 minutes at room temperature. The solutions were taken in 1 ml syringes with metallic needle of 0.4 mm outer diameter and the syringe was positioned horizontally on the syringe pump (KD Scientific, KDS 101). Then the positive electrode of the high voltage power supply (Spellman, SL60) was clamped to the metal needle. Metal plate collector covered by a piece of aluminum foil was placed across the horizontally positioned syringe to collect nanofibers. Electrospinning was performed by applying 15 kV voltage, 0.5 ml/h flow rate and 12 cm distance from the collector in the completely enclosed plexiglas box and the inside temperature and relative humudity were around 23°C and 20%, respectively. After the electrospinning, the collected nanofibers were dried over night at room temperature inside the fume hood in order to remove any residual solvent.

2.4. Characterization and Measurement

Proton nuclear magnetic resonance spectrometer (^{1}H NMR, Bruker Advance III 400 MHz) was used to confirm the structure of the synthesized BA-a, thymol and eugenol-based benzoxazine monomers, PBA-ad6, PBA-ad12, DHBP-ad6 and DHBP-ad12 MCPBzs. Samples were prepared by dissolving about 20 mg/ml benzoxazines in deuterated chloroform ($CDCl_3$). ^{1}H NMR spectra of the samples were measured with 16 scans in the range of 0-10 ppm.

Fourier transform infrared (FTIR, Bruker-VERTEX70) spectrometer was employed to verify the structure of the synthesized BA-a, thymol and eugenol-based benzoxazine monomers, PBA-ad6, PBA-ad12, DHBP-ad6 and DHBP-ad12 MCPBzs. Production of polymer/polybenzoxazine and CD/polybenzoxazine composite nanofibers were investigated by FTIR spectroscopy. Ring opening and cross-linking reactions of the benzoxazine monomers and MCPBzs during the curing process were investigated by FTIR spectroscopy as well. FTIR spectra of samples were obtained with 64 scans at a resolution of 4 cm^{-1} within 4000-400 cm^{-1} range. Samples were prepared by grinding with KBr in a ratio around 3:100 (3 mg sample: 100 mg KBr) and then compressed to form discs.

Gel permeation chromatography (GPC, Waters) equipped with Waters 515 HPLC pump, Stragel HR 3-4 columns and refractive index detector was used to determine molecular weight and polydisperdity index of the PBA-ad6, PBA-ad12, DHBP-ad6 and DHBP-

ad12. THF was used as the mobile phase at a flow rate of 1 ml/min. Samples were dissolved in the THF at approximately 5 mg/ml and filtered through a 0.45 mm teflon filter prior to being injected. Calibration of the system was performed with polystyrene standards having molecular weight of 500-1x10^6 g/mol. Calibration curve obtained from PS standards with K (1. 10 4 dl/g) and a (0.68) values at room temperature in THF solvent were used for the calculation. Molecular weights of the samples were calculated by using same K and a values as the PS standards.

High performance liquid chromatograph (HPLC, An Agilent 1200 series) equipped with an Agilent 6224 high resolution mass time-of-flight (TOF) mass spectrometer and an electrospray ionization (ESI) source was used for the molecular weight determination of the synthesized bio-based benzoxazines. 1 mg/ml samples in ACN was prepared for the measurements.

A rheometer (Physica MCR 301, Anton Paar) equipped with a cone/plate accessory (D:25 mm) was used to measure the viscosity of the PBA-ad6 and PBA-ad12 solutions in chloroform/ DMF (4:1, v/v) with a constant shear rate of 100 s^{-1} at 22ºC. Results recorded with 33 rotation of the cone/plate for each sample and averages of these measurements were calculated.

Scanning electron microscope (SEM, Quanta 200 FEG, FEI) was used to investigate the morphology and the diameter distribution of the nanofibers. Samples were coated with 5

nm Au/Pd (PECS-682) prior to the SEM imaging and the average fiber diameter (AFD) was calculated by analyzing around 100 fibers from the SEM images.

Differential scanning calorimetry (DSC, TA Instruments Q20) experiments were conducted to study thermal transitions of MCPBz nanofibrous mats under nitrogen atmosphere at a heating rate of 10 ºC/min.

A thermogravimetric analyzer (TGA) (Q500, TA Instruments) was used for the investigation of the thermal properties of the benzoxazine monomers, polybenzoxazines, MCPBz nanofibers, CA, CA/BA-a, CA/PBA-a, PC, PC/BA-a, PC/PBA-a, CDs, CD/BA-a, CD/PBA-a nanofibers. TGA of the samples was carried out from 25ºC to 800ºC at 20ºC/min heating rate and nitrogen was used as a purge gas.

Dynamic mechanical analyzer (DMA, Q800 TA Instruments) equipped with tensile fixture was used to measure the mechanical properties of the DHBP-ad6, DHBP-ad12, CA, CA/PBA-a nanofibrous mats. Rectangular shaped samples were prepared with dimensions of around 15 mm (length) x 2.0 mm (width) x 0.03 mm (thickness) for DHBP-ad12, 5 mm (gap) x 2.0 mm (width) x 0.04 mm (thickness) for DHBP-ad12 and ~4 mm (gap) x ~3.0 mm (width) x ~0.02 mm (thickness) for CA/BA-a and CA/PBA-a nanofibrous mats. Stress-strain curve of the three replicate from each nanofibrous mats were obtained at 0.025 N/min force ramp. Ultimate stress and elongation at break of electrospun nanofibers were determined from the obtained stress-strain curves and young modulus was calculated from the linear region of these curves. The average and

standart deviation of these values were calculated. The dynamic thermo mechanical properties of the PC and PC/PBA-a composite nanofibers was measured using DMA in tension film clamp at a constant frequency of 1 Hz. The samples having size of 20 mm (gap) × ~3.0 mm (width) × ~0.15 mm (thickness) was measured. The amplitude was 20 μm with the fiber aligning direction in the samples parallel to the stretching direction. The storage modulus and loss tangent (tan δ) of the nanofibrous mats were recorded in the range of 50-150 °C at a heating rate of 3 °C/min.

The UV-vis-NIR spectrophotometer (Varian Cary 5000, USA) was used in the wavelength range of 200-500 nm for the structural characterization of the DHBP-ad6 and DHBP-ad12 resins. UV-vis spectra were obtained by dissolving the MCPBzs in chloroform. For the dye removal experiments of HPβCD/PBA-a and HPβCD/E-f composite nanofibers, UV-vis spectra were obtained in the wavelength range of 200-800 nm.

High performance liquid chromatography (HPLC, Agilent 1200 Series) was used to investigate the phenanthrene removing performance of both CA and CA-CD nanofibers. The separation of phenanthrene was performed with Zorbax Eclipse XDB-C18 column 5 μm (150 × 4.6 mm) and it was detected at 254 nm wavelength. Acetonitrile (100%) was used as mobile phase at a flow rate of 0.3 ml/min and the injection volume was kept at 10 μl. The phenanthrene was solved in acetonitrile and then diluted with water to carry out the measurements. The 50 mg weighted nanofibers were immersed in 1.8 ppm phenanthrene included water solutions (30 ml) and 0.5 ml aliquots were taken from the

system at definite time intervals. The calibration curve of phenanthrene was prepared by using stock solutions in 4 different concentrations; 1.8 μg/ml, 0.9 μg/ml 0.45 μg/ml, and 0.23 μg/ml. The measurement results were adapted to this calibration curve in terms of peak area under curves. The experiments were carried out in triplicate and the results were given with their standard deviations.

Inductively coupled plasma mass spectroscopy (ICP-MS, Thermo, X Series II) was used to determine the removal efficiencies of the HPβCD, HPβCD/PBA-a and HPβCD/PE-f nanofibrous mats by measuring the residual concentration of metal ions. Standard solutions of metal ion mixture were prepared with 1ppm, 500 ppb, 250 ppb, 50 ppb and 25 ppb of metal ions and calibration curves were obtained from these standard solutions. Removal efficiencies of the nanofibrous mats were measured both from the metal ion mixture solutions and separate solution of each metal ions.

Gas chromatography-mass spectrometry (GC-MS, Agilent Technologies 7890A) analyses were performed on an gas chromatograph coupled to an Agilent Technologies 5975C inert MSD with triple-axis detector. 1 μl of hexane solution was injected to GC-MS by using headspace injector (MSU 011-00A, volume = 10 ml, scale = 54mm). The separation of compounds was performed on an HP-5MS (Hewlett-Packard, Avondale, PA) capillary column (30 m × 0.25 mm ID, 0.25 μm film thickness). Column temperature was held at 80°C for 2 min and increased to 250°C rate of 10°C/min and equilibrated at this temperature for 2 min. Helium was used as a carrier gas at a flow rate of 1.2 ml/min. Thermal desorption was carried out in the splitless mode. The

temperatures of the ion source and the transfer line were 230°C and 290°C, respectively. Firstly, the GC-MS analyses were carried out in the complete scanning mode (SCAN) to determine the all PAH peaks and PAHs were identified by comparing their mass spectrum with the libraries. Then SIM mode was used to during whole measurement. The retention time of fluoranthene, phenanthrene and pyrene were 17.33, 14.51 and 17.84 min, and the major peaks of these PAH molecules were 202.1, 178.1 and 202.1 mass over charge, respectively.

2.5. Curing Studies

2.5.1. Curing studies of the bio-based benzoxazine monomers

Samples were put in the standard oven and kept for 1 hour at different temperatures (150, 175, 200, 225 and 250ºC) to provide opening and cross-linking of the oxazine ring in the structure of bio-based benzoxazine monomers with thermal curing. Small amount of sample was taken from each bio-based benzoxazine at each temperature step to investigate the ring-opening reaction and cross-linking by FTIR.

2.5.2. Curing studies of PBA-ad6 and PBA-ad12 nanofibers

In order to obtain cross-linked polybenzoxazine, curing experiments were performed for PBA-ad6 and PBA-ad12 nanofibrous mats in a standard temperature control oven. Initially, a piece of sample (2 x 5 cm) from each nanofiberswere put in the oven and kept for 1 hour at different temperatures (50, 60, 75, 90, 100 and 120ºC) separately to observe the change in fiber morphology with thermal treatment. Afterwards, step curing was performed for PBA-ad6 and PBA-ad12 mats by heating additional 1 hour at each temperature (75, 90, 120, 150, 180 and 220ºC) and small amount of sample was taken from each MCPBz mat at different temperatures to investigate the ring opening reaction by FTIR.

2.5.3. Curing studies of DHBP-ad6 and DHBP-ad12 nanofibers

Two-step curing (photo and thermal) procedure was applied to DHBP-ad6 and DHBP ad12 nanofibers to obtain cross-linked polybenzoxazine nanofibers. In the first step, a piece of sample (~2 x 5 cm) from each nanofibers were put under the UV lamp (Osram Ultravitalux, 300 W) from different distances (7, 10 and 15 cm) and various irradiation times (15 min-12 h) in order to determine optimum parameters for photo curing. For DHBP-ad6 nanofibers, curing time and distance between UV lamp and the sample were determined to be 1 hour and 10 cm, respectively. On the other hand, for the DHBP-ad12 nanofibrous, these parameters were determined to be 1 hour and 15 cm, respectively. In the second step, photocured samples were put ino standard oven and kept for 1 hour at different temperatures (150, 175, 200 and 225ºC) to provide opening and cross-linking of the oxazine ring in the structure of nanofibers with thermal curing. Small amount of sample was taken from each MCPBz nanofibers at different temperatures to investigate the ring-opening reaction and cross-linking by FTIR.

2.5.3. Curing studies of CA/BA-a composite nanofibers

Thermal curing of CA/BA-a nanofibers were carried out at different temperatures by step-wise. Initially CA/BA-a nanofibers were put in the standard oven heated at 150°C and kept for one hour at that temperature. Then, the same procedure was followed at 175, 200 and 225°C to provide opening and cross-linking of the oxazine ring in the structure of CA/BA-a nanofibers.

2.5.4. Curing studies of PC/BA-a composite nanofibers

Thermal curing of PC/BA-a nanofibers were carried out at different temperatures at step-wise. Initially PC/BA-a nanofibers were put in the standard oven heated at 100°C and kept for one hour at that temperature. Then, the same procedure was followed at 120, 140 and 160°C to provide opening and cross-linking of the oxazine ring in the structure of PC/BA-a nanofibers.

2.5.5. Curing studies of modified CD/BA-a composite nanofibers

Thermal curing of CD/BA-a nanofibers were carried out at different temperatures at step-wise. Initially CD/BA-a nanofibers were put in the standard oven heated at 150°C and kept for one hour at that temperature. Then, the same procedure was followed at 175, 200 and 225°C to provide opening and cross-linking of the oxazine ring in the structure of CD/BA-a nanofibers.

2.5.6. Curing studies of HPβCD/E-f composite nanofibers

Thermal curing of HPβCD/E-f nanofibers were carried out at different temperatures at step-wise. Initially HPβCD/E-f nanofibers were put in the standard oven heated at 140°C and kept for one hour at that temperature. Then, the same procedure was followed at 160, 180, 200 and 220°C to provide opening and cross-linking of the oxazine ring in the structure of HPβCD/E-f nanofibers.

2.6. Solubility and stability tests

2.6.1. Solubility and stability test of cross-linked DHBP-ad6 and DHBP-ad12 nanofibers

Solubility of the cross-linked DHBP-ad6 and DHBP-ad12 nanofibers after photo curing and after thermal curing were tested with some good solvents; chloroform, N,N-dimethylformamide (DMF), 1,4-dioxane, dimethylacetamide (DMAc) and tetrahydrofuran (THF). In addition, stability of these cross-linked nanofibers in harsh conditions were evaluated by HCl, HNO_3, H_2SO_4. 5 M aqueous solutions were prepared from each type of acid and 5 ml of acid solutions were poured into vials. Likewise, 5 ml of solvent was poured into vials and a piece of sample with the dimensions of around 1x1 cm from each photo and thermal-cured DHBP-ad6 and DHBP-ad12 nanofibers were placed into vials separately. Samples were kept in solvents and acid solutions for 24 hours and then dried at room temperature in the fume hood over night. In addition, thermal stability of cross-linked DHBP-ad6 and DHBP-ad12 nanofibers were investigated by keeping nanofibers at different temperatures (250, 300, 350 and 400ºC)

2.6.2. Solubility test of HPβCD/PBA-a composite nanofibers

Solubility of the HPβCD/PBA-a composite nanofibers were tested in acetone, ACN, chloroform, DCM, DMF, DMSO, ethanol, methanol, THF and water. A piece of

HPβCD/PBA-a nanofibers immersed separately into petri dishes including each solvent. Samples were kept overnight in these solvents and then dried at room temperature.

2.7. Adsorption experiments

2.7.1. Molecular entrapment of dye molecules from liquid environment by HPβCD/PBA-a composite nanofibers

Methylene blue (MB) as a positively charged and methyl orange (MO) as a negatively charged dye molecules were chosen and dye mixture solutions were prepared in order to investigate the selectivity of HPβCD/PBA-a composite nanofibers to specific dye molecule. 5 mg sample was added into 5 ml of different concentration of dye solutions varying from 5 ppm to 100 ppm and agitated at 150 rpm on a mechanical shaker under ambient conditions for 6 hours. Dye concentration was determined to be to 20 mg/l in solution and experiment was performed by agitating samples different time intervals ranging from 5 min to 360 min in order to investigate the time dependent removal efficiency of the HPβCD/PBA-a composite nanofibers. The UV-vis NIR spectrophotometer was used in the wavelength range of 200-800 nm to follow the absorbance decrease of the dye mixture solution over time as a results molecular filtration of HPβCD/PBA-a composite nanofibers.

2.7.2. Molecular entrapment of polyaromatic hydrocarbons from liquid environment by HPβCD/PBA-a composite nanofibers

Three different polyaromatic hydrocarbons (PAHs), fluoranthene, phenanthrene and pyrene were used as a model organic pollutant in order to investigate the removal

efficiency of HPβCD/PBA-a composite nanofibers. Three different fluoranthene, phenanthrene and pyrene mixture solutions were prepared by adjusting the concentration of the each PAH as 200, 400 and 600 ppb in the mixture solution. Initially appropriate amount of PAHs were dissolved separately in ACN and then these solutions were diluted with water to obtain desired concentration. Removal experiments were performed by adding 5 mg sample into 5 ml of three different concentration of PAHs mixture solutions separately and agitated at 150 rpm on a mechanical shaker under ambient conditions for 6 hours. GC-MS was used to follow the concentration decrease of the PAH mixture solution over time as a results molecular filtration of HPβCD/PBA-a composite nanofibers. Procedure was followed for activated charcoal as a comparison. 400 ppb mixture solution concentration was determined for the time dependent molecular filtaration experiments of HPβCD/PBA-a composite nanofibers. Again 5 mg sample was added into 5 ml of 400 ppb PAH mixture solution and agitated at 150 rpm on a mechanical shaker under ambient conditions for different time intervals ranging from 10 min to 360 min in order to investigate the time dependent removal efficiency of the HPβCD/PBA-a composite nanofibers. For the GC-MS measurement samples were prepared by liquid- liquid extraction with hexane 1ml solution from each sample mixed with 1 ml hexane and stirred 1 hour at 1000 rpm on the shaker to provide the extraction of PAH molecules into hexane. Then samples were kept 30 min at room temperature without stirring to allow the phase separation and 0.5 ml sample was taken from the hexane phase for the measurement.

2.7.3. Molecular entrapment of PAHs from liquid environment by CA/PBA-a composite nanofibers

Molecular filtration performance of the nanofibrous mats was tested by using phenanthrene as a model polycyclic aromatic hydrocarbon (PAH). The appropriate amount of phenanthrene was dissolved in acetonitrile and then diluted with water at the maximum solubility level of phenantherene and 1.8 ppm phenanthrene solution was obtained. The 50 mg nanofibers were immersed in 30 ml phenanthrene solutions and 0.5 ml of each solution was withdrawn to measure phenanthrene concentration in the solution and replenished with same amount of water at pre-determined time intervals. The phenanthrene filtration performance from aqueous solution by PET and PET/CDP nanofibrous mats was investigated by high performance liquid chromatography (HPLC, Agilient 1200 series) equipped with VWD UV detector. The column was Agilient C18, 150 mm x 4.6 mm (5 µm pores) and the detection was accomplished at 254 nm. Mobile phase, flow rate, injection volume and total run time were acetonitrile (100%), 0.6 ml/min, 10 µl and 5 min, respectively. As a result, the amount of phenanthrene remaining in the solution was determined from the area of phenanthrene peak observed in HPLC chromatograms. Then the calibration curve was prepared by using phenanthrene solutions (1.8 ppm, 0.9 ppm, 0.45 ppm, 0.23 ppm, 0.12 ppm) and R^2 was calculated as 0.985. The peak area under curves was converted to concentration (ppm) according to the calibration curve. This experiment was repeated three times for each sample. The results were reported as the average±standard deviation of phenanthrene

concentration remaining in the solution. The calibration curve of phenanthrene was prepared by using stock solutions in 4 different concentrations; 1.8 μg/ml, 0.9 μg/ml 0.45 μg/ml, and 0.23 μg/ml R^2 was calculated as 0.99. The results were adapted to this calibration curve in terms of peak area under curves. The peak area under curves was converted to concentration (ppm) according to the calibration curve. This experiment was repeated three times for each sample. The results were reported as the average ± standard deviation of phenanthrene concentration remaining in the solution

2.7.4. Removal of heavy metals from liquid environment by HPβCD/PBA-a and HPβCD/PE-f composite nanofibers

50 ppm stock solution of each metal ion (Cd^{2+}, Cu^{2+}, Mn^{2+}, Ni^{2+}, Pb^{2+} and Zn^{2+}) was prepared by dissolving the appropriate amount of the metal salt precursors in 50 ml deionized water separately. Then, the desired low concentrations of metal ions were prepared by diluting the stock solution. Batch adsorption experiments were performed to measure the removal efficiency of composite nanofibers for toxic metal ions (Cd^{2+}, Cu^{2+}, Mn^{2+}, Ni^{2+}, Pb^{2+} and Zn^{2+}) in water. 5 mg of each HPβCD/PBA-a and HPβCD/PE-f composite nanofibers were placed in 1 ppm 5 ml metal ion solutions separately and agitated at 150 rpm on a mechanical shaker under ambient conditions for 6 hours. The solutions were evaluated by using ICP-MS.

3. RESULTS and DISCUSSIONS

Chapter 1: Bio-based benzoxazine monomers

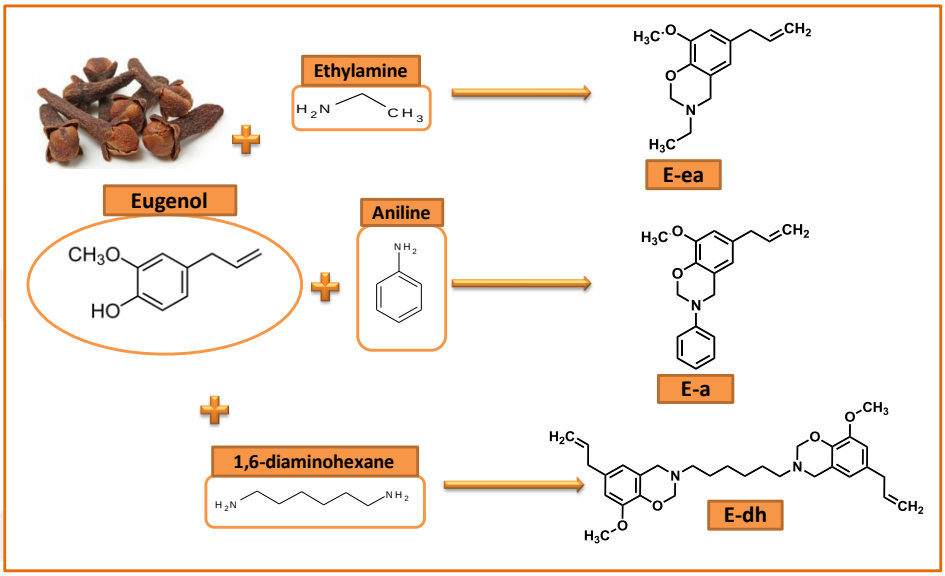

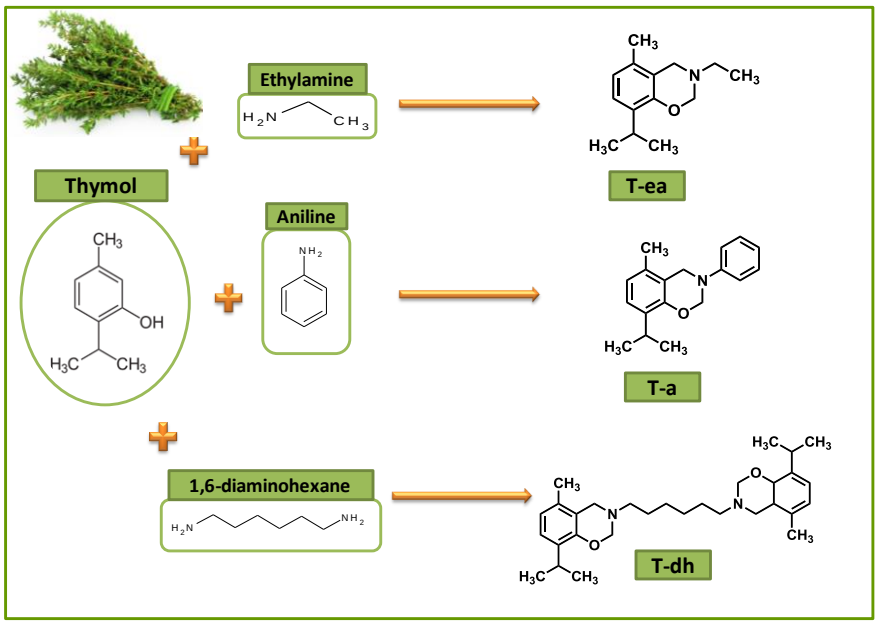

3.1. Eugenol-based bio-benzoxazine monomers

Until most recently, benzoxazine monomers are synthesized from petroleum-based phenolic derivatives, formaldehyde and primary amines either in solution or by a melt-state reaction. However, petroleum-based phenolics are nonrenewable resources and shortage of these materials encouraged the scientist to develop and commercialize novel benzoxazines which can decrease the widespread dependence on fossil fuels [229]. Recently, naturally occuring phenolic compounds such as cardanol, guiacol, urushiol, eugenol, and so on have been used for the synthesis of bio-benzoxazines [230-239]. These type of phenolic compounds are plant-derived and widely found in variety of plants.

In this study, we have chosen eugenol as phenolic compound and three different amines with different functionalities (aliphatic, aromatic and di-funcional aliphatic) for the synthesis of novel eugenol-based bio-benzoxazine monomers. Eugenol is a pale yellow oily liquid extracted from clove oil, nutmeg, cinnamon, basil and bay leaf [240-242]. Although several studies were done for the synthesis of eugenol-based bio-benzoxazine monomers, affect of aliphatic, aromatic and di-funcional aliphatic amines on the curing process and properties of the cured product have not been reported.

3.1.1. Synthesis and structural characterization of the eugenol-based bio-benzoxazine monomers

Conventionally, benzoxazine monomers are synthesized by heating a solution of the appropriate primary amine, phenolic derivative and formaldehyde. Since in this type of synthesis method solvent is used, extensive formation of oligomers and limited solubility are two main shortcomings that may cause low yield and a difficult purification process [2]. Therefore, a solventless synthesis procedure has been applied to prepare the bio-based benzoxazine monomers in this study [243]. As shown in Figure 9, eugenol-based bio-benzoxazines E-a, E-ea, and E-dh were prepared by condensation reactions of eugenol and paraformaldehyde with three different functional amines, aniline (aromatic), ethylamine (aliphatic) and 1,6-diaminohexazne (difunctional), respectively. E-a and E-ea were obtained as cinnamon like colour viscous resin, while E-dh was obtained as highly viscous yellow resin. These eugenol-based bio-benzoxazines were found to be soluble in acetone, chloroform, DMF, DMSO, DMAc, toluene and THF indicating that they have good processing capabilities in solution processes.

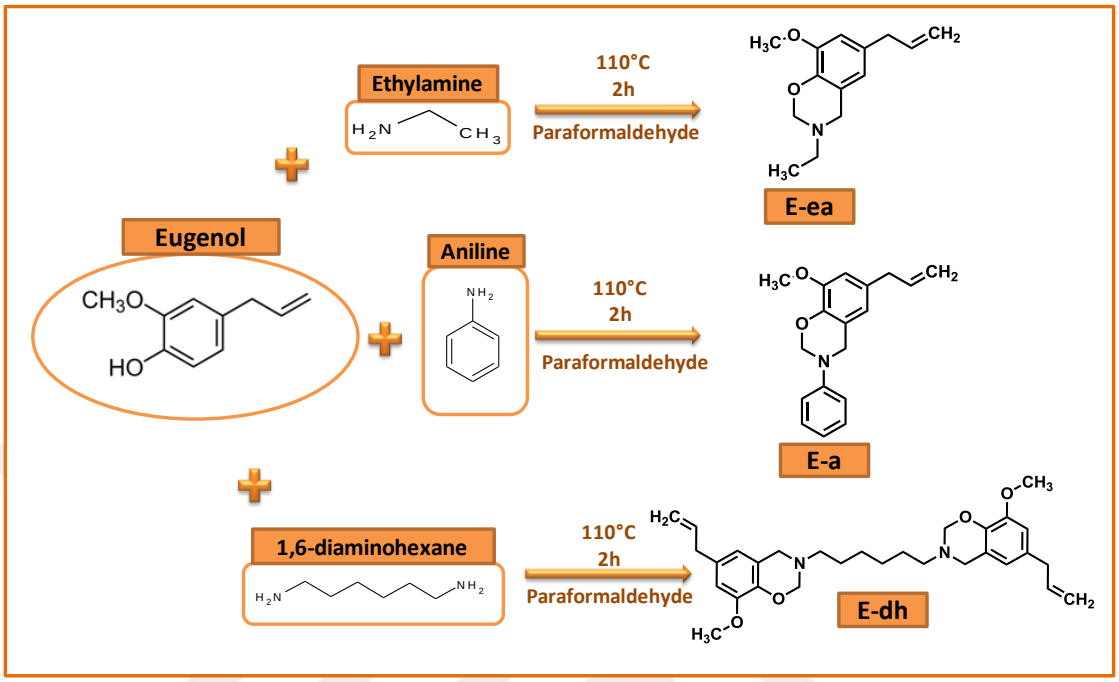

Figure 9. Synthesis of eugenol-based bio-benzoxazine monomers.

The structures of the novel eugenol-based bio-benzoxazine monomers are confirmed by ^{1}H NMR and FTIR spectroscopies. Figure 10 represents the proposed chemical structures and ^{1}H NMR spectra of eugenol-based bio-benzoxazine monomers namely, E-ea, E-a and E-dh. Main evidence for the formation of the benzoxazine structure is the existence of the two new resonances with 1:1 ratio belong to methylene protons in the oxazine ring (Ph-CH_2-N and O-CH_2-N). Accordingly, the resonances attributed to the methylene protons of Ph-CH_2-N and O-CH_2-N of the oxazine ring were observed at around 5.41 and 4.59 ppm, 4.79 and 3.88 ppm, 4.76 and 3.85 ppm in the ^{1}H NMR spectra of E-a, E-ea and E-dh, respectively. These resonances were observed similar values for E-ea and E-dh compared to E-a, presumably the high shilding effect of the

benzene ring in the structure of E-a compared to aliphatic groups in the structure of E-ea and E-dh. All the protons found in the structure of the eugenol based bio-benzoxazine monomers were shown detailed in the ^{1}H NMR spectra of each compound verifying the synthesis of the desired benzoxazine molecules was achieved (Figure 10).

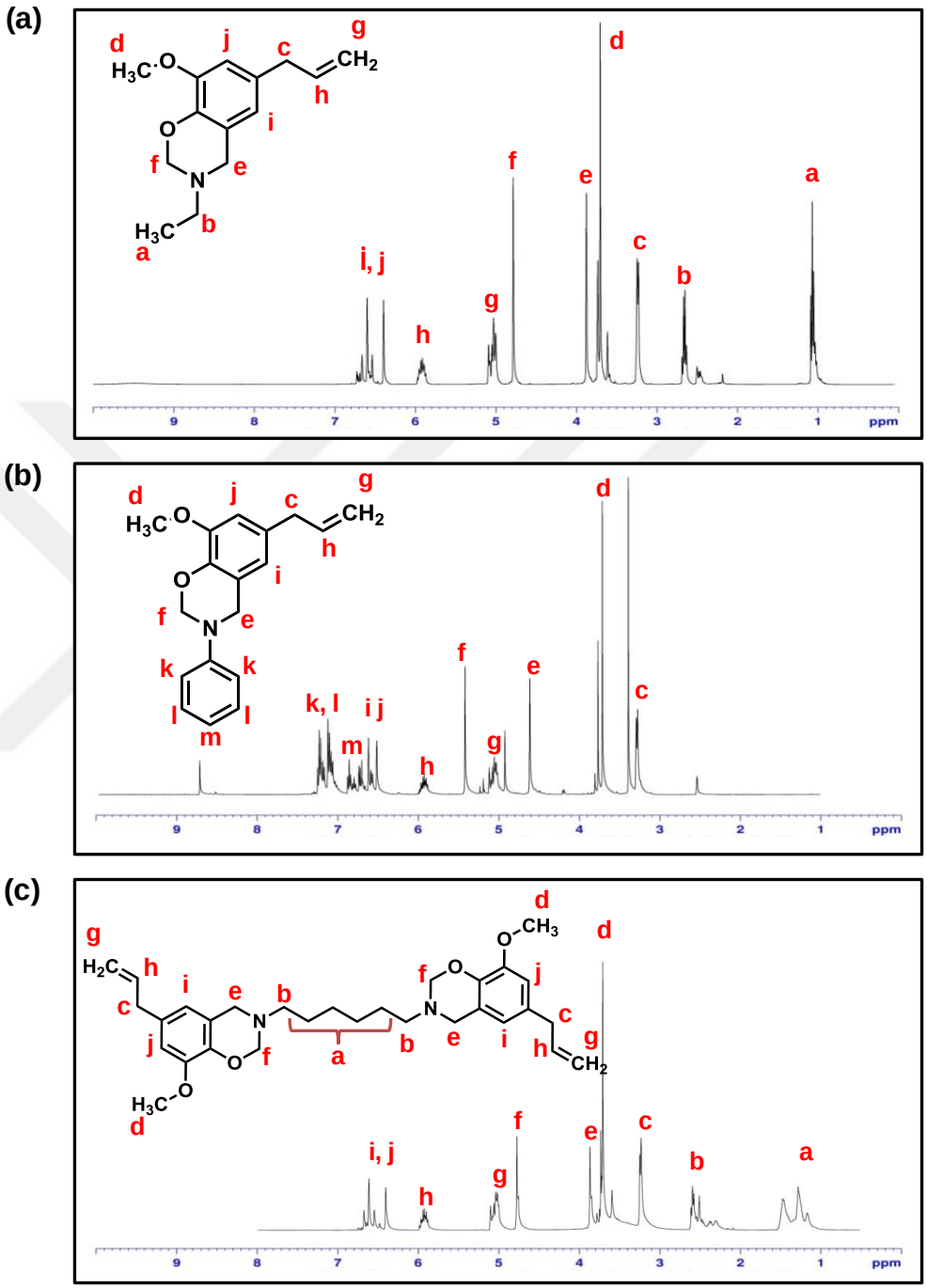

Figure 10. The proposed chemical structures and ^{1}H NMR spectra of (a) E-ea, (b) E-a and (c) E-dh in d6-DMSO.

FTIR spectra of the E-ea, E-a and E-dh are shown in Figure 11. The FTIR spectrum of E-ea shows characteristic oxazine ring absorbance bands at 1229 cm^{-1} may be attributed the asymmetric stretching of C–O–C. The other characteristic peak observed at 917 cm^{-1} with high intensity which is attributed the C–H out-of-plane deformation mode of the benzene ring attached to the oxazine ring. The spectrum also shows sharp peak at 1495 cm^{-1} due to C-H in-plane deformation mode of three substituted benzene ring and peak at 1366 cm^{-1} due to tetra substituted benzene ring. Small peaks appearing at 3070 cm^{-1} may be attributed to C–H stretching vibration of benzene ring and high intensity peaks between 2997 and 2834 cm^{-1} may be attributed the asymmetric and symmetric alkyl side chain of eugenol and ethyl amine. FTIR spectrum of E-ea is consistent with the proposed benzoxazine structure.

Similarly, FTIR spectrum of E-a shown in Figure 11b demonstrates characteristic oxazine ring peak at 1229 cm^{-1} attributed to the asymmetric of C–O–C. The other characteristic band observed at 940 cm^{-1} may be attributed the C–H out-of-plane deformation mode of the benzene ring attached to the oxazine ring. The spectrum also shows a sharp and very strong peak at 1494 cm^{-1} due to in-plane deformation mode of three substituted benzene ring and peak at 1366 cm^{-1} due to tetra substituted benzene ring. C–H stretching vibration of benzene ring appears at 3058 and 3010 cm^{-1} and asymmetric and symmetric stretching vibrations of the methylene group of the oxazine ring and alkyl side chain of eugenol between 2947 and 2824 cm^{-1}. The FTIR spectrum of E-a is consistent with the proposed benzoxazine structure.

Finally, very similar results were obtained for the E-dh. The FTIR spectrum of E-dh given in Figure 11c shows characteristic oxazine ring absorbance at 1226 cm^{-1} attributed the asymmetric stretching vibration of C–O–C. The other characteristic absorbance observed at 922 cm^{-1} which is attributed C–H out-of-plane deformation mode of the benzene ring attached to the oxazine ring. The spectrum also shows sharp peak at 1494 cm^{-1} due to in-plane deformation mode of three substituted benzene ring. Here additionally, small peaks are observed at 3072 cm^{-1} attributed to C–H stretching vibration of benzene ring and other peaks high intensity peaks between 2997 and 2849 cm^{-1} attributed the asymmetric and symmetric stretching vibrations of the methylene group of the oxazine ring, alkyl side chain of eugenol and hexamethylene diamine. FTIR spectrum of E-ea is consistent with the proposed benzoxazine structure.

Mass spectra of eugenol-based benzoxazines are given in Figure 12 which also indicate successful synthesis of the benzoxazine molecules.

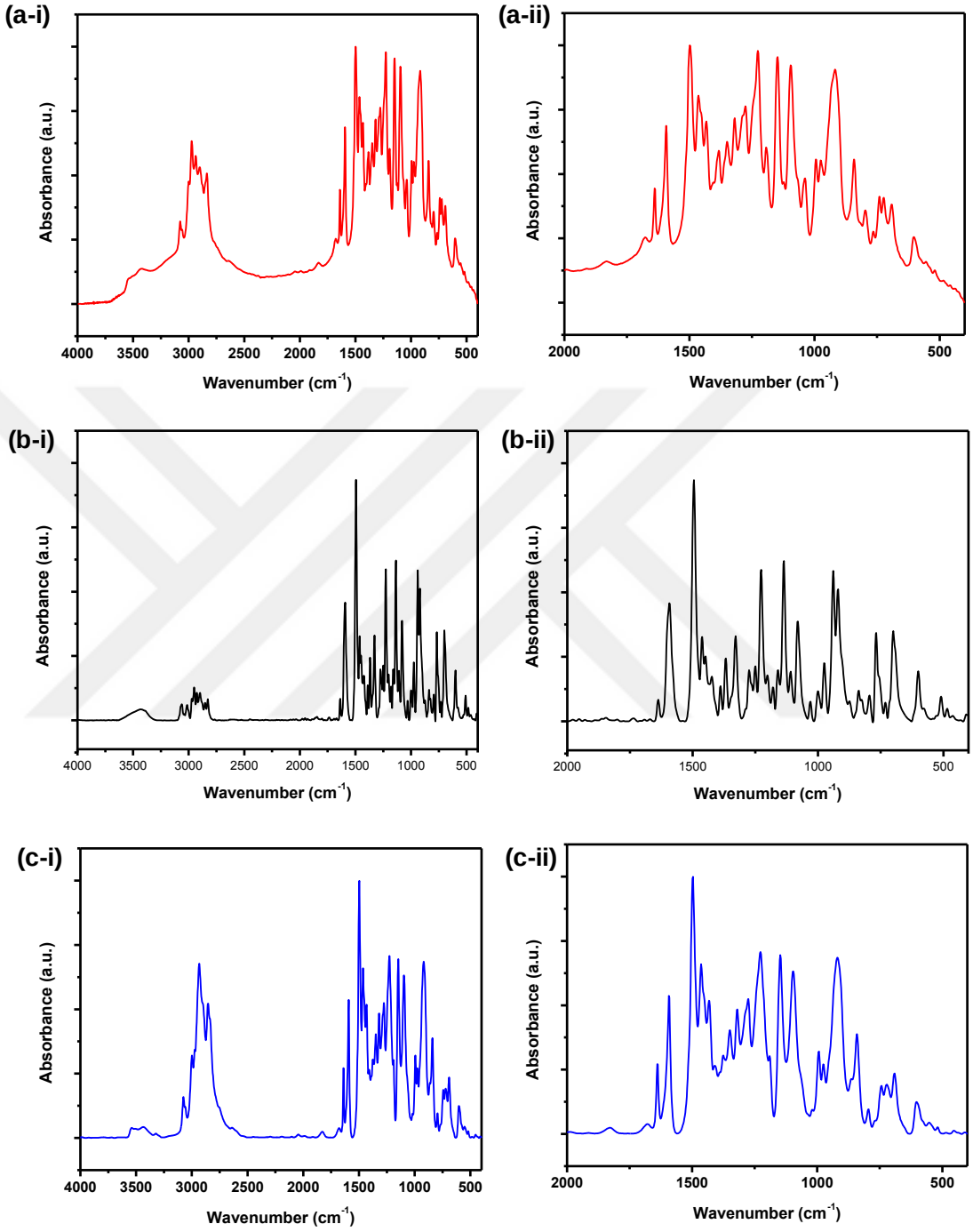

Figure 11. FTIR spectra of (a) E-ea, (b) E-a and (c) E-dh, (i) in the range of 4000-400cm^{-1} and (ii) in the range of 2000-400cm^{-1}.

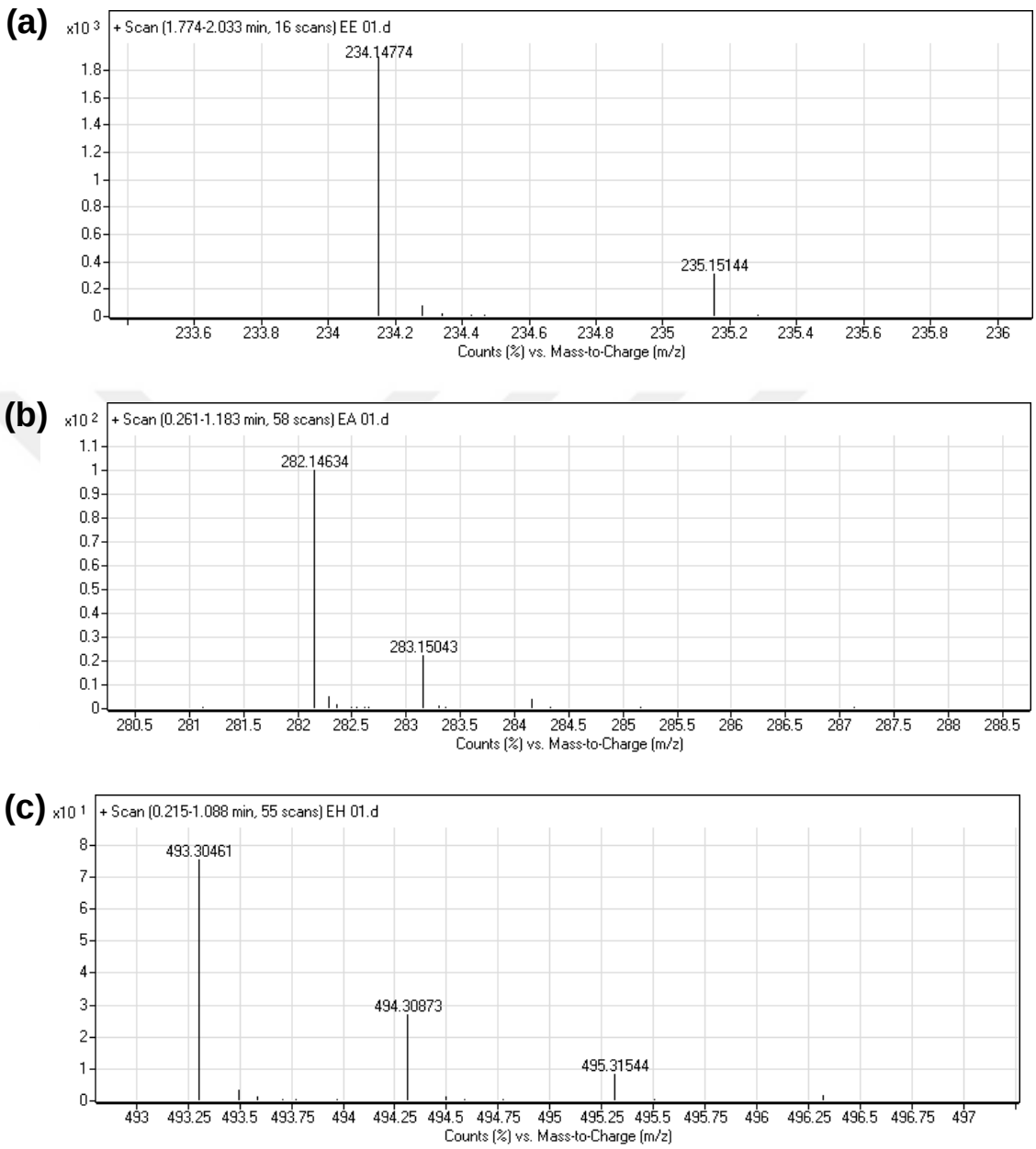

Figure 12. Mass spectra of (a) E-ea; $[M+H]^+$ (calculated): 234.1489, $[M+H]^+$ (observed): 234.1477, (b) E-a; $[M+H]^+$ (calculated): 282.1489, $[M+H]^+$ (observed): 282.1463, and (c) E-dh; $[M+H]^+$ (calculated): 493.3061, $[M+H]^+$ (observed): 493.3046.

In addition to the mass spectroscopy analysis, elemental analysis of eugenol-based benzoxazine monomers were performed as well. Table 1 summarizes the weight percentages of each element found in the structure of E-a, E-ea and E-dh as experimentally measured and theoretically calculated values. As it is observed from the table, experimental and theoretical values are very close to each other indicating the synthesis of desired molecules is achieved. Negligible differeneces in the elemental compositions might be resulted from the unreacted species. However, this is not a disadvantage for the benzoxazines because unreacted species especially, phenols behave as a catalyst during the thermal curing and decrease the polymerization temperature.

Table 1. Atomic weight percentages of elements in eugenol-based bio-benzoxazines.

	Benzoxazine	N (%)	C (%)	H (%)	O (%)
Experimental values	E-a	5,13	74,97	6,78	
	E-ea	5,21	71,28	7,90	
	E-dh	5,84	71,15	8,18	
Theoretical values	E-a	4,98	76,84	6,81	11,37
	E-ea	6,01	72,07	8,21	13,71
	E-dh	5,69	73,14	8,18	12,99

3.1.2. Polymerization of the eugenol-based bio-benzoxazine monomers by thermal curing; their structural and thermal characterizations

The typical polymerization rection to obtain polybenzoxazines is based on the opening of oxazine ring and cross-linking of the molecules by thermal curing. Here, eugenol-

based benzoxazine monomers namely E-ea, E-a and E-dh were polymerized by thermally initiated ring opening rections which is performed step-wise at 150, 175, 200, 225 and 250ºC, consequently polybenzoxazines which are denoted as PE-ea, PE-a and PE-dh were obtained, respectively. All of the polybenzoxazines were dark-brown which is a typical colour of polybenzoxazines when they are thermally cured. The molecular structures of the eugenol-based bio-benzoxazine monomers (E-ea, E-a and E-dh) and their predicted polymers (PE-ea, PE-a and PE-dh) obtained by thermal curing are represented in Figure 13. In order to confirm the cross-linking achieved by step-wise curing, FTIR spectroscopy was used and after each step of thermal curing FTIR spectra of samples were recorded. In order to investigate the ring-opening, characteristic absorbance peaks of the oxazine ring which are asymmetric stretching vibration of C–O–C and C–H out-of-plane deformation mode of the benzene ring attached to the oxazine ring were taken into consideration. Because, oxazine ring opens by heating at temperatures in the range between 160 and 220ºC [36], and intensity of the characteristic oxazine peaks decraeses with increasing temperature.

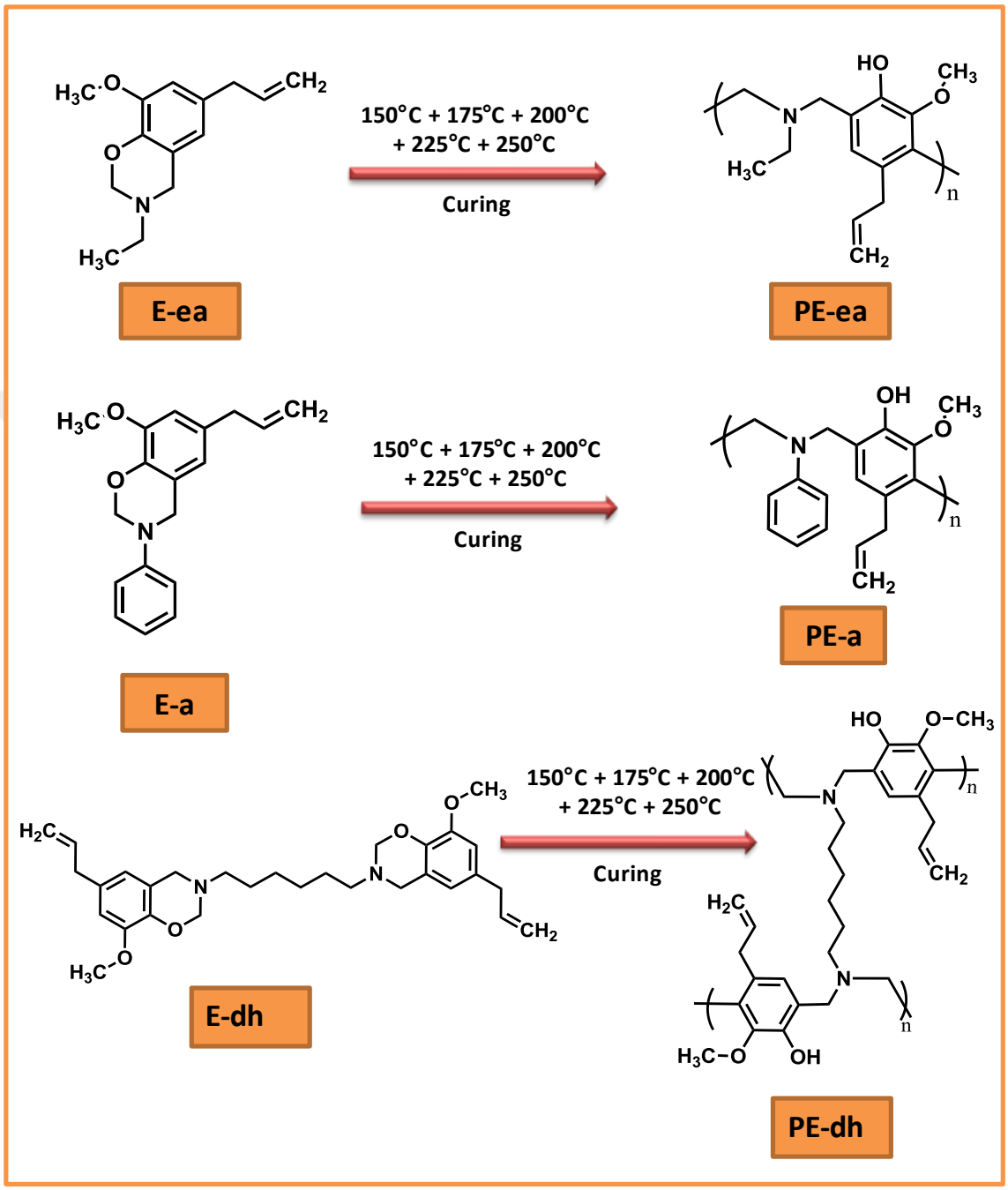

Figure 13. Polymerization of eugenol-based bio-benzoxazines with thermally initiated ring-openning reaction.

FTIR spectra of E-ea, E-a, E-dh, after one hour heating each bio-benzoxazine at 150ºC and additional heating at 175, 200, 225 and 250ºC are given in Figure 14. As it is shown on the spectra, intensity of the characteristic oxazine ring absorbance peaks decreased with increasing temperature and almost disappeared after 250ºC. In addition, very broad band at around 3400 cm^{-1} was observed especially after heating 200ºC and the intensity/broadness of this band increased with increasing temperature. For PE-ea, PE-a, PE-dh, this broad band mainly may be attributed the combination of interactions; O^{-}...$H^{+}N$ intermolecular hydrogen bonding, OH…N intermolecular hydrogen bonding, OH...O intramolecular hydrogen bonding and OH...π intermolecular hydrogen bonding [244, 245]. Increasing the intensity of this band with heating and also disappearence of the characteristic oxazine peaks show that polymerization as a result opening of the oxazine rings each bio-benzoxazine was achived.

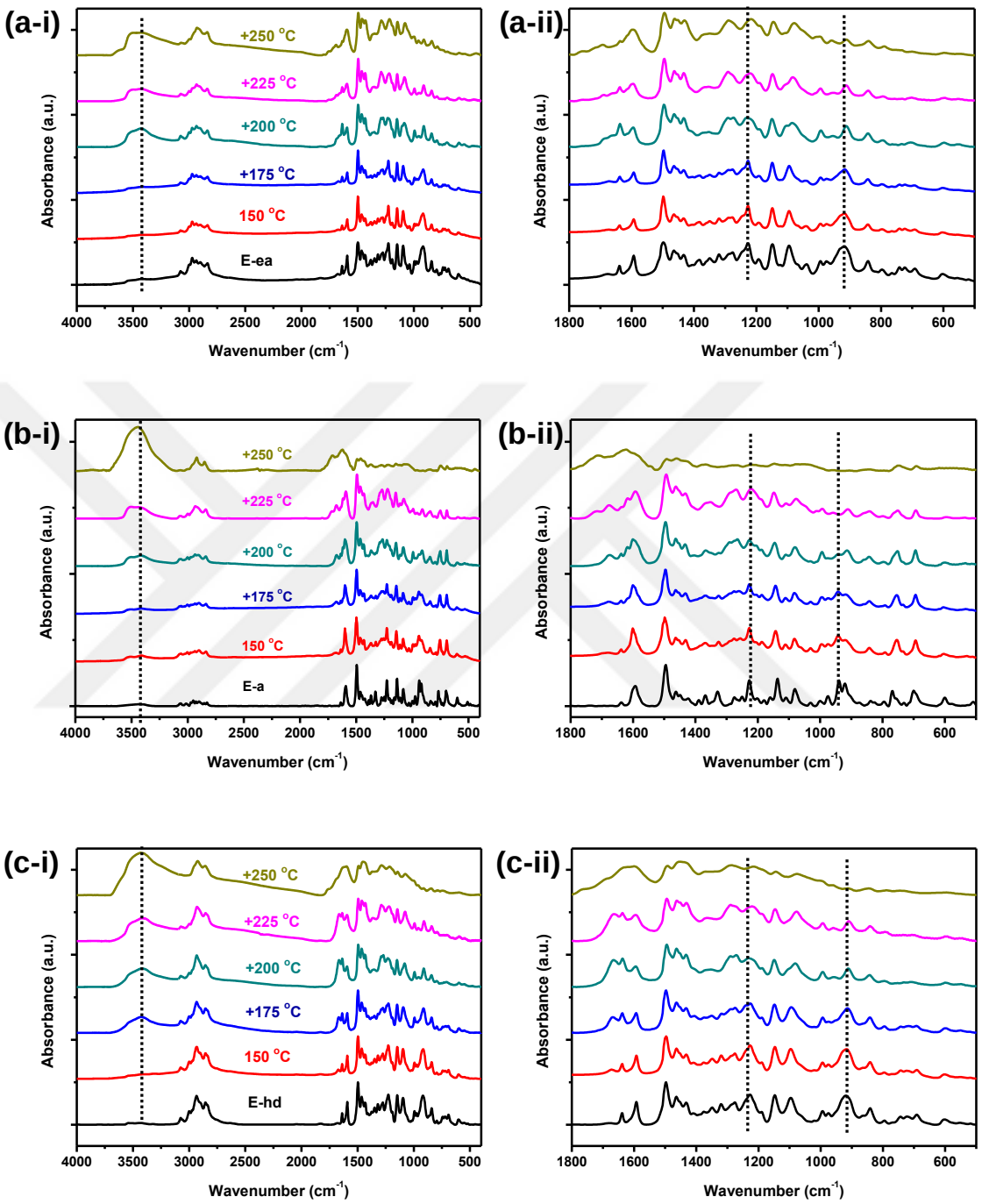

Figure 14. FTIR spectra of (a) E-ea, (b) E-a and (c) E-dh; before and after each thermal curing step (i) in the range of 4000-400cm^{-1} and (ii) in the range of 2000-400cm^{-1}.

Furthermore, thermal properties of the bio-benzoxazines and their polymers were investigated by TGA under nitrogen atmosphere. Figure 15 demonstrates the TGA thermograms of E-ea, E-a, E-dh and cured PE-ea, PE-a, PE-dh. As it is observed, three step thermal decomposition profile of all bio-benzoxazines became one step after curing demonstarting the polymerization was achieved. Table 2 summarizes the data obtained from TGA profiles. As it is seen in Table 2 the highest 5 and 15% weight loss temperatures (T_5 and T_{15}) were observed for the E-dh, presumably the di-functional benzoxazine structure of E-dh provided more group for the cross-linking which resulted the higher termal decomposition temperatures. On the other hand, decomposition temperatures (T_d) of cured bio-benzoxazines were very close to each other and PE-a have the highest T_d most probably additional benzene containing polybenzoxazines are superior to the typical aliphatic amine-based polybenzoxazines. The char yields (CY) were also calculated from the TGA profiles from Figure 15. A notable enhancement of the char yield was observed for all bio-benzoxazines after thermal curing indicating the high cross-linked density achived by polymerization.

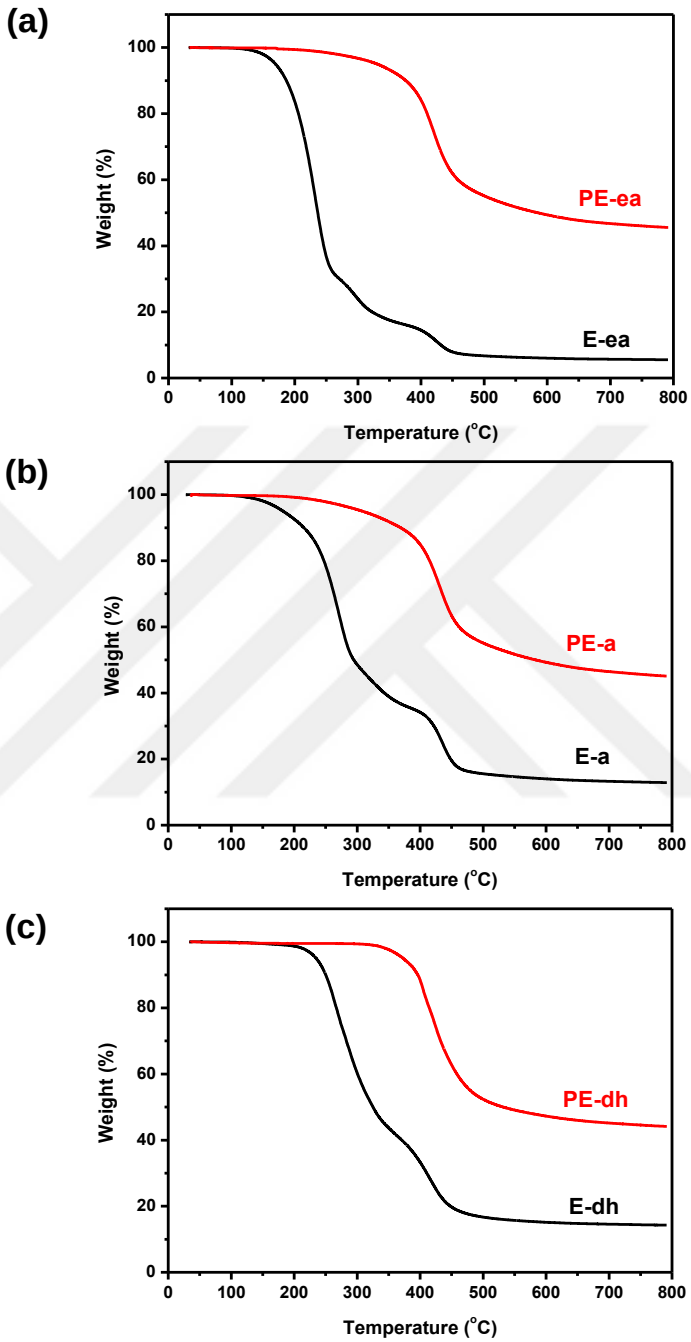

Figure 15. TGA thermograms of (a) E-ea and ET-ea (b) E-a and PE-a (c) E-dh and PE-dh.

Table 2. Thermal properties of the eugenol-based bio-benzoxazines before and after thermal curing.

Benzoxazine	T_5 (ºC)	T_{15} (ºC)	T_d (ºC)			CY (%)
E-ea	170	198	233	270	427	5.5
PE-ea	333	398		420		45.6
E-a	182	235	271	335	436	12.9
PE-a	310	400		432		45.1
E-dh	236	258	274	324	420	14.3
PE-dh	373	405		424		44.1

3.2. Thymol-based bio-benzoxazine monomers

Although several eugenol-based bio-benzoxazine were synthesized and their curing studies were performed [231, 233, 234, 237, 246], thymol has not been used as a phenolic derivative. Therefore, thymol which is a white crystalline compound found in thyme and other various plant was used to produce novel type of bio-benzoxazine monomers. Again, as previous study three different amines with different functionalities (aliphatic, aromatic and di-funcional aliphatic) were used for the synthesis of novel thymol-based bio-benzoxazine monomers. Effects of these types of functional amines on the curing process and properties of the cured product were investigated. Also, detailed molecular characterizations of the synthesized thymol-based bio-benzoxazine monomers and cured polybenozaxazines were done to understand fundamental benzoxazine chemistry.

3.2.1. Synthesis and structural characterization of the thymol-based bio-benzoxazine monomers

In a similar way of eugenol-based bio-benzoxazines, thymol-based bio-benzoxazines namely T-a, T-ea, and T-dh were prepared by condensation reactions of thymol and paraformaldehyde with three different functional amines, aniline (aromatic), ethylamine (aliphatic) and 1,6-diaminohexazne (difunctinal), respectively (Figure 16). All thymol-based bio-benzoxazines were obtained as yellow fluid, yet, T-dh was highly viscous most probably its higher molecular weight. These thymol-based bio-benzoxazines were

found to be soluble in acetone, chloroform, DMF, DMSO, DMAc, toluene and THF indicating that they have good processing capabilities in solution processes.

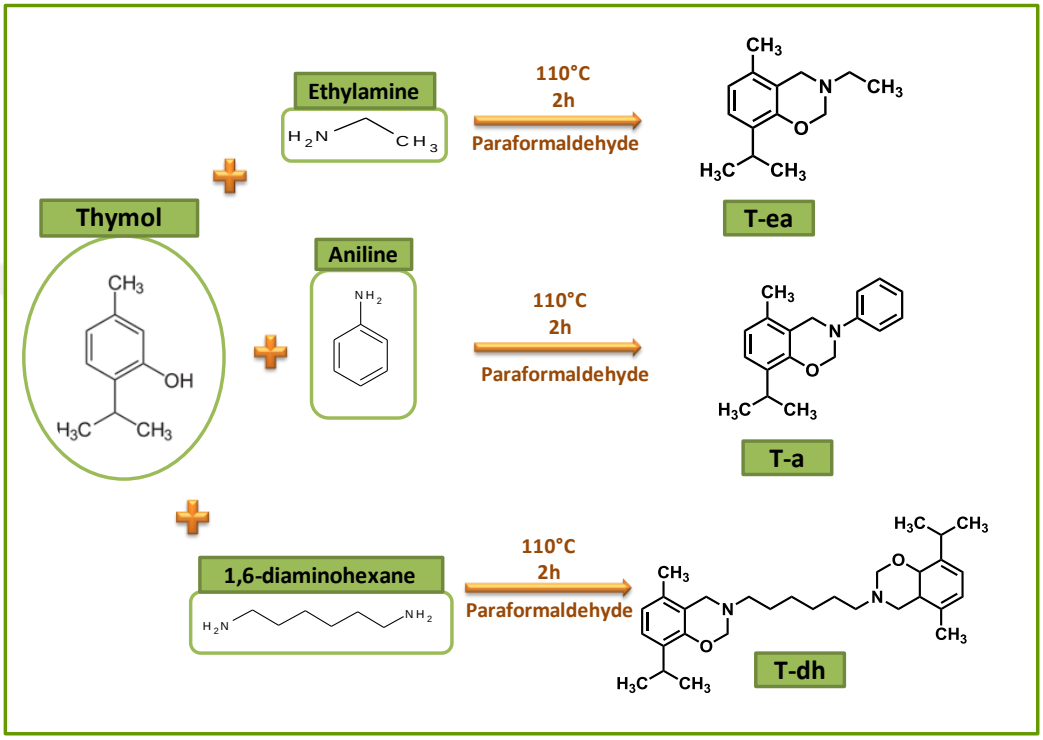

Figure 16. Synthesis of thymol-based bio-benzoxazine monomers.

The structures of the novel thymol-based bio-benzoxazine monomers are confirmed by ^{1}H NMR and FTIR spectroscopy. Figure 17 represents the proposed chemical structures and ^{1}H NMR spectra of eugenol-based bio-benzoxazine monomers namely, T-ea, T-a and T-dh. Main evidence for the formation of the benzoxazine structure is the existence of the two new resonances with 1:1 ratio belong to methylene protons in the oxazine ring. Accordingly, the resonances attributed to the methylene protons of Ph-CH_2-N and O-CH_2-N of the oxazine ring at around 5.39 and 4.51 ppm, 4.76 and 3.80 ppm, 4.89 and

3.81 ppm were observed in the ^{1}H NMR spectra of T-a, T-ea and T-dh, respectively confirming the formation of the oxazine ring. These resonances were observed very similar values for T-ea and T-dh compared to T-a, presumably the high shilding effect of the benzene ring in the structure of T-a compared to aliphatic groups in the structure of E-ea and E-dh. All the protons found in the structure of the eugenol based bio-benzoxazine monomers were shown in the ^{1}H NMR spectra of each compound verifying the synthesis of the desired benzoxazine molecules were achieved (Figure 17).

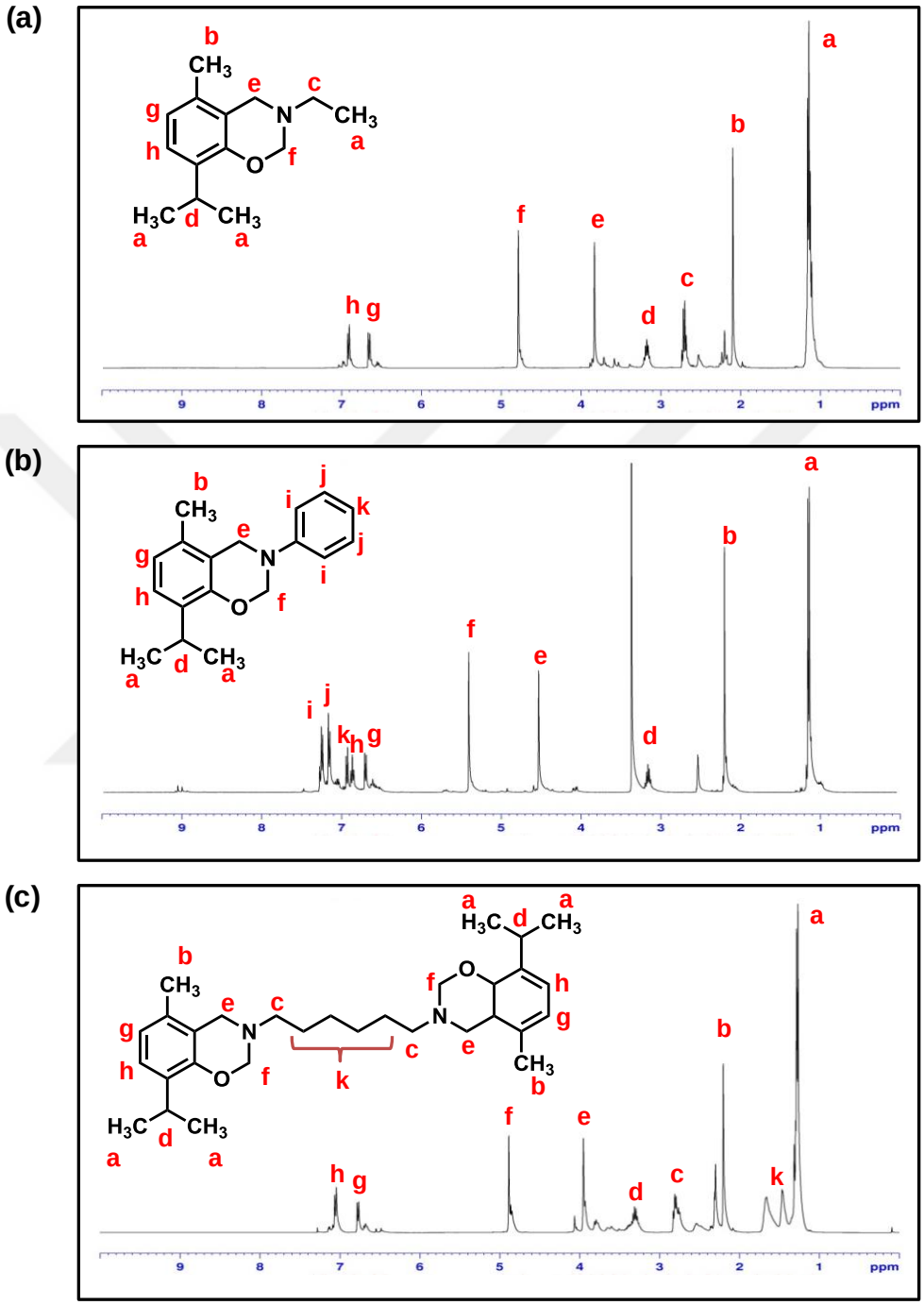

Figure 17. The proposed chemical structures and ^{1}H NMR spectra of a) T-ea, b) T-a and c) T-dh in DMSO-*d*6.

FTIR spectra of the T-ea, T-a and T-dh are shown in Figure 18. The FTIR spectrum of T-ea shows characteristic oxazine ring absorbance band at 1222 cm^{-1} attributed to the asymmetric stretching of C–O–C. The other characteristic peak observed at 945 cm^{-1} is attributed to the C–H out-of-plane deformation mode of the benzene ring attached to the oxazine ring. The spectrum also shows a sharp peak at 1492 cm^{-1} due to in-plane deformation mode of three substituted benzene ring and peak at 1349 cm^{-1} due to tetra substituted benzene ring. The peaks between 2961 and 2872 cm^{-1} attributed to the asymmetric and symmetric streching vibrations of the alkyl side chains of thymol and ethyl amine. The FTIR spectrum of T-ea is consistent with the proposed benzoxazine structure.

Similarly, FTIR spectrum of T-a shown in Figure 18b demonstrates characteristic oxazine ring peaks at 1223 cm^{-1} attributed to the asymmetric of C–O–C. The other characteristic band observed at 945 cm^{-1} attributed to the C–H out-of-plane deformation mode of the benzene ring attached to the oxazine ring. The spectrum also shows a sharp and very strong peak at 1496 cm^{-1} due to in-plane deformation mode of three substituted benzene ring and peak at 1375 cm^{-1} due to tetra substituted benzene ring. C–H stretching vibration of benzene ring appears at 3060 and 3026 cm^{-1}. Asymmetric and symmetric stretching vibrations of the methylene group of the oxazine ring and alkyl side chain of thymol are observed between 2960 and 2868 cm^{-1}. The FTIR spectrum of T-a is consistent with the proposed benzoxazine structure.

Finally, very similar results were obtained for the T-dh. The FTIR spectrum of T-dh given in Figure 18c shows characteristic oxazine ring absorbance bands at 1226 cm^{-1} attributed to the asymmetric stretching vibration of C–O–C. The other characteristic peak at 947 cm^{-1} attributed to the C–H out-of-plane deformation mode of the benzene ring attached to the oxazine ring. The spectrum also shows a sharp peak at 1490 cm^{-1} due to in-plane deformation mode of three substituted benzene ring. Other peaks between 2953 and 2864 cm^{-1} attributed to the asymmetric and symmetric stretching vibrations of the methylene group of the oxazine ring, alkyl side chain of thymol and hexamethylene diamine. The FTIR spectrum of T-dh is consistent with the proposed benzoxazine structure.

Mass spectra of thymol-based bio-benzoxazines given in Figure 19 also indicating the successful synthesis of the benzoxazine molecules.

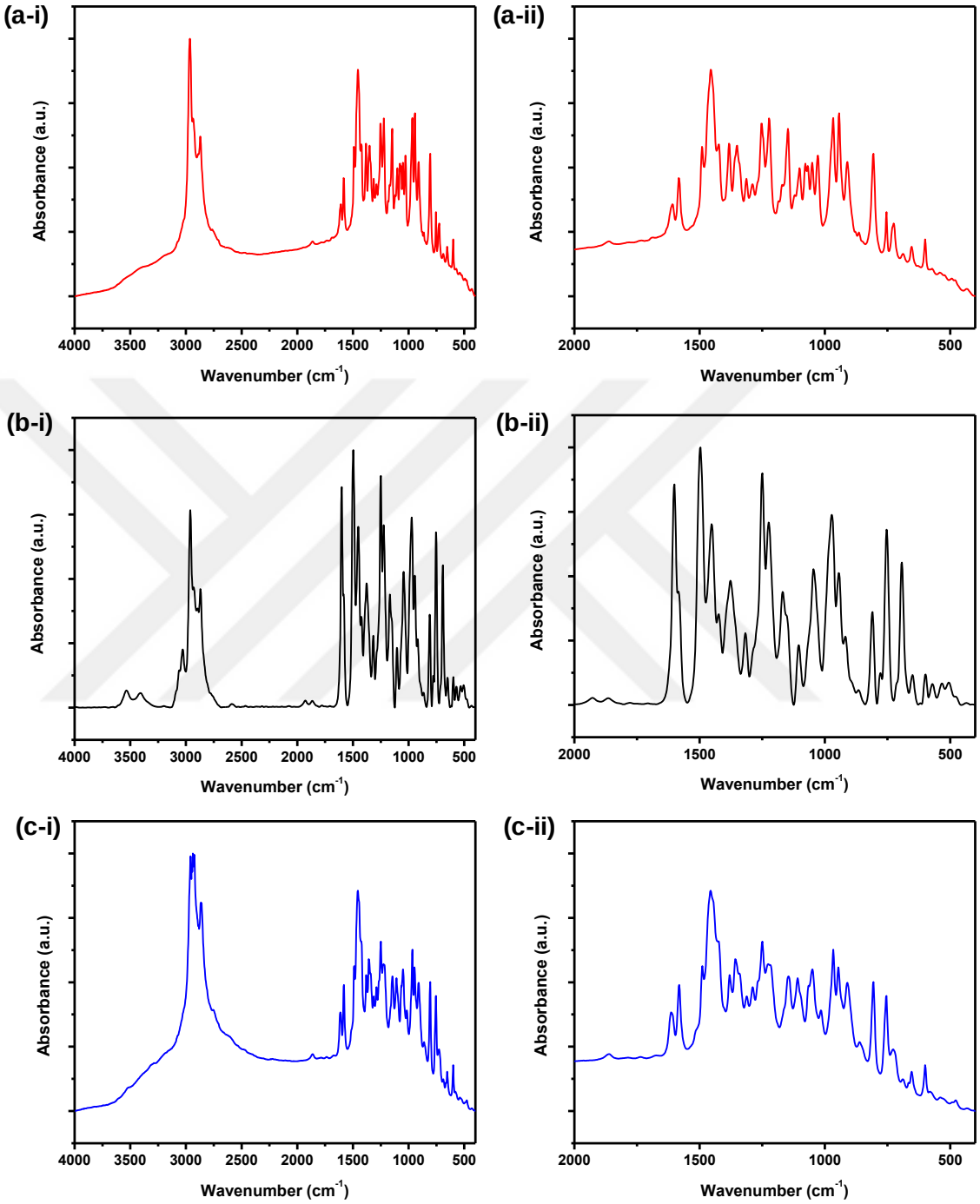

Figure 18. FTIR spectra of (a) T-ea, (b) T-a and (c) T-dh, (i) in the range of 4000-400cm^{-1} and (ii) in the range of 2000-400cm^{-1}.

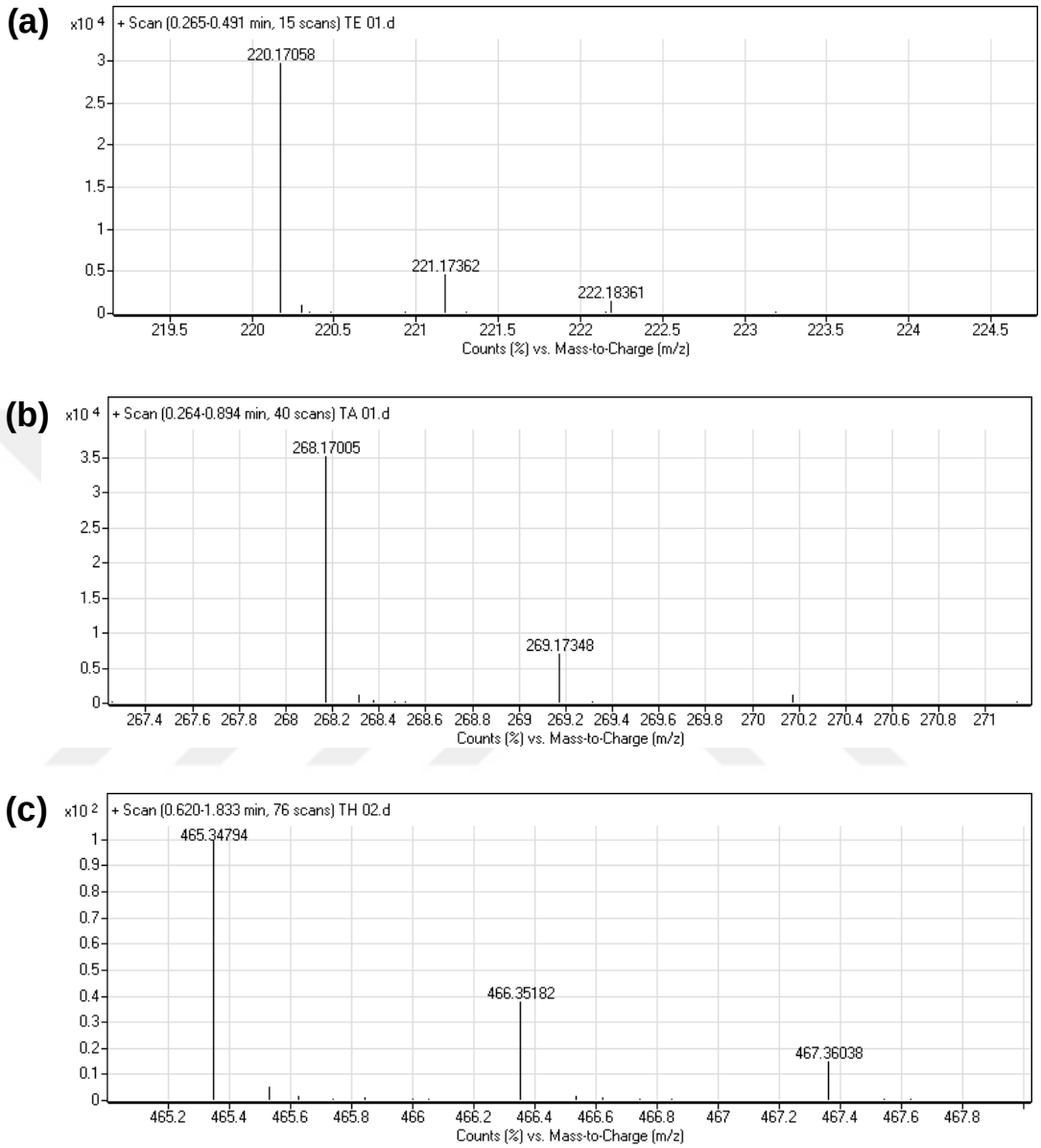

Figure 19. Mass spectra of (a) T-ea; $[M+H]^+$ (calculated): 220.1695, $[M+H]^+$ (observed): 220.1705, (b) T-a; $[M+H]^+$ (calculated): 268.1695, $[M+H]^+$ (observed): 268.1700, and (c) T-dh; $[M+H]^+$ (calculated): 465.3475, $[M+H]^+$ (observed): 465.3479.

In addition to the mass spectroscopy analysis, elemental analysis of eugenol-based benzoxazine monomers were performed as well. Table 3 summarizes the weight percentages of each element found in the structure of T-a, T-ea and T-dh as experimentally measured and theoretically calculated values. As it is observed from the Table 3, experimental and theoretical values are very close to each other illusturating the synthesis of desired molecules is achieved. Negligible diffreneces in the elemental compositions might be resulted from the unreacted species. However, this is not a disadvantage for the benzoxazines because unreacted species especially, phenols behave as a catalyst during the thermal curing and decrease the polymerization temperature.

Table 3. Atomic weight percentages of elements in synthesized thymol based bio-benzoxazines.

	Benzoxazine	N (%)	C (%)	H (%)	O (%)
Experimental values	T-a	5,40	80,45	7,94	
	T-ea	6,31	75,29	8,83	
	T-dh	6,18	75,88	8,76	
Theoretical values	T-a	5,24	80,86	7,92	5,98
	T-ea	6,39	76,67	9,65	7,29
	T-dh	6,03	77,54	9,54	6,88

3.2.2. Polymerization of the thymol-based benzoxazine monomers by thermal curing; their structural and thermal characterizations

The typical polymerization rection to obtain polybenzoxazines is based on the opening of oxazine ring and cross-linking of the molecules by thermal curing. Here, eugenol-based benzoxazine monomers namely T-ea, T-a and T-dh were polymerized by thermally initiated ring opening rections which is performed step-wise at 150, 175, 200, 225 and 250ºC, consequently polybenzoxazines which are denoted as PT-ea, PT-a and PT-dh were obtained, respectively. All of the polybenzoxazines were dark-brown which is a typical colour of polybenzoxazines when they are thermally cured. The molecular structures of the eugenol-based bio-benzoxazine monomers (T-ea, T-a and T-dh) and their predicted polymers (PT-ea, PT-a and PT-dh) obtained by thermal curing are represented in Figure 20. In order to confirm the cross-linking achieved by step-wise curing, FTIR spectroscopy was used and after each step of thermal curing FTIR spectrum of samples was taken. In order to investigate the ring-opening, characteristic absorbance peaks of the oxazine ring which are asymmetric stretching vibration of C–O–C and C–H out-of-plane deformation mode of the benzene ring attached to the oxazine ring were taken into consideration. Because, oxazine ring opens by heating at temperatures in the range between 160 and 220ºC [36], and intensity of the peaks decraeses with increasing temperature.

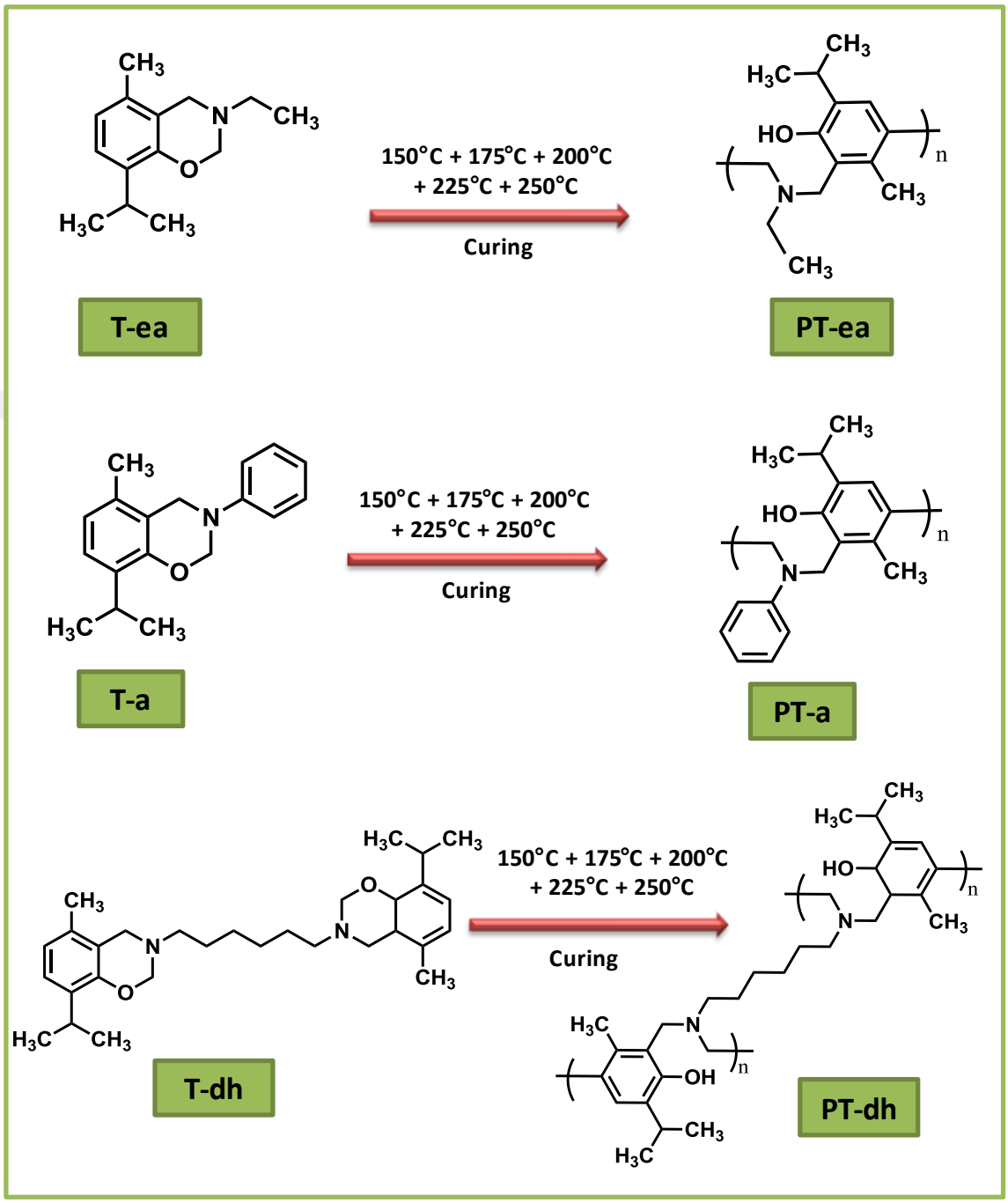

Figure 20. Polymerization of thymol-based bio-benzoxazines with thermally initiated ring-opening reaction.

FTIR spectra of T-ea, T-a, T-dh, after one hour heating each bio-benzoxazine at 150 ºC and additional heating at 175, 200, 225 and 250ºC are given in Figure 21. As it is shown on the spectra, intensity of the characteristic oxazine ring absorbance peaks decreased with increasing temperature and almost disappeared heating at 250ºC. In addition, very broad absorbance peak at around 3400 cm^{-1} was obseved especially after heating 200ºC and the intensity/broadness of this peak increased with increasing temperature. For PT-ea, PT-a, PT-dh, this broad band mainly may be attributed the combination of interactions; $O^{-}...H^{+}N$ intermolecular hydrogen bonding, OH…N intermolecular hydrogen bonding, OH...O intramolecular hydrogen bonding and OH...π intermolecular hydrogen bonding [244, 245]. The increasing the intensity of this peak with heating show that opening of the oxazine rings as a result polymerization of each bio-benzoxazine was achived.

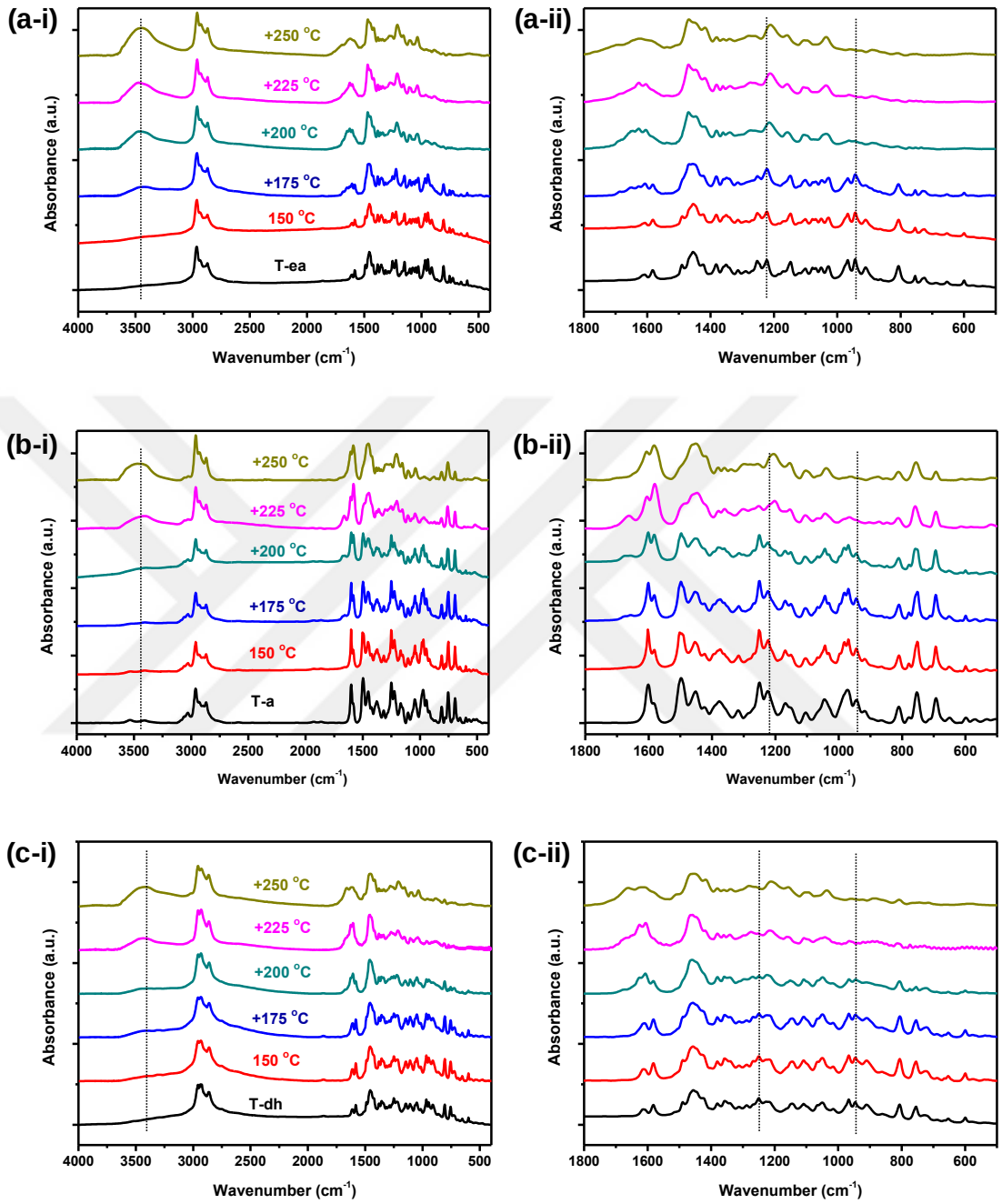

Figure 21. FTIR spectra of (a) T-ea, (b) T-a and (c) T-dh after each thermal curing step (i) in the range of 4000-400cm^{-1} and (ii) in the range of 2000-400cm^{-1}.

Furthermore, the thermal properties of the bio-benzoxazines and their polymers were investigated by TGA under nitrogen atmosphere. Figure 22 demonstrates the TGA thermograms of T-ea, T-a, T-dh and cured PT-ea, PT-a, PT-dh. As it is observed, three step thermal decomposition profile of all bio-benzoxazines became one step after curing indicating the polymerization was achieved. Table 4 summarizes the data obtained from TGA profiles. Only, in the case of T-hd, T_5 and T_{15} values could not be calculated properly, most probably water adsorption of the benzoxazine monomer. T_5 , T_{15} and Td values of the T-ea and T-a were very similar to each other. In addition, main decomposition temperatures of cured bio-benzoxazines were very close to each other and PT-a has the highest value since additional benzene containing polybenzoxazines are superior to the typical aliphatic amine-based polybenzoxazines. The char yields (CY) were also calculated from the TGA profiles in Figure 22. A notable enhancement of the char yield was observed for all bio-benzoxazines after thermal curing indicating the high cross-linked density achived by polymerization.

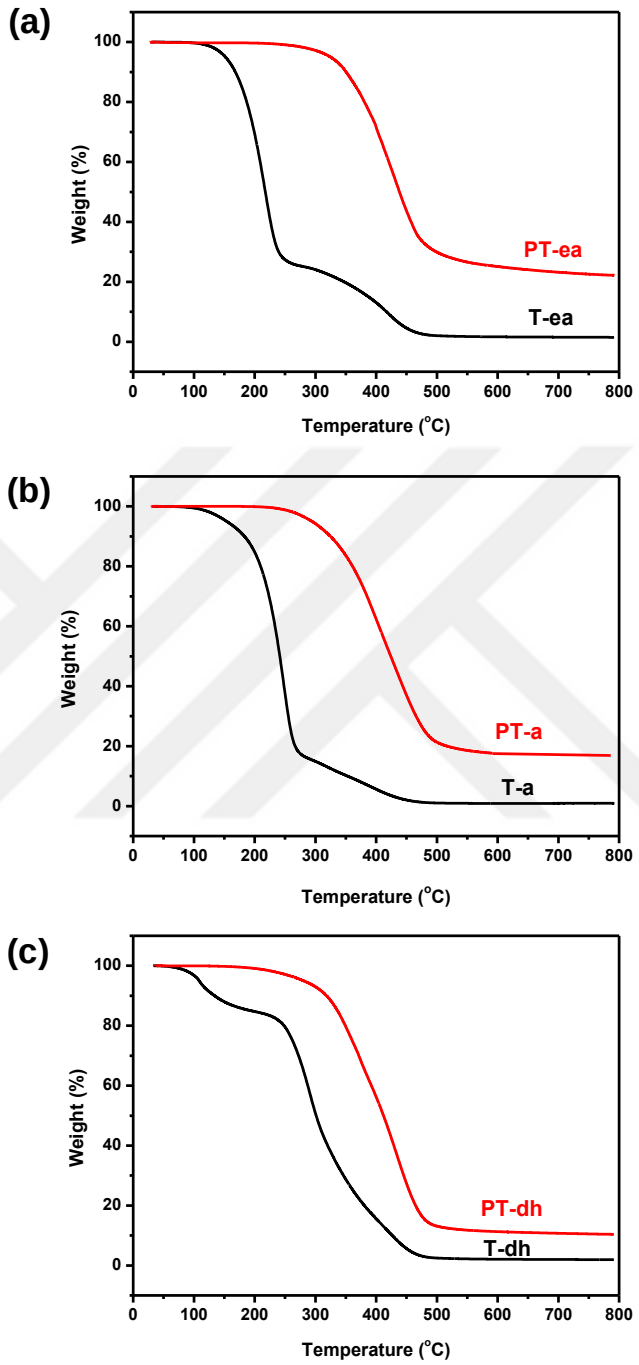

Figure 22. TGA thermograms of (a) T-ea and PT-ea (b) T-a and PT-a (c) T-dh and PT-dh.

Table 4. Thermal properties of the thymol-based bio-benzoxazines before and after thermal curing.

Benzoxazine	T_5 (ºC)	T_{15} (ºC)	T_d (ºC)			CY (%)
T-ea	151	178	218	317	420	1.5
PT-ea	324	366		431		22.2
T-a	154	199	247	319	400	0.9
PT-a	298	344		436		17.6
T-dh	126	198	295	336	427	0.6
PT-dh	281	336		432		12

Chapter 2: Main-chain polybenzoxazine nanofibers

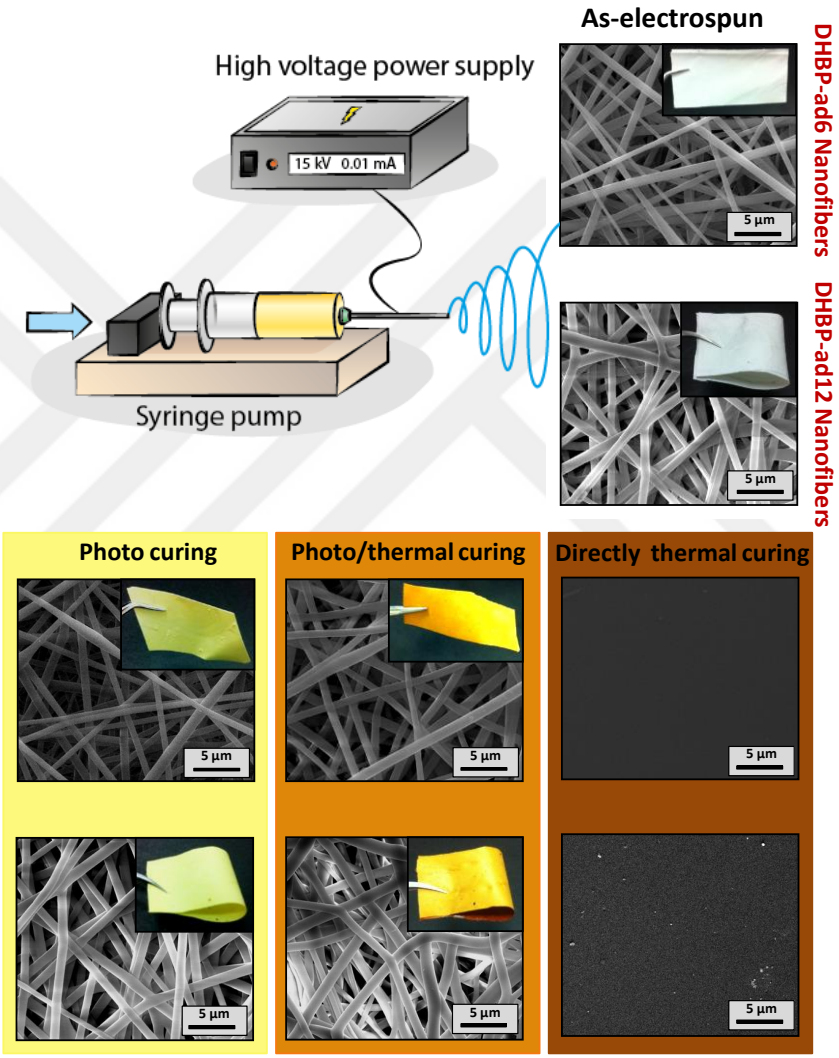

3.3. Bisphenol-A based main-chain polybenzoxazine nanofibers

Basically, benzoxazines are synthesized from mono-functional phenols and amines with different substitutional groups. Besides, any combination of a difunctional phenol and primary amine and in a similar manner, diamine and mono-functional phenol can be used for the synthesis of benzoxazines [1]. However, a more recent concept of benzoxazine resins involves the use of a difunctional phenolic derivative and a diamine, producing a linear polymer having oxazine rings in the main-chain called as main-chain polybenzoxazine (MCPBz) [1]. As MCPBz can be obtained by using difunctional amines and phenolic derivative, and they can also be synthesized as repeating unit of a polymer chain, block copolymer or as a side chain as well [16-33]. The thermal and mechanical performance of polybenzoxazine thermosets obtained from MCPBz are affirmed to be excellent than those obtained from the benzoxazine monomers [25]. In other words, some of the characteristics; for instance easy processibility, flexibility, high density of crosslink after curing and lower fragility for cured end-structures were achieved for polybenzoxazines. In one respect, MCPBz have potentials as an easy processable and crosslinkable thermoplastic, which become thermosets at ~200°C *via* opening of oxazine ring by thermal activation [34, 35].

MCPBz can be quite useful for the production of nanofibers from this kind of materials since chain entanglement and overlapping is the key factor for the production of nanofibers by electrospinning. Electrospinning is a widely used technique to produce multifunctional nanofibers from remarkable range of organic and inorganic materials including polymers, polymer blends, composites, sol-gels, ceramics and so on [86, 87]. Nanofibers produced by this technique have a very large surface area to volume ratio and nanoscale pores having distinctive chemical, physical and mechanical properties when compared to their bulk or film forms. Polybenzoxazines are extensively studied in the literature with their different forms such as bulk [67, 167-170], film [61, 72, 171-182], aerogel [183-188], porous membrane [189, 190], so on. for various applications. On the other hand, electrospinning of nanofibers from polybenzoxazine resins is a new concept. In this chapter, we focus on the electrospinning of MCPBz nanofibers and their curing studies in order to obtain novel polybenzoxazine based materials.

3.3.1. Synthesis and structural characterization of the bisphenol-A based main-chain polybenzoxazines; PBA-ad6 and PBA-ad12

In this study, we used bisphenol-A as a phenolic derivative and two different types of amine with different chain lenght (1,6-diaminohexane and 1,12-diaminododecane) for the synthesis of two MCPBz namely, PBA-ad6 and PBA-ad12. Synthesis of PBA-ad6 and PBA-ad12 are shown in Figure 23. The structure of the synthesized PBA-ad6 and PBA-ad12 were confirmed by ^{1}H NMR and FTIR spectroscopies.

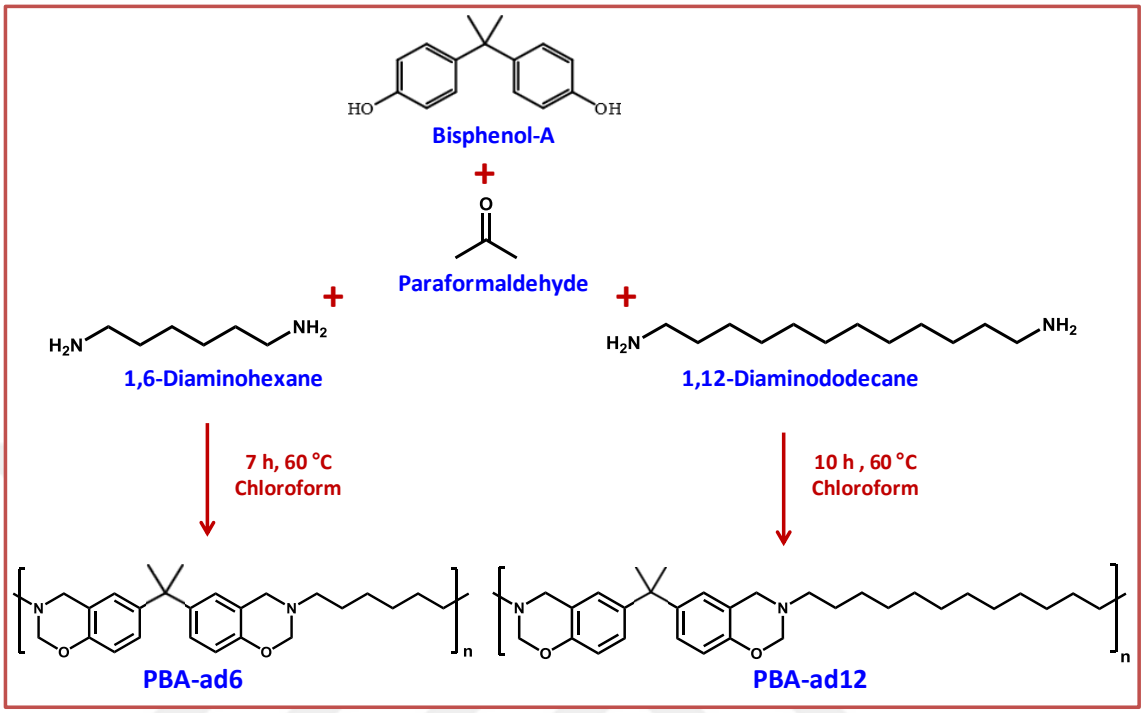

Figure 23. Synthesis of the PBA-ad6 and PBA-ad12 resins.

The proposed chemical structures and ^{1}H NMR spectra of PBAad6 and PBA-ad12 are given in Figure 24. The characteristic benzoxazine resonances attributed to the methylene units of oxazine ring; O-CH_2-N and the Ph-CH_2-N raised as singlets at 3.94 and 4.82 ppm for PBA-ad6 and 3.95 and 4.84 ppm for PBA-ad12, respectively. Resonance bands of aliphatic protons were observed at 1.36 and 2.73 ppm for PBA-ad6, and 1.27 and 2.74 ppm for PBA-ad12. In addition, resonance bands of methyl group protons of bisphenol-A appeared at 1.60 ppm and aromatic structure resonance bands observed at 6.68-6.98 ppm region for both of the polybenzoxazine [33, 84, 247, 248]. In brief, the ^{1}H NMR data confirm the successful synthesis of the two MCPBz. Moreover, generally the resonance around 3.7 ppm assigned for the Mannich bridge protons of

open oxazine rings were not observed in the ^{1}H NMR spectra of synthesized MCPBz. The ^{1}H NMR results indicated that the synthesized MCPBz were free of ring-opened oligomers and purification with cold methanol was good enough to obtain high purity MCPBz.

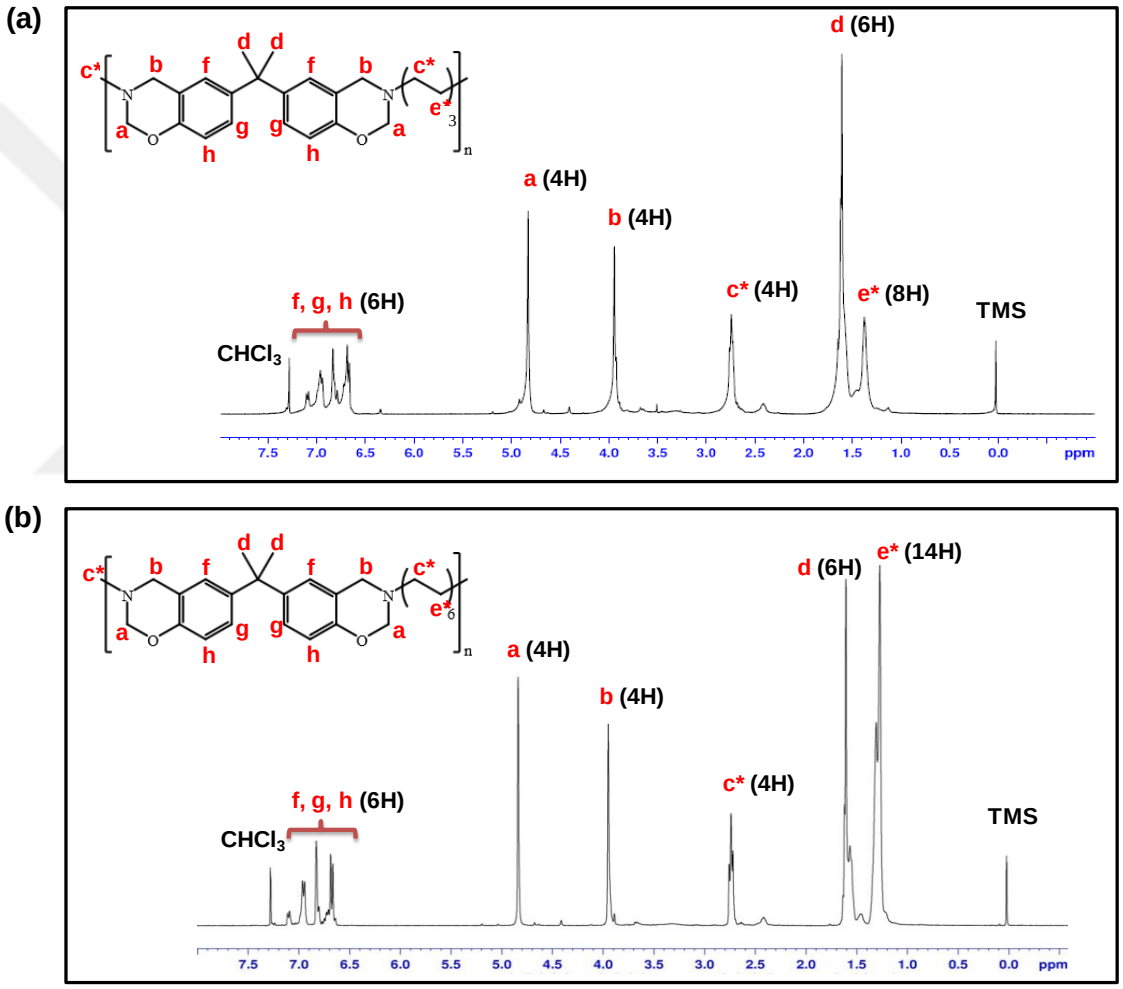

Figure 24. ^{1}H NMR spectra of (a) PBA-ad6 and (b) PBA-ad12 in $CDCl_3$ (c* corresponds to methylene protons attached to N; e* corresponds to aliphatic protons of diamine). (Copyright © 2014, Reprinted from Ref. [191] with permission from Elsevier)

Figure 25 represents the FTIR spectra of the PBA-ad6 and PBA-ad12. The characteristic peaks of the benzoxazine structure were observed at exactly the same wavenumbers with different intensities for both MCPBz. Existence of the strong band at 936 cm^{-1} which is ascribed to the benzene ring mode that is attached to the oxazine ring was the great evidence for the synthesis of target MCPBz. In addition, the very intense and sharp peak appearing at 1503 cm^{-1} is due to the in-plane CH bending mode of the tri-substituted benzene ring and the strong peak appearing at 1232 cm^{-1} is due to the aromatic ether stretching of C-O-C. These peaks confirmed the presence of benzoxazine ring structure in MCPBz samples. Apart from these, strong and sharp peaks were observed at 2928 and 2848 cm^{-1} correspond to the antisymmetric and symmetric stretching of CH2 groups in the aliphatic regions. Relatively medium intensity peak at 824 cm^{-1} is due to the CH out-of-plane bending mode of the tri-substituted benzene ring. The FTIR spectra of MCPBz samples correlate with the literature [84, 247-249] and prove that the synthesis of PBA-ad6 and PBA-ad12 were successfully achieved.

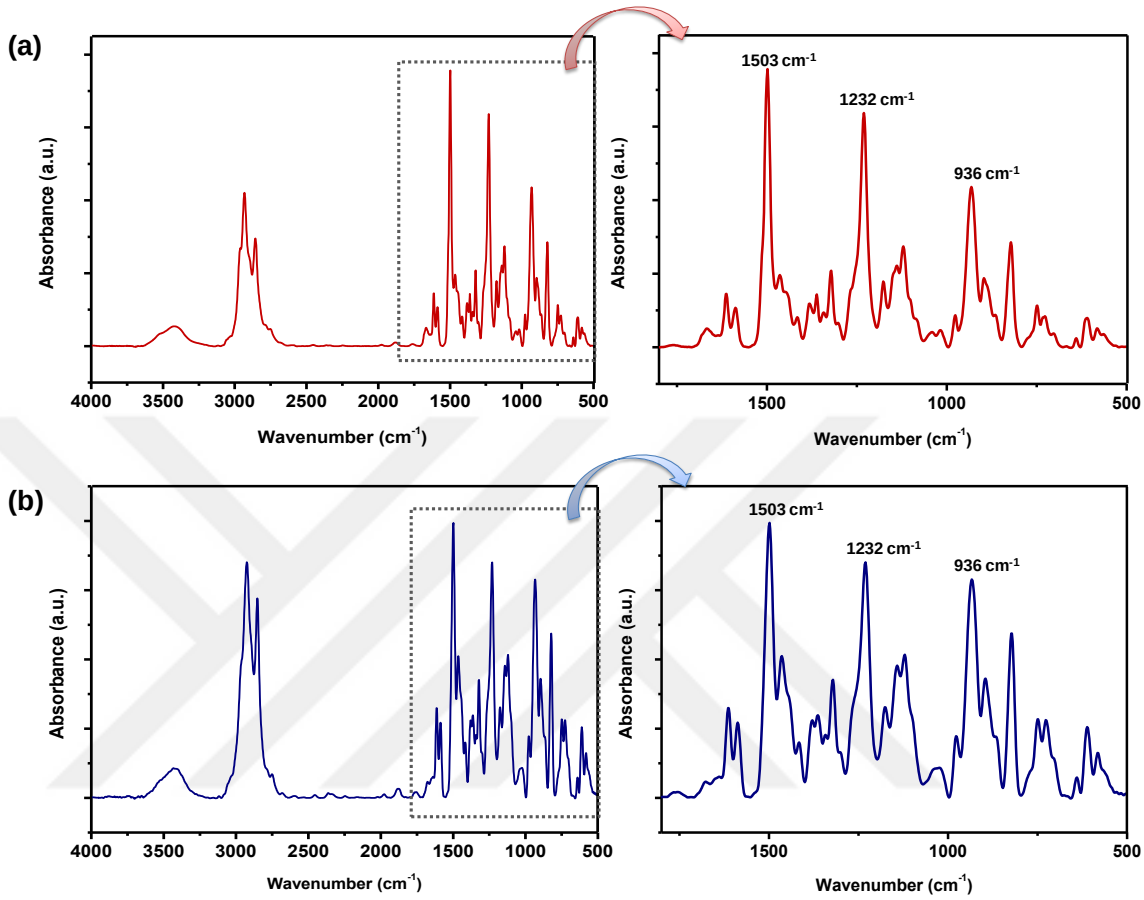

Figure 25. FTIR spectra and magnified region between 1800 and 500 cm^{-1} of (a) PBA-ad6 and (b) PBA-ad12. (Copyright © 2014, Reprinted from Ref. [191] with permission from Elsevier)

3.3.2. Electrospinning of PBA-ad6 nanofibers

Electrospinning of PBA-ad6 nanofibers was achieved by using chloroform/DMF (4:1, v/v) solvent system. The concentration of the PBA-ad6 solution was varied from 30% to 45% (w/v) to find out the most favorable concentration required for bead-free and

uniform nanofibers. Table 5 summarizes the properties of PBA-ad6 solutions and the morphological features of the electrospun nanofibers. When the concentration of the solution increased from 30 to 45% (w/v), the viscosity of the solution increased as well. This is an expected result which is due to the higher number of polymer chain entanglement and overlapping at higher solution concentration. Figure 26 represents the SEM images and fiber diameter distribution of PBA-ad6 nanofibers electrospun from 30, 35, 40, and 45% (w/v) polymer solutions. Electrospinning of 30% (w/v) PBA-ad6 solution resulted beaded morphology with ultrafine fibers having diameter range of 100-400 nm (AFD=260±70 nm) (Figure 26a,b). At low solution viscosity, it is common to observe beads along with the fibers because of the higher amount of solvent and fewer chain entanglements causing a prevailing effect during electrospinning [86, 106]. As the polymer concentration increased from 30% to 35% (w/v), the number of beads decreased dramatically and elongated beaded nanofibers in the range of 300-1000 nm diameter (AFD=590±138 nm) were produced (Figure 26c,d). This is due to the relatively lower viscosity which resulted in destabilization of the electrified jet during the electrospinning process and thus caused the formation of elongated beads instead of uniformfibers. When the polymer concentration reached to 40% (w/v) in solution, transformation from beaded nanofibers to bead free nanofibers was achieved. The increase in the viscosity which is due to the higher polymer chain entanglements in the solution is required for the electrospinning jet to be fully stretched for uniform fiber formation [86]. Bead-free nanofibers were produced at 40% (w/v) and 45% (w/v) for

PBA-ad6 solutions emphasizing the requirement of high solution viscosity. However, nanofibers electrospun from 40% (w/v) PBA-ad6 solution were more uniform and finer (AFD = 745±136 nm, fiber diameter distribution: 400-1100 nm) than the that of 45% (w/v) PBA-ad6 solution (AFD=1618±576 nm, fiber diameter distribution: 400-3200 nm) (Figure 26e-h). Notably, with the increase in viscosity/concentration, the diameter of the electrospun fiber also increases. As it is observed from the SEM images (Figure 26), the diameter of PBA-ad6 nanofibers spanned from nanometer to micron scale when the concentration of the polymer solution increased. The reason for the increase in fiber diameter is the greater resistance of the solution to be stretched because of the more chain entanglements at higher polymer concentration [86].

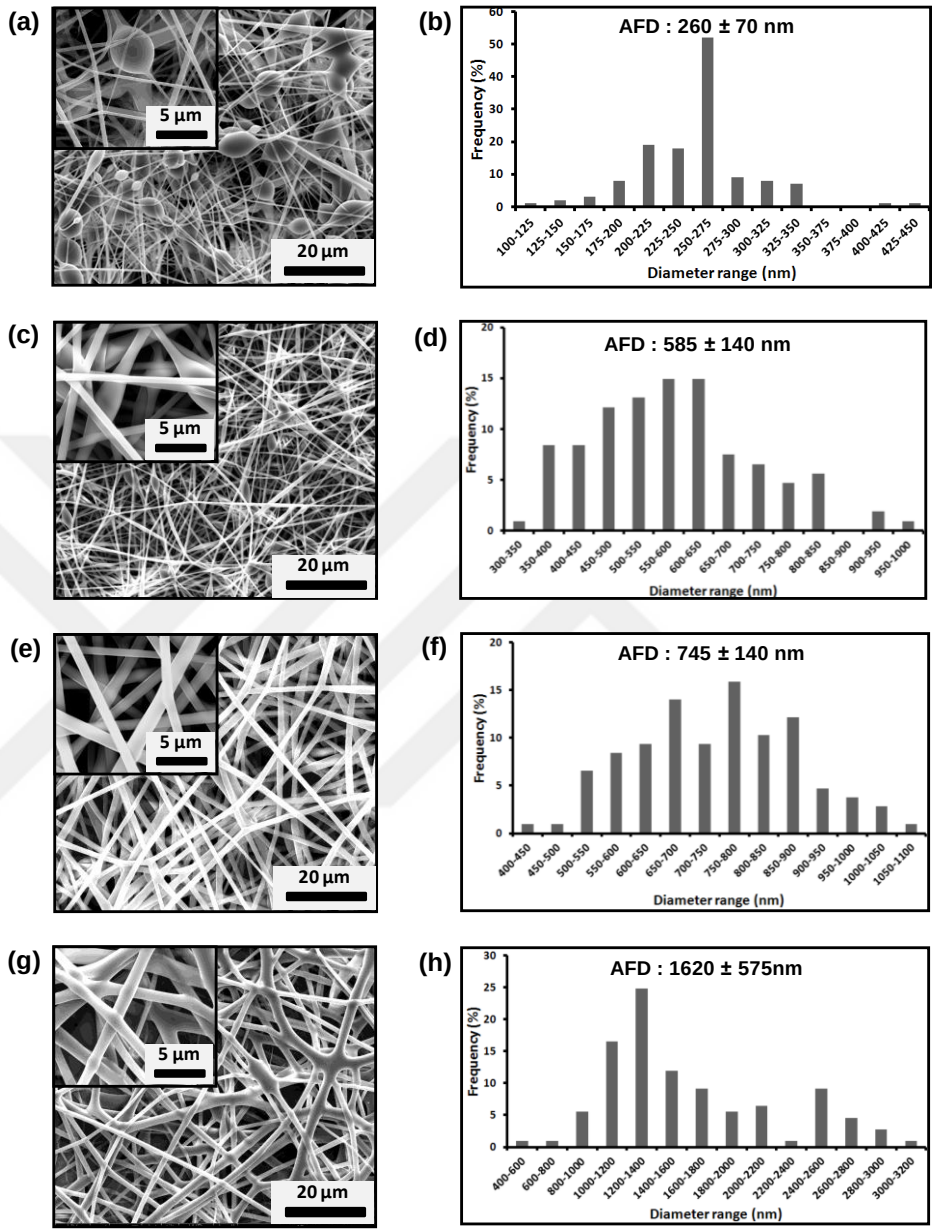

Figure 26. SEM images and corresponding fiber diameter distributions of the electrospun nanofibers obtained from solutions of PBA-ad6 (a, b) 30%, (c, d) 35%, (d, e) 40% and (g, h) 45%. Inset shows magnified view of a typical region. (Copyright © 2013, Reprinted from Ref. [191] with permission from Elsevier)

Table 5. The characteristics of the PBA-ad6, PBA-ad12 solutions and their electrospun fibers. (Copyright © 2014, Reprinted from Ref. [191] with permission from Elsevier)

Solutions	% Polymer (w/v)	Viscosity (Pa.s)	Average fiber diameter (nm)	Diameter range (nm)	Fiber morphology
PBA-ad6_30%	30	0.29	260 ± 70	100-450	Beaded nanofibers
PBA-ad6_35%	35	0.59	590 ± 140	300-1000	Beaded nanofibers
PBA-ad6_40%	40	0.77	745 ± 140	400-1100	Bead-free nanofibers
PBA-ad6_45%	45	1.15	1620 ± 580	400-3200	Bead-free nanofibers
PBA-ad12_15%	15	0.46	430 ± 110	200-700	Beaded nanofibers
PBA-ad12_18%	18	1.24	805 ± 220	400-1500	Bead-free nanofibers
PBA-ad12_20%	20	2.73	1840 ± 610	1000-3200	Bead-free microfibers

3.3.3. Electrospinning of PBA-ad12 nanofibers

Electrospinning of PBA-ad12 nanofibers was also performed in chloroform/DMF (4:1, v/v) solvent system similar to that of PBAad6. According to GPC measurements, PBA-ad12 has a higher molecular weight (Mw= ~17,000) than PBA-ad6 (Mw= ~11,500) because of its longer aliphatic chain structure. As it is known, the molecular weight of the polymer stand for the length of the polymer chain, which affects the viscosity of the solution since the polymer chain length determines the amount of entanglement of chains in a solvent [86]. Therefore the solution properties and electrospinning parameters of this polymer is expected to be different. Table 6 summarizes the solution characteristics and the morphological findings of the electrospun PBA-ad12 nanofibers. As mentioned earlier, higher molecular weight and longer chain causes more chain entanglements, thus electrospinning of PBA-ad12 was performed at relatively lower polymer concentrations. For this polymer, nanofibers were electrospun from 15, 18 and 20% (w/v) polymer solutions to determine the most suitable concentration for obtaining

bead-free and uniform nanofibers. Figure 27 illustrates the SEM images of the nanofibers electrospun from these three solutions. Although, the concentrations of the solutions were very close to each other, there was distinct differences between the viscosities (Table 6) of these solutions which greatly affect the morphology and the AFD of the resulting electrospun nanofibers (Figure 27). As it is observed from the SEM images, 15% (w/v) PBA-ad12 solution yielded beaded nanofibers having diameter range of 200-750 nm (AFD=430±110 nm) because of the low viscosity of the polymer solution (Figure 27a,b). Solely, bead-free and uniform nanofibers were obtained when the PBA-ad12 solution concentration was at 18% (w/v). The diameter of the nanofibers electrospun from 18% (w/v) PBA-ad12 solution was ranging between 400 and 1500 nm (AFD=805±220 nm) (Figure 27c,d). It is a typical behavior of polymeric systems in the electrospinning process that beaded nanofibers transform to bead-free fibers when the concentration and/or viscosity of the polymer solution is optimized [86]. The viscosity of this solution was high enough to stretch with electrified continuously resulting in a bead-free and continuous morphology. When the concentration of the PBA-ad12 solution increased to 20% (w/v), thefiber diameter distribution became broader (1000-3200 nm) and the diameters of the fibers became thicker (AFD =1840±610 nm) because of the high solution viscosity (Figure 27e,f).

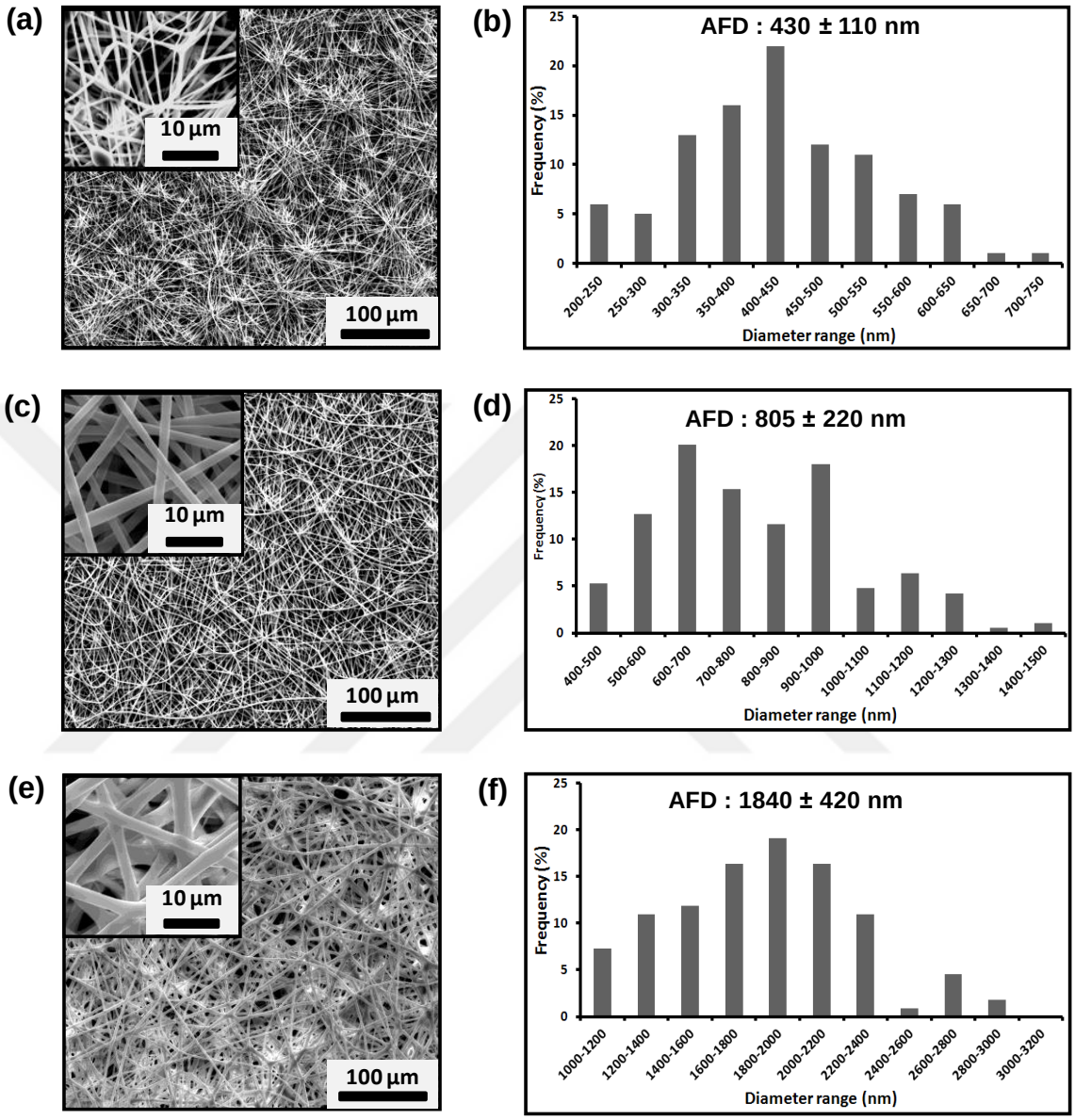

Figure 27. SEM images and corresponding fiber diameter distributions of the electrospun nanofibers obtained from solutions of PBA-ad12 (a, b) 15%, (c, d) 18% and (d,e) 20%. Inset depicts magnified view of a typical region. (Copyright © 2014, Reprinted from Ref. [191] with permission from Elsevier)

3.3.4. Curing studies of PBA-ad6 and PBA-ad12 nanofibrous mats

Nanofibrous mats obtained from these two MCPBz have shown some differences in mechanical properties. PBA-ad6 nanofibers was kind of delicate and could not be separated from the aluminum foil completely in one piece (Figure 28a). On the other hand, PBA-ad12 nanofibers can be easily handled and it has a flexible characteristic (Figure 28b). Moreover, their thermal properties are also different from each other because of the difference in their chemical structures.

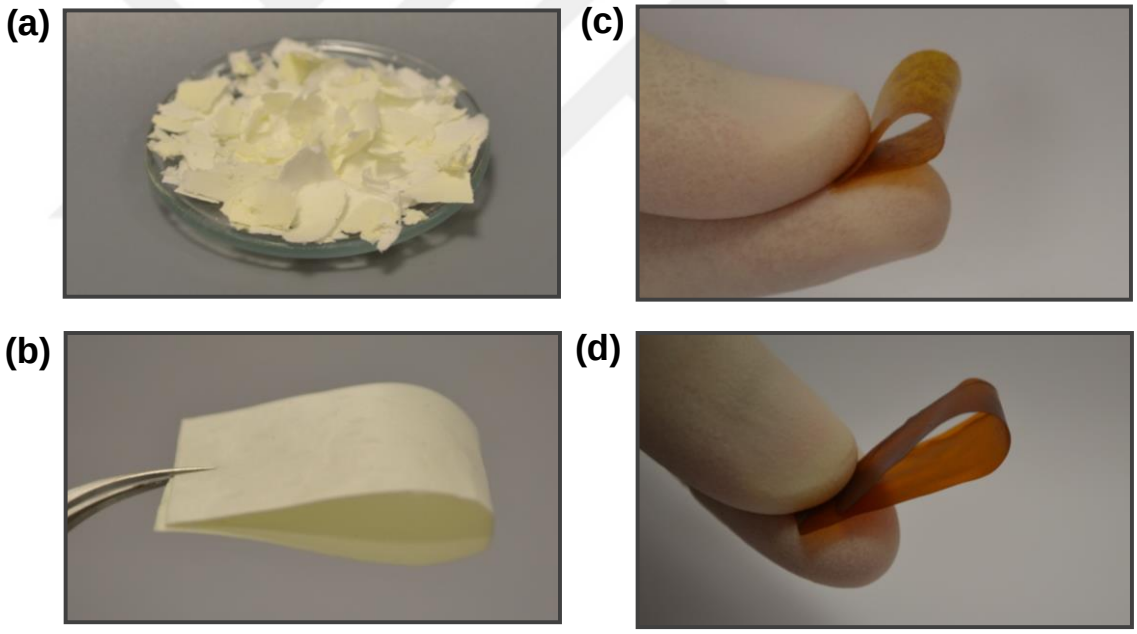

Figure 28. Photographs of the electrospun nanowebs from (a) 40% PBA-ad6, (b) 18% PBA-ad12 and after curing (c) PBA-ad6, (d) PBA-ad12 step by step at 75°C; 1h, 90 °C; 1h, 120 °C; 1h, 150°C;1h , 180°C; 1h and 220 °C; 1h. (Copyright © 2014, Reprinted from Ref. [191] with permission from Elsevier)

Figure 29 shows the DSC thermograms of PBA-ad6 and PBA-ad12 nanofibrous mats. Melting transition was observed for PBA-ad6 and PBA-ad12 nanofibrous mats at 73 and 42ºC, respectively. This difference possibly arised from the longer aliphatic chain of PBA-ad12 which caused the decrease in the melting point. In addition, two exothermic overlapping peaks centered at 205 and 253ºC for PBA-ad6; 203 and 248ºC for PBA-ad12 nanofibrous mats appeared in the DSC thermograms. The low temperature peaks could be attributed to the crosslinking reaction (of methylol groups) and the higher temperature peaks assigned to typical benzoxazine polymerization by the consumption of benzoxazine groups in the main chain [33].

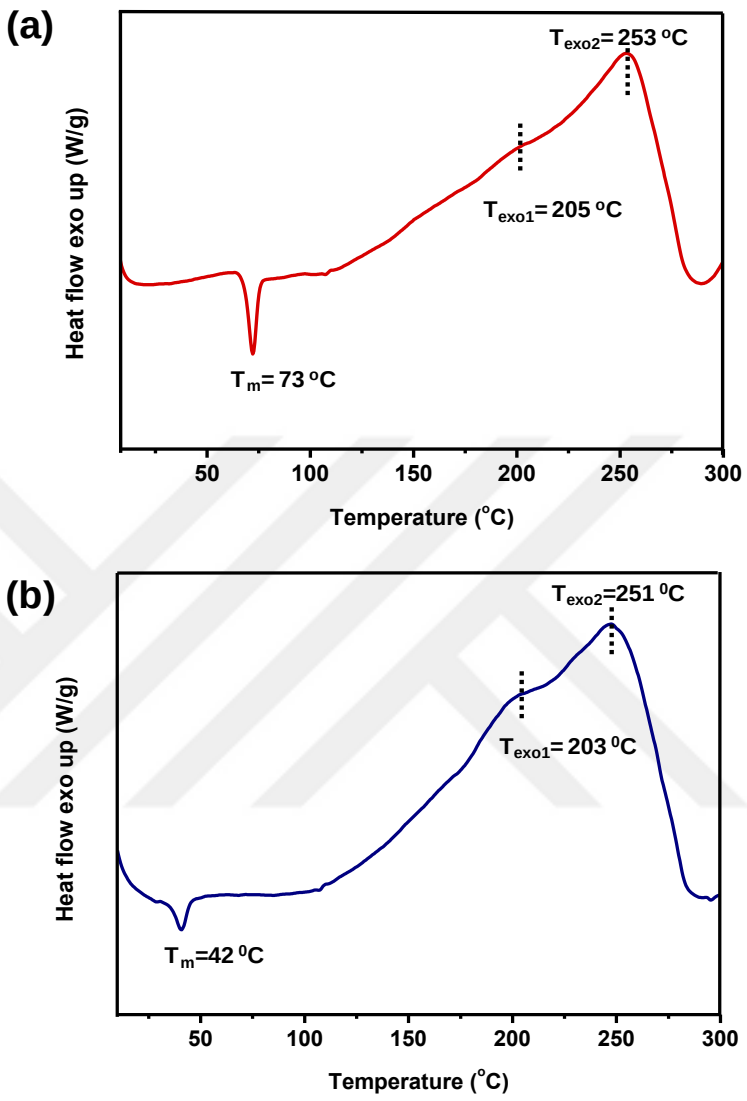

Figure 29. DSC thermograms of (a) PBA-ad6 and (b) PBA-ad12 nanofibers. (Copyright © 2014, Reprinted from Ref. [191] with permission from Elsevier)

Conventionally, benzoxazine monomers and MCPBz are able to form cross-linked thermosets polybenzoxazines ~200ºC by thermally activated ring opening polymerization [16]. In order to investigate the crosslinking behavior of PBA-ad6 and

PBA-ad12 nanofibers, curing experiments were performed for these two nanofibers. Although melting transitions were observed in the DSC thermograms of the PBA-ad6 and PBA-ad12 nanofibers, SEM images were also taken from two MCPBz nanofibers after each temperature step to confirm the melting of nanofibers with thermal treatment (Figure 30). As it is observed from the SEM images (Figure 30c,d), PBA-ad6 nanofibers have already started melting at ~90ºC and completely melted at 120ºC. The fiber structure is deteriorated and a film formed (Figure 30e).

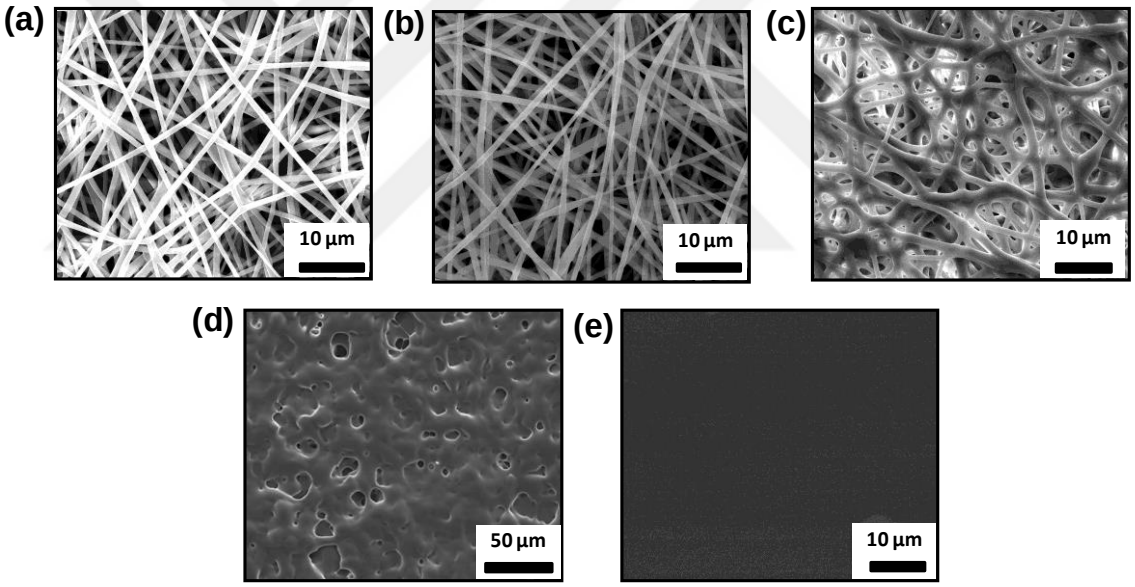

Figure 30. SEM images of the electrospun nanofibers before and after thermal treatment; (a) 40% PBA-ad6, (b) 75°C; 1h, (c) 90°C; 1h, (d) 100°C; 1h, (e) 120°C; 1h. (Copyright © 2014, Reproduced from Ref. [191] with permission from Elsevier)

On the other hand, PBA-ad12 nanofibers started to melt at relatively lower temperatures, ~50ºC and completely melted at 75ºC forming a film (Figure 31). This result correlates

with the measured melting temperature of PBA-ad12 nanofibrous mats by DSC method. Since melting temperature was 42ºC, we observed partially melted fiber morphology after keeping this sample 1 hour at 50 ºC. Consequently, PBA-ad6 and PBA-ad12 nanofibrous mats could not preserve their fiber structure during the thermal treatment because of their low melting points and they became uniform film at 120ºC. Nevertheless, curing studies were performed for these samples to determine curing temperatures of two MCPBz mats which can be used to produce composite materials by blending with other polymers.

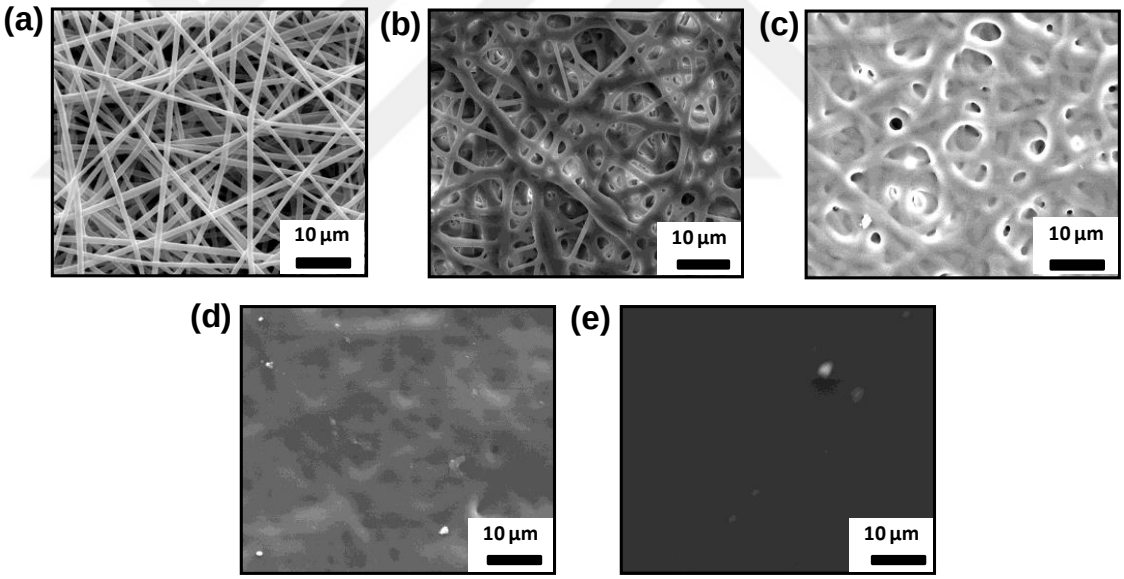

Figure 31. SEM images of the electrospun nanofibers before and after thermal treatment; (a) 18% PBA-ad12, (b) 50°C ;1h, (c) 60°C ;1h (d) 75°C; 1h and (e) 120 °C; 1h. (Copyright © 2014, Reproduced from Ref. [191] with permission from Elsevier)

FTIR spectroscopy was used to investigate the structural changes of PBA-ad6 and PBA-ad12 films after heating at each curing temperature, since characteristic peaks observed at 936 cm^{-1} (benzene ring mode that is attached to the oxazine ring) and 1232 cm^{-1} (aromatic ether stretching of C-O-C) disappear with the ring opening reaction. Therefore, we were able to determine the proper temperature required for complete curing. Even though, there was a remarkable difference in melting transitions of these two MCPBz nanofibrous mats, no significant change was observed their curing temperatures in DSC thermograms, thus, curing studies were performed at same temperature steps. FTIR spectra of PBA-ad6 and PBA-ad12 mats that were step cured at 75, 90, 120, 150, 180 and 220ºC for 1 h at each step are given in Figure 32. As it is observed from the spectra, curing has not yet completed for both MCPBz mats at 120 ºC where they have fully melted and formed films (Figure 30e and Figure 31e), hence, we could not obtain cross-linked nanofibers. On the other hand, the intensity of the peaks at 936 $cm^{-1}$and 1232 cm^{-1} decreased with increasing of temperature from 120 to180ºC and the peaks almost disappeared at 220 ºC which is the required temperature for the curing of these two MCPBz mats. This result confirms the DSC findings where curing temperatures of PBA-ad6 and PBA-ad12 mats were measured as 205 and 203ºC, respectively. Finally, we obtained very fine and flexible films from both MCPBz (Figure 28c,d).

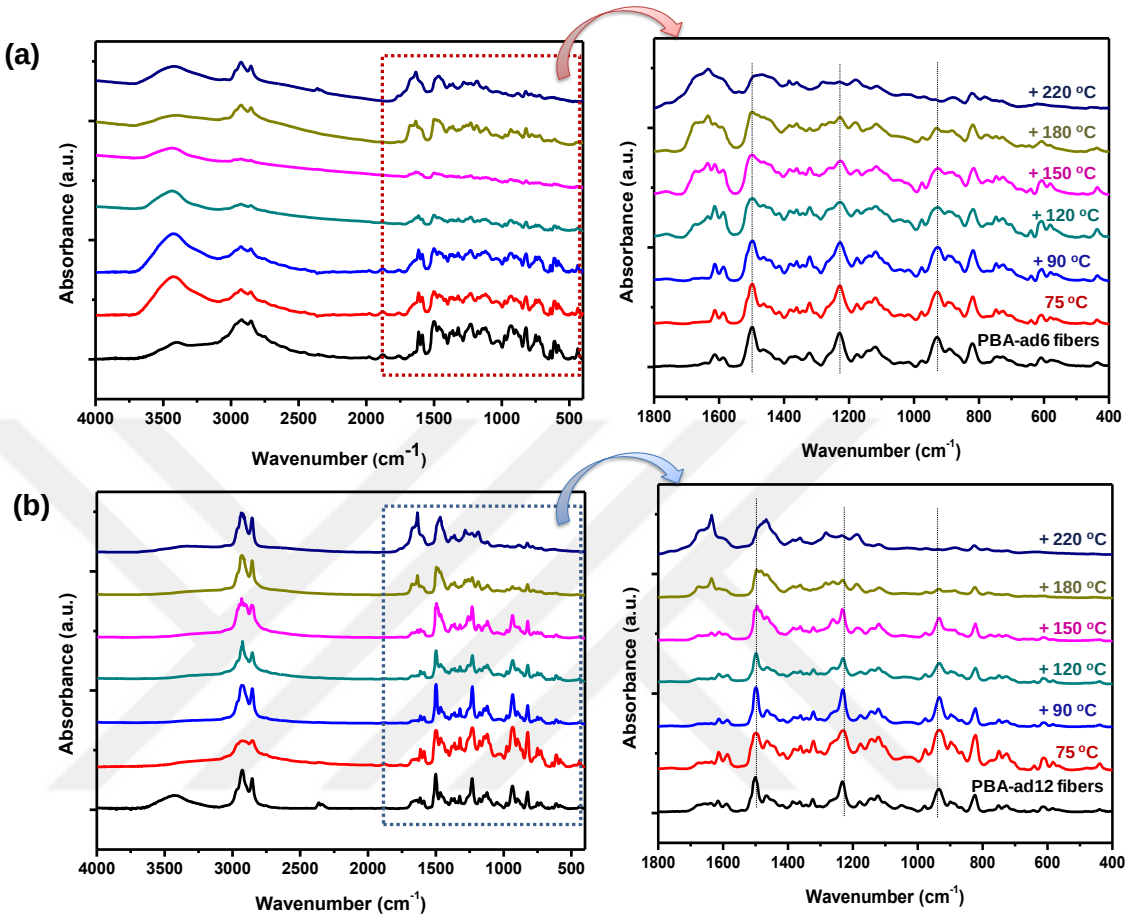

Figure 32. FTIR spectra and magnified region between 1800 and 400 cm^{-1} of (a) PBA-ad6 and (b) PBA-ad12 nanofibers before and after step cured at 75°C; 1h, 90°C; 1h, 120°C; 1h, 150°C;1h , 180°C; 1h and 220°C; 1h. (Copyright © 2014, Reprinted from Ref. [191] with permission from Elsevier)

Although, PBA-ad6 nanofibers are brittle and not easily handable, after curing the sample gained better mechanical properties and we obtained more flexible cross-linked PBA-ad6 films. Yet, we observed that cured PBA-ad12 film was more flexible than

cured PBA-ad6 film. The thermal stability of MCPBz films after curing was studied by TGA. Figure 33 shows the TGA thermograms and derivative weight losses of PBA-ad6 and PBA-ad12 films after curing. In addition to the FTIR results, one step thermal decomposition TGA thermograms also confirm the crosslinking of PBA-ad6 and PBA-ad12 films after heating up to 220ºC by step curing. Td_5 and Td_{10} values obtained from the TGA thermograms of MCPBz films are 328 and 360ºC for PBA-ad6films, 344 and 379ºC for PBA-ad12 films, respectively. The char yield of PBA-ad6 film is 22.8% while this value is 12.7% for PBAad12 that can be explained by the longer aliphatic chain of this MCPBz. As the length of aliphatic chains increased, decrease in the char yield of MCPBz was observed.

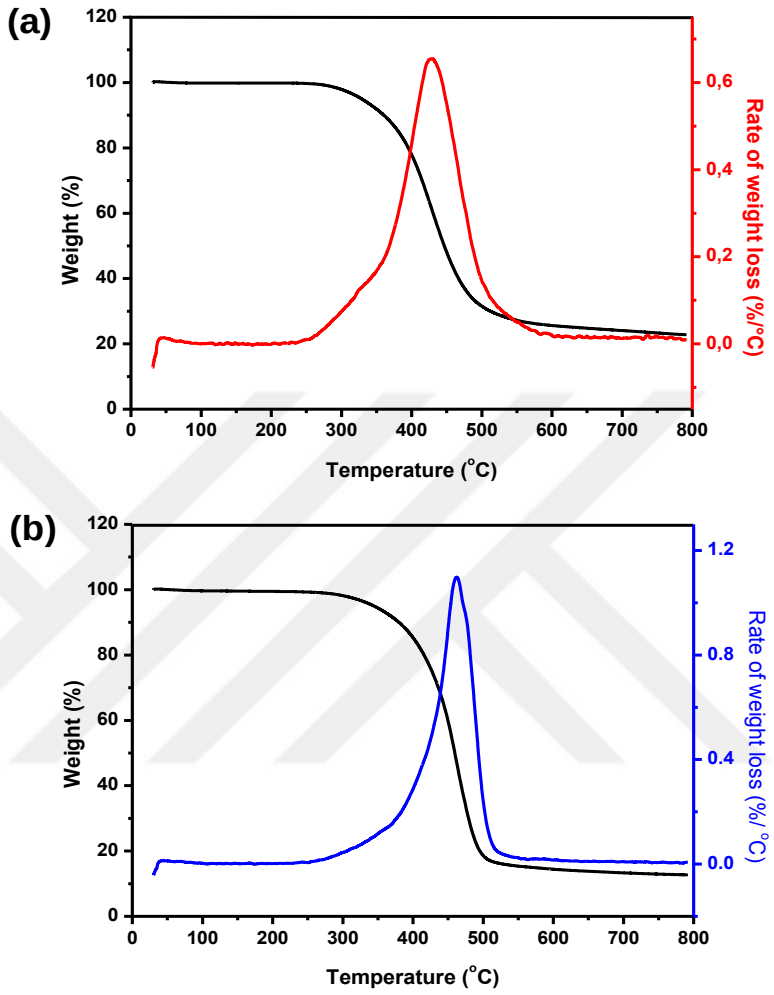

Figure 33. TGA thermograms and derivative weight losses of (a) PBA-ad6 and (b) PBA-ad12 nanofibers after step cured at 75°C; 1h, 90°C; 1h, 120°C; 1h, 150°C;1h, 180°C; 1h and 220°C; 1h. (Copyright © 2014, Reprinted from Ref. [191] with permission from Elsevier)

Here, we report the first study that accomplished to produce bead-free and uniform polybenzoxazine nanofibers from MCPBz (PBA-ad6 or PBA-ad12) without using any

carrier polymeric matrix. The morphological characterization of the electrospun MCPBz nanofibers carried out by SEM imaging revealed that the optimal electrospinning concentrations was 40% and 18% (w/v) for PBA-ad6 and PBA-ad12, respectively. PBA-ad12 nanofibers were more flexible than PBA-ad6 nanofibers which was possibly resulted from the longer chain structure and higher molecular weight. The fibrous structure could not be preserved during the thermal curing of PBA-ad6 and PBA-ad12 nanofibrous mats due to the low melting point of these MCPBz, yet, flexible and freestanding cross-linked films were obtained. As this is being the starting point of the electrospinning of polybenzoxazines without using carrier polymer matrix, this study provides the essential guidance for the production of nanofibers from different types of polybenzoxazines. Nonetheless, further developments are needed especially for the curing process without losing the fiber structure. Still, these nanofibers can be useful in composite material production with enhanced thermal and mechanical properties due to unique properties of polybenzoxazines. We anticipate that these MCPBz nanofibrous mats if curable while retaining their fiber morphology can be promising as high performance fibrous materials.

3.4. Cross-linked main-chain polybenzoxazine nanofibers by photo and thermal curing

Generally, polymerization/cross-linking of benzoxazines can be achieved by thermal curing which is a thermally induced ring opening reaction of benzoxazines and MCPBz occur at around 200°C [16]. However, in our previous study we could not able to produce cross-linked nanofibers from long linear aliphatic diamine based MCPBz nanofibers by directly thermal curing because of the very low melting points of PBA-ad6 and PBA-ad12 nanofibers (73 and 42ºC) which are quite lower than their curing temperatures (203 and 205ºC). Therefore, we focus on two steps curing procedure including the photo and thermal curing for the cross-linking of this type of MCPBz nanofibers. Besides, photo-curing is another method that can be used to obtain cross-linked materials from benzoxazines having photo active group or part in their structure. Although, thermal curing is very common and basic method to polymerize or cross-link benzoxazines and MCPBz, there are few studies that uses photo-curing for the polymerization of benzoxazines [222, 223]. In addition, benzophenone based benzoxazine monomers were synthesized and used as photoinitiator for the photopolymerization of acrylate monomers [224-227]. Besides, both photopolymerization as a preliminary step and thermally activated polymerization for the ring-opening and cross-linking of methacryloyl functional benzoxazines were studied [24]. All these research works provide us useful information on designing new

kind of benzoxazine resins to improve the curing procedure of MCPBz nanofibers in order to achieve cross-linking without deteriorating the fiber structure. For this purpose, initially, two novel MCPBz (DHBP-ad6 and DHBP-ad12) which consist of a benzophenone unit in the polymer main-chain were synthesized. Due to the presence of benzophenone unit in the main-chain, DHBP-ad6 and DHBP-ad12 nanofibers are able to crosslink by UV-light initiated free radical polymerization. Therefore, by synthesizing benzophenone containing MCPBz, we aimed to provide preliminary cross-linking through photo curing to enhance the thermal stability of nanofibers for thermal curing in which ring-opening and almost complete cross-linking can be achieved as maintaining the nanofibrous structure.

3.4.1. Structural characterization of DHBP-ad6 and DHBP-ad12 resins

DHBP-ad6 and DHBP-ad12 were synthesized as two novel MCPBz by using difunctional amines (1,6-diaminohexane and 1,12-diaminododecane), difunctional phenol (1,4-dihydroxybenzophenone) (DHBP) and paraformaldehyde as starting materials. Since there are two hydroxyl groups on DHBP and two amino groups on both 1,6-diaminohexane and 1,12-diaminododecane, two oxazine rings are formed in one repeating unit of each MCPBz as shown in Figure 34. The synthesized polybenzoxazines are main-chain type polybenzoxazine (MCPBz) consisting of repeating units of bifunctional benzoxazine structure bonded to different chain length of aliphatic diamine to form the macromolecular chain which possess benzophenone and coinitiator amine in the main-chain. Formation of this structure is the evidence of successful synthesis of the

benzoxazines and this structure of the synthesized DHBP-ad6 and DHBP-ad12 were confirmed by 1H NMR, FTIR and UV-Vis spectroscopies.

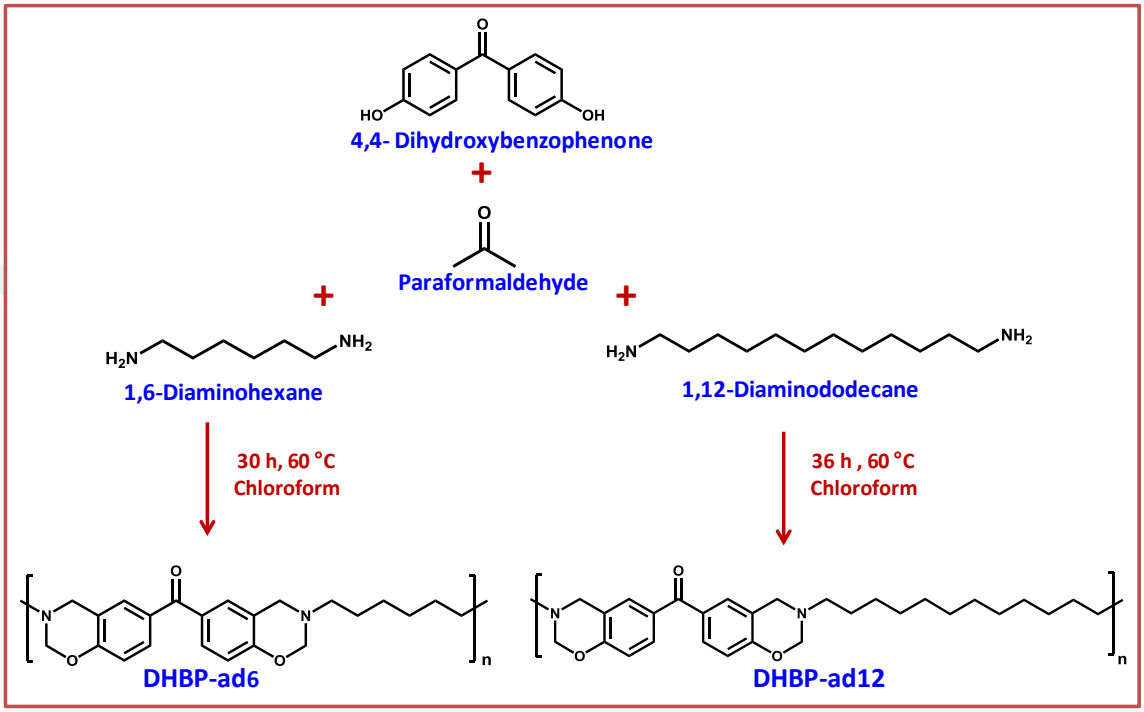

Figure 34. Synthesis of the DHBP-ad6 and DHBP-ad12 main-chain polybenzoxazine resins. (Copyright © 2016, Reproduced from Ref. [228] with permission from Elsevier)

The proposed chemical structures and ^{1}H NMR spectra of DHBPad6 and DHBP-ad12 are given in Figure 35. For both MCPBz, the characteristic benzoxazine resonance bands corresponding to the methylene units of oxazine ring; O-CH_2-N and the Ph-CH_2-N were observed at 4.04 and 4.95 ppm, respectively. Resonance bands of aliphatic protons were observed at 1.37 and 2.74 ppm for DHBPad6, and 1.28 and 2.74 ppm for DHBP ad12. In addition, resonance bands of aromatic protons were observed at 6.80-7.52 ppm region as

multiplet for both of the MCPBz resin. The existence of these characteristic bands in the ^{1}H NMR spectra of the both MCPBz was the evidence for the synthesis of desired benzoxazine structures.

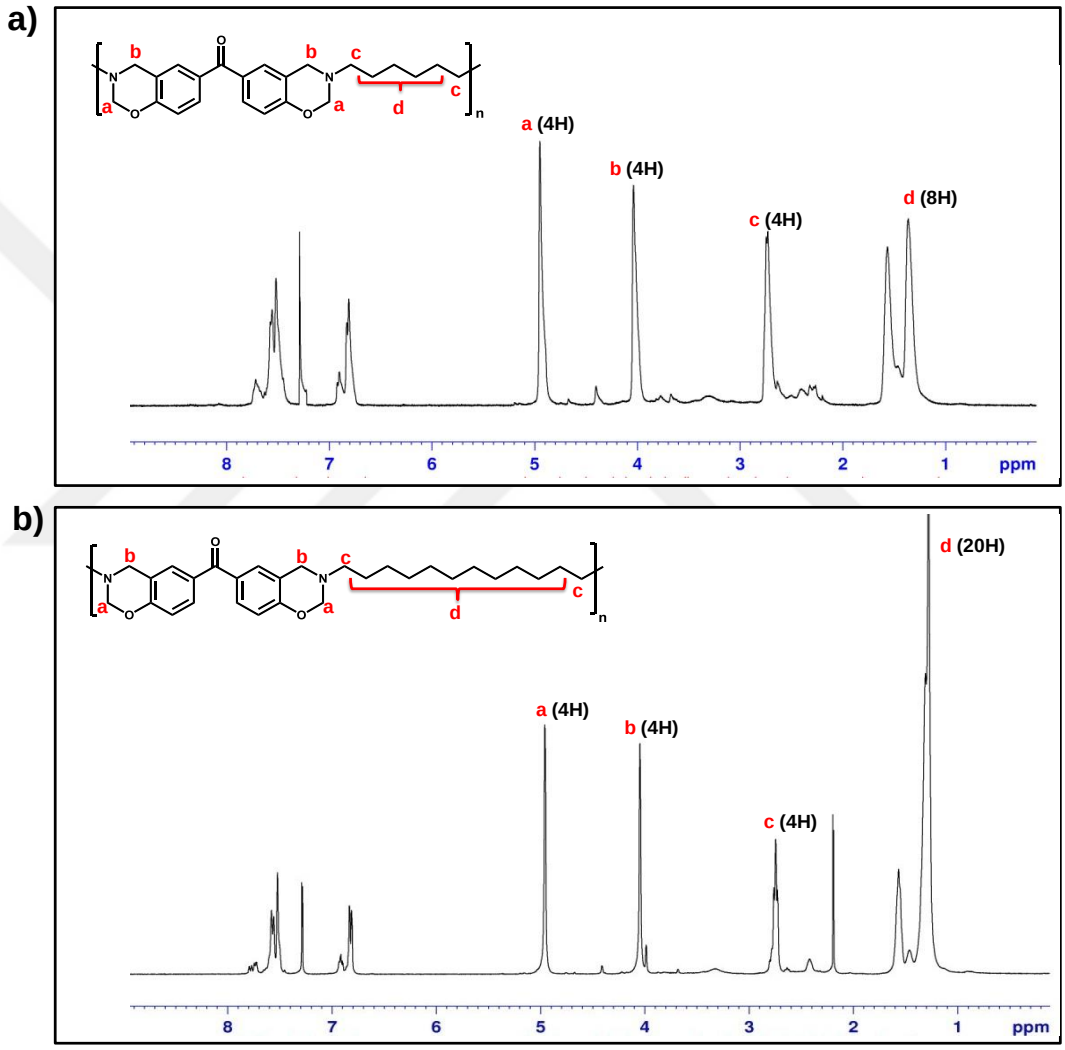

Figure 35. The proposed chemical structures and ^{1}H NMR spectra of a) DHBP-ad6 and b) DHBP-ad12 resins in $CDCl_3$. (Copyright © 2016, Reprinted from Ref. [228] with permission from Elsevier)

Figure 36 represents the FTIR spectra of the DHBP-ad6 and DHBPad12 resins. Characteristic absorption bands of the benzoxazine structure of the both MCPBz were observed at the same wavenumbers with different intensities. Absorption band existing at 918 cm^{-1} due to the out-of-plane C-H vibration mode of the benzene ring attached to oxazine ring. Sharp absorption band observed at 1231 cm^{-1} due to the asymmetric stretching of C-O-C in the oxazine ring. In addition, the very intense and sharp band existing at 1496 cm^{-1} is due to the in-plane C-H bending mode of the tri-substituted benzene ring. FTIR results are good agreement with the ^{1}H NMR data confirming the synthesis of two novel MCPBz resins was achieved.

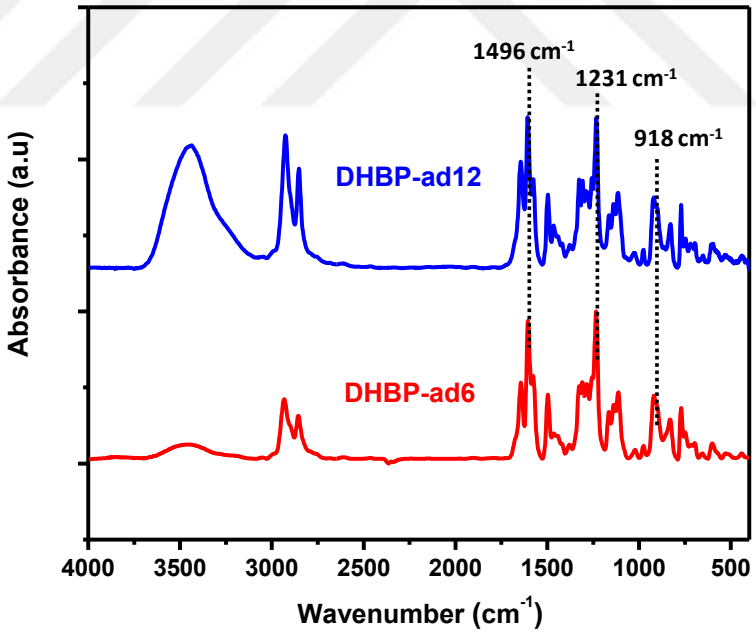

Figure 36. FTIR spectra of DHBP-ad6 and DHBP-ad12 resins. (Copyright © 2016, Reprinted from Ref. [228] with permission from Elsevier)

Moreover, further characterization on the structure of these resins was carried out with UV-Vis spectrophotometer. Since these novel MCPBzs including benzophenone unit as a part of main-chain, it is expected to observe UV absorption for both MCPBz. UV-Vis spectra of DHBP-ad6 and DHBP-ad12 are given in Figure 37. The main benzenoid $\pi \rightarrow \pi^*$ type transitions of BP exist in the region of 250-300 nm [250], however, significantly red-shifted maximal absorption band observed for the synthesized novel MCPBz (Figure 37) indicating the successful formation of oxazine rings. In brief, FTIR, ^{1}H NMR and UV-vis spectroscopy analysis results show that benzophenone based MCPBz resines were successfully synthesized with the desired structure.

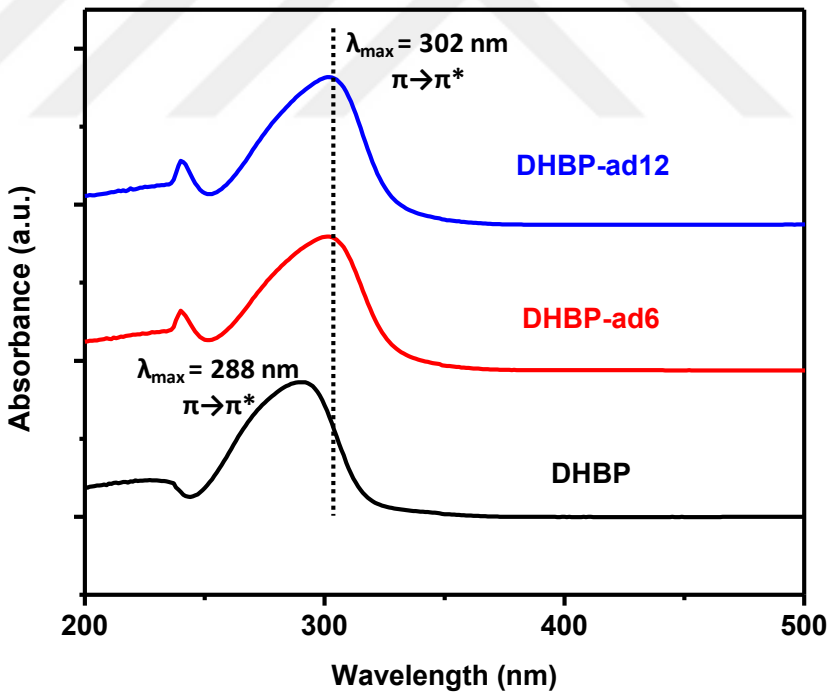

Figure 37. UV-vis spectra of DHBP, DHBP-ad6 and DHBP-ad12 resins. (Copyright © 2016, Reprinted from Ref. [228] with permission from Elsevier)

3.4.2. Electrospinning of DHBP-ad6 and DHBP-ad12 nanofibers

As it is known, morphological properties of the electrospun nanofibers are strongly depends on the polymer type, molecular weight of the polymer, solvent, concentration, surface tension and the conductivity of the polymer solutions [90]. For the polymers with very similar chemical structure as DHBP-ad6 and DHBP-ad12 resins, molecular weight is the main factor that effects the concentration of the polymer solution, hence, molecular weight ofthese resins plays a vital role on their electrospinning ability. Here, the only difference between DHBP-ad6 and DHBP-ad12 resins is the chain length of the aliphatic diamine used as a precursor for the synthesis of these resins. As abbreviated, DHBP-ad6 contains 6-C aliphatic diamine and DHBP-ad12 contains 12-C aliphatic diamine, and their molecular weights were measured by GPC as ~10,000 and ~15,000 g/mol, respectively. Therefore, measured molecular weight of the DHBP-ad6 and DHBP-ad12 resins were taken into consideration while preparing the electrospinning solutions. Before determining the concentration range for the electrospinning solutions, suitable solvents system have been chosen as chloroform/DMF (4:1, v/v) in which both MCPBz resins have formed homogenous and clear solutions. Then, different concentrations of the DHBP-ad6 and DHBP-ad12 solutions were prepared in order to produce bead-free and uniform nanofibers and here, the concentration range was given as 25-35% (w/v) for DHBP-ad6 and 15-25% (w/v) for DHBP-ad12 in which the significant morphological changes were observed. Accordingly, the morphological characteristics of the electrospun nanofibers are summarized in Table 6.

Table 6. The characteristics of the electrospun DHBP-ad6 and DHBP-ad12 nanofibers. (Copyright © 2016, Reprinted from Ref. [228] with permission from Elsevier)

Solutions	% Polymer (w/v)	Average fiber diameter (nm)	Diameter range (nm)	Fiber morphology
DHBP-ad6	25	220 ± 105	50-550	Beaded nanofibers
	30	440 ± 130	150-800	Beaded nanofibers
	35	605 ± 145	200-950	Bead-free nanofibers
DHBP-ad12	15	225 ± 90	100-500	Beaded nanofibers
	20	380 ± 115	150-650	Beaded nanofibers
	25	620 ± 160	100-1000	Bead-free nanofibers

SEM images of the nanofibers electrospun from 25, 30, and 35% (w/v) DHBP-ad6 solutions are shown in Figure 38a-c. Electrospinning of 25% (w/v) DHBP-ad6 solution resulted beaded structure with ultrafine fibers having average fiber diameter (AFD) of 220±105 nm (Figure 38a). At low solution viscosity, fewer chain entanglements and higher amount of solvent have dominant effect on the electrospinning jet resulting the formation of beads along with the fibers [90]. As the polymer concentration increased to 30% (w/ v), the number of beads decreased dramatically and elongated beaded structures with nanofibers having AFD of 440±130 nm were produced (Figure 38b). When the polymer concentration reached to 35% (w/v) in solution, bead free nanofibers having AFD of 605±145 nm were obtained due to the higher polymer chain entanglements in the solution provided electrospinning jet to be fully stretched for uniform fiber formation (Figure 38c) [90]. SEM images of the nanofibers electrospun from 15%, 20%, and 25% (w/v) DHBP-ad12 solutions are given in Figure 38 d-f. As it is observed from the SEM images, 15% (w/v) DHBP-ad12 solution yielded beaded nanofibers having AFD of

225±90 nm because of the low viscosity of the polymer solution (Figure 38d). Bead-free and uniform nanofibers were obtained when the DHBP-ad12 solution concentration was at 20% (w/v). AFD of the nanofibers electrospun from 20% (w/v) DHBPad12 solution was 380±115 nm (Figure 38e). It is a typical behavior of polymeric systems in the electrospinning process that beaded nanofibers transform to bead-freefibers when the concentration and/or viscosity of the polymer solution is optimized. As the concentration of the DHBP-ad12 solution increased to 25% (w/v), the fiber diameter became thicker (AFD=620±160 nm) because of the high solution viscosity (Figure 38f).

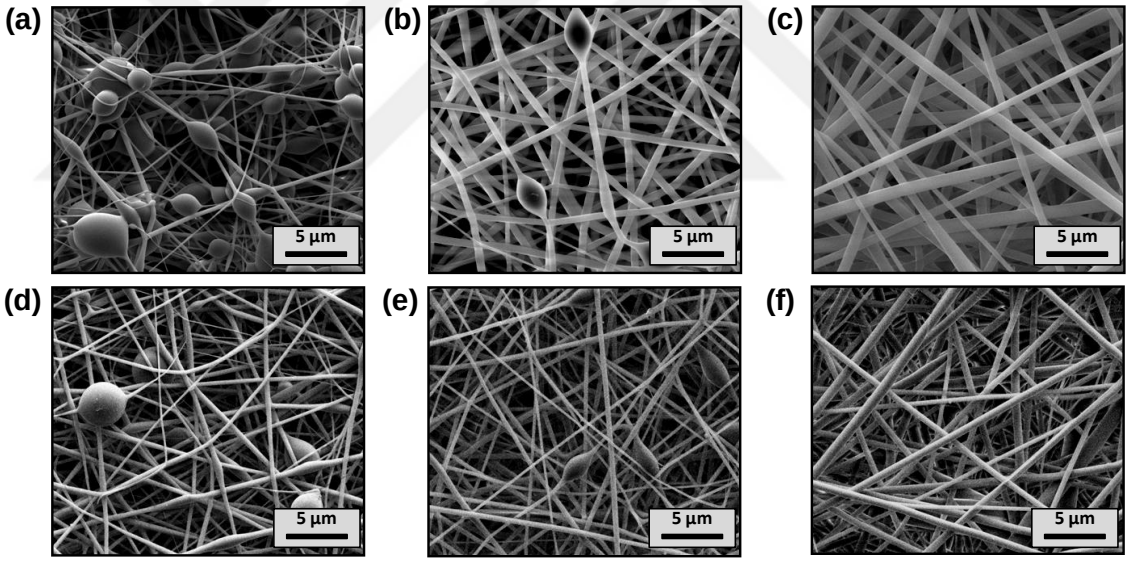

Figure 38. SEM images of the electrospun nanofibers obtained from solutions of DHBP-ad6 a) 25%, b) 30%, c) 35% and DHBP-ad12 d) 15%, e) 20%, f) 25%. (Copyright © 2016, Reprinted from Ref. [228] with permission from Elsevier)

Remarkably, with the increase in viscosity/concentration, the diameter of the electrospun fiber also increases. The reason for increase in fiber diameter is the greater resistance of the solution to be stretched because of the more chain entanglements at higher polymer concentration [90]. Furthermore, it is clearly observed that the aliphatic diamine chain length, accordingly the molecular weight of the MCPBz resins play an important role on their electrospinning ability. Presumably, higher molecular weight and longer aliphatic chain of the DHBP-ad12 resulted in more chain entanglement and overlapping in the polymer solution, thus, we achieved to obtain bead-free and uniform nanofibers at lower solution concentration for DHBP-ad12 (25% w/v) compared with the DHBP-ad6 (35% w/v).

3.4.3. Curing studies of DHBP-ad6 and DHBP-ad12 nanofibers

Generally, cross-linking and polymerization of the benzoxazines achieved by thermally initiated ring-opening reactions. First example of the cross-linking of polybenzoxazine-based nanofibers by directly thermal curing was given by Li and co-workers [29]. They produced nanofibers from MCPBz synthesized by using 4,4-diaminophenylether and bisphenol-A, and then they were able to obtain cross-linked MCPBz nanofibers by thermal curing at 240 ºC for 3 h. On the contrary, our previous study demonstrated that nanofibers produced by MCPBz based on the bisphenol-A and diamines with long aliphatic chains (1,12-diaminododecane and 1,6-diaminohexane) have not shown resistance to the heat treatment during the thermal curing and nanofibers lost the fiber morphology at low temperatures around 75-100ºC [191]. Presumably, 4,4-

diaminophenylether provided more rigid structure to the MCPBz nanofibers compared to 1,12-diaminododecane and 1,6-diaminohexane, hence, the melting temperature of the nanofibers obtained from the former one is much higher than the others. Therefore, they achieved to preserve fiber structure during the thermal treatment and obtained crosslinked nanofibers by thermal curing. Here, in order to improve the curing process of MCPBz nanofibers obtained from long aliphatic diamine-based polybenzoxazines, structure of the MCPBz tailored to be able to crosslink by photo curing and DHBP-ad6 and DHBP-ad12 resins consisting of a benzophenone unit in the polymer main-chain were synthesized. Initially, DSC experiments were performed to measure the thermal transition temperatures of the nanofibers obtained from these two MCPBz resins. As it is expected, melting transition was observed for DHBP-ad6 and DHBPad12 nanofibers at low temperatures 73 and 54ºC, respectively (Figure 39). Nonetheless, these nanofibers were directly thermal cured and not surprisingly DHBP-ad6 and DHBP-ad12 nanofibers lost the fiber morphology by forming film even at first step of the thermal curing (150ºC) (Figure 39b,f). In addition, exothermic peak centered at 217ºC was observed in DSC thermogram of the both MCPBz nanofibers attributed to ring opening reaction and crosslinking. Since these nanofibers have such low melting points and their curing temperatures are very high (above 200ºC), photo curing was performed as a first step. Interestingly, after UV irradiation, melting transition peak was not observed in DSC thermograms of both DHBP-ad6 and DHBP-ad12 nanofibers verifying the enhancement of the thermal stability probably owing to the cross-linking provided by photo curing (40

a,b). In addition, SEM images of DHBP-ad6 and DHBP-ad12 nanofibers show that UV irradiation did not deteriorate the fiber morphology (Figure 39c,g). Therefore, subsequently thermal curing was performed as a second step for UV-irradiated nanofibers step-wise from 150 to 225ºC to provide almost complete ring opening and cross-linking of the benzoxazine . Although directly thermal-cured MCPBz nanofibers lost the fibrous structure even at 150ºC, UV-irradiated nanofibers perfectly preserved the fiber morphology during the thermal treatment which confirms the cross-linking achieved by two step curing without deteriorating the fiber morphology (Figure 39d, h).

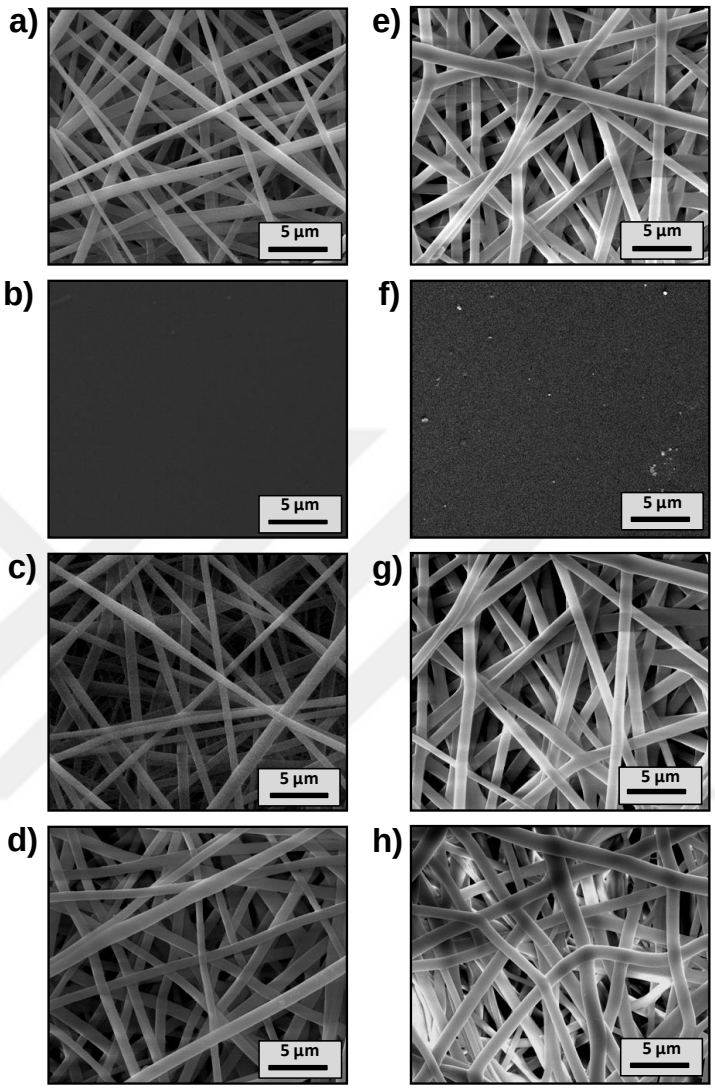

Figure 39. SEM images of a) DHBP-ad6 nanofibers, b) directly thermal-cured DHBP-ad6 nanofibers, c) photo-cured DHBP-ad6 nanofibers, d) photo and thermal-cured DHBP-ad6 nanofibers, e) DHBP-ad12 nanofibers, f) directly thermal-cured DHBP-ad12 nanofibers, g) photo- cured DHBP-ad12 nanofibers, h) photo and thermal-cured DHBP-ad12 nanofibers. (Copyright © 2016, Reproduced from Ref. [228] with permission from Elsevier)

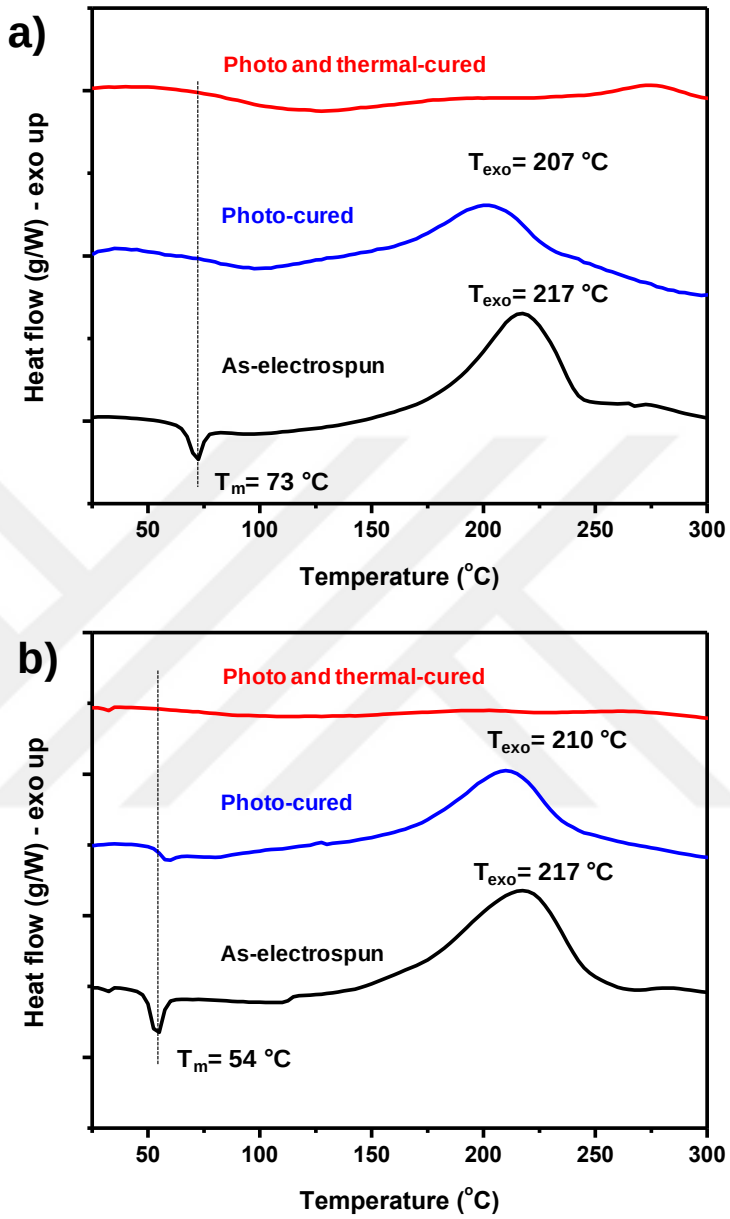

Figure 40. DSC thermograms of a) DHBP-ad6 and b) DHBP-ad12 nanofibers. (Copyright © 2016, Reproduced from Ref. [228] with permission from Elsevier)

In order to investigate the cross-linking of DHBP-ad6 and DHBPad12 nanofibers more detailed, the chemical structural changes occurring during the curing process were examined by FTIR spectroscopy, since characteristic benzoxazine peaks observed at 920 cm^{-1} (the benzene ring mode attached to the oxazine ring) and 1230 cm^{-1} (aromatic ether stretching of C-O-C) and 1496 cm^{-1} (three substituted benzene ring mode) disappear with the ring opening reactions. Figure 41 represents the FTIR spectra of DHBP-ad6 and DHBP-ad12 nanofibers, after photo-curing with 1 hour UV-irradiation and after additional step-wise thermal curing of UV-irradiated samples at 150, 175, 200 and 225ºC (1 hour at each step). For both of the MCPBz nanofibers, characteristic benzoxazine peaks were appeared at wavenumbers (920, 1230 and 1496 cm^{-1}) since they have very similar chemical structure. After UV irradiation, characteristic absorbance peaks were still observed in the FTIR spectra suggesting the ring opening and complete crosslinking were not achieved by photo-curing. However, intensity of the characteristic benzoxazine rings peaks in the FTIR spectra decreased and almost disappeared with the increasing temperature confirming the ring-opening and cross-linking through thermal curing.

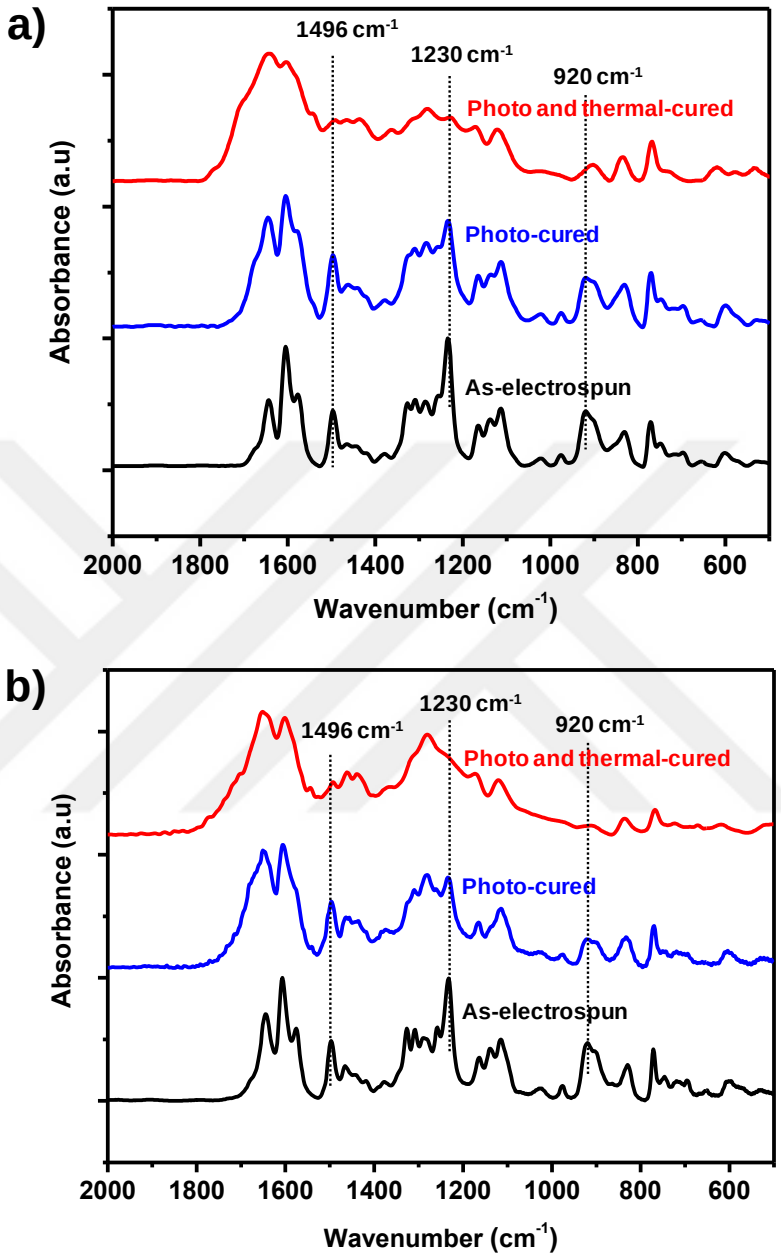

Figure 41. FTIR spectra of a) DHBP-ad6 and b) DHBP-ad12 nanofibers. (Copyright © 2016, Reproduced from Ref. [228] with permission from Elsevier)

Besides the SEM images and the FTIR spectroscopy results, physical properties of the MCPBz nanofibers after photo and thermal curing also confirm the cross-linking. First of all, the clear color change was observed during the curing process. As it is observed from the photographs in Figure 42, white color of the as-electrospun nanofibers transformed to yellow with photo curing and then, yellow color of the UV-irradiated nanofibers transformed to brownish yellow which is a typical color of benzoxazine resins when they are thermally cured. Secondly, as-electrospun DHBP-ad6 nanofibers were very brittle, yet, after two-step curing they gained mechanical integrity and became more flexible. Although, both of the nanofibrous mats were obtained as free standing material, DHBP-ad12 nanofibers were more flexible than the DHBP-ad6 nanofibers presumably owing to the longer aliphatic chain structure of the DHBP-ad12 resins and they maintained the flexibility even after the two-step curing (Figure 42).

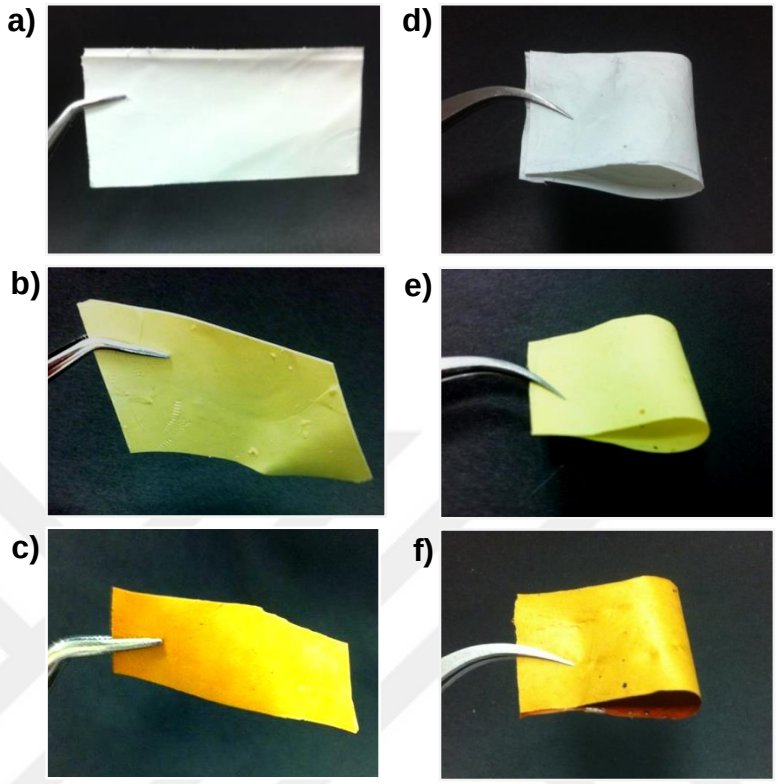

Figure 42. Photographs of (a) as-electrospun DHBP-ad6 nanofibers, (b) photo-cured DHBP-ad6 nanofibrous mat, (c) photo and thermal-cured DHBP-ad6 nanofibrous mat, (d) as-electrospun DHBP-ad12 nanofibrous mat, (e) photo-cured DHBP-ad12 nanofibers and (f) photo and thermal cured DHBP-ad12 nanofibers. (Copyright © 2016, Reproduced from Ref. [228] with permission from Elsevier)

In addition to the bending ability, mechanical properties of the photo and thermal-cured DHBP-ad6 and DHBP-ad12 nanofibers were investigated. Stress-strain curves of both cross-linked MCPBz nanofibrous mats obtained by DMA are given in Figure 43. Three samples were used from each type of MCPBz nanofibrous mats for mechanical test and

the results are summarized in Table 7. After photo and thermal curing, DHBP-ad6 and DHBP-ad12 nanofibrous mats showed significantly high Young's modulus compared to the directly thermal-cured MCPBz nanofibrous mats reported in the literature [168]. Young's modulus of DHBP-ad6 and DHBP-ad12 nanofibers were calculated as 2070±243 and 264±59.66 MPa, respectively and this difference is expected since this value is highly dependent on the chain length. As the flexible aliphatic chain length decreases, stiffness of the polymeric material increases [83], hence, cross-linked DHBP-ad6 nanofibers showed remarkably higher Young's modulus then the cross-linked DHBP-ad12 nanofibers. In addition, ultimate tensile stress of the cross-linked DHBPad6 and DHBP-ad12 nanofibers were measured as 22.53±2.04 and 15.29±2.48 MPa, respectively and these values are also fairly higher than the reported work [83]. Here again not surprisingly the effect of the aliphatic chain length on the yield stress of the MCPBz nanofibrous mats was observed and cross-linked DHBP-ad6 nanofibers having shorter aliphatic chain exhibited higher stress at yield which is very similar trend that was observed for the previously reported cross-linked polybenzoxazines [168]. Besides these, cross-linked DHBP-ad12 nanofibers showed remarkably higher strain at break (12.04±0.09) compared to the crosslinked DHBP-ad6 nanofibers (1.83 ±0.15) since as the aliphatic chain length increases, strain at break increases as well and these results consistent with the reported data [177].

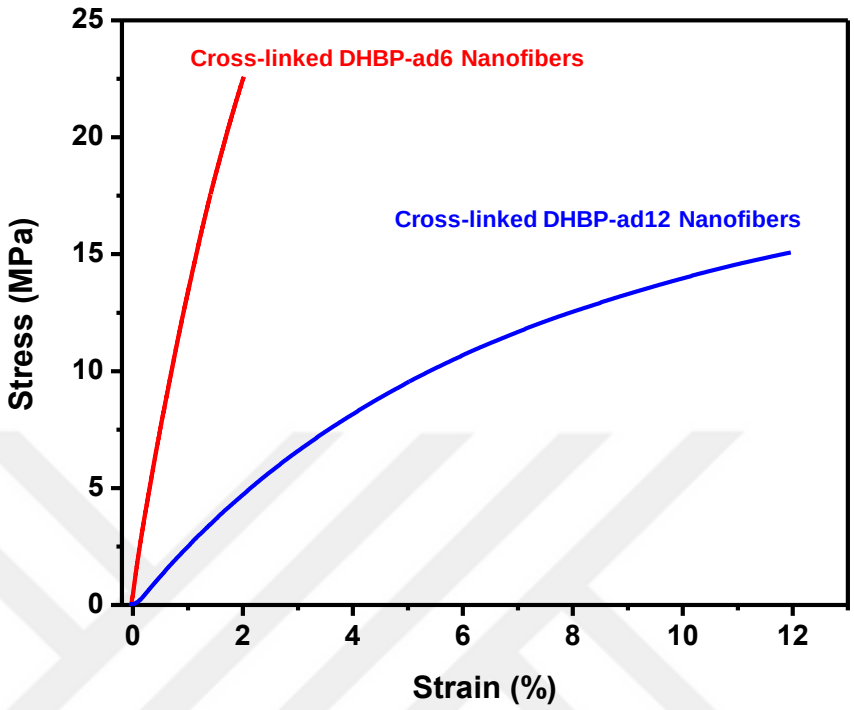

Figure 43. Representative stress-strain curves of the photo and thermal-cured DHBP-ad6 and DHBP-ad12 nanofibrous mats. (Copyright © 2016, Repriented from Ref. [228] with permission from Elsevier)

Table 7. Mechanical properties of the DHBP-ad6 and DHBP-ad12 nanofibers after photo and thermal curing. (Copyright © 2016, Repriented from Ref. [228] with permission from Elsevier)

Nanofibers	Stress at yield (MPa)	Strain at break (%)	Young's modulus (MPa)
DHBP-ad6	22.53 ± 2.04	1.83 ± 0.15	2070 ± 243
DHBP-ad12	15.29 ± 2.48	12.04 ± 0.09	264 ± 59.66

The thermal properties of DHBP-ad6 and DHBP-ad12 nanofibers were studied by TGA. After photo-curing, no significant change was observed in degradation temperatures (Td) of the nanofibers. On the other hand, thermal stability of the nanofibers was increased significantly after thermal curing (Figure 44). Td onset and Td maximum values of the DHBP-ad6 nanofibers were observed at 231 and 450ºC after photo curing. On the other hand, an increase was observed in Td onset and Td maximum values of the DHBP-ad6 nanofibers after thermal curing which was measured as 250 and 458ºC, respectively. In addition char yield of the DHBP-ad6 nanofibers increased from 41 to 53% after photo and thermal curing. Likewise, thermal properties of DHBP-ad12 nanofibers showed the same trend each step of curing. Td onset, Td maximum and char yield were measured as 245ºC, 474ºC and 18.4%, respectively. There was no significant change in these values of the DHBP-ad12 nanofibers after photo curing (242ºC, 473ºC and 20.3%); however, remarkable increase was observed especially at Td onset and char yield of these materials after thermal curing (270ºC, 476ºC and 35.1%) (Figure 44 and Table 8). These findings indicate that through two-step curing, as the chain length increases, the thermal stability of MCPBz nanofibers increases whereas the char yield of the MCPBz nanofibers decreases as reported the earlier work [168].

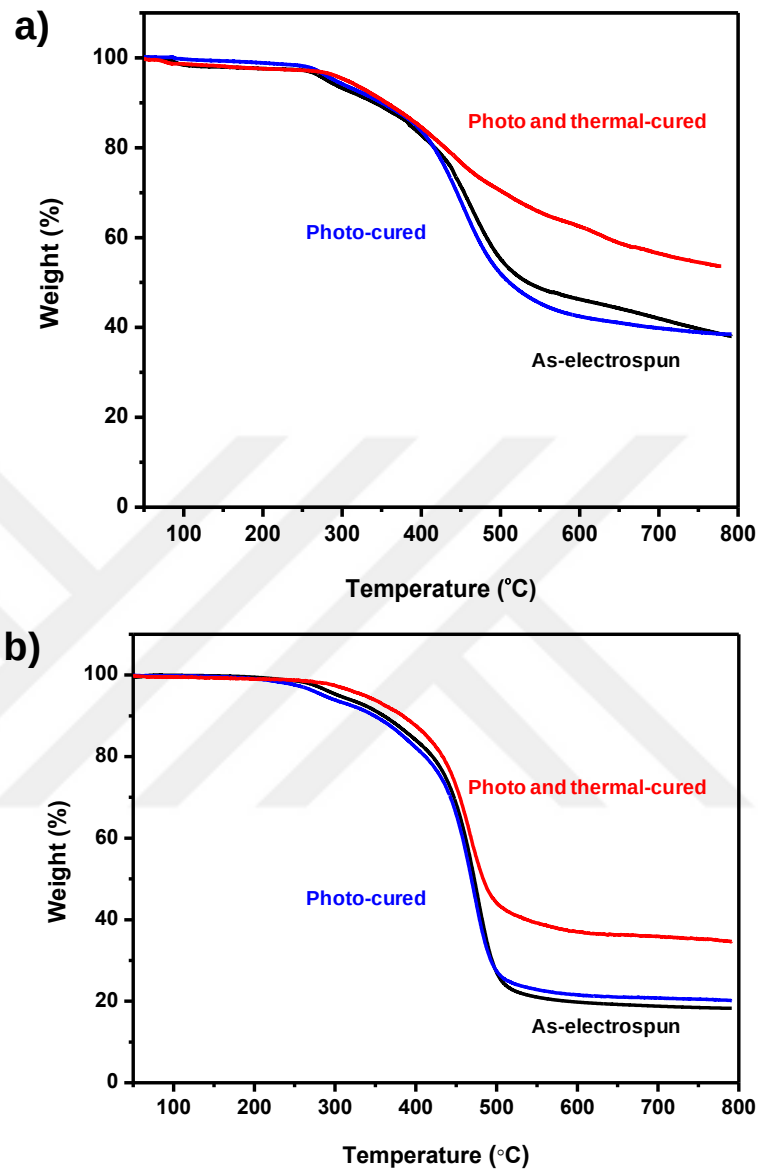

Figure 44. TGA thermograms of a) DHBP-ad6 and b) DHBP-ad12 nanofibers. (Copyright © 2016, Repriented from Ref. [228] with permission from Elsevier)

Table 8. The decomposition temperatures (Td) and char yield of the DHBP-ad6 and DHBP-ad12 nanofibers. (Copyright © 2016, Repriented from Ref. [228] with permission from Elsevier)

	Nanofibers	Td onset (°C)	Td maximum (°C)	Char yield (%)
DHBP-ad6	As-spun nanofibers	233	451	41.2
	After photo curing	231	450	38.5
	After thermal curing	250	458	53.1
DHBP-ad12	As-spun nanofibers	245	474	18.4
	After photo curing	242	473	20.3
	After thermal curing	270	476	35.1

3.4.5. Solubility and stability test of cross-linked DHBP-ad6 and DHBP-ad12 nanofibers

Cross-linking of the photo and thermal-cured nanofibers were further investigated by solubility and stability tests. In this part, photo and thermal-cured nanofibers were immersed for 24 hours into different solvents such as chloroform, DMF, 1,4-dioxane, DMAc and THF which are very good solvents for the DHBP-ad6 and DHBP-ad12 resins. Figure 45 represents the SEM images of photo and thermal-cured DHBP-ad6 and DHBP-ad12 nanofibers after the solubility test in above solvents. It is clearly observed that photo and thermal-cured DHBP-ad6 and DHBP-ad12 nanofibers were not dissolved even in chloroform and DMF in which the homogenous electrospinning solutions were prepared to produce bead free and uniform DHBP-ad6 and DHBP-ad12 nanofibers. Although, photo-cured DHBP-ad12 nanofibers have shown negligible deformation with lower mechanical integrity after immersing in these solvents, photo-cured DHBP-ad6

nanofibers maintained the fibrous structure. On the other hand, after two step (photo and thermal) curing, both DHBP-ad6 and DHBP-ad12 nanofibers have gained better mechanical integrity and they preserved the original fiber morphology.

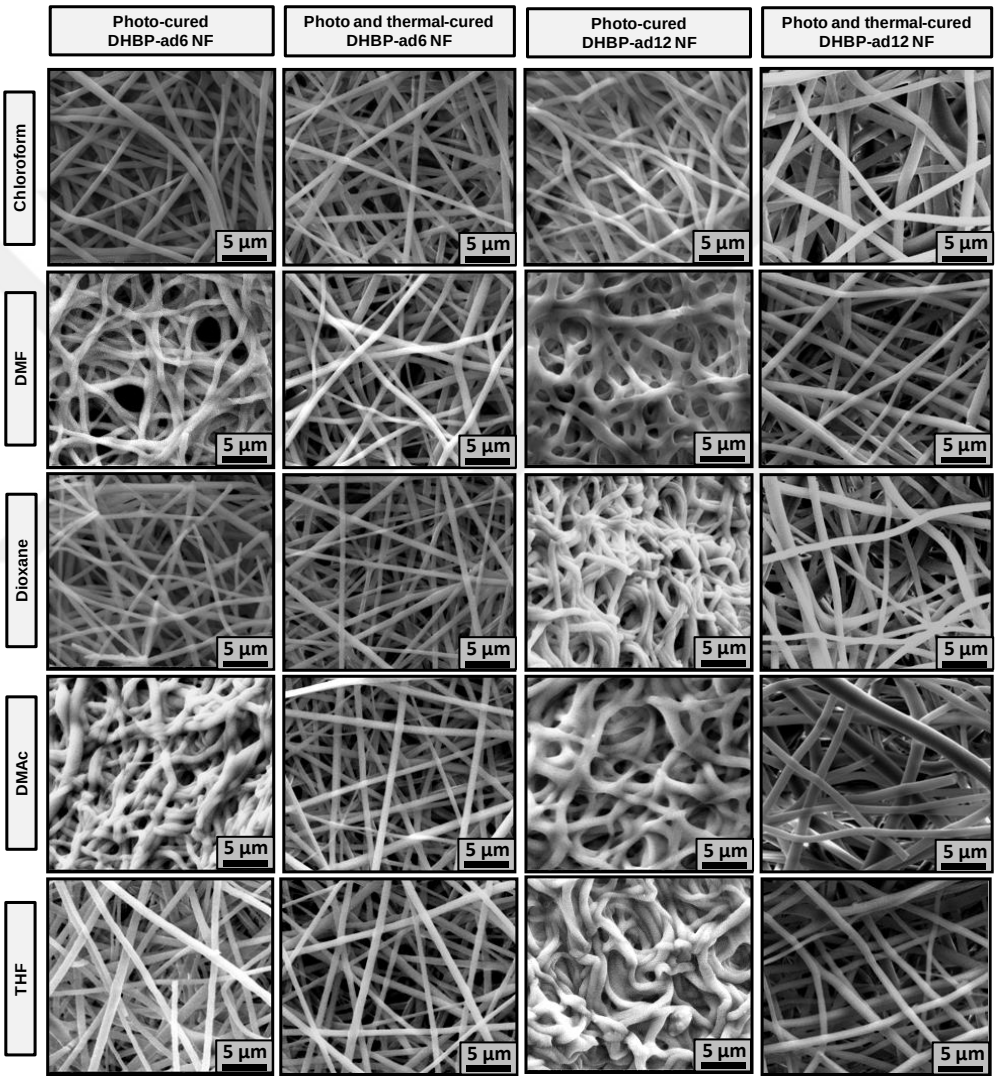

Figure 45. SEM images of cross-linked DHBP-ad6 and DHBP-ad12 nanofibers after immersing 24 hours in chloroform, DMF, 1,4-dioxane, DMAc and THF. (Copyright © 2016, Reproduced from Ref. [228] with permission from Elsevier)

Moreover, thermal stability of cross-linked DHBP-ad6 and DHBP-ad12 nanofibers were investigated within the temperature range (250-400ºC) which is higher than the curing temperatures and the lower than the decomposition temperatures of the crosslinked MCPBz nanofibers. It was observed that DHBP-ad6 and DHBP-ad12 nanofibers are structurally stable even at very high temperatures (400ºC) demonstrating that they are highly crosslinked thermoset materials having nanofibrous morphology (Figure 46).

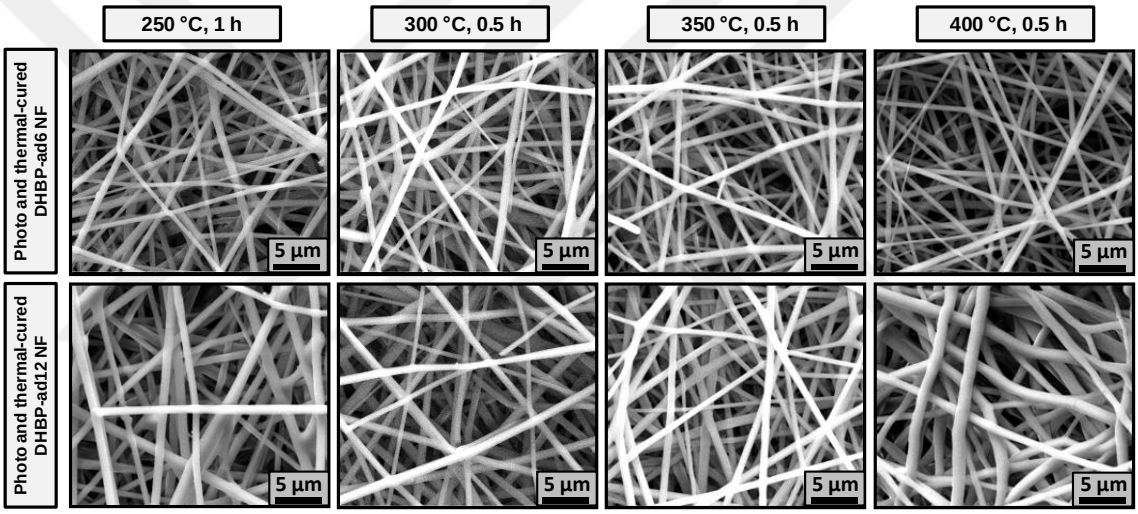

Figure 46. SEM images of the cross-linked DHBP-ad6 and DHBP-ad12 nanofibers after treating different temperatures in high temperature tube furnace at open air. (Copyright © 2016, Reproduced from Ref. [228] with permission from Elsevier)

In addition, strong acids were used to test the stability of cross-linked nanofibers in harsh conditions. High concentration solutions (5 M) of HCl, HNO_3 and H_2SO_4 were prepared to demonstrate the stability of DHBP-ad6 and DHBP-ad12 nanofibers. Since ring opening and complete cross-linking was not provided by photocuring, fibrous

structure of DHBP-ad6 was deteriorated in HCl and lost completely in HNO_3 and H_2SO_4 (Figure 47). In the case of photo-cured DHBP-ad12 nanofibers, the fibrous structure was maintained when treated with HCl and HNO_3 whereas H_2SO_4 deformed the nanofibers. On the other hand, structural integrity of the photo and thermal-cured DHBP-ad6 and DHBP-ad12 nanofibers were great, thus they were able to stay as free standing webs under strong acid treatments and the fibrous structure were preserved perfectly (Figure 47).

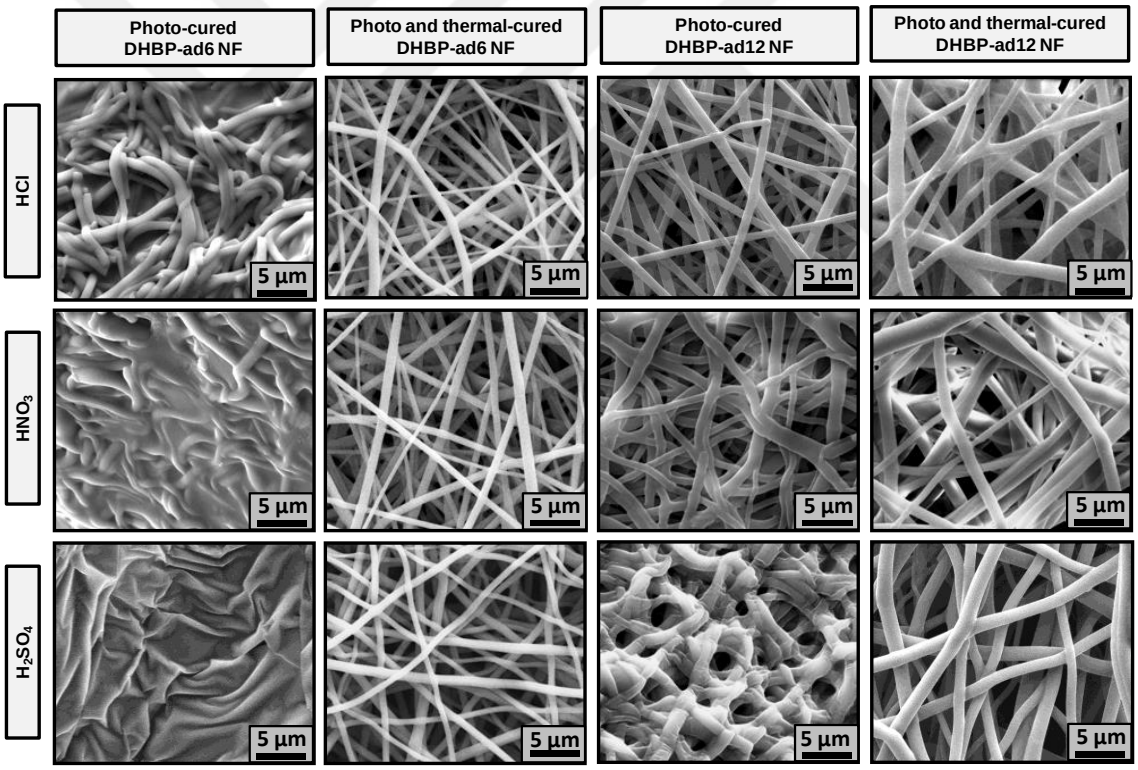

Figure 47. SEM images of cross-linked DHBP-ad6 and DHBP-ad12 nanofibers after immersing 24 hours in 5M HCl, HNO_3 and H_2SO_4 solutions. (Copyright © 2014, Reproduced from Ref. [228] with permission from Elsevier)

Chapter 3: Polymer/polybenzoxazine composite nanofibers

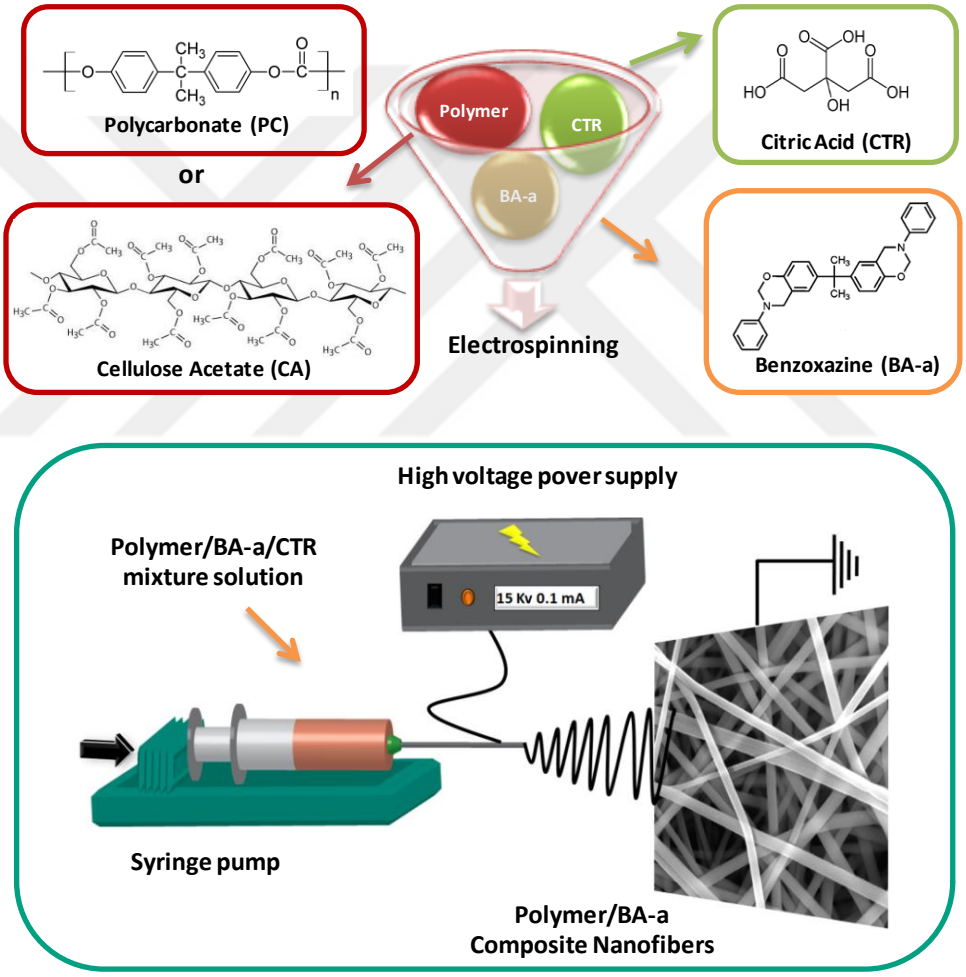

3.5. Cellulose acetate/BA-a composite nanofibers

Polybenzoxazines have many fascinating properties such as near-zero volumetric change upon curing, no by-products without any catalysts during curing, low water absorption, high glass transition temperature, high char yield, good mechanical and thermal properties [16]. These properties of polybenzoxazines make them good candidate as a blending material for the production of high performance composite materiasl not only bulk state but also fabrication at nano-scale.

Polymeric nanofibers have several characteristics such as high surface area to volume ratio, high density of pores with size range from tens of nanometer to several micrometers, interconnected open pore structureand high permeability for gases that make them very attractive material in filtration technology [251]. Electrospinning as a simple and versatile nanofiber production tecnique provides the functionalization of the polymeric nanofibers by simply blending the polymers with desired substances readily in the electrospinning solution to produce composite nanofibers with enhanced properties. Amoung the polymers, cellulose acetate (CA) is one of the widely used polymer type for the production of filtration membrane. Although, CA nanofibrous membranes or functionalized CA nanofibers posses very good filtration performance to variety of substances such as metal ions [252-255], dye [256, 257], polyaromatic hydrocarbons [258], and so on, its thermal and mechanical properties need to be enhanced for the application especially in harsh conditions.

In this chapter, we aimed to get benefit from the attractive properties of the polybenzoxazines in order to enhance especially the thermal and mechanical properties of the CA nanofibers while maintaining or even enhancing the filtration performance by simply producing CA/polybenzoxazine composite nanofibers through electrospinning. For this purpose, bisphenol-A and aniline-based benzoxazine monemer (BA-a) used as a blending material. Two oxazine rings of BA-a contribute the cross-linking reactions through opening of the oxazine rings by thermal activation and results with highly cross-linked structure with benzene side groups. It is well now that, benzene or cyclic side groups have higher effect on the thermal and mechanical properties compared to aliphatic chains. Therefore BA-a is a very good blending material as a benzoxazine to enhance the thermal and mechanical properties of CA nanofibers.

3.5.1. Structural characterization of BA-a

BA-a monomer was synthesized from bisphenol-A, aniline and paraformaldehyde by solventless method (Figure 48). Reaction was carried out at 110 °C for 1 hour and typical yellow colour benzoxazine was obtained with high purity. The structure of the synthesized BA-a was confirmed by ^{1}H NMR and FTIR spectroscopy. Figure 49 represents the ^{1}H NMR of BA-a. The characteristic benzoxazine resonances attributable to the O-CH_2-N and the Ph-CH_2-N methylene of the oxazine ring were observed at 5.36 ppm and 4.31 ppm, respectively. Existence of these peaks with the 1:1 ratio was the evidence for the synthesis of high purity BA-a.

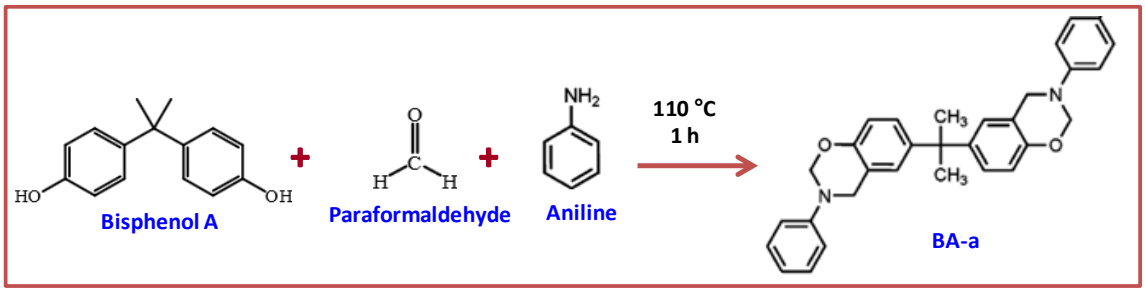

Figure 48. Synthesis of BA-a.

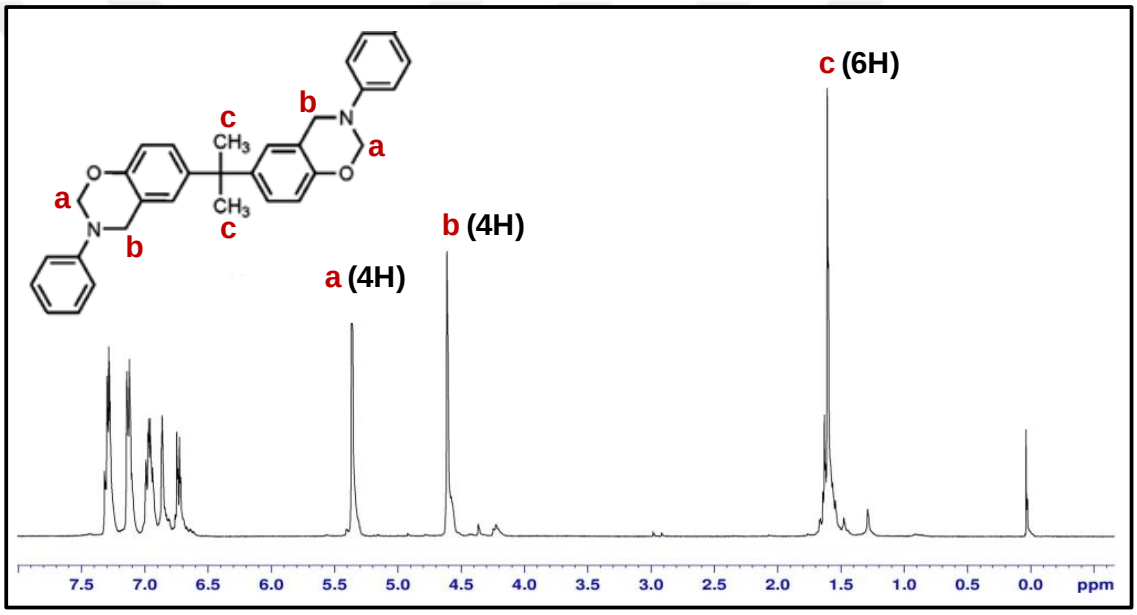

Figure 49. The proposed chemical structure and 1H NMR spectrum of BA-a in CDCl3.

Figure 50 reprsents the FTIR spectra of BA-a. The characteristic peaks of the benzoxazine peaks were observed in the FTIR spectra as well. Initially, strong peak at 946 cm^{-1} ascribed to the benzene ring mode attached to the oxazine ring. In addition, the very intense and sharp peak existing at 1496 cm^{-1} is due to the in-plane C-H bending mode of the tri-substituted benzene ring and the strong peak appearing at 1232 cm^{-1} is

due to the aromatic ether stretching of C-O-C in the oxazine ring.These findings correlate with the ^{1}H NMR results indicating the synthesis of BA-a was achieved.

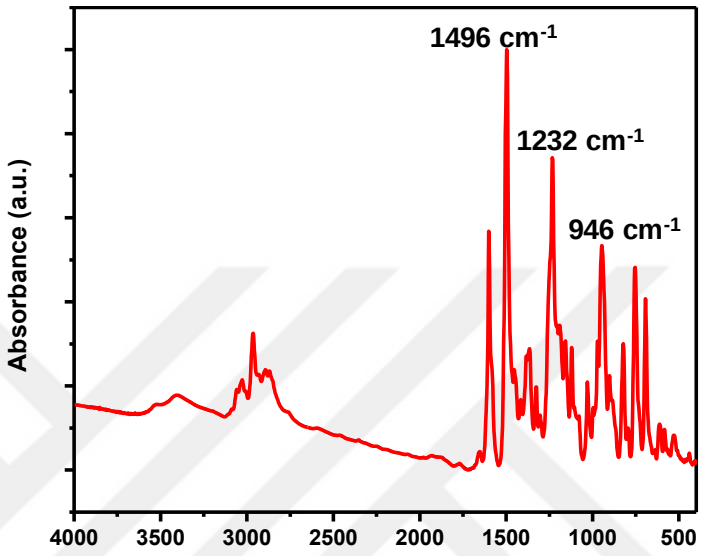

Figure 50. The FTIR spectrum of BA-a.

3.5.2. Electrospinning of cellulose acetate and cellulose acetate/BA-a composite nanofibers

Homogenous solutions of the cellulose acetate (CA) and mixture solutions of CA and BA-a (CA/BA-a) were prepared in DCM/methanol (4:1, v/v) binary solvent system. As reported, bead free and uniform CA nanofibers were obtained at 12% CA (w/v) concentration [258]. Therefore, in order to produce CA/BA-a composite nanofibers, different compositions of the CA/BA-a precursor solution were prepared by varying the concentration of CA (10 and 12 % (w/v)), BA-a (2 and 5 % (w/v)) in the mixture solution. These solutions are denoted as CAx:BA-ay, where x is the concentration of the

CA and y is the concentration of the BA-a. As a result, three different compositions of the CAx:BA-ay were obtained as follow; CA10/BA-a2, CA10/BA-a5 and CA12/BA-a2. SEM images of the nanofibers obtained from these solutions revealed the successful production of bead free and uniform nanofibers from all composition of CAx/BA-ay solutions. CA nanofibers were also produced as a comparison (Figure 51). In order to investigate the effect of the BA-a amount on the fiber diameter, average fiber diameter (AFD) of the nanofibers were calculated from SEM images. AFD of CA nanofibers obtained 12% (w/v) CA solution were 720±295 nm . Although total concentration of the CA and BA-a were maintained 12% (w/v) in CA10/BA-a2 as pure CA solution, thinner nanofibers with the AFD of 621±196 nm were obtained from CA10/BA-a2 presumably the lower CA concentration. In the second composition, CA concentration was maintained 10% (w/v) as previous one and BA-a amount was increased as much as possible in the mixture solution in order to provide the formation of nanofibers. Here, 5% (w/v) was determined to be the highest BA-a amount that allows the formation of uniform bead free nanofibers, yet, no significant difference was observed on the AFD of CA10/BA-a5 nanofibers which is calculated as 630±250 nm. On the other hand, increasing the CA concentration to 12% (w/v) and using 2% (w/v) BA-a yielded thicker nanofibers with the AFD of 758±245 nm. These results clearly demonstrated that the polymer concentration has more dominant effect on the fiber diameter rather than the BA-a amount which is an expected result since CA polymer has higher molecular weight than BA-a monomer.

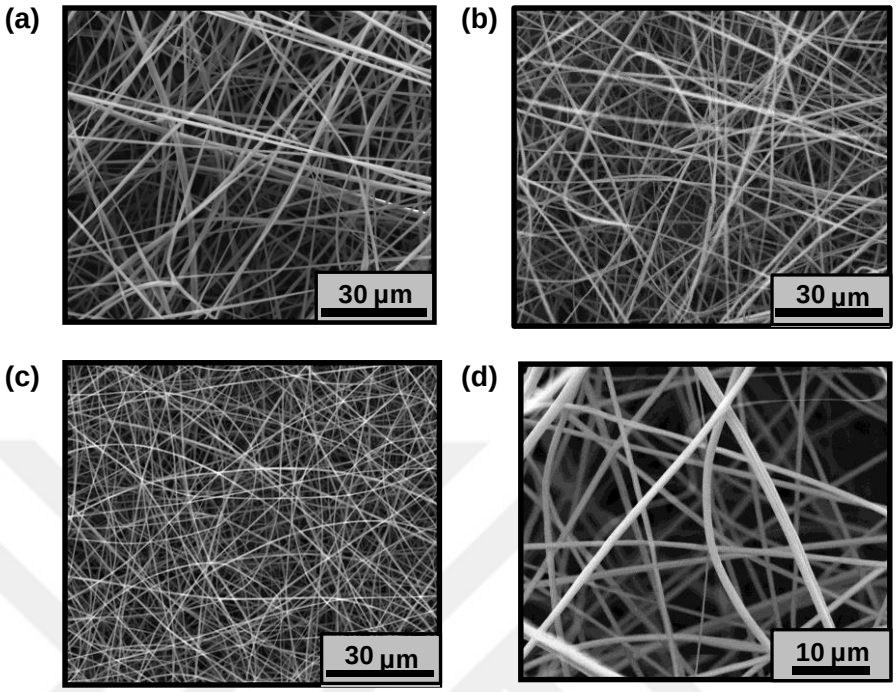

Figure 51. SEM images of (a) CA nanofibers, (b) CA10/BA-a2, (c) CA10/BA-a5 and (d) CA12/BA-a2 composite nanofibers.

3.5.3. Structural and morphological characterization of the CA/BA-a composite nanofibers after thermal curing

Cross-linking of the CA/BA-a composite nanofibers were achieved by thermal curing. Curing studies were performed in the temperature range which the polymerization of the BA-a can be achieved without decomposing the CA polymer. As it is known decomposition temperature of the CA is around 230ºC and polymerization of the BA-a is up to 240ºC [2], hence, CA10/BA-a2, CA10/BA-a5 and CA12/BA-a2 were thermally cured by keeping the composite nanofibers in a standard oven heated step-wise at

following temperatures; 150, 175, 200 and 225ºC. During the thermal curing, BA-a monomer polymerized (PBA-a) by ring-opening and cross-linking reactions and CA10/PBA-a2, CA10/PBA-a5 and CA12/PBA-a2 composite nanofibers were obtained. SEM images of the cured nanofibers revealed that the fibrous morphology was preserved for all samples (Figure 52).

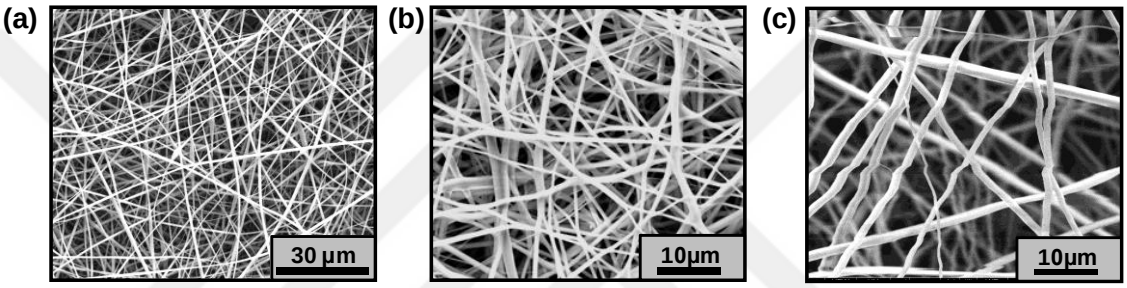

Figure 52. SEM images of (a) CA10/BA-a2, (b) CA10/BA-a5 and (c) CA12/BA-a2 composite nanofibers cured step-wise at 150, 175, 200 and 225ºC.

However, these nanofibers could not retain the fiber structure and dissolved in time when they were immersed in DCM and methanol which are very good solvents for the pure CA and the electrospinning solutions were prepared from these solvents to produce composite nanofibers. This finding shows the cross-linking of CA was not achieved. Therefore, in order to prevent the solubility of composite nanofibers in these organic solvents by providing the cross-linking of not only BA-a but also CA, citric acid (CTR) was used as a cross-linking agent. CTR is polycarboxyl organic compound that acts as a cross-linking agent because of the carboxyl groups in its molecular structure. It is reported that carboxylic acids cross-link the hydroxyl groups in cellulose and the cross-

linking reaction occur temperature range 165-175ºC [259]. As mentioned above, uniform nanofibers were produced from all compositions, yet, CA10/BA-a5 composition was chosen for the production of composite nanofibers due to the highest amount of the BA-a and availability of thinner fiber production. 1% (w/v) CTR was added to the CA10/BA-a5 mixture solution and bead free uniform nanofibers were able to obtain (Figure 53a). Nanofibers obtained from this composition were denoted as CA10/BA-a5/CTR1. These composite nanofibers were also cured by step-wise at 150, 175, 200 and 225ºC, as a result, CA10/PBA-a5/CTR1 were obtained. SEM image of the CA10/BA-a5/CTR1 showed that the addition of the CTR did not affect the fiber morphology and even after the curing nanofibers preserved the fibrous structure (Figure 53b).

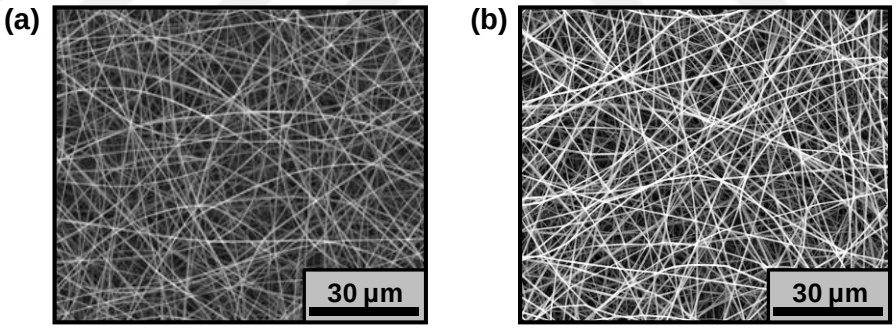

Figure 53. SEM images of (a) CA nanofibers and (b) CA10/PBA-a5/CTR1 composite nanofibers cured step-wise at 150, 175, 200 and 225ºC.

Furthermore, in order to investigate the cross-linking of the CA10/PBA-a5/CTR1 nanofibers, solubility tests were performed. Although, cured CA10/PBA-a5 composite nanofibers which are not including CTR dissolved immediately in DCM and methanol,

CA/PBA-a/CTR1 composite nanofibers preserved the mechanical integrity even over night immersing which is the evidence of the cross-linking. Further indicate the cross-linking provided by thermal curing and also molecular structural changes occurring during the thermal curing, FTIR spectroscopy technique was used. Generally characteristic absorbance peaks of the benzoxazine ring in the FTIR spectrum were investigated during the thermal curing studies. Characteristic benzoxazine peaks for the BA-a were observed at 946 cm^{-1} (out-of-plane C-H vibration mode of the benzene ring attached to oxazine ring), 1232 cm^{-1} (asymmetric stretching of C-O-C in the oxazine ring) and 1496 cm^{-1} (in-plane C=H bending mode of the tri-substituted benzene ring). As it is known, heat treatment provides the opening of oxazine rings and the intensity of these characteristic benzoxazine peaks dicreases with the thermal curing. In order to differentiate the origin of the peaks, FTIR spectra of CA, BA-a, CA10/BA-a5/CTR1 and CA10/PBA-a5/CTR1 were recorded. Firstly, characteristic benzoxazine peaks which are not overlapping with the CA peaks were determined in order to investigate the ring opening and cross-linking reactions. As it is observed, while peaks at 946 cm^{-1} and 1496 cm^{-1} belonging to the BA-a is clearly differentiated in the FTIR spectrum of CA10/BA-a5/CTR1, peak at 1232 cm^{-1} is overlapping with the C-O-C stretching of the CA, hence, peaks at 946 cm^{-1} and 1496 cm^{-1} were used to investigate ring opening reactions. After the thermal curing, these peaks were disappeared in the FTIR spectrum of CA10/PBA-a5/CTR1 confirming the achievement of the cross-linking and polymerization of BA-a. Although polymerization of BA-a was clearly identified by

FTIR, cross-linking of CA with CTR was not differentiated due to the overlapping peaks. CA has very strong absorption peak in the range of around 1690-1880 cm^{-1} belongs to the C=O stretching of the ester group [260]. Although, it is expected to observe formation of new C=O stretching band of carboxyl group of CTR around 1750-1735 cm^{-1} and C-O stretching band between 1000-1300 cm^{-1} in the FTIR spectrum of CA10/BA-a5/CTR1 because of the involvement of CTR to the CA and BA-a mixture, these bands could not be differentiated due to the overlapping with the absorption peaks of CA. In addition, since the amount of the CTR (1 %, w/v) in the composition is very less when compared with the CA (10%, w/v), it is not surprise to do not observe the formation of new peaks belong to CTR. Nevertheless, it can be suggested that both polymerization/cross-linking of BA-a and cross-linking of CA in the composite nanofibers were achieved by thermal curing after the addition of CTR according to the solubility test results since insoluable nanofibers were obtained.

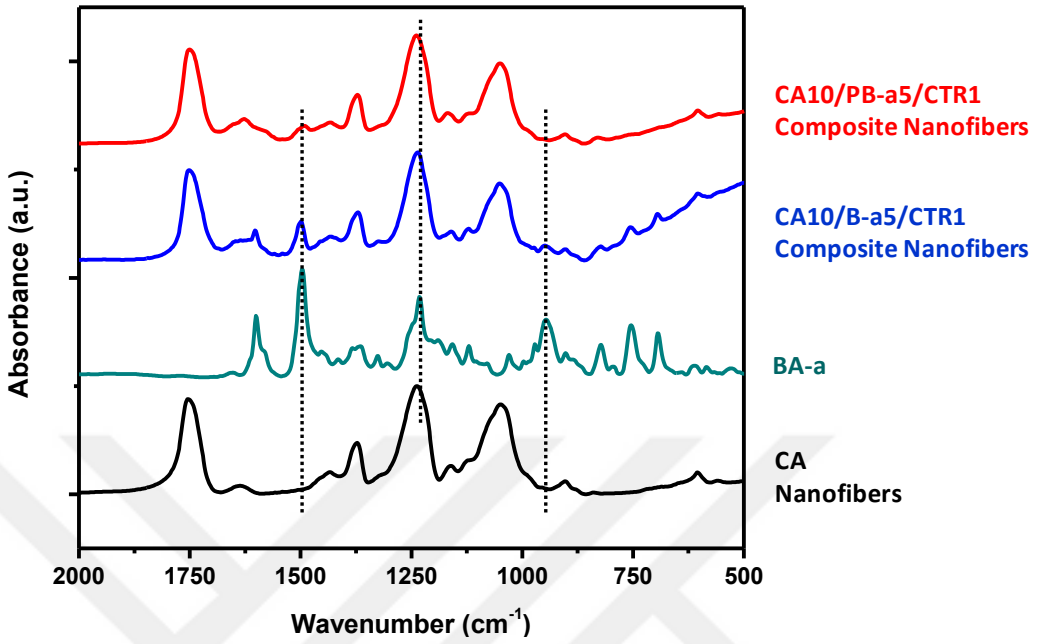

Figure 54. FTIR spectra of BA-a, CA nanofibers, CA10/BA-a5/CTR1 and CA10/PBA-a5/CTR1 composite nanofibers cured step-wise at 150, 175, 200 and 225°C.

Moreover, physical appearance of the nanofibers also confirms the cross-linking. As it is observed in Figure 55, the distinct color change was observed from white to brownish yellow after thermal curing owing to the cross-linking/polymerization of the BA-a. This is a kind of polybenzoxazine color which is obtained after curing. Moreover, fluffy structure of CA nanofibers has transformed to film like structure and the surface of the nanofibersbecame smother after the formation of CA10/PBA-a5/CTR1 composite nanofibers. In this composite form nanofibers looks as free standing material and has the bending ability by transforming the its original structure without any deformation. On the other hand, although CA nanofibersalso look as free standing material, when it is

bended fibers stick to each other and nanofibers became fluffier. In brief, CA10/PBA-a5/CTR1 composite nanofibersis more handable and flexible compared to the CA nanofibers which make it more suitable for the membrane applications.

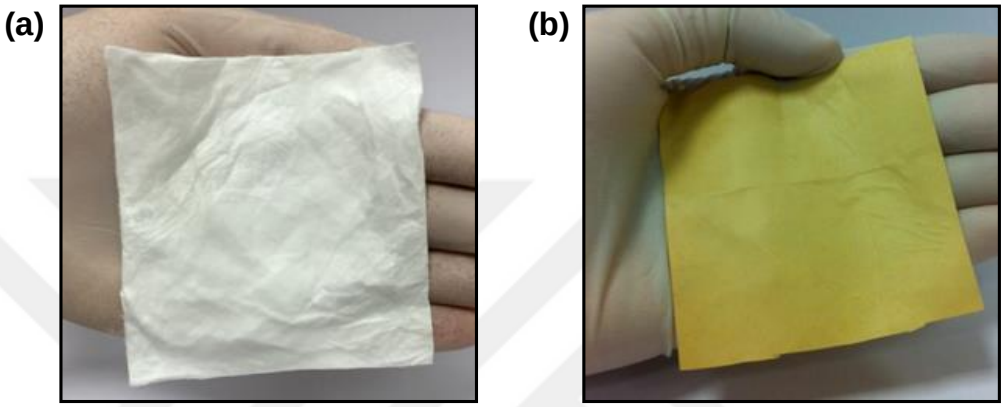

Figure 55. Photograps of (a) CA nanofibers and (b) CA10/PBA-a5/CTR1 composite nanofibers.

3.5.4. Thermal and mechanical Properties of CA and CA10/PBA-a5/CTR1 composite nanofibers

TGA was used to investigate the changes occurring in thermal properties of CA nanofibers after the formation of CA10/PBA-a5/CTR1 composite nanofibers. TGA curves of the these two nanofibers are given in Figure 56. Composite nanofiber formation did not affect the degradation temperature (Td) of the CA nanofibers significantly. Td onset and Td maximum values of the CA nanofibers were measured as 243°C and 378°C, respectively. After the CA10/PBA-a5/CTR1 composite nanofiber formation, these values were measured as 257°C and 378°C, respectively. On the other

hand, char yield of the CA nanofibers have increased remarkably and measured as 12.2% and 24.7% for CA and CA10/PBA-a5/CTR1, respectively.

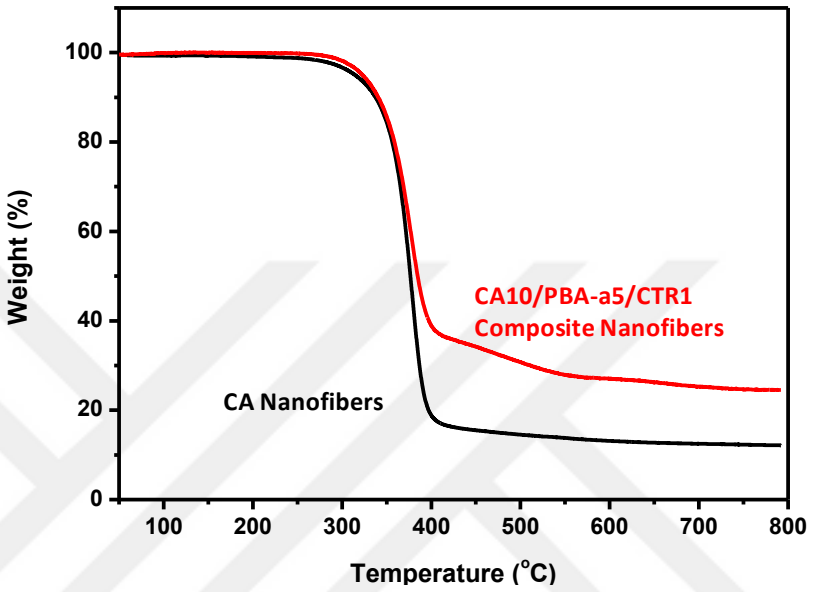

Figure 56. TGA thermograms of the (a) CA10/BA-a5/CTR1 and (b) CA10/PBA-a5/CTR1 composite nanofibers.

Mechanical properties of the CA, CA10/BA-a5/CTR and CA10/PBA-a5/CTR nanofibrous mats were studied by DMA. Since CA nanofibers have fluffy structure, it was not possible to perform DMA measurement properly. Even during the sample preparation process, CA nanofibers separated from each other causing the deterioration of whole sample and resulting the mistakes in the measurement. Stress-strain curve of the as-spun CA nanofibers are given in the Figure 57 not representing the actual elongation because of the sliding and the separation of nanofibers one by one instead of breaking the nanofibers (Figure 58). Since proper measurement could not performed for

CA nanofibers, DMA measurement was carried out for CA10/BA-a5/CTR1 nanofibers showing to compact structure. CA10/BA-a5/CTR1 nanofibers considered as a reference in order to investigate the mechanical properties of nanofibers before and after cross-linking. The stress–strain curves and the tensile data of the electrospun nanofibrous mats before and after the cross-linking are given in Figure 57 and Table 9. The results show that even the addition of BA-a and CTR without the curing enhanced the mechanical properties of the CA. However, remarkable enhancement was observed after the cross-linking achieved by thermal curing. As summarized in Table 9, tensile strength, ultimate tensile stress and Young's modulus of the CA10/BA-a5/CTR1 measured as 2.42±0.75 MPa, 3.54±0.96 %, 93.01±30.79 MPa, respectively and these values for CA10/PBA-a5/CTR1 measured as 8.64±0.63 MPa, 8.93±0.12 %, 213.87±30.79 MPa, respectively. This significant enhancement in mechanical performance of CA nanofibers can be attributed to the stiffening effect of the BA-a with polymerization and also cross-linking of CA nanofibers.

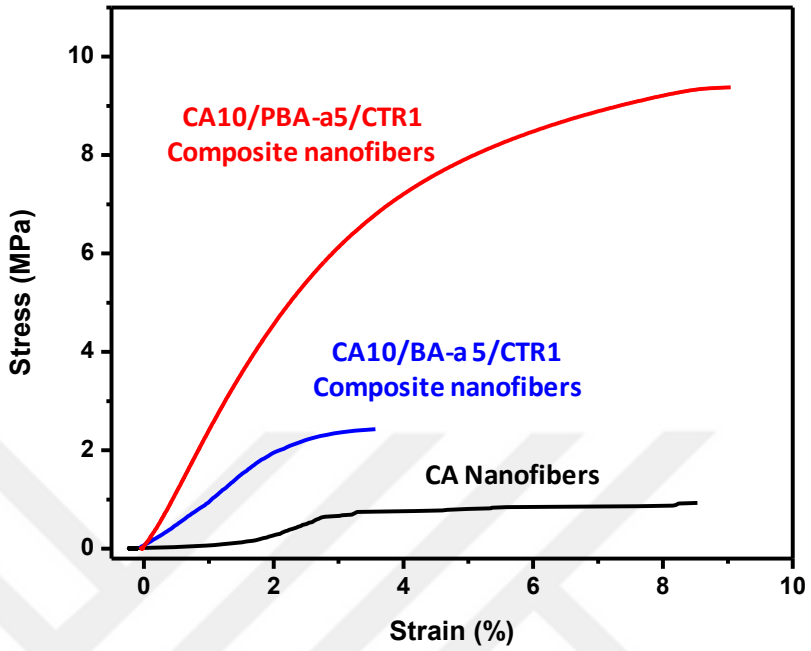

Figure 57. DMA curves of CA nanofibers, CA10/BA-a5/CTR1 and CA10/PBA-a5/CTR1 composite nanofibers.

Figure 58. Photograph of the CA nanofibers after DMA measuement.

Table 9. Data obtained from the DMA curves of CA10/BA-a5/CTR1 and CA10/PBA-a5/CTR1 composite nanofibers.

Nanofibers	Stress at yield (MPa)	Strain at break (%)	Young's modulus (MPa)
CA10/BA-a5/CTR1	2.42 ± 0.75	3.54 ± 0.96	93.01 ± 23.90
CA10/PBA-a5/CTR1	8.64 ± 0.63	8.93 ± 0.12	213.87 ± 30.79

3.5.5. Molecular entrapment efficiency of CA/PBA-a composite nanofibers with polyaromatic hydrocarbons

Polyaromatic hydrocarbons (PAHs) are organic pollutants which threat the human health seriously due to their mutagenic and carcinogenic effect. Phenanthrene is the well known type amoung the other hydrocarbons, thus it was chosen as a model PAH to investigate the molecular filtration performance of CA nanofibers and CA10/PBA-a5/CTR1 composite nanofibers. Figure 59 shows the decrease of phenanthrene concentration (%) in time when CA nanofibers and CA10/PBA-a5/CTR1 composite nanofibers were being kept in phenanthrene aqueous solution. It is observed that, both CA nanofibers and CA10/PBA-a5/CTR1 composite nanofibers adsorbed the phenanthrene effectively. Even after 10 mins of nanofibers dipping, CA nanofibers and CA10/PBA-a5/CTR1 composite nanofibers reach to 66 and 78% removal efficiency, respectively. The difference between adsorbed amount of phenanthrene by CA

nanofibers and CA10/PBA-a5/CTR1 composite nanofibers increased with time and while approaching the end of the experiment after 150 mins, removal efficiency became almost stable for both nanofibers. At the end of the experiment, CA10/PBA-a5/CTR1 composite nanofibers removed the 98.5% of the initial concentration of the phenanthrene, wheares CA nanofibers removed the 92% of that.

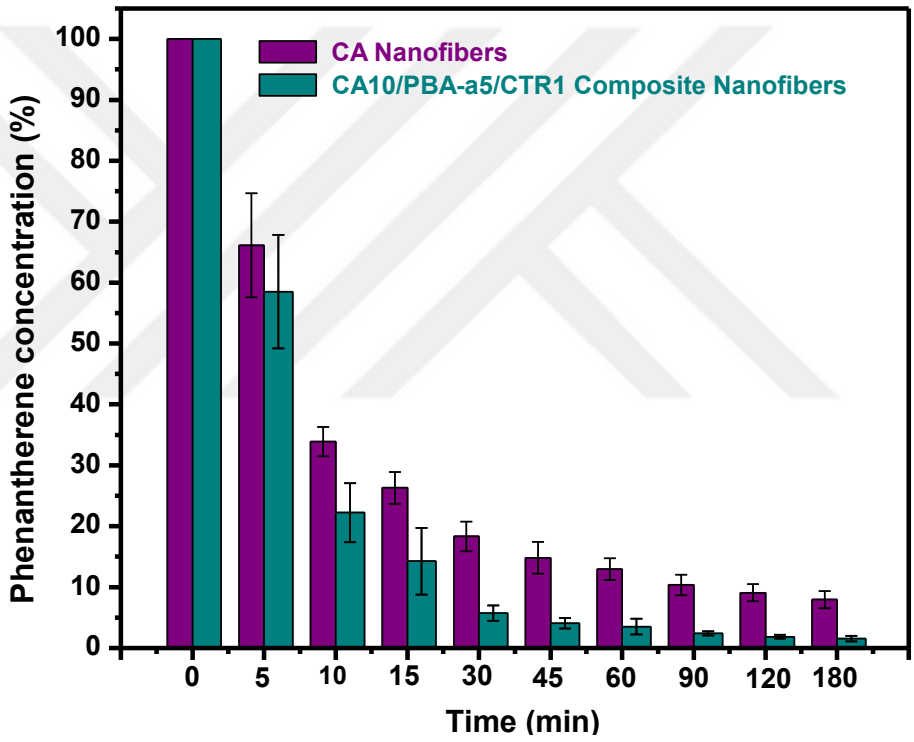

Figure 59. The time dependent phenanthrene removal efficiency CA nanofibers and CA10/PBA-a5/CTR1 composite nanofibers.

The higher removal efficiency of CA10/PBA-a5/CTR1 composite nanofibers presumably resulted from the incorporation of the BA-a to the hydrophilic CA

nanofibers. Because, after thermal curing, BA-a polymerized by ring-opening and formed highly cross-linked structure with benzene rings (Figure 60) which provided hydrophobic characteristic to the CA nanofibers. Since phenanthrene is a hydrophobic molecule, most probably higher hydrophobic interactions occured between CA10/PBA-a5/CTR1 composite nanofibers and phenanthrene molecule than CA nanofibers. In addition, benzene rings found in the structure of PBA-a, consecuently in the structure of CA10/PBA-a5/CTR1 composite nanofibers provided additional interactions such as π-π stacking between CA10/PBA-a5/CTR1 composite nanofibers and phenathrene . It is well known that, π–π bonding interaction has been used to explain the adsorption of organic molecules with a C–C double bond or a benzene ring [261].

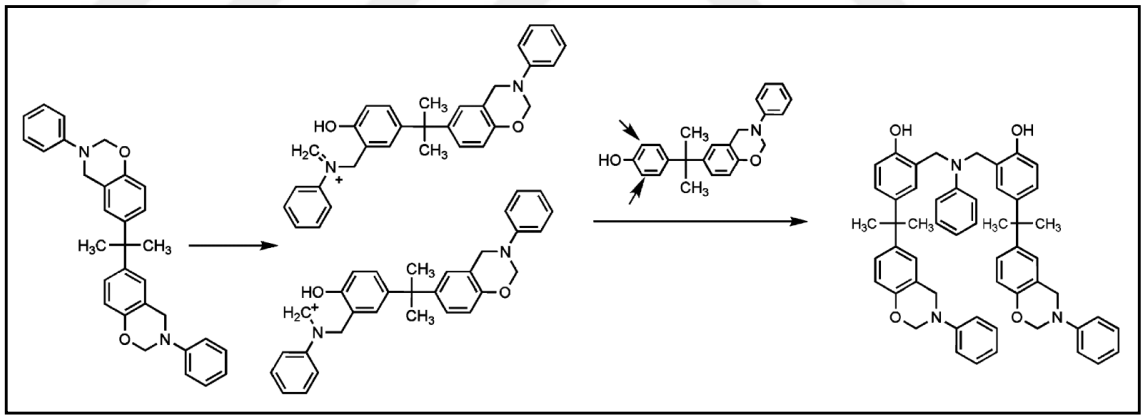

Figure 60. Cross-linking of BA-a monomer with thermally induced ring-openning reaction.

Also, it was observed that, both CA nanofibers and CA10/PBA-a5/CTR1 composite nanofibers preserved their fiber structure after the filtration experiment while the

mechanical integrity of the CA10/PBA-a5/CTR1 composite nanofibers were better than the CA nanofibers. CA10/PBA-a5/CTR1 composite nanofibers preserve the original form perfectly only some crinkle was observed after the filtration test (Figure 61).

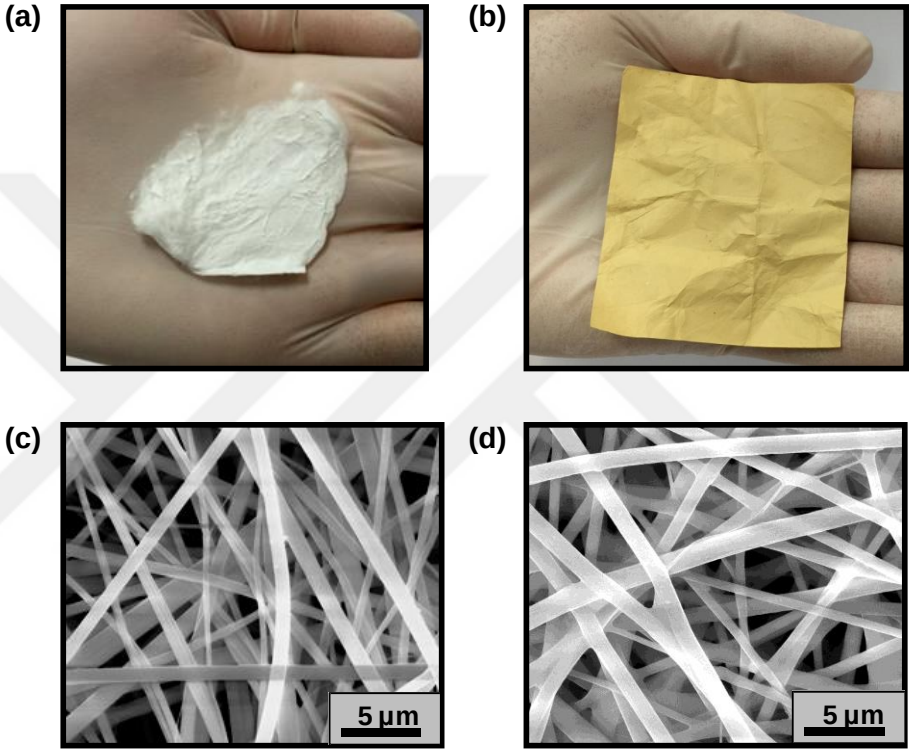

Figure 61. Photographs and SEM images of (a,c) CA nanofibers, (b,d) CA10/PBA-a5/CTR1 composite nanofibers after the filtration test.

3.6. Polycarbonate/BA-a composite nanofibers

Various studies show that the blending BA-a and other benzoxazines with different polymers such as polyurethane [262], polycarbonate [263], poly(ε-caprolactone) [264, 265], poly(N-vinyl-2-pyrrolidone) [266], so on. enhanced the thermal and/or mechanical/thermomechanical properties of the pristine polymer after the thermal curing. Although it was demonstrated for bulk composites, similar improvement can be expected for the polymer/polybenzoxazine composite nanofibers.

In this study, PC was chosen as a thermoplastic polymer for the enhancement of its thermomechanical properties. Also, PC posses relatively high toughness compared to other polymers and polybenzoxazines are brittle materials, thus combination of these two materials can provide fundamental contribution to the production of high performance polymer/polybenzoxazine composite nanofibers. PC has carbonyl groups having high potential to form intermolecular hydrogen-bond with the polybenzoxazine main chain which provides good missibility of these two component [263]. Therefore uniform composite nanofibers can be obtained from these two different types of material; one of them is crystallizable and the other one highly cross-linked. This might be an interesting study to demonstrate the missibility of thermoplastic polmer with thermoset resin in the nano-scale nanofiber production process.

3.6.1. Electrospinning of Polycarbonate and Polycarbonate/BA-a composite nanofibers

Homogenous solutions of the polycarbonate (PC) and mixture solutions of PC with BA-a (PC/BA-a) were prepared in THF/DMF (4:1, v/v) binary solvent system. Concentration range of the electrospinning solutions of PC/BA-a were determined to be 25% (w/v) and different compositions of the PC/BA-a precursor solution were prepared by varying the concentration of PC (18 and 20% (w/v)), BA-a (3, 5 and 7% (w/v)) and CTR (2% (w/v)) in the mixture solution in order to find out the most favorable compositon for the production of uniform PC/BA-a composite nanofibers. Initially, only PC and BA-a mixture solutions were prepared to determine the concentration of the main components of the precursor solution and these solutions are denoted as PCx:BA-ay, where x is the concentration of the PC and y is the concentration of the BA-a. Consequently, five different mixture solutions of the PCx:BA-ay were obtained as follow; PC18/BA-a5, PC18/BA-a7, PC20/BA-a3, and PC20/BA-a5. PC nanofibers were also prepared for comparison. SEM images of the nanofibers obtained from these solutions are shown in Figure 62. As it is observed, nanofibers were obtained with different morphologies and bead free uniform nanofibers were produced from the PC20/BA-a5 mixture solution (Figure 62a-e), thus 2% CTR was added to this composition to decrease the temperature of cross-linking reaction achieved by thermal curing. CTR did not effect the fiber morphology and uniform nanofibers were also

obtained from 2% CTR containing PC20/BA-a5 mixture solution (PC20/BA-a5/CTR2) (Figure 62f).

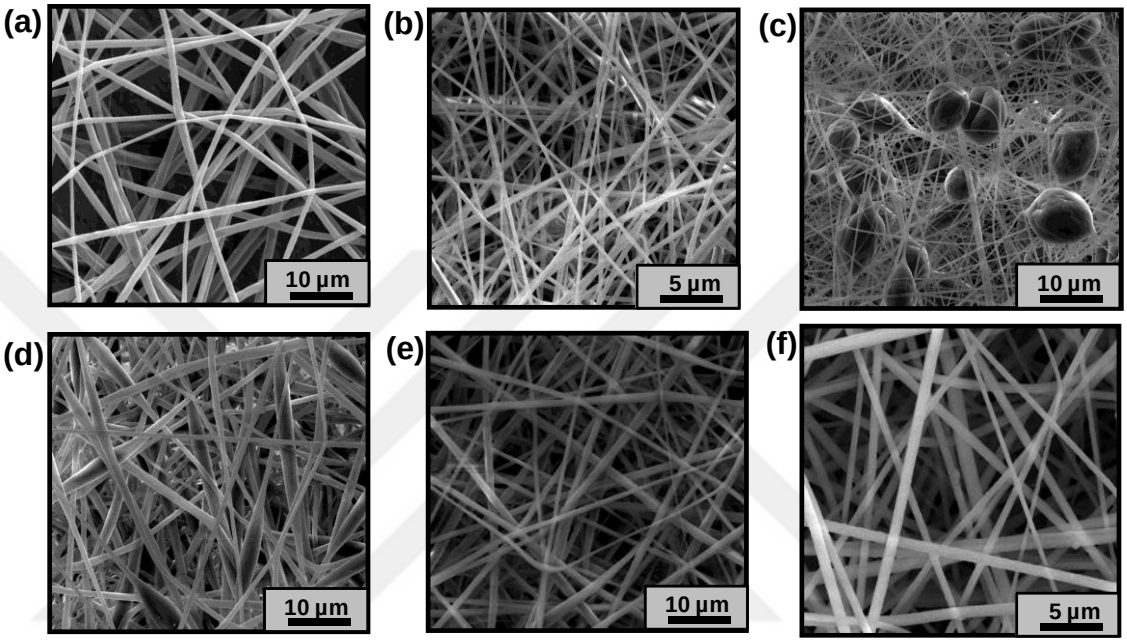

Figure 62. SEM images of the (a) PC nanofibers, (b) PC18/BA-a5, (c) PC18/BA-a7, (d) PC20/BA-a3, (e) PC20/BA-a5 and (f) PC20/BA-a5/CTR2 composite nanofibers.

3.6.2. Structural and morphological characterizations of the cross-linked PC20/PBA-a5/CTR2 composite nanofibers

It is known that, PC flows above about 155ºC and BA-a monomer has very high curing temperature which is about 240ºC [2]. Therefore it is essential to decrease curing temperature in order to obtained cross-linked composite nanofibers from PC and BA-a while preserving the fiber morphology. Here, addition of CTR is very critical. PC20/BA-

a5/CTR2 composite nanofibers were thermally cured by keeping the composite nanofibers in a standard oven starting from low temperatures at about 100ºC and the additional one hour curing was performed under the temperature where melting is observed. The morphological changes occuring during the thermal curing were investigated by SEM. Figure 63 represents the SEM images of the PC20/BA-a5/CTR2 composite nanofibers which are cured step-wise at 100, 120, 140 and 160ºC. As mention earlier, during the thermal curing, BA-a monomer polymerized (PBA-a) by ring-opening and cross-linking reactions and PC20/PBA-a5/CTR2 composite nanofibers were obtained. SEM images of the cured nanofibers revealed that although some deformation was observed at 120 and 140ºC, the fibrous morphology was preserved under the 160ºC. When nanofibers were being kept at 160ºC, they started to melt and lost the fibrous structure. It is an expected result, since the melting is observed for pristine PC at around 155ºC. Therefore, 140ºC is determined to be a last temperature step for the curing studies.

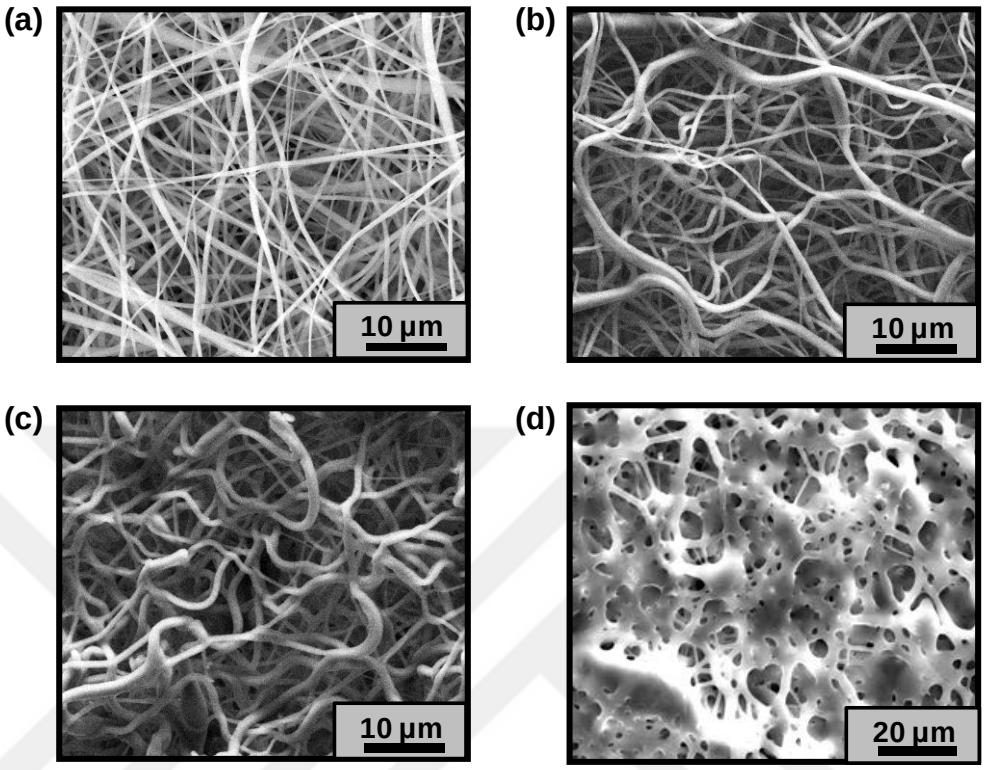

Figure 63. SEM images of the PC20/BA-a5/CTR2 composite nanofibers cured step-wised at (a) 100°C , (b) +120°C, (c) +140°C and (d) +160°C ('+' is used to show additional 1 hour heat treatment).

In order to investigate the cross-linking of the PC20/PBA-a5/CTR2 nanofibers, solubility tests were performed. Although, cured PC20/PBA-a5 composite nanofibers which are not including CTR dissolved immediately in THF and DMF, PC20/PBA-a5 /CTR2 composite nanofibers preserved the mechanical integrity even over night immersing which is the evidence of cross-linking. Further prove the cross-linking provided by thermal curing and also molecular structural changes occurring during the

thermal curing, FTIR spectroscopy technique was used. Generally characteristic absorbance peaks of the benzoxazine ring in the FTIR spectrum were investigated during the thermal curing studies. Characteristic benzoxazine peaks for the BA-a were observed at 946 cm^{-1} (out-of-plane C-H vibration mode of the benzene ring attached to oxazine ring) and 1232 cm^{-1} (asymmetric stretching of C-O-C in the oxazine ring) As it is known, heat treatment provides the opening of oxazine rings and the intensity of these characteristic benzoxazine peaks decreases with the thermal curing. In order to differentiate the origin of the peaks, FTIR spectra of PC, BA-a, PC20/BA-a5/CTR2 and PC20/BA-a5/CTR2 were recorded in the range of 2000-200 cm^{-1}. Firstly, characteristic benzoxazine peaks which are not overlapping with the PC peaks were determined in order to investigate the ring opening and cross-linking reactions. As it is observed, while peak at 946 cm^{-1} belonging to the BA-a was clearly differentiated in the FTIR spectrum of PC20/BA-a5/CTR2, absorbance peak at 1232 cm^{-1} was overlapping with the C-O-C stretching of the PC. Therefore, absorbance peak at 946 cm^{-1} attributed to the out-of-plane C-H vibration mode of the benzene ring attached to oxazine ring was chosen to investigate ring opening reactions. After the thermal curing, this peak was disappeared in the FTIR spectrum of PC20/PBA-a5/CTR2 confirming the achievement of the cross-linking and polymerization of BA-a. In brief, FTIR results show that addition of 2% CTR decreased the curing temperature of PC nanofibers and cross-linked PC20/PBA-a5/CTR2 composite nanofibers were obtained even at low temperatures.

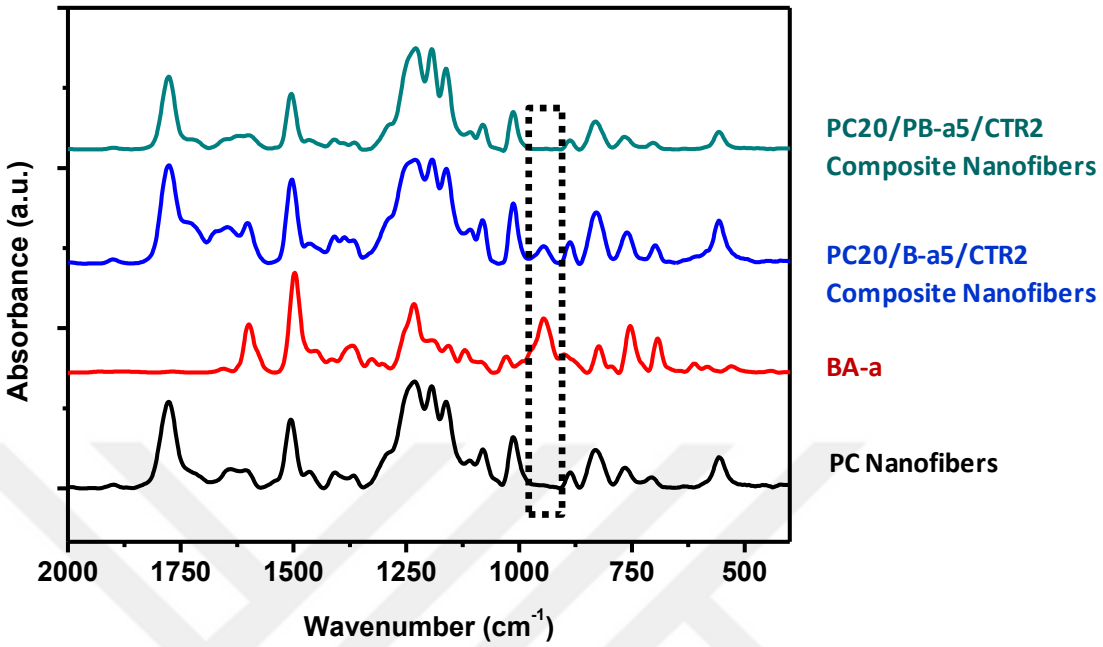

Figure 64.FTIR spectra of BA-a, PC nanofibers, PC20/ BA-a5/CTR2 composite nanofibers and PC20/ PBA-a5/CTR2 composite nanofibers cured step-wise at 100, 120 and 140°C.

3.6.3. Thermal and thermomechanical properties of PC and PC20/PBA-a5/CTR2 composite nanofibers

TGA was used to investigate the thermal properties of PC nanofibers and PC10/PBA-a5/CTR2 composite nanofibers. TGA curves of these two samples are given in Figure 65. For PC nanofibers, one step weight loss was observed with the derivative peak maximum at 465ºC which is the main degredation temperature of PC. For PC10/PBA-a5/CTR2 composite nanofibers three steps weight loss was observed with the derivative peak at 215, 387 and 503ºC. Main degration occured at 503ºC degredation of PC. After

the PC10/PBA-a5/CTR1 composite nanofiber formation, main degradation temperature of the PC shifted remarkably to the higher temperature. However, no significant change was observed in char yield of PC nanofibers and PC10/PBA-a5/CTR2 composite nanofibers which are determined as 23 and 27%, respectively.

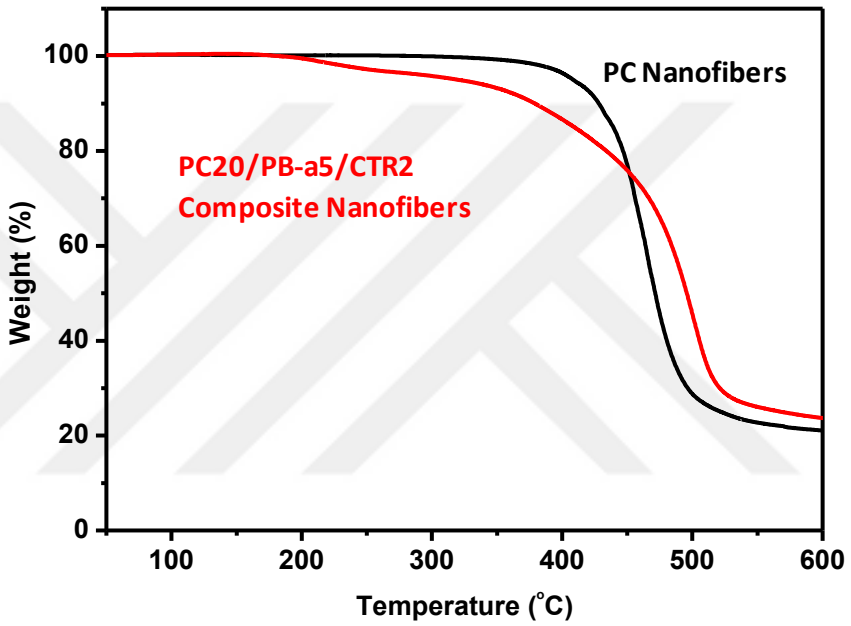

Figure 65. TGA thermograms of the PC nanofibers and PC20/PBA-a5/CTR2 composite nanofibers cured step-wise at 100, 120 and 140°C.

DMA was used to evaluate thermomechanical properties of PC20/BA-a5/CTR2 composite nanofibers cured at different temperatures. First, DMA measurement of PC20/BA-a5/CTR2 composite nanofibers (before curing) were performed in order to demonstrate the initial thermomechanical properties of composite nanofibers. The storage modulus of the PC20/BA-a5/CTR2 composite nanofibers were recorded up to

150°C (Figure 66). At the begining, the storage modulus of the uncured PC20/BA-a5/CTR2 composite nanofibers increased up to 55 Mpa from 20 Mpa and then decreased gradually with increasing temperature. The reason of the increasing storage modulus is most probably cross-linking occured by heating as a result mechanical properties of the composite nanofibers were enhanced during the measurement. DMA curves of PC20/BA-a5/CTR2 composite nanofibers cured up to 120 ºC and 140 ºC suggest that PC20/BA-a5/CTR2 composite nanofibers cured up to 140ºC has higher storage modulus in the glassy region than the cured up to 120ºC, as observed from their respective room-temperature values of 71 and 124 Mpa. Then, storage modulus of both samples begin to decrease indicating the transition from glassy state to rubbery state which is the beginning of the glass transition range. It was observed that with higher curing temperatures, the transition in the storage modulus progressively moves to higher temperatures which indicates that glass transition temperature (Tg) increasing with cure temperature.

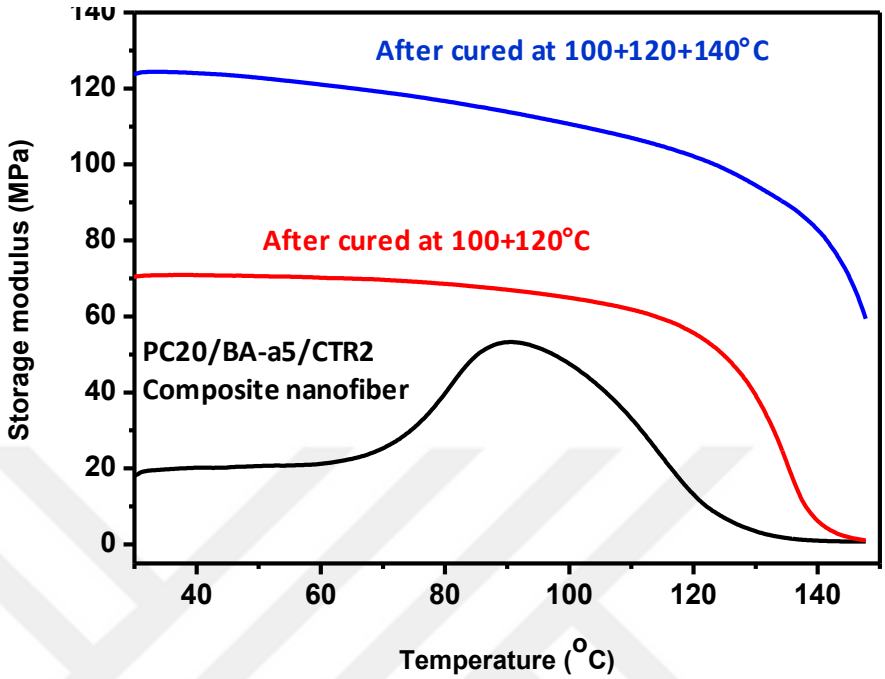

Figure 66. DMA curves of the PC20/ PBA-a5/CTR2 composite nanofibers before and afer cured step-wise at different temperatures.

Chapter 4: Cyclodextrin/polybenzoxazine composite nanofibers

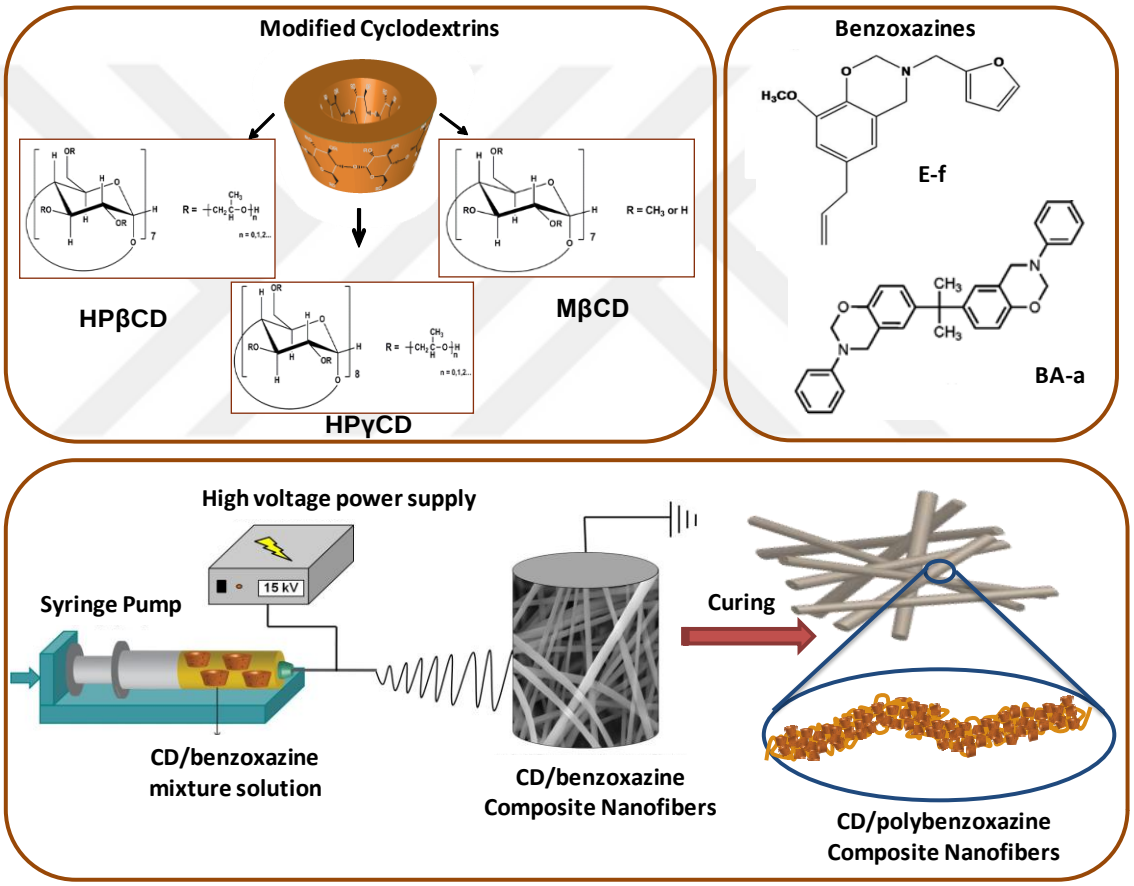

3.7. Water insoluable cyclodextrin nanofibers by using BA-a as a cross-linking agent

Cyclodextrins (CDs) are cyclic oligosaccharides consisting of (1,4)-linked glucopyranose units. They are produced from the enzymatic conversion of starch so they are natural and non-toxic [267-269]. CDs are truncated cone-shaped molecules which have three main types; α-CD, β-CD and γ-CD having six, seven and eight glucopyranose units, respectively. Moreover, by the chemical modifications of CDs (e.g. methyl-CD and hydroxy-propyl-CD), the regenerative CD types such as hydroxypropyl-β-cyclodextrin (HPβCD), hydroxypropyl-γ-cyclodextrin (HPγCD) and methyl-β-cyclodextrin (MβCD) can be obtained with higher solubility compared to native ones [268-270] (Figure 67a,b). Due to the high solubility, highly concentrated homogeneous solutions can be prepared from these modified CDs for the production of CD nanofibers.

In the electrspinning process, generally high molecular weight polymers and highly concentrated polymer solutions are used. Because for the formation of uniform nanofibers required chain entanglement and overlapping can be provided especially in these conditions. Therefore, the electrospinning of non-polymeric systems was considered as a challenge, However, in earlier studies of our group, bead free and uniform nanofibers were obtained from three different CD derivatives, HPβCD, HPγCD, MβCD without using polymeric carrier matrix due to self-assembly and aggregation property of CD molecules [271] (Figure 67c).

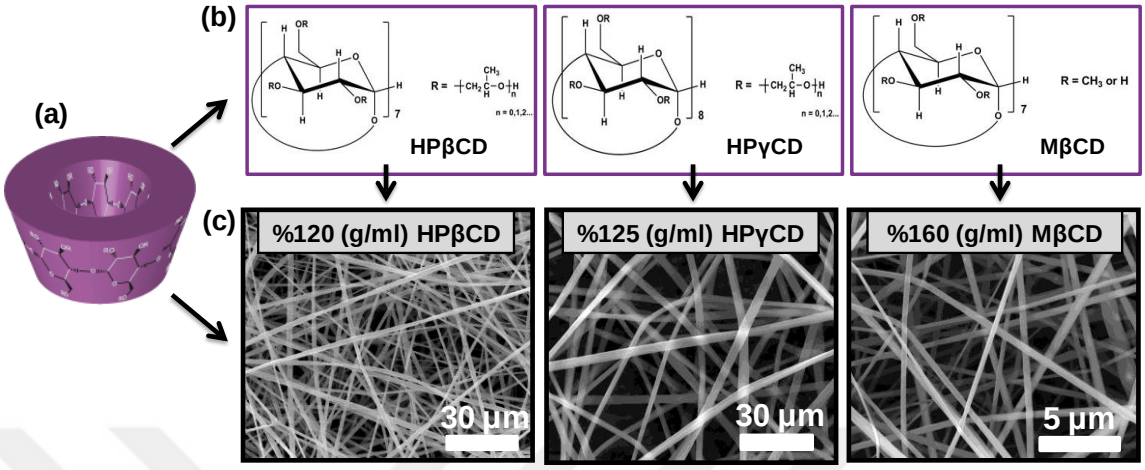

Figure 67. Schematic view and (b) chemical structures of modified HPβCD, HPγCD and MβCD and (c) SEM images of the electrospun nanofibers obtained from the highly concentrated solutions of modified HPβCD, HPγCD and MβCD.

The specific shape of CDs enables the formation of non-covalent host-guest inclusion complexes between variety of molecules [267-269, 272] provides also removal of the undesired molecules from the environment. Therefore, nanofibers functionalized by CDs or produced from only CDs might be a promising filtration material for the removal of organic pollutants, dye molecules and heavy metal ions. Although, they have very attractive properties, their solubility in water limit their usage especially in liquid media therefore producing water insoluable CD nanofibers have became more essential in recent years. Therefore in this chapter, we used benzoxazine monomers as cross-linking agent and we produced water insoluable modified CD/polybenzoxazine composite nanofibers with enhanced physical and thermal properties. Main purpose to obtain water insoluable CD nanofibers is to produce molecular filtration material which can be used

for the waste water treatments. Advantage of the nanofibers such as high surface area and porous structures provide the adsorption of molecules more effectively, so high efficiency materials can be obtained by achieving the cross-linking of CD nanofibers.

3.7.1. Electrospinning of modified cyclodextrin/BA-a composite nanofibers

In this study, we used three different CD derivatives (HPβCD, HPγCD and MβCD) and benzoxazine monomer (BA-a) in order to obtain water insoluable CD nanofibers. Initially, the ratios between CD derivative and BA-a were varied within the different ranges three different composion of the CD/BA-a were prepared as follow; 75/50, 75/75, 100/25 (w:w/v) for HPβCD, HPγCD and 75/50, 75/75, 120/25 (w:w/v) for MβCD (w:w/v) to obtain bead free and uniform nanofibers and nanofibers obtained from these solutions were denoted as CDx/BA-ay, where x is the concentration of the CD molecules and y is the concentration of the BA-a in the mixture solution. SEM images of the nanofibers obtained from all these compositions are given in Figure 68. In all compositions with lower CD and BA-a concentration, CD75/BA-a50 non-uniform beads with different size range were obtained owing to the insufficient amount of CD aggregates. This is resulte destabilization of the electrified jet during the electrospinning, thus resulted with beads instead of continuous fibers which is also typical behaviour of the polymeric systems with low concentration due to the insufficient chain entanglements and overlapping [90, 273]. In the composition of CD75/BA-a75, different structures were observed for all CD types. When HPβCD75/BA-a75 solution was electrospun thicker fibers with almost uniform structure were obtained. In the case of

electrospinning of HPγCD75/BA-a75 and MβCD75/BA-a75 solutions nanofibers with bead structures were obtained, however, MβCD75/BA-a75 solutions yielded higher amount of beads most probably lower amount of CD aggregates**.** As it is observed, bead free and uniform nanofibers were obtained when HPβCD100/BA-a25, HPγCD100/BA-a25 and MβCD120/BA-a25 mixture solutions were electrospun. It is well known that for the polymeric system bead-free fibers are usually obtained when the polymer concentration is increased [90, 106, 273, 274]. Because high concentration polymer solutions posses more chain entanglements which play a critical role to keep the continuity of the jet during the electrospinning process. Here, we observed a very similar behavior for the electrospinning of CD/BA-a nanofibers. Since CDs have more contribution for the formation of nanofibers with forming CD agregates due to hydrogen bonding, increase in their concentration significantly affected the nanofibers morphology rather than the increase in BA-a concentration.

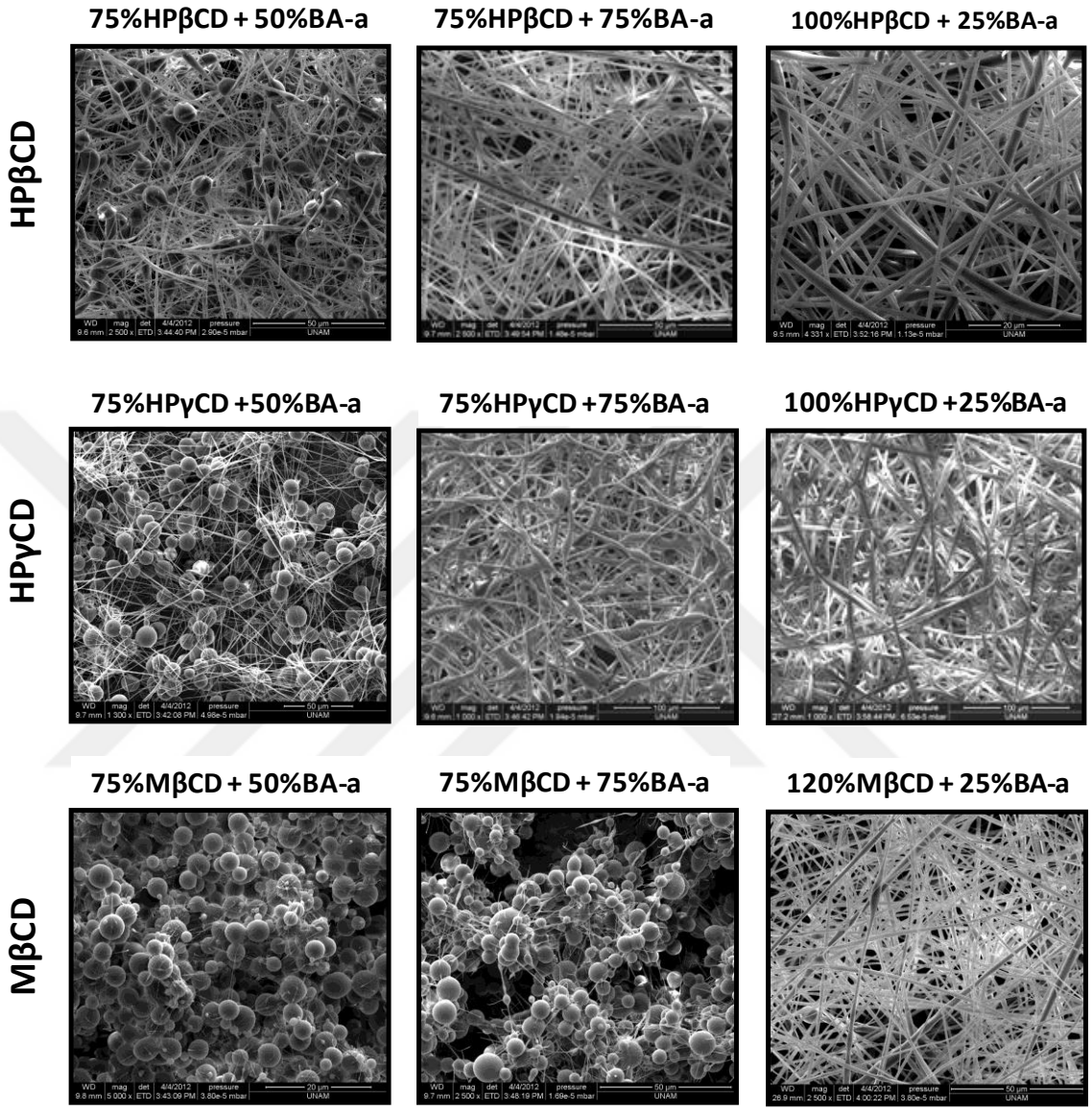

Figure 68. SEM images of the nanofibers obtained from different compositions of CD/BA-a solutions.

3.7.2. Structural and morphological and thermal characterization of the modified CD/PBA-a composite nanofibers after thermal curing

After determining the suitable ratio for the production of bead free and uniform nanofibers, curing experiments were carried out for HPβCD100/BA-a25, HPγCD100/BA-a25 and MβCD125/BA-a25 composite nanofibers. Curing studies were performed by starting from 150°C and temperature increased step-wise up to 200 ºC where melting of the HPγCD100/BA-a25 and MβCD125/BA-a25 composite nanofibers were observed (Figure 69). Since HPβCD100/BA-a25 composite nanofibers were more durable to the heating, HPβCD100/BA-a25 composite nanofibers was chosen for the further investigation of the properties of the composite nanofibers.

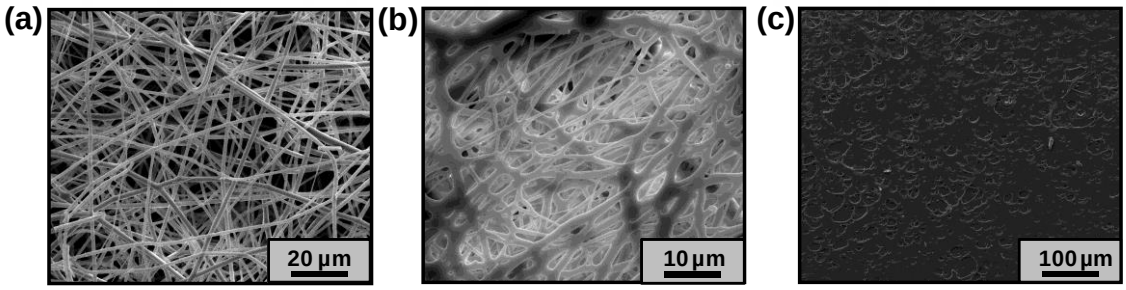

Figure 69. SEM images of the (a) HPβCD100/BA-a25, (b) HPγCD100/BA-a25 and MβCD125/BA-a25 composite nanofibers after step-wise curing at 150, 175, and 200ºC.

At higher temperatures (225ºC) some structural deformations were also observed for HPβCD100/BA-a25 composite nanofibers. Therefore, different approach was developed to obtained cross-linked HPβCD100/BA-a25 composite nanofibers without deteorating

the nanofibers. In order to provide complete cross-linking while maintaining the fiber morphology, citric acid (CTR, 5% and 15% w/v) was added to HPβCD100/BA-a25 mixture solution as a crosslinking agent. In addition to the HPβCD100/BA-a25, HPβCD/CTR solution was also prepared as a control to investigate the effect of citric acid and BA-a in the curing capabilities of nanofibers. As a result, four different compositions of mixture solutions (HPβCD100/BA-a25/CTR5, HPβCD100/BA-a25/CTR15, HPβCD100/BA-a25 and HPβCD100/CTR15 were obtained and bead free uniform nanofibers were produced from each solution (Figure 70 (ai-di)). Curing studies were carried out by step-wise heating in the tempearture range 150-225°C. As it is known, BA-a monomer polymerizes by thermally induced ring opening and form polybenzoxazine (PBA-a). Therefore after the curing, HPβCD100/PBA-a25/CTR5, HPβCD100/PBA-a25/CTR15, HPβCD100/PBA-a25 composite nanofibers and HPβCD100/CTR15 film were obtained as shown in Figure 70 (aii, bii). While HPβCD100/PBA-a25 composite nanofibers could not preserve the fibrous structure after heating up to 225ºC, only CTR including composite nanofibers were decomposed completely after the curing process. Here, it is clear that CTR itself is not sufficient for the cross-linking of CD nanofibers. On the other hand, both CTR and BA-a containing composite nanofibers maintained the fiber morphology perfectly even after keeping nanofibers one hour at 225ºC which demonstrated the achievement of cross-linking (Figure 70 (cii, dii)).

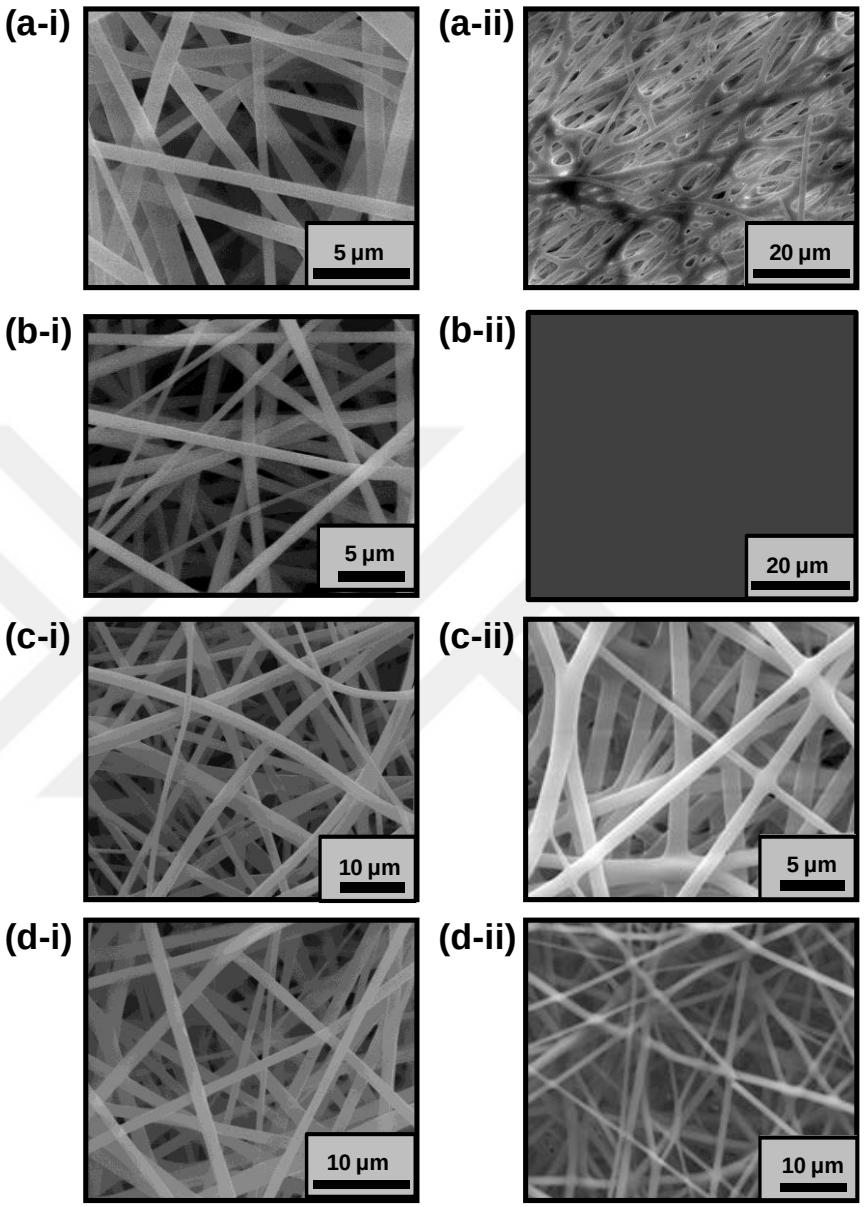

Figure 70. SEM images of (a) HPβCD100/BA-a25, (b) HPβCD100/CTR15, (c) HPβCD100/BA-a25/CTR5 and (d) HPβCD100/BA-a25/CTR15; (i) as-electrospun nanofibers and (ii) after step-wise curing at 150, 175, 200 and 225ºC .

Furthermore, FTIR spectroscopy was used to investigate the molecular structural changes occuring during the thermal curing. Figure 71 shows the FTIR spectra of the HPβCD100/PBA-a25/CTR5, HPβCD100/PBA-a25/CTR15, HPβCD100/PBA-a25 composite nanofibers cured up to 225ºC and HPβCD100/CTR15 composite nanofibers cured up to 200ºC where the fibrous structure of the all nanofibers were maintained. For all samples, at the begining characteristic peaks of the BA-a which are not overlapping with the HPβCD CD peaks was observed except HPβCD100/CTR15. After thermal curing, these peaks disappeared in the FTIR spectra indicating the polymerization of BA-a (Figure 71).

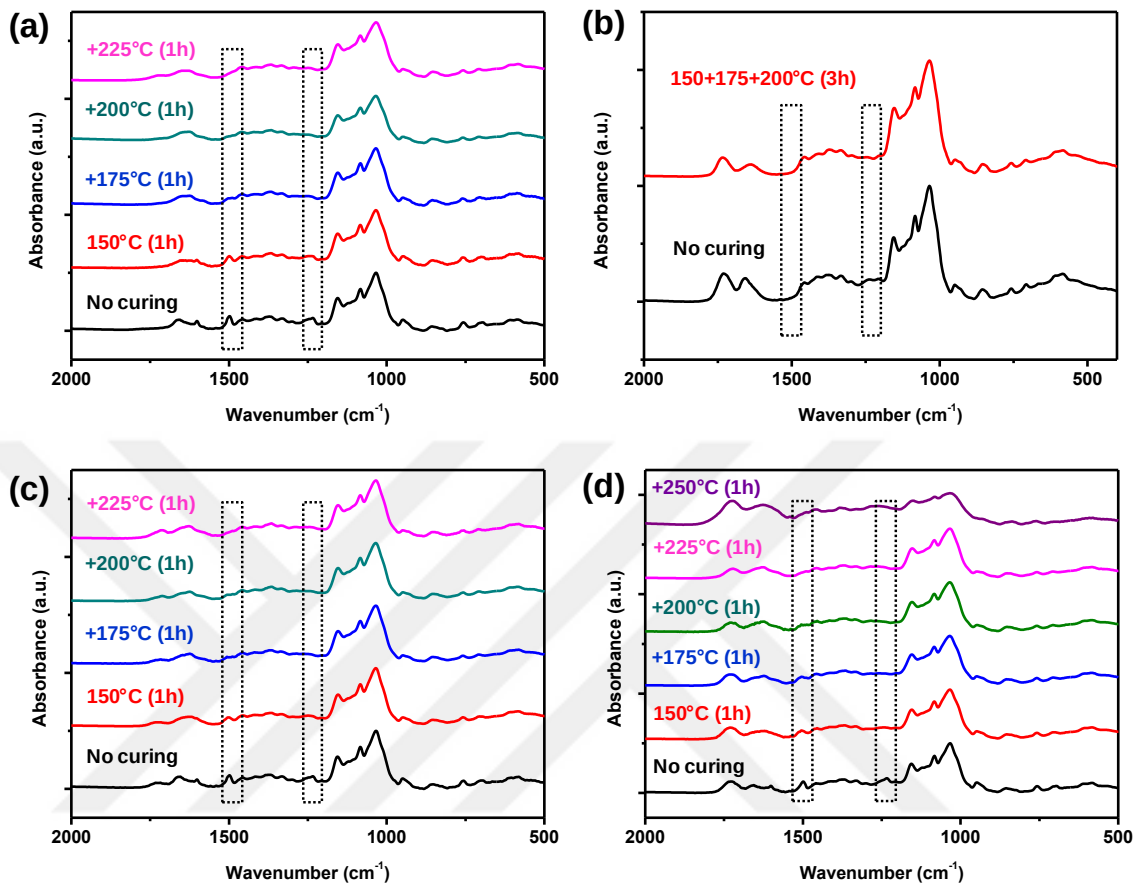

Figure 71. FTIR spectra of (a) HPβCD100/PBA-a25, (b) HPβCD100/CTR15, (c) HPβCD100/PBA-a25/CTR5 and (d) HPβCD100/PBA-a25/CTR15 composite nanofibers obtained at each step of thermal curing.

Thermal properties of the composite nanofibers were investigated by TGA. TGA themograms of the BA-a, HPβCD nanofibers, HPβCD100/PBA-a25/CTR5, HPβCD100/PBA-a25/CTR15, HPβCD100/PBA-a25 and HPβCD100/CTR15 composite nanofibers before and after curing are given in Figure 72. It is observed that thermal decomposition temperature of the pure HPβCD nanofibers (352ºC) was shifted to

higher temperatures (~364ºC) by forming composite nanofibers. In addition, char yield of the pure HPβCD nanofibers (7.3 %) increased with composite nanofiber formation and highest char yield was observed in the case of HPβCD100/PBA-a25/CTR5 and HPβCD100/PBA-a25/CTR15 with the same value (20.1%).

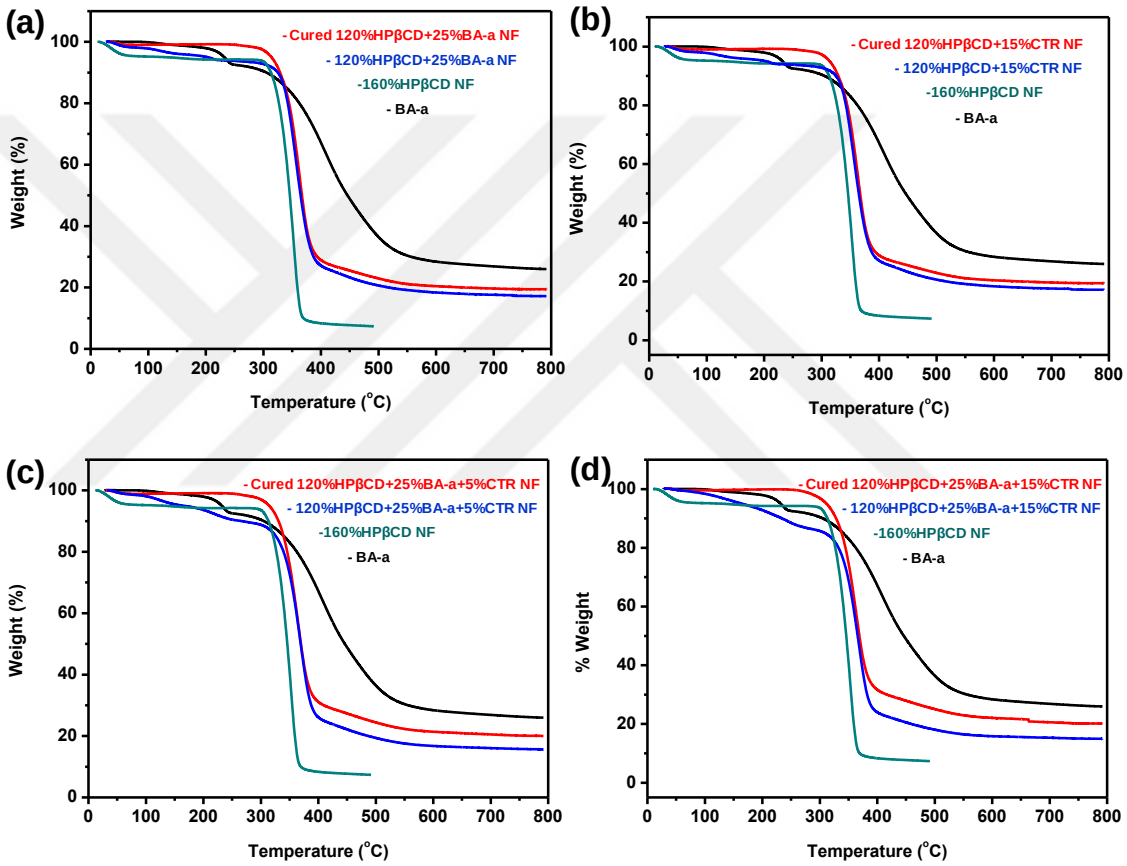

Figure 72. FTIR spectra of (a) HPβCD100/PBA-a25, (b) HPβCD100/CTR15, (c) HPβCD100/PBA-a25/CTR5 and (d) HPβCD100/PBA-a25/CTR15 composite nanofibers obtained at each step of curing.

Further investigate the cross-linking, HPβCD100/PBA-a25, HPβCD100/CTR15, HPβCD100/PBA-a25/CTR5 and HPβCD100/PBA-a25/CTR15 composite nanofibers were immersed in water. Although, HPβCD100/PBA-a25/CTR15 composite nanofibers did not dissolved in water after over night immersing, HPβCD100/PBA-a25, HPβCD100/CTR15, HPβCD100/PBA-a25/CTR5, and HPβCD100/PBA-a25/CTR15 composite nanofibers were completely dissolved in progressing time. Therefore, it is concluded that complete cross-linking was achieved only in the case of HPβCD100/PBA-a25/CTR15 composite nanofibers.

In order to investigate the solubility of HPβCD100/PBA-a25/CTR15 composite nanofibers more detailed various solvent such as acetone, ACN, chloroform, DCM, DMF, DMSO, ethanol, methanol, THF and water were used and nanofibers were immersed in these solvents overnight. As hown in Figure 73, HPβCD100/PBA-a25/CTR15 composite nanofibers showed high stability even in water, DMF and DMSO which are very good solvents for the CDs. These nanofibers were aimed to be used as an adsorbant for the waste water treatments therefore it is good that they are highly stable in water.

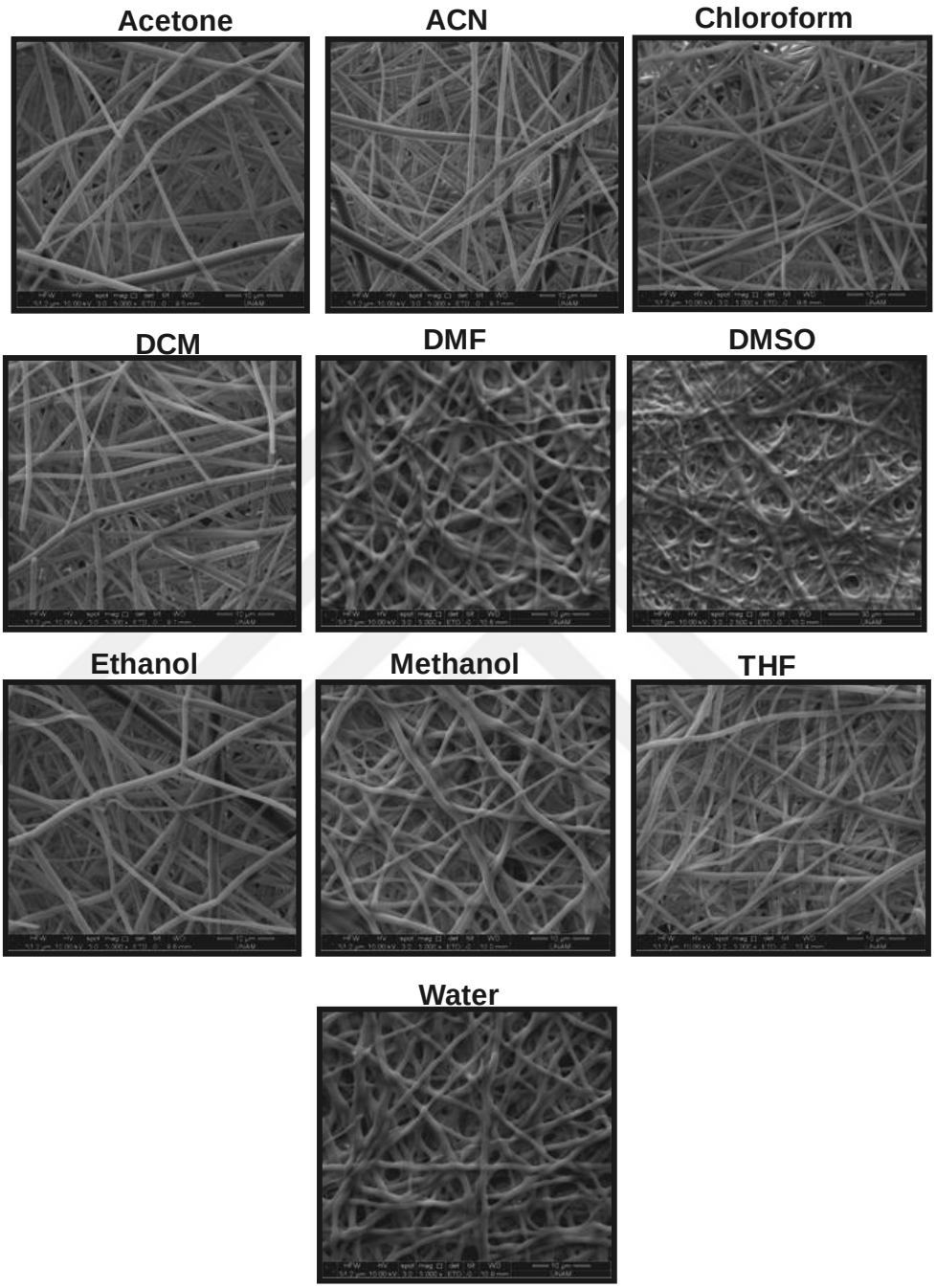

Figure 73. SEM images of the HPβCD100/PBA-a25/CTR15 composite nanofibers after overnight immersing in different solvents.

3.7.3. Polyaromatic hydrocarbons entrapment efficiency of HPβCD100/PBA-a25/CTR15 composite nanofibers

Polyaromatic hydrocarbons (PAHs) molecular entrapment efficiency of HPβCD100/PBA-a25/CTR15 composite nanofibers were investigated by three different PAH molecules; fluoranthene (FLUT), phenanthrene (PHE) and pyrene (PYR) (Figure 74a). Here, inclusion complexation capability of the HPβCD found in the HPβCD100/PBA-a25/CTR15 composite nanofibers with the PAHs (Figure 74b) is the main driving force for the removal of the PAHs from the aqueous solutions.

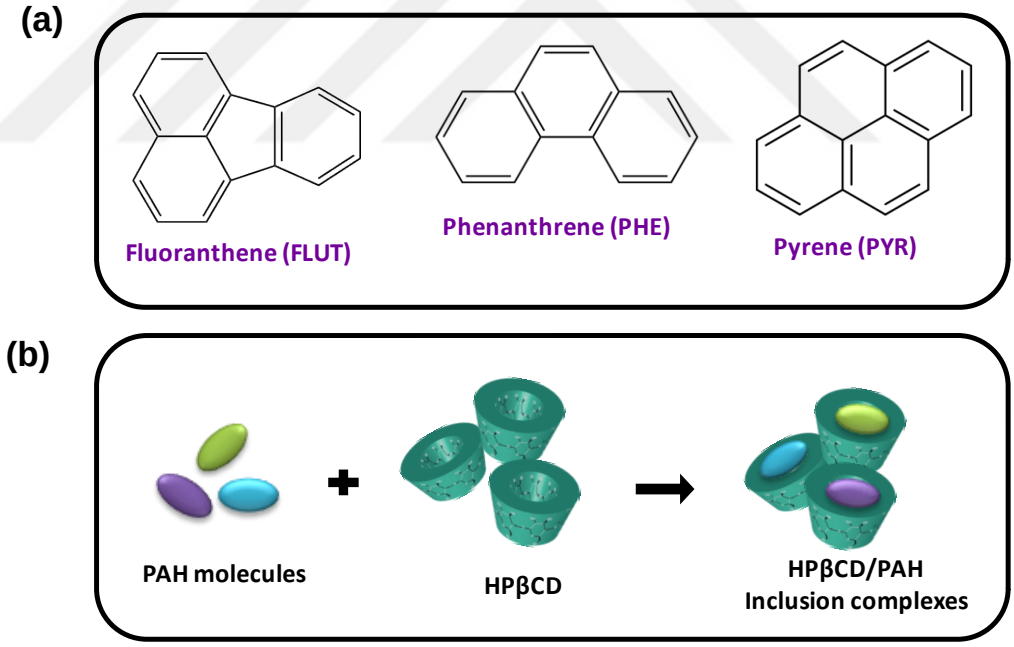

Figure 74. (a) Molecular structure of the PAHs used in the removal experiments and (b) schematic representation of the inclusion complex formation between PAHs and HPβCD.

In order to determine the optimum time interval for the efficient removal of PAHs molecules, 400 ppb PAHs mixture solution was prepared. Since the solubilities of PAHs are very low in the water, after some solubility test, 400 ppb was determined to be moderate concentration for testing the time dependent removal efficiency of HPβCD100/PBA-a25/CTR15 composite nanofibers, although we were able to prepare well dissolved 600 ppb PAHs homegenous solutions as well. As observed in Figure 75a, removal efficiency of the HPβCD100/PBA-a25/CTR15 composite nanofibers increased with progressing time intervals and became almost stable after 3 hours. On the other hand, highest removal efficiency (85-90 %) was achieved after 6 hours shaking for all PAHs type. Therefore, 6 hours determined to be a sufficient time interval in which HPβCD100/PBA-a25/CTR15 composite nanofibers able to remove the PAHs molecules effectively from water.

Then, 200, 400 and 600 ppb PAHs mixture solutions were prepared from FLUT, PHE and PYR in order to evaluate the removal potential of HPβCD100/PBA-a25/CTR15 composite nanofibers in low, moderate and high concentartions of PAHs mixture solutions. Figure 75b demonstrates the removal efficiency of the HPβCD100/PBA-a25/CTR15 composite nanofibers after 6 hours shaking of 200, 400 and 600 ppb PAHs mixture solutions. As observed, HPβCD100/PBA-a25/CTR15 composite nanofibers showed very high removal efficiency with more than 80% for the removal of FLUT, PHE and PYR in all concentrations.

Finally, PAHs removal effciency of the HPβCD100/PBA-a25/CTR15 composite nanofibers were compared with that of activeted charcoal which is a very efficient commercial product used for the removal of PAHs from waste waters. Figure 75c represents the removal efficiency of the activeted carcoal after 6 hours shaking in 200, 400 and 600 ppb PAHs mixture solutions. Even though, very similar removal efficiecy values were obtained for the activeted carcoal, HPβCD100/PBA-a25/CTR15 composite nanofibers showed slightly higher removal efficiency than activeted carcoal indicating that these nanofibers can be a novel potential adsorbent for the effective removal of PAHs from waste waters.

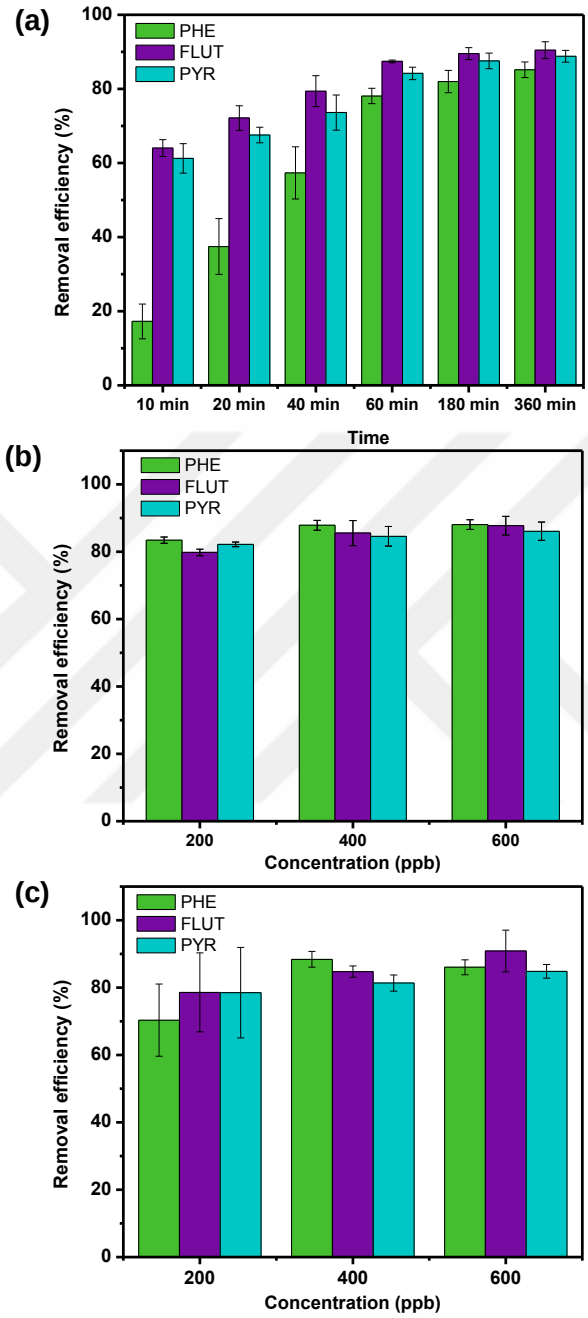

Figure 75. (a) Time and (b) concentration dependent removal efficiency of the HPβCD100/PBA-a25/CTR15 composite nanofibers from the PAHs mixture solution and (c) removal efficiency of the activated charcoal from the PAHs mixture solution.

3.7.4. Dye molecules entrapment efficiency of HPβCD100/PBA-a25/CTR15 composite nanofibers

Dye molecules entrapment efficiency of HPβCD100/PBA-a25/CTR15 composite nanofibers were investigated by the mixture of two different dyes; methyl orange (MO) and methylene blue (MB). As shown in Figure 76a, MO is negatively charged and MB is possitively charged dye molecules. Here, we demonstrated the selectivity of HPβCD100/PBA-a25/CTR15 composite nanofibers to MB dye and removing of MB molecules from the aqueous solution by inclusion complex formation (Figure 76b).

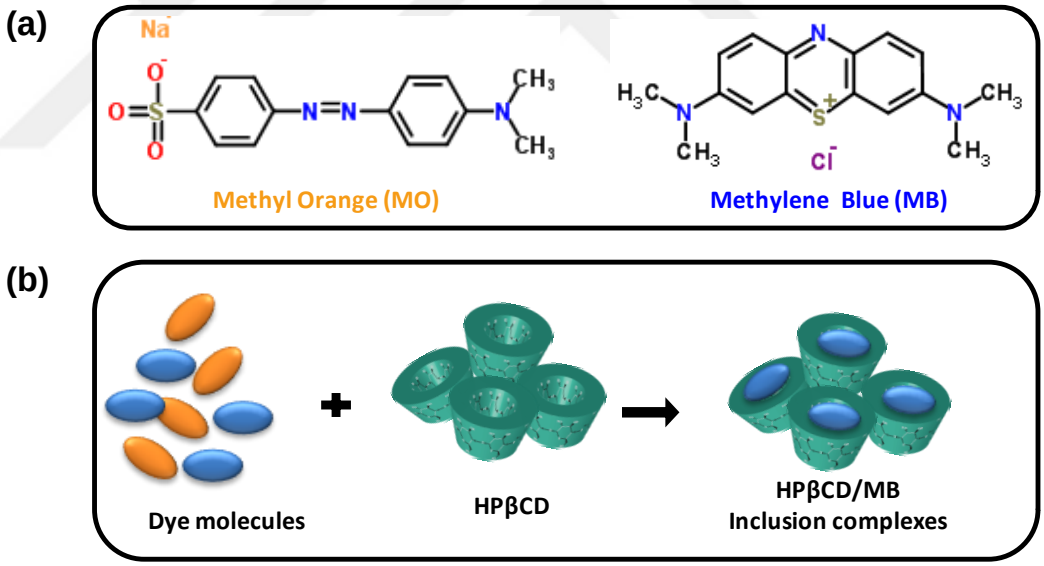

Figure 76. (a) Molecular structure of the dye molecules used in the removal experiments and (b) schematic representation of the inclusion complex formation between MB molecules and HPβCD.

Adsorption of dye molecules by HPβCD100/PBA-a25/CTR15 composite nanofibers were investigated by UV-Vis spectroscopy. Initially, 20 ppm MO, MB and MO/MB mixture solutions were prepared and UV-Vis spectrum of each solution taken in the 200-800 nm wavelenght range to show existence of spesific absorbance bands of two dye molecules in the UV-vis spectra of MO/MB (Figure 77). MO has a characteristic absorbance band at 668 nm with a shoulder at 609 nm and MO has a broad band with a maximum at 466 nm. As it is observed from the UV-vis specta, characteristic peaks of the both MO and MB appeared in the UV-vis pectrum of MO/MB mixture solution indicating the well mixed MO/MB mixture solution is obtained.

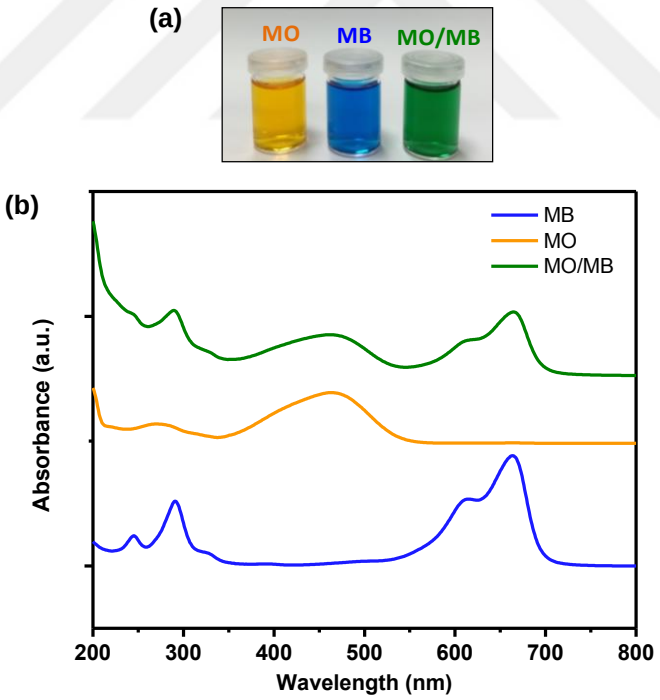

Figure 77. (a) Photographs and (b) UV-vis spectra of 20 ppm MO, MB and MO/MB mixture solution.

Time dependent dye removal experiments were conducted in order to determine the required time interval for the effective removal of the dye molecules. Figure 78 shows the photographs of the MO/MB mixture solutions taken progressing time intervals and represents the UV-vis spectra of the MO/MB mixture solution before and after 6 hours removal experimet. As it is observed, green color of the MO/MB mixture solution became yellow and the intensity of MB absorption band decreased while no significant change observed in the MO absorption band indicated only MB molecules adsorbed by HPβCD100/PBA-a25/CTR15 composite nanofibers. Actually, it is an expected result since MB dye is possitively charged and HPβCD molecules have carboxylic groups which are partially negatively charged. Most probably, due to the attractive interactions and also better size fit between MB molecules and HPβCD, MB molecules were effectively removed from the MO/MB mixture solution by inclusion complex formation.

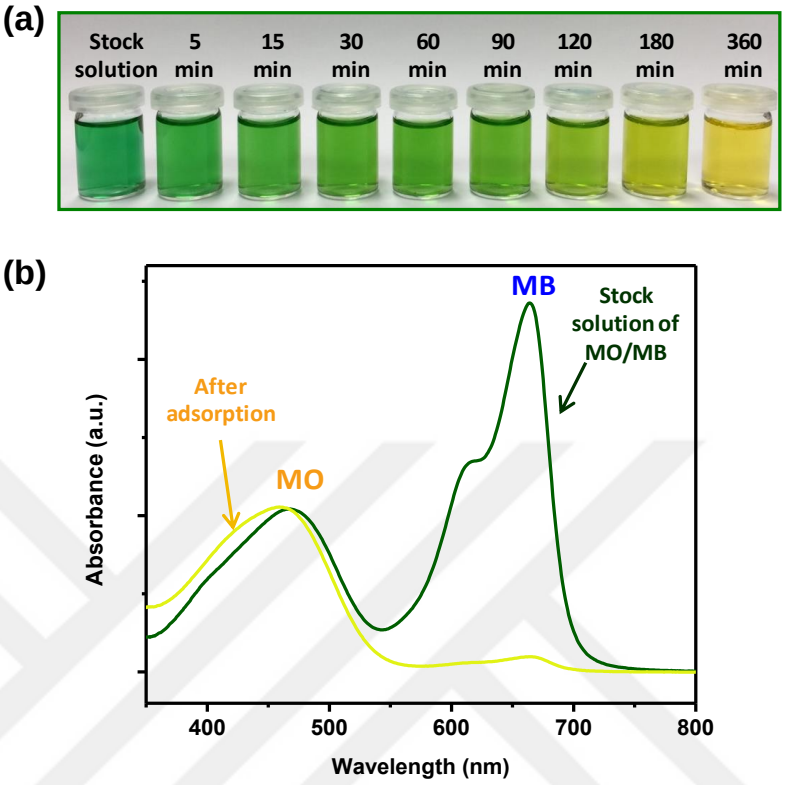

Figure 78. (a) Photographs of the MO/MB mixture solutions after the removal experiment performed at certain time intervals and (b) UV-Vis Spectra of MO/MB dye mixture solution before and after 6 hours removal experiment.

In order to calculate the adsoption capacity of the HPβCD100/PBA-a25/CTR15 composite nanofibers, different concentrations of the MO/MB mixture solution were preapared up to no precipitaion was observed. Therefore, 100 ppm determined to be the highest concentration in which homogeneous dye solution was preapared and homogenity of the solution was preserved during the experiment. Adsorption capacity

and the removal efficiency of HPβCD100/PBA-a25/CTR15 composite nanofibers were calculated by using the following equations;

$$\text{Adsorption capacity}\left(q_e\right)=\frac{\left(C_0-C_e\right)\times V}{m}$$

equation 1

$$\text{Removal efficiency}\left(\%\right)=\frac{\left(C_0-C_e\right)}{C_0}\times 100$$

equation 2

q_e is the adsorption capacity (mg g^{-1}), C_0 and C_e are the concentration of MB dye in the aqueous solution before and after the adsorption, respectively (mg L^{-1}), V is the volume of the solution (L), and m is the weight of the HPβCD100/PBA-a25/CTR15 composite nanofibers.

Adsorption capacity of HPβCD100/PBA-a25/CTR15 composite nanofibers was calculated as 58.3 ± 2.4 mg g^{-1}. Removal efficiencies of HPβCD100/PBA-a25/CTR15 composite nanofibers in each concentration of the MO/MB dye mixture solutions were calculated and summarized in the graph shown in Figure 79a. As it is observed removal efficiency of HPβCD100/PBA-a25/CTR15 composite nanofibers decreased with increasing concentration since they have a specific capacity. The photographs of the MO/MB solutions show the effective removal of the MB dye molecules up to 20 ppm. At higher concentrations, greenish yellow solutions were obtained after the removal experiments indicating 20 ppm is the optimum concentration for the effective removal of MB dye molecules in this experiment conditions and 92% removal efficiency is achieved (Figure 79b,c).

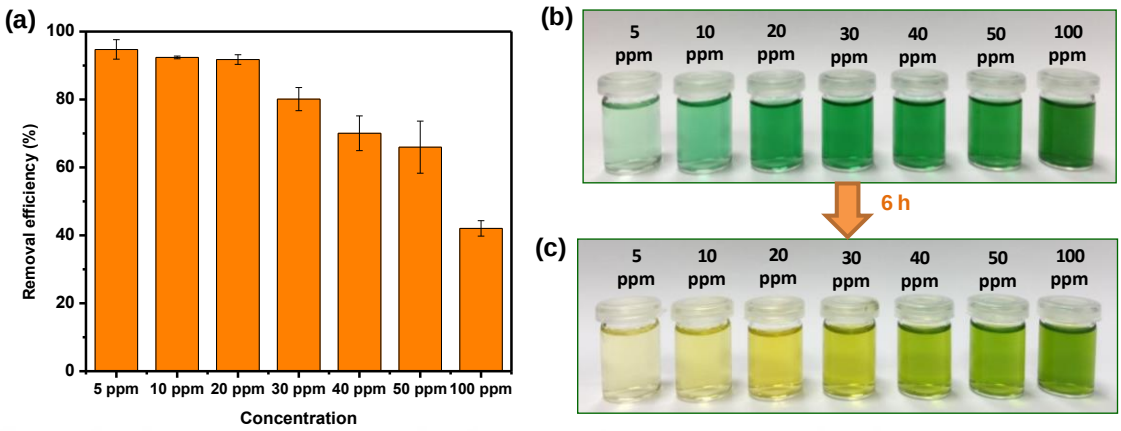

Figure 79. (a) The removal efficiency of HPβCD100/PBA-a25/CTR15 composite nanofibers in different concentration of MO/MB dye mixture solutions after 6 hours removal experiment, Photograps of different concentration MO/MB dye mixture solutions (b) before and (c) after the removal experiment.

3.7.5. Heavy metal removal performance of HPβCD100/PBA-a25/CTR15 composite nanofibers

Several common metal ion (Cd^{+2}, Cu^{+2}, Mn^{+2} , Ni^{+2} , Pb^{+2} , Zn^{+2}) aqueous solutions were perapared to test the metal ion removal performance of HPβCD100/PBA-a25/CTR15 composite nanofibers. Experiment was conducted in two parts. First, solution was prepared by mixing all metal ions so that the concentration of the each meal ion to be 1 ppm in the mixture solution. Then, 1ppm solutions were prepared from each metal ion separately and removal experiments were performed by shaking the the solutions over night (12 hours) at room temperature. After the experiments HPβCD100/PBA-a25/CTR15 composite nanofibers were removed from the solution and

the remaining metal ion concentration was measured by ICP-MS. Figure 80 represents the metal ion removal efficiency of HPβCD100/PBA-a25/CTR15 composite nanofibers calculated from the ICP-MS results. As it is observed from the graphs, removal efficiency of HPβCD100/PBA-a25/CTR15 composite nanofibers showed similar behaviour to all metal ions in both case, however in the case of removal experiment performed in seperate metal solutions higher removal efficiency was observed. Table 10 summarizes the removal efficiency of HPβCD100/PBA-a25/CTR15 composite nanofibers in mixture and separate metal ion solutions. Although HPβCD100/PBA-a25/CTR15 composite nanofibers have capability to remove each metal ion, they showed higher tendency to remove Cu^{+2} and Pb^{+2} ions.

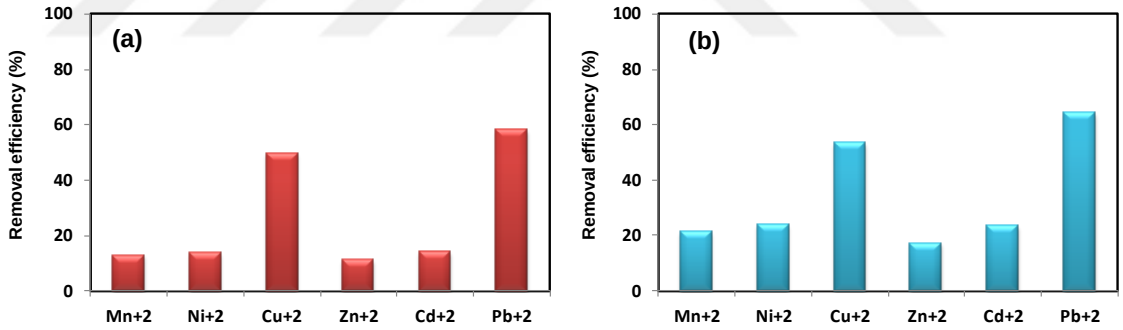

Figure 80. Heavy metal removal efficiency of the HPβCD100/PBA-a25/CTR15 composite nanofibers in (a) mixture metal ion solution and (b) separate solution of each metal ion.

Table 10. Heavy metal ion removal efficiency of the HPβCD100/PBA-a25/CTR15 composite nanofibers in the mixture and separate solutions of metal ions.

	Mn^{+2}	Ni^{+2}	Cu^{+2}	Zn^{+2}	Cd^{+2}	Pb^{+2}
Mixture solution	12.51	13.58	49.63	11.14	14.18	58.0
Separate solution	21.24	23.68	53.56	17.2	23.27	63.99

3.8. Water insoluable HPβCD nanofibers by fully bio-based benzoxazine

In our previous study, common benzoxazine monomer, BA-a was used as a cross-linking agent to obtain water insoluable HPβCD/PBA-a composite nanofibers after curing. Production of water insoluable nanofibers was achieved after optimizing the CD, BA-a and CTR concentrations and curing process. Since CDs are non-toxic and natural compounds, we aimed to provide cross-linking by using fully bio-based benzoxazines. In this tudy, recently synthesized novel bio-based benzoxazine obtained from the eugenol and furfurylamine was used as across-linking agent. HPβCD was chosen as a CD type because HPβCD based nanofibers showed higher thermal stability.

3.8.1. Structural characterization of the eugenol and furfurylamine based fully bio-benzoxazine monomer (E-f)

Fully bio-based benzoxazine monomer was synthesized from naturally occuring compounds eugenol and furfurylamine by solventless method (Figure 81). Reaction was carried out at 110 °C for 2 hours and cinemon like colour benzoxazine denoted as E-f was obtained. The structure of E-f was confirmed by ^{1}H-NMR spectroscopy. Figure 82 represents the ^{1}H-NMR spectra of eugenol and E-f. As it is observed, the characteristic benzoxazine resonance bands attributed to the O-CH_2-N and the Ph-CH_2-N methylene of the oxazine ring were observed at 5.09 ppm and 4.01 ppm, respectively (Figure 82b).

Existence of these peaks with the 1:1 ratio was the evidence for the synthesis of E-f. In addition resonance band at 8.7 ppm attributed to the OH proton of the eugenol was not observed in the ^{1}HNMR spectrum of E-f demonstrating the OH group of the eugenol was contributed highly the oxazine ring formation and E-f is obtained almost eugenol free. In addition, all the protons found in the molecular structure of E-f is shown detailed on its ^{1}HNMR spectrum confirming the synthesis of desired E-f.

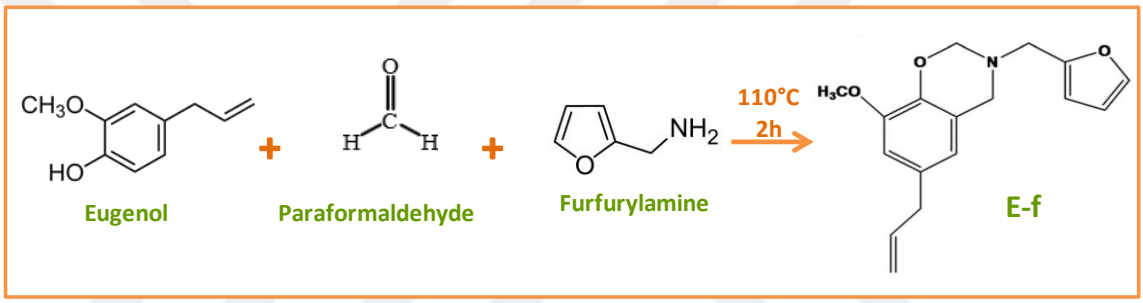

Figure 81. Synthesis of E-f.

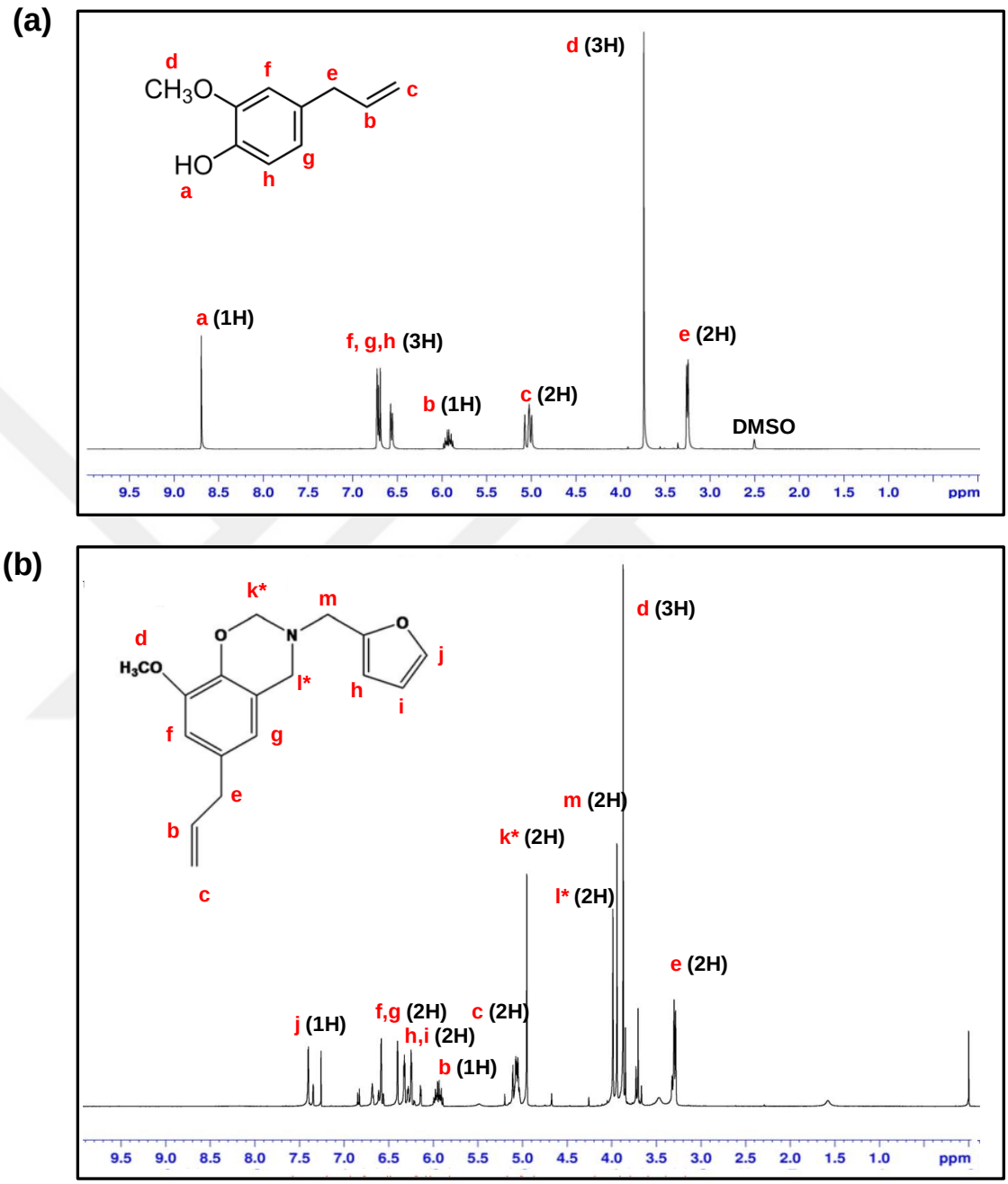

Figure 82. ^{1}H NMR spectra of (a) eugenol in d*6*-DMSO and (b) E-f in $CDCl_3$.

3.8.2. Electrospinning of HPβCD/E-f composite nanofibers

In our previous study, we observed that HPβCD is the more durable CD type for thermal treatment, therefore we have chosen HPβCD for the production of water insoluble cyclodextrin nanofibers. In order to produce HPβCD/E-f composite nanofibers, different electrospinning solutions were prepared with the composition of HPβCD/E-f/CTR as follow; 100:20:10, 100:20:15, 100:25:10 % (w:w:w/v). Bead free nanofibers were obtained from all compositions not surprisingly, because we have already optimized the concentration of the HPβCD and benzoxazine monomer in the previous study. Obtained nanofibers from these solutions were denoted as HPβCDx/E-f-y/CTR, where x, y and z are the concentrations of the HPβCD, E-f and CTR in the mixture solution, respectively. SEM images of the nanofibers obtained from HPβCD100/E-f-20/CTR10, HPβCD100/E-f-20/CTR15 and HPβCD100/E-f-25/CTR10 mixture solutions given in Figure 83 showing the bead free and uniform nanofibers were obtained.

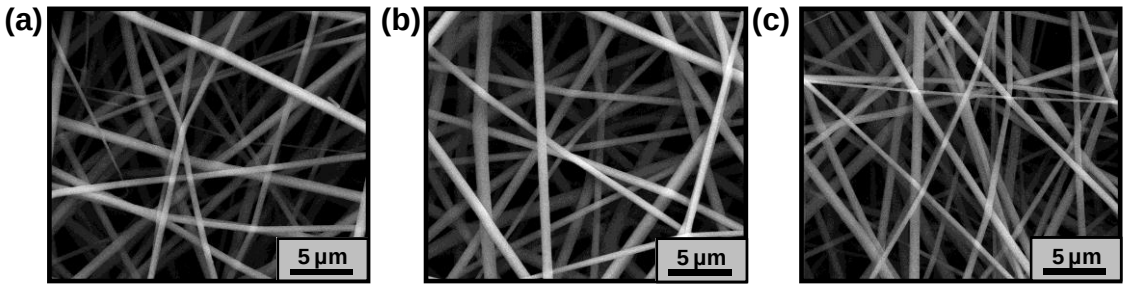

Figure 83. SEM images of (a) HPβCD100/E-f-20/CTR10, (b) HPβCD100/E-f-20/CTR15 and (c) HPβCD100/E-f-25/CTR10 composite nanofibers.

3.8.3. Morphological characterization of the HPβCD/E-f composite nanofibers after thermal curing

In order to produce water insoluable nanofibers, HPβCD100/E-f-20/CTR10, HPβCD100/E-f-20/CTR15 and HPβCD100/E-f-25/CTR10 composite nanofibers were cured step-wise at following temperatures; 140, 160, 180, 200 and 220°C. As a result, HPβCD100/PE-f-20/CTR10, HPβCD100/PE-f-20/CTR15 and HPβCD100/PE-f-25/CTR10 composite nanofibers were obtained. As it was obseved from the SEM images of the cured nanofibers given in Figure 84, HPβCD100/E-f-20/CTR15 composite nanofibers were preserved the fiber morhlogy perfectly wheares some deteoration were observed for HPβCD100/PE-f-20/CTR10 and HPβCD100/PE-f-25/CTR10 composite nanofibers.

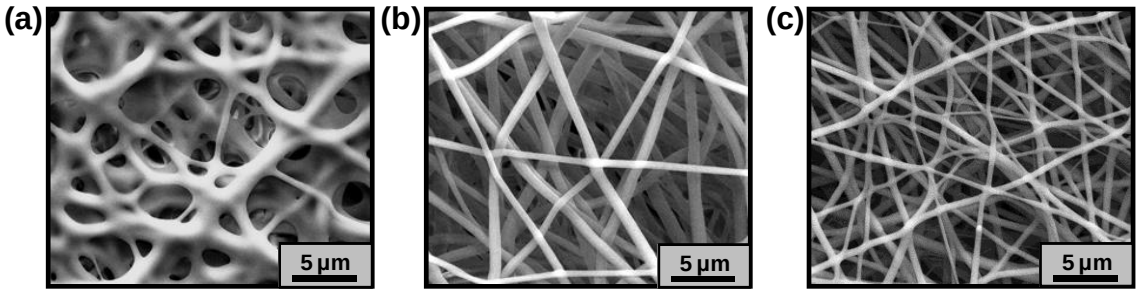

Figure 84. SEM images of (a) HPβCD100/PE-f-20/CTR10, (b) HPβCD100/PE-f-20/CTR15 and (c) HPβCD100/PE-f-25/CTR10 composite nanofibers cured step-wise at 140, 160, 180, 200 and 220°C.

In addition, these nanofibers were tested in liquid media by immersing HPβCD100/PE-f-20/CTR10, HPβCD100/PE-f-20/CTR15 and HPβCD100/PE-f-25/CTR10 composite

nanofibers in water. It is observed that the HPβCD100/E-f-20/CTR15 composite nanofibers were more stable than the others. It maintained the mechanical integrity and did not dissolve in water after overnight immersing. However, HPβCD100/PE-f-20/CTR10 and HPβCD100/PE-f-25/CTR10 composite nanofibers lost their integrity and almost dissolved most probably use of less amount of CTR during the production of nanofibers these nanofibers resulted with insufficient cross-linking during the curing.

3.8.4. Heavy metal removal performance of HPβCD100/E-f-20/CTR15 composite nanofibers

Several common metal ion (Cd^{+2}, Cu^{+2}, Mn^{+2} , Ni^{+2} , Pb^{+2} , Zn^{+2}) aqueous solutions were perapared to test the metal ion removal performance of HPβCD100/E-f-20/CTR15 composite nanofibers. Experiment was conducted in two parts. First, solution was prepared by mixing all metal ions so that the concentration of the each meal ion to be 1 ppm in the mixture solution. Then, 1ppm solutions were prepared from each metal ion separately and removal experiments were performed by shaking the the HPβCD100/E-f-20/CTR15 composite nanofibers including solutions over night (12 hours) at room temperature. After the experiments nanofibers were removed from the solution and the remaining metal ion concentration was measured by ICP-MS. Figure 85 represents the metal ion removal efficiency of HPβCD100/E-f-20/CTR15 composite nanofibers calculated from the ICP-MS results. As it is observed from the graphs, removal efficiency of HPβCD100/E-f-20/CTR15 composite nanofibers showed similar behaviour to all metal ions in both case, however in the case of removal experiment

performed in seperate metal solutions higher removal efficiency was observed. Table 11 summarizes the removal efficiency of HPβCD100/E-f-20/CTR15 composite nanofibers in mixture and separate metal ion solutions. Although HPβCD100/E-f-20/CTR15 composite nanofibers have capability to remove each metal ion, they showed higher tendency to remove Cu^{+2} and Pb^{+2} ions with the removal efficiencies of 80 and 84%, respectively.

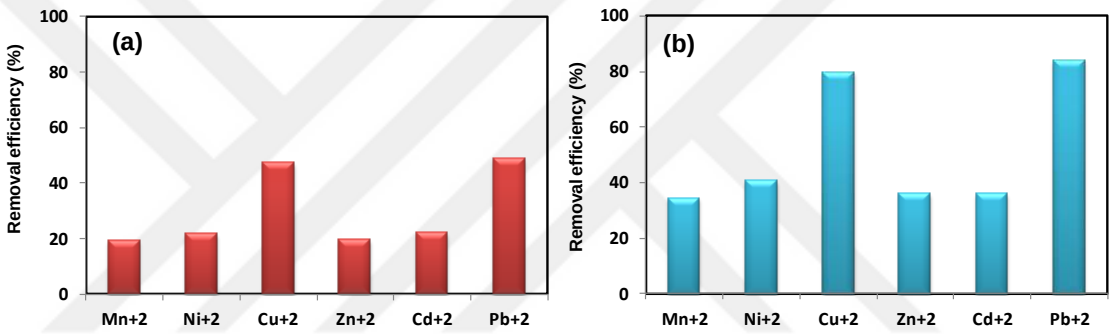

Figure 85. Heavy metal removal efficiency of the HPβCD100/E-f-20/CTR15 composite nanofibers in (a) mixture metal ion solution and (b) separate solution of each metal ion.

Table 11. Heavy metal ion removal efficiency of the HPβCD100/E-f-20/CTR15 composite nanofibers in mixture and separate solutions of metal ions.

	Mn^{+2}	Ni^{+2}	Cu^{+2}	Zn^{+2}	Cd^{+2}	Pb^{+2}
Mixture solution	19.12	22.09	48.23	19.94	22.85	49.13
Separate solution	35.14	41.08	80.52	36.02	36.27	84.01

4. CONCLUSION AND FUTURE PROSPECTS

In this dissertation, initially novel bio-benzoxazine monomers were synthesized from naturally existing phenolic compounds eugenol and thymol. In both case, three different amines with different functionalities, ethyl amine (aliphatic), aniline (aromatic) and 1,6-diaminohexane (di-functional aliphatic) were used to investigate the effect of the functionality of amine on the curig process and the properties of the cured polybenzoxazines. Since this study was considered as a priliminary study of this dissertation, all characterizations related with both synthesis of bio-benzoxazine monomers and polymerization of these monomers by step-wise thermal curing were done detailed to understand the basic concepts of benzoxazine chemistry. Although petroluem based products were used widely for the synthesis of benzoxazine monomers, bio-benzoxazine monomers attracted more attention most recently, thus novel benzoxazines were synthesized from naturally occuring phenolic compounds. Molecular structural characterizations of the novel eugenol and thymol based bio-benzoxazine monomers were performed by ^{1}H NMR and FTIR spectroscopies confirming the synthsesis of desired bio-benzoxazine molecules. Curing studies of all eugenol and thymol based bio-benzoxazines were carried out step-wise at same temperature range (150-250ºC). According to the FTIR spectra recorded at each step of curing of all bio-benzoxazines, opening and coss-linking of the oxazine ring was achieved by heating up to 250ºC. Although, no significant difference was observed on the curing process and thermal properties of cured samples having different amine

groups, remarkable difference was observed for the cured samples obtained from different phenolic compound. In brief, eugenol based bio-benzoxazine monomers showed significantly high char yield, presumably the contribution of the allyl groups of eugenol to coss-linking reactions resulted with higher coss-linked density.

In Chapter 2, we focus on the production of nanofibers from polybenzoxazine resins without using polymeric carrier matrix. For this purpose, main-chain polybenzoxazines (MCPBz) were preferred since chain entanglement and overlappings are the main factors affecting the formation of nanofibers. Here, two different MCPBz were synthesized from of bisphenol-A, paraformaldehyde, 1,6-diaminohexane (6C) and 1,12-diaminododecane (12C) having different lenght of aliphatic chain and denoted as PBA-ad6 and PBA-ad12, respectively. Then, first time we achieved to produce bead-free and uniform PBA-ad6 or PBA-ad12 nanofibers from MCPBz. Although, both nanofibers were obtained as free standing nanofibers, PBA-ad12 nanofibers were more flexible than PBA-ad6 nanofibers possibly the longer aliphatic chain structure and higher molecular weight. The fibrous structure could not be preserved during the thermal curing of PBA-ad6 and PBA-ad12 nanofibrous mats due to the low melting point of these MCPBz, yet, flexible and free standing cross-linked films were obtained. As this is being the starting point of the electrospinning of polybenzoxazines without using carrier polymer matrix, this study provides the essential guidance for the production of nanofibers from different types of polybenzoxazines. In the second study, we demonstrated the feasibility of the cross-linking of polybenzoxazine based electrospun nanofibers obtained from the main-

chain polybenzoxazines (MCPBz) with long aliphatic chain by two-step curing. The structure of the MCPBz were tailored to be able to crosslink through UV-light initiated free radical polymerization and thermally induced ring-opening reactions, and as a result DHBP-ad6 and DHBP-ad12 resins having aliphatic chain length were synthesized. Bead-free and uniform nanofibers were obtained from both MCPBz. DSC measurements indicated that melting transition peak of as-electrospun MCPBz nanofibers were disappeared after photo curing illustrating the enhancement of the thermal stability of MCPBz nanofibers. In addition, SEM images of the photo and thermal-cured nanofibers show that the fiber morphology was preserved after each step of curing. Although characteristic absorbance peaks of the benzoxazine structure were observed after photo curing, those peaks were disappeared during the thermal curing verifying the achievement of ring-opening and cross-linking only by thermal curing. Moreover, TGA thermograms of DHBP-ad6 and DHBP-ad12 nanofibers show that the Td onset and char yield of the MCPBz nanofibers increased only through thermal curing. Furthermore, DMA analysis illustrated that cross-linked DHBP-ad6 and DHBP-ad12 nanofibers have quite high Young's modulus (2070 ± 243 and 264 ± 59.66 MPa, respectively) and tensile stress (22.53 ± 2.04 and 15.29 ± 2.48 MPa, respectively) compared to the previously reported MCPBz nanofibrous web. Also, tensile strain of the cross-linked DHBP-ad12 nanofibers was significantly higher than the cross-linked DHBP-ad6 nanofibers suggesting the longer aliphatic chain length probably has increased the flexibility of nanofibers resulted in higher elongation at break. Besides, solubility and

stability experiments demonstrated that these nanofibers preserved the fibrous structure and mechanical integrity in good solvents (chloroform, DMF, 1,4-dioxane, DMAc and THF), highly concentrated (5M) strong acids (HCl, HNO_3, H_2SO_4) and at high temperatures (400°C). In brief, we obtained highly cross-linked thermoset nanofibrous polybenzoxazine-based materials with good mechanical and thermal properties and high stability in organic solvents and harsh acidic conditions. We anticipate that these properties may be quite useful for the certain applications requiring high temperatures and harsh acidic conditions or organic solvents.

In Chapter 3, composite nanofibers were produced from polymer and benzoxazine mixture solutions to enhance the thermal and mechanical properties of thermoplastic polymers. For this purpose, we have chosen two thermoplastic polymer cellulose acetate (CA) and polycarbonate (PC). Initially we achieved to produce CA/BA-a composite nanofibers by varying the concentration of CA (10 and 12 % (w/v)) and BA-a (2 and 5 % (w/v)) in the electrospinning solution and we obtained bead-free nanofibers from the composition of CA10/BA-a5 mixture solution. However, we observed that cured nanofibers are soluble in DCM and methanol in which the homogenous electrospinning solutions were prepared to produce electrospun nanofibers. Therefore, 1% CTR was added as a cross-linking agent into the CA10/BA-a5 mixture solution in order to obtain the insoluble composite nanofibers. In this case, production of insoluable CA10/PBA-a5/CTR1 composite nanofibers were achieved. Structural characterization of the cured composite nanofibers were performed by FTIR spectroscopy revaling the opening and

the cross-linking of the oxazine ring in the structure of the composite nanofibers were achieved by thermal curing. In addition, morphology of the composite nanofibers were preserved during the thermal curing. Moreover, fluffy structure of the CA nanofibers which partially limits the usage of these materials as a membrane transformed the smoth and flat form which is more handable than the initial form. Furthermore, we observed enhancement in thermal and mechanical properties of the CA nanofibers. Although, slight increase from 243 to 247ºC was observed in the thermal decomposition onset of CA nanofibers by production of composite nanofibers, significant increase from 12.2 to 24.7% was detected in the char yield. In addition, according to the DMA measurements, remarkable enhancement was observed after the cross-linking achieved by thermal curing. Tensile strength, ultimate tensile stress and Young's modulus of the CA10/BA-a5/CTR1 measured as 2.42±0.75 MPa, 3.54±0.96 %, 93.01±30.79 MPa, respectively and these values for CA10/PBA-a5/CTR1 measured as 8.64±0.63 MPa, 8.93±0.12 %, 213.87±30.79 MPa, respectively. Finally, polyaromatic hydrocarbons entrapment efficiency of CA10/BA-a5/CTR1 composite nanofibers were investigated by phenatherene. We observed that, CA10/PBA-a5/CTR1 composite nanofibers removed the 98.5% of the initial concentration of the phenanthrene after 3 hours, wheares CA nanofibers removed the 92% of that. Here, we can conclude that not only thermal and mechanical properties of the CA nanofibers were improved but also moleculer filtration efficiency of CA nanofibers was enhanced by production of CA10/PBA-a5/CTR1 composite nanofibers which can be a very promising high performance membrane

material for the removal of PAHs from the waste water. Then, as a second study we produced PC/BA-a composite nanofibers by varying the concentration of PC (18 and 20 % (w/v)), BA-a (3, 5 and 7 % (w/v)) and CTR (2% (w/v)) in the electrospinning solution. We obtained bead-free and uniform nanofibers from the composition of PC20/BA-a5/CTR2 mixture solution and we performed curing studies by heating step-wise at 100, 120, 140 and 160ºC. Since PC has melting temperature at around 155ºC, nanofibrous structure could not preserved when the PC20/BA-a5/CTR2 nanofibers were heated up to 160ºC, so final curing temperature determined to be 140ºC. Although, some deformations were observed in the PC20/BA-a5/CTR2 composite nanofibers, nanofibrous structure was preserved curing at 140ºC. FTIR analysis demonstarted that opening and cross-linking of the oxazine ring was achieved by heating up to 140ºC. Also, solubility test of PC20/BA-a5/CTR2 composite nanofibers in DMF and THF show that insoluable composite nanofibers were obtained. Thermal properties PC20/BA-a5/CTR2 composite nanofibers were investigated by TGA demonstrating the remarkable enhancement in the main degradation temperature of the PC nanofibers which was shifted to 503 from 465ºC owing to the production of PC20/BA-a5/CTR2 composite nanofibers. In addition, great improvement was observed in the thermomechanical properties of PC nanofibers. Even, we were not able to measure the thermomechanical properties of the pure PC nanofibers owing to the fluffy structure, we observed enhancement in the thermomechanical properties of the PC20/BA-a5/CTR2 composite nanofibers with increasing cure temperature from 120 to 140ºC. While the initial storage

modulus of PC20/BA-a5/CTR2 composite nanofibers were measured as 20 MPa in the glassy region, it was measured as 71 and 124 MPa after heating up to 120 and 140ºC, respectively. Also, thermal transition temperature of the PC20/BA-a5/CTR2 composite nanofibers shifted to higher temperature indicating the enhancement in Tg with increasing of curing temperature. These results show that we achieved to enhance thermomechanical properties of the PC nanofibers by producing PC20/BA-a5/CTR2 composite nanofibers which can be a high performance filtration material due to the highly porous nanofibrous structure and great thermomechanical properties.

In Chapter 4, we focus on the production of water insoluble CD nanofibers by producing composite nanofibers with benzoxazine monomers (BA-a and E-f). Firstly we optimized the concentration of the CDs and BA-a in order to obtain water insoluable CDs nanofibers through thermal curing of the electrospun nanofibers. Although, we were able to produce uniform nanofibers from each type of CD derivatives, we observed that during the thermal curing which performed up to 200ºC, HPγCD100/BA-a25 and MβCD125/BA-a25 composite nanofibers could not preserve the initial fiber morpholgy even MβCD125/BA-a25 composite nanofibers melted while HPβCD100/BA-a25 composite nanofibers were still maintaining the fibrous structure. However, at higher temperatures (225ºC) HPβCD100/BA-a25 composite nanofibers also could not preserve the fiber structure. Even though, HPβCD100/BA-a25 composite nanofibers deteriorated at 225ºC, they were the most durable CD/BA-a composite nanofibers, thus, further studies were performed with HPβCD100/BA-a25 composite nanofibers. In order to

enhance their curing ability while retaining the fiber structure 5 and 15% (w/v) CTR was added as a cross-linking agent into the HPβCD100/BA-a25 mixture solution and curing studies were performed up to 225ºC. We observed that addition of CTR improved their curing process and after the curing fibrous structure of the HPβCD100/BA-a25/CTR5 and HPβCD100/BA-a25/CTR15 composite nanofibers. On the other hand, when these composite nanofibers immersed in water 5% (w/v) CTR including composite nanofibers dissolved rapidly while 15% (w/v) CTR including nanofibers were stable over night in the water indicating the achivement of cross-linking only with 15% (w/v) CTR. In addition to the water, HPβCD100/PBA-a25/CTR15 composite nanofibers were stable in acetone, ACN, chloroform, DCM, DMF, DMSO, ethanol, methanol and THF as well. Although, most of them are very good solvents for the CDs, being stable at overnight in these solvents showing the succesful production of the insoluable HPβCD100/PBA-a25/CTR15 composite nanofibers. Since these nanofibers were insoluable in various solvents and having the both attractive properties of nanofibers (high surface area, porous structure, so on) and CDs (inclusion complex formation), their molecular entrapment efficiency to the PAHs (phenanthrene, fluoranthene and pyrene) and dye molecules (methylene blue, methyl orange) were tested in aqueous solutions. It was observed that HPβCD100/PBA-a25/CTR15 composite nanofibers are promising material for the removal of phenanthrene, fluoranthene and pyrene with the removal efficiency range 80-85% in three different concentration solutions of PAHs (200, 400 and 600 ppb). Also HPβCD100/PBA-a25/CTR15 composite nanofibers showed

selective adsorption of the MB dye molecules most probably in both case dimensional fit and specific interaction between CD and PAH/dye molecules were dominant effect on the removal of molecules. Finally the adsorption experiments were performed with several metal ions (Cd^{+2}, Cu^{+2}, Mn^{+2} , Ni^{+2} , Pb^{+2} and Zn^{+2}) in order to investigate if HPβCD100/PBA-a25/CTR15 composite nanofibers have capacity to remove heavy metal ions. It was observed that HPβCD100/PBA-a25/CTR15 composite nanofibers also able to remove all these metal ions in some extend but their efficiency was higher for the adsorption of Cu^{+2} and Pb^{+2} showing their selectivity to these metal ions. Most probably, electrsotatic interactions between these ions and O containing group of CDs were sufficient or more effective than the other metal ions. In brief, we achieved to produce water insoluable HPβCD100/PBA-a25/CTR15 composite nanofibers having high surface area and porous structure which can be very attractive material for the waste water treatment. As a second study of this chapter, HPβCD/E-f/CTR composite nanofibers were produced from different composition of HPβCD/E-f/CTR (100:20:10, 100:20:15, 100:25:10 % (w:w:w/v)). Even though, bead free and uniform nanofibers were obtained each composition, HPβCD/E-f/CTR composite nanofibers having the ratio of 100:20:15 (w:w:w/v) were more stable during the thermal curing indicating the higher cross-linked density achieved for this composition. In addition, its high stability in water demostrated the succesful production of water insoluable HPβCD100/E-f20/CTR15 composite nanofibers. Then, these composite nanofibers were used as an adsorbant to examine the heavy metal removal efficiency and it was observed that these

nanofibers were able to remove all metal ions (Cd^{+2}, Cu^{+2}, Mn^{+2} , Ni^{+2} , Pb^{+2} and Zn^{+2}) some extend from the 1ppm solutions, yet showing the highest removal efficiency of Pb^{+2} and Cu^{+2} ions with the removal efficiencies of 80 and 84%, respectively.

In summary, in this dissertation, we were able to produce high performance polybenzoxazine based nanofibers by two approach. In the first aproach, we produced MCPBz nanofibers without blending with any polymeric carrier matrix. Then, we improved the curing process by designing the structure of MCPBz and we were able to produce cross-linked MCPBz nanofibers which are highly cross-linked thermoset nanofibrous polybenzoxazine-based materials with good mechanical and thermal properties. Also they are highly stable in organic solvents and harsh acidic conditions which make these materials quite useful for the certain applications requiring high temperatures and harsh acidic conditions or organic solvents. In the second approach, we produced polybenzoxazine based composite nanofibers from both polymeric materials and non-polymeric systems (cyclodextrins) with enhanced thermal and mechanical properties. Also, some of the polybenzoxazine based composite nanofibers showed high efficiency for the removal of PAHs, dye molecules and heavy metal ions indicating that these cross-linked polybenzoxazine based composite nanofibers have potential to be used as an adsorbant material for the waste water treatment.

LIST OF PUBLICATINS

Book Chapter

1) **Yelda Ertas** and Tamer Uyar "Polybenzoxazine based nanofibers by electrospinning", Advanced and emerging polybenzoxazine science and technology, PART VI, Chapter 33, Ishida, H. Ed., Elsevier, Amsterdam, 2017. (in press)

Publications from thesis studies

2) **Yelda Ertas** and Tamer Uyar* "Cross-linked main-chain polybenzoxazine nanofibers by photo and thermal curing: stable at high temperatures and harsh acidic conditions" Polymer, 84, 72-80, 2016. DOI:10.1016/j.polymer.2015.12.026

3) **Yelda Ertas** and Tamer Uyar*, "Main-chain polybenzoxazine nanofiber via electrospinning" Polymer, 55, 556-564, 2014. DOI:10.1016/j.polymer.2013.12.018.

4) **Yelda Ertas** and Tamer Uyar, "Cellulose acetate/polybenzoxazine composite nanofibers with enhanced polyaromatic hydrocarbons adsorption efficiency". (ready for submission)

5) **Yelda Ertas,** Asli Celebioglu and Tamer Uyar, "Heavy metal, polyaromatic hydrocarbon and dye removal performance of cross-linked HPβCD/Polybenzoxazine composite annofibers". (ready for submission)

6) **Yelda Ertas** and Tamer Uyar, "Novel bio-based benzoxazine monomers from naturally occuring phenolic compounds, thymol and eugenol". (ready for submission)

7) **Yelda Ertas,** Asli Celebioglu and Tamer Uyar, "Selective dye removal performance of cross-linked HPβCD/Polybio-benzoxazine composite nanofibers composite nanofibers from waste waters ". (in preparation)

8) **Yelda Ertas** and Tamer Uyar, "Polycarbonate/Polybenzoxazine composite nanofibers with enhanced mechanical properties ". (in preparation)

Others

9) Sesha Vempati*, **Yelda Ertas**, Veluru Jagadeesh Babu*, and Tamer Uyar*, Optoelectronic Properties of Layered Titanate Nanostructure and Polyaniline Impregnated Devices, Chem Phys Chem, cphc.201600950. (under revision)

10) Veluru Jagadeesh Babu*, Sesha Vempati*, **Yelda Ertas** and Tamer Uyar*, "Excitation dependent recombination studies on SnO_2/TiO_2 electrospun nanofibers", RSC Advances, 5, 66367-66375, 2015. DOI: 10.1039/C5RA09787H

11) Sesha Vempati*, **Yelda Ertas** and Tamer Uyar*, "Sensitive Surface States and their Passivation Mechanism in CdS Quantum Dots" The Journal of Physical Chemistry C, 117, 21609-21618, 2013. DOI: 10.1021/jp408160h

12) Fatma Kayaci, **Yelda Ertas** and Tamer Uyar* "Enhanced thermal stability of Eugenol by Cyldextrin Inclusion Complex Encapsulated in Electrospun Polymeric Nanofibers" Journal of Agricultural and Food Chemistry, 61, 8156–8165, 2013. DOI: 10.1021/jf402923c

BIBLIOGRAPHY

[1] A. Knop, L.A. Pilato, Phenolic resins: chemistry, applications and performance. 2013: Springer Science & Business Media.

[2] X. Ning, H. Ishida, Phenolic materials via ring-opening polymerization: Synthesis and characterization of bisphenol-A based benzoxazines and their polymers, Journal of Polymer Science Part A: Polymer Chemistry 32 (1994) 1121-1129.

[3] F.W. Holly, A.C. Cope, Condensation products of aldehydes and ketones with o-aminobenzyl alcohol and o-hydroxybenzylamine, Journal of the American Chemical Society 66 (1944) 1875-1879.

[4] W.J. Burke, J. Bishop, E.M. Glennie, W. Bauer Jr, A new aminoalkylation reaction. Condensation of phenols with dihydro-1, 3-aroxazines1, The Journal of Organic Chemistry 30 (1965) 3423-3427.

[5] W.J. Burke, E.M. Glennie, C. Weatherbee, Condensation of Halophenols with Formaldehyde and Primary Amines1, The Journal of Organic Chemistry 29 (1964) 909-912.

[6] W. J. Burke, K. Murdock, G. Ec, Condensation of hydroxyaromatic compounds with formaldehyde and primary aromatic amines, Journal of the American Chemical Society 76 (1954) 1677-1679.

[7] W.J. Burke, R.P. Smith, C. Weatherbee, N, N-bis-(hydroxybenzyl)-amines: synthesis from phenols, formaldehyde and primary amines1, Journal of the American Chemical Society 74 (1952) 602-605.

[8] W.J. Burke, M.J. Kolbezen, C.W. Stephens, Condensation of Naphthols with Formaldehyde and Primary Amines1, Journal of the American Chemical Society 74 (1952) 3601-3605.

[9] W.J. Burke, C.W. Stephens, Monomeric products from the condensation of phenol with formaldehyde and primary amines, Journal of the American Chemical Society 74 (1952) 1518-1520.

[10] W.J. Burke, C. Weatherbee, 3, 4-Dihydro-1, 3, 2H-Benzoxazines. Reaction of Polyhydroxybenzenes with N-Methylolamines1, Journal of the American Chemical Society 72 (1950) 4691-4694.

[11] H.P. Higginbottom, Polymerizable compositions comprising polyamines and poly (dihydrobenzoxazines). 1985, Google Patents.

[12] H.P. Higginbottom, M.F. Drumm, Process for deposition of resin dispersions on metal substrates. 1985, Google Patents.

[13] H.P. Higginbottom, M.F. Drumm, Aqueous dispersions of polyamines and poly (dihydrobenzoxazines). 1985, Google Patents.

[14] G. Reiss, J. Schwob, G. Guth, M. Roche, B. Lande, In Advances in Polymer Synthesis; Culbertson, BM, McGrath, JE, Eds. 1985, Plenum: New York.

[15] E.T. Turpin, D.T. Thrane, Self-curable benzoxazine functional cathodic electrocoat resins and process. 1988, Google Patents.

[16] H. Ishida, T. Agag, Handbook of Benzoxazine Resins. 2011, Netherlands: Elsevier.

[17] K.D. Demir, B. Kiskan, S.S. Latthe, A.L. Demirel, Y. Yagci, Thermally curable fluorinated main chain benzoxazine polyethers via Ullmann coupling, Polymer Chemistry 4 (2013) 2106-2114.

[18] K.D. Demir, B. Kiskan, B. Aydogan, Y. Yagci, Thermally curable main-chain benzoxazine prepolymers via polycondensation route, Reactive & Functional Polymers 73 (2013) 346-359.

[19] C. Sawaryn, K. Landfester, A. Taden, Advanced chemically induced phase separation in thermosets: Polybenzoxazines toughened with multifunctional thermoplastic main-chain benzoxazine prepolymers, Polymer 52 (2011) 3277-3287.

[20] K.D. Demir, M.A. Tasdelen, T. Uyar, A.W. Kawaguchi, A. Sudo, T. Endo, Y. Yagci, Synthesis of Polybenzoxazine/Clay Nanocomposites by In Situ Thermal Ring-Opening Polymerization Using Intercalated Monomer, Journal of Polymer Science Part a-Polymer Chemistry 49 (2011) 4213-4220.

[21] K.D. Demir, B. Kiskan, Y. Yagci, Thermally Curable Acetylene-Containing Main-Chain Benzoxazine Polymers via Sonogashira Coupling Reaction, Macromolecules 44 (2011) 1801-1807.

[22] S. Bagherifam, B. Kiskan, B. Aydogan, Y. Yagci, J. Hacaloglu, Thermal degradation of polysiloxane and polyetherester containing benzoxazine moieties in the main chain, Journal of Analytical and Applied Pyrolysis 90 (2011) 155-163.

[23] C. Altinkok, B. Kiskan, Y. Yagci, Synthesis and Characterization of Sulfone Containing Main Chain Oligobenzoxazine Precursors, Journal of Polymer Science Part a-Polymer Chemistry 49 (2011) 2445-2450.

[24] L. Jin, T. Agag, Y. Yagci, H. Ishida, Methacryloyl-functional benzoxazine: photopolymerization and thermally activated polymerization, Macromolecules 44 (2011) 767-772.

[25] J. Liu, T. Agag, H. Ishida, Main-chain benzoxazine oligomers A new approach for resin transfer moldable neat benzoxazines for high performance applications, Polymer 51 (2010) 5688-5694.

[26] B. Kiskan, B. Aydogan, Y. Yagci, Synthesis, Characterization, and Thermally Activated Curing of Oligosiloxanes Containing Benzoxazine Moieties in the Main Chain, Journal of Polymer Science Part a-Polymer Chemistry 47 (2009) 804-811.

[27] A. Chernykh, T. Agag, H. Ishida, Synthesis of linear polymers containing benzoxazine moieties in the main chain with high molecular design versatility via click reaction, Polymer 50 (2009) 382-390.

[28] A. Chernykh, T. Agag, H. Ishida, Effect of Polymerizing Diacetylene Groups on the Lowering of Polymerization Temperature of Benzoxazine Groups in the Highly Thermally Stable, Main-Chain-Type Polybenzoxazines, Macromolecules 42 (2009) 5121-5127.

[29] P. Velez-Herrera, K. Doyama, H. Abe, H. Ishida, Synthesis and characterization of highly fluorinated polymer with the benzoxazine moiety in the main chain, Macromolecules 41 (2008) 9704-9714.

[30] A. Sudo, R. Kudoh, H. Nakayama, K. Arima, T. Endo, Selective Formation of Poly(N,O-acetal) by Polymerization of 1,3-Benzoxazine and Its Main Chain Rearrangement, Macromolecules 41 (2008) 9030-9034.

[31] A. Nagai, Y. Kamei, X.S. Wang, M. Omura, A. Sudo, H. Nishida, E. Kawamoto, T. Endo, Synthesis and crosslinking behavior of a novel linear polymer bearing 1,2,3-triazol the main chain by and benzoxazine groups in a step-growth click-coupling reaction, Journal of Polymer Science Part a-Polymer Chemistry 46 (2008) 2316-2325.

[32] B. Kiskan, Y. Yagci, H. Ishida, Synthesis, characterization,, and properties of new thermally curable polyetheresters containing benzoxazine moieties in the main chain, Journal of Polymer Science Part a-Polymer Chemistry 46 (2008) 414-420.

[33] A. Chernykh, J.P. Liu, H. Ishida, Synthesis and properties of a new crosslinkable polymer containing benzoxazine moiety in the main chain, Polymer 47 (2006) 7664-7669.

[34] B. Kiskan, Y. Yagci, Synthetic Strategies to Combine High Performance Benzoxazine Thermosets with Polymers, in Polychar-18 World Forum on Advanced Materials, W. Mormann, Editor. 2010. p. 145-153.

[35] Y. Yagci, B. Kiskan, N.N. Ghosh, Recent Advancement on Polybenzoxazine-A Newly Developed High Performance Thermoset, Journal of Polymer Science Part a-Polymer Chemistry 47 (2009) 5565-5576.

[36] X. Ning, H. Ishida, Phenolic materials via ring-opening polymerization of benzoxazines: Effect of molecular structure on mechanical and dynamic mechanical properties, Journal of Polymer Science Part B: Polymer Physics 32 (1994) 921-927.

[37] C.H. Lin, H.T. Lin, J.W. Sie, K.Y. Hwang, A.P. Tu, Facile, one-pot synthesis of aromatic diamine-based phosphinated benzoxazines and their flame-retardant thermosets, Journal of Polymer Science Part A: Polymer Chemistry 48 (2010) 4555-4566.

[38] C.H. Lin, S.X. Cai, T.S. Leu, T.Y. Hwang, H.H. Lee, Synthesis and properties of flame-retardant benzoxazines by three approaches, Journal of Polymer Science Part A: Polymer Chemistry 44 (2006) 3454-3468.

[39] C.W. Chang, C.H. Lin, H.T. Lin, H.J. Huang, K.Y. Hwang, A.P. Tu, Development of an aromatic triamine-based flame-retardant benzoxazine and its high-performance copolybenzoxazines, European Polymer Journal 45 (2009) 680-689.

[40] C. Zuniga, M.S. Larrechi, G. Lligadas, J.C. Ronda, M. Galia, V. Cadiz, Phosphorus flame retardant polybenzoxazine foams based on renewable diphenolic acid, Polymer Degradation and Stability 98 (2013) 2617-2626.

[41] H.Q. Yan, C. Sun, Z.P. Fang, X.Q. Liu, J. Zhu, H. Wang, Synthesis of an intrinsically flame retardant bio-based benzoxazine resin, Polymer 97 (2016) 418-427.

[42] S.Q. Huo, J. Wang, S. Yang, B. Zhang, Y.S. Tang, A phosphorus-containing phenolic derivative and its application in benzoxazine resins: Curing behavior, thermal, and flammability properties, Journal of Applied Polymer Science 133 (2016).

[43] T.T. Zhang, W.W. Men, Y. Liu, Z.J. Lu, Synthesis and characterization of polybenzoxazine containing phosphorus, Chinese Journal of Polymer Science 30 (2012) 250-257.

[44] D.X. Wang, B. Li, Y.H. Zhang, Z.J. Lu, Triazine-containing benzoxazine and its high-performance polymer, Journal of Applied Polymer Science 127 (2013) 516-522.

[45] L.K. Lin, C.S. Wu, W.C. Su, Y.L. Liu, Diethylphosphonate-containing benzoxazine compound as a thermally latent catalyst and a reactive property modifier for polybenzoxazine-based resins, Journal of Polymer Science Part a-Polymer Chemistry 51 (2013) 3523-3530.

[46] C.H. Lin, S.X. Cai, T.S. Leu, T.Y. Hwang, H.H. Lee, Synthesis and properties of flame-retardant benzoxazines by three approaches, Journal of Polymer Science Part a-Polymer Chemistry 44 (2006) 3454-3468.

[47] N.N. Ghosh, B. Kiskan, Y. Yagci, Polybenzoxazines - New high performance thermosetting resins: Synthesis and properties, Progress in Polymer Science 32 (2007) 1344-1391.

[48] F. Zuo, X. Liu, Synthesis and curing behavior of a novel benzoxazine-based bisphthalonitrile monomer, Journal of Applied Polymer Science 117 (2010) 1469-1475.

[49] H. Kim, Z. Brunovska, H. Ishida, Synthesis and thermal characterization of polybenzoxazines based on acetylene-functional monomers, Polymer 40 (1999) 6565-6573.

[50] H.J. Kim, Z. Brunovska, H. Ishida, Molecular characterization of the polymerization of acetylene-functional benzoxazine resins, Polymer 40 (1999) 1815-1822.

[51] G. Cao, W. Chen, J. Wei, W. Li, X. Liu, Synthesis and characterization of a novel bisphthalonitrile containing benzoxazine, Express Polymer Letters 1 (2007) 512-518.

[52] Z. Brunovska, H. Ishida, Thermal study on the copolymers of phthalonitrile and phenylnitrile-functional benzoxazines, Journal of Applied Polymer Science 73 (1999) 2937-2949.

[53] Z. Brunovska, R. Lyon, H. Ishida, Thermal properties of phthalonitrile functional polybenzoxazines, Thermochimica acta 357 (2000) 195-203.

[54] A.S. Parveen, P. Thirukumaran, M. Sarojadevi, Low dielectric materials from fluorinated polybenzoxazines, Polymers for Advanced Technologies 25 (2014) 1538-1545.

[55] J. Liu, H. Ishida, High yield synthesis of fluorinated benzoxazine monomers and their molecular characterization, Polymers and Polymer Composites 10 (2002) 191-204.

[56] Z.E.T. Anbin, Synthesis of low dielectric constant benzoxazine [J], New Chemical Materials 1 (2007) 014.

[57] C.H. Lin, S.L. Chang, H.H. Lee, H.C. Chang, K.Y. Hwang, A.P. Tu, W.C. Su, Fluorinated benzoxazines and the structure-property relationship of resulting polybenzoxazines, Journal of Polymer Science Part A: Polymer Chemistry 46 (2008) 4970-4983.

[58] T. Agag, L. Jin, H. Ishida, A new synthetic approach for difficult benzoxazines: Preparation and polymerization of 4, 4′-diaminodiphenyl sulfone-based benzoxazine monomer, Polymer 50 (2009) 5940-5944.

[59] K. Zhang, Q. Zhuang, X. Liu, R. Cai, G. Yang, Z. Han, Synthesis and copolymerization of benzoxazines with low-dielectric constants and high thermal stability, Rsc Advances 3 (2013) 5261-5270.

[60] Y.L. Liu, C.I. Chou, High performance benzoxazine monomers and polymers containing furan groups, Journal of Polymer Science Part A: Polymer Chemistry 43 (2005) 5267-5282.

[61] K. Zhang, Q. Zhuang, Y. Zhou, X. Liu, G. Yang, Z. Han, Preparation and properties of novel low dielectric constant benzoxazole-based polybenzoxazine, Journal of Polymer Science Part A: Polymer Chemistry 50 (2012) 5115-5123.

[62] S. Rimdusit, H. Ishida, Development of new class of electronic packaging materials based on ternary systems of benzoxazine, epoxy, and phenolic resins, Polymer 41 (2000) 7941-7949.

[63] Y.-C. Su, F.-C. Chang, Synthesis and characterization of fluorinated polybenzoxazine material with low dielectric constant, Polymer 44 (2003) 7989-7996.

[64] J. Liu, T. Agag, H. Ishida, Main-chain benzoxazine oligomers: A new approach for resin transfer moldable neat benzoxazines for high performance applications, Polymer 51 (2010) 5688-5694.

[65] Y.X. Wang, H. Ishida, Development of low-viscosity benzoxazine resins and their polymers, Journal of Applied Polymer Science 86 (2002) 2953-2966.

[66] L.W.S.S.Y. Ruilian, Y.C.F. Zhihai, Recent Development of Phenolic Resins for RTM Processing [J], Aerospace Materials & Technology 2 (2004) 003.

[67] P. Yang, Y. Gu, A novel benzimidazole moiety-containing benzoxazine: Synthesis, polymerization, and thermal properties, Journal of Polymer Science Part A: Polymer Chemistry 50 (2012) 1261-1271.

[68] B. Koz, B. Kiskan, Y. Yagci, A novel benzoxazine monomer with methacrylate functionality and its thermally curable (co) polymers, Polymer Bulletin 66 (2011) 165-174.

[69] H. Zhong, Y. Lu, J. Chen, W. Xu, X. Liu, Preparation, characterization, and polymerization of novel maleimidobenzoxazine containing carboxylic moiety and its cocuring behaviors with epoxy resin, Journal of Applied Polymer Science 118 (2010) 705-710.

[70] W. Men, Z. Lu, Z. Zhan, Synthesis of a novel benzoxazine precursor containing phenol hydroxyl groups and its polymer, Journal of Applied Polymer Science 109 (2008) 2219-2223.

[71] R. Andreu, J. Reina, J. Ronda, Carboxylic acid-containing benzoxazines as efficient catalysts in the thermal polymerization of benzoxazines, Journal of Polymer Science Part A: Polymer Chemistry 46 (2008) 6091-6101.

[72] L. Qu, Z. Xin, Preparation and Surface Properties of Novel Low Surface Free Energy Fluorinated Silane-Functional Polybenzoxazine Films, Langmuir 27 (2011) 8365-8370.

[73] J. Liu, X. Lu, Z. Xin, C.L. Zhou, Synthesis and Surface Properties of Low Surface Free Energy Silane-Functional Polybenzoxazine Films, Langmuir 29 (2013) 411-416.

[74] K.C. Chen, H.T. Li, S.C. Huang, W.B. Chen, K.W. Sun, F.C. Chang, Synthesis and performance enhancement of novel polybenzoxazines with low surface free energy, Polymer International 60 (2011) 1089-1096.

[75] K.C. Chen, H.T. Li, W.B. Chen, C.H. Liao, K.W. Sun, F.C. Chang, Synthesis and characterization of a novel siloxane-imide-containing polybenzoxazine, Polymer International 60 (2011) 436-442.

[76] C.S. Liao, J.S. Wu, C.F. Wang, F.C. Chang, Modification of polymer substrates with low surface free energy material by low-temperature cured polybenzoxazine, Macromolecular Rapid Communications 29 (2008) 52-56.

[77] R.C. Lin, M.G. Mohamed, K.C. Hsu, J.Y. Wu, Y.R. Jheng, S.W. Kuo, Multivalent photo-crosslinkable coumarin-containing polybenzoxazines exhibiting enhanced thermal and hydrophobic surface properties, Rsc Advances 6 (2016) 10683-10696.

[78] C.-F. Wang, Y.-T. Wang, P.-H. Tung, S.-W. Kuo, C.-H. Lin, Y.-C. Sheen, F.-C. Chang, Stable superhydrophobic polybenzoxazine surfaces over a wide pH range, Langmuir 22 (2006) 8289-8292.

[79] H.-C. Lin, H.-L. Chang, C.-F. Wang, C.-F. Huang, F.-C. Chang, Polybenzoxazine—silica hybrid surface with environmentally responsive

wettability behavior, Journal of Adhesion Science and Technology 23 (2009) 503-511.

[80] S.-W. Kuo, Y.-C. Wu, C.-F. Wang, K.-U. Jeong, Preparing low-surface-energy polymer materials by minimizing intermolecular hydrogen-bonding interactions, The Journal of Physical Chemistry C 113 (2009) 20666-20673.

[81] V. Kishore, R. Dhanya, K. Sreekumar, R. Joseph, C.S. Kartha, Spectral distribution of photocurrent in poly (6-tert-butyl-3-methyl-3, 4-dihydro-2H-1, 3-benzoxazine), Synthetic Metals 158 (2008) 676-680.

[82] K. Sreekumar, R. Dhanya, V. Kishore, C. Sudha Kartha, J. Rani, Photophysical and Electrochemical Investigations on Photoconducting Poly (6-tert-butyl-3, 4-dihydro-2H-1, 3-benzoxazine), (2009).

[83] D.J. Allen, H. Ishida, Polymerization of linear aliphatic diamine-based benzoxazine resins under inert and oxidative environments, Polymer 48 (2007) 6763-6772.

[84] D.J. Allen, H. Ishida, Physical and mechanical properties of flexible polybenzoxazine resins: Effect of aliphatic diamine chain length, Journal of Applied Polymer Science 101 (2006) 2798-2809.

[85] D.J. Allen, H. Ishida, Effect of phenol substitution on the network structure and properties of linear aliphatic diamine-based benzoxazines, Polymer 50 (2009) 613-626.

[86] K.F. S. Ramakrishna, W. Teo, T. Lim and Z. Ma, , An Introduction to Electrospinning and Nanofibers, . 2005: World Scientific Publishing Company, .

[87] J.H. Wendorff, S. Agarwal, A. Greiner, Electrospinning: Materials, Processing, and Applications. 2012, Germany: Wiley-VCH.

[88] S. Agarwal, A. Greiner, On the way to clean and safe electrospinning—green electrospinning: emulsion and suspension electrospinning, Polymers for Advanced Technologies 22 (2011) 372-378.

[89] J.H. Wendorff, S. Agarwal, A. Greiner, Electrospinning: materials, processing, and applications. 2012: John Wiley & Sons.

[90] S. Ramakrishna, K. Fujihara, W.-E. Teo, T.-C. Lim, Z. Ma, An introduction to electrospinning and nanofibers. Vol. 90. 2005: World Scientific.

[91] A. Greiner, J.H. Wendorff, Electrospinning: a fascinating method for the preparation of ultrathin fibers, Angewandte Chemie International Edition 46 (2007) 5670-5703.

[92] X. Lu, C. Wang, Y. Wei, One-Dimensional Composite Nanomaterials: Synthesis by Electrospinning and Their Applications, Small 5 (2009) 2349-2370.

[93] C. Kriegel, K. Kit, D.J. McClements, J. Weiss, Nanofibers as carrier systems for antimicrobial microemulsions. Part I: fabrication and characterization, Langmuir 25 (2008) 1154-1161.

[94] H.S. Lim, S.H. Park, S.H. Koo, Y.-J. Kwark, E.L. Thomas, Y. Jeong, J.H. Cho, Superamphiphilic janus fabric, Langmuir 26 (2010) 19159-19162.

[95] T. Uyar, P. Kingshott, F. Besenbacher, Electrospinning of cyclodextrin–pseudopolyrotaxane nanofibers, Angewandte Chemie International Edition 47 (2008) 9108-9111.

[96] J. Song, M. Chen, M.B. Olesen, C. Wang, R. Havelund, Q. Li, E. Xie, R. Yang, P. Bøggild, C. Wang, Direct electrospinning of Ag/polyvinylpyrrolidone nanocables, Nanoscale 3 (2011) 4966-4971.

[97] X. Lu, C. Wang, Y. Wei, One-Dimensional Composite Nanomaterials: Synthesis by Electrospinning and Their Applications, Small 5 (2009) 2349-2370.

[98] S. Agarwal, J.H. Wendorff, A. Greiner, Chemistry on electrospun polymeric nanofibers: merely routine chemistry or a real challenge?, Macromolecular rapid communications 31 (2010) 1317-1331.

[99] S. Ramakrishna, K. Fujihara, W.-E. Teo, T. Yong, Z. Ma, R. Ramaseshan, Electrospun nanofibers: solving global issues, Materials Today 9 (2006) 40-50.

[100] H. Fong, I. Chun, D.H. Reneker, Beaded nanofibers formed during electrospinning, Polymer 40 (1999) 4585-4592.

[101] K.H. Lee, H.Y. Kim, H.J. Bang, Y.H. Jung, S.G. Lee, The change of bead morphology formed on electrospun polystyrene fibers, Polymer 44 (2003) 4029-4034.

[102] P. Gupta, C. Elkins, T.E. Long, G.L. Wilkes, Electrospinning of linear homopolymers of poly(methyl methacrylate): exploring relationships between fiber formation, viscosity, molecular weight and concentration in a good solvent, Polymer 46 (2005) 4799-4810.

[103] S.L. Shenoy, W.D. Bates, H.L. Frisch, G.E. Wnek, Role of chain entanglements on fiber formation during electrospinning of polymer solutions: good solvent, non-specific polymer-polymer interaction limit, Polymer 46 (2005) 3372-3384.

[104] J.H. Yu, S.V. Fridrikh, G.C. Rutledge, The role of elasticity in the formation of electrospun fibers, Polymer 47 (2006) 4789-4797.

[105] C. Wang, H.S. Chien, C.H. Hsu, Y.C. Wang, C.T. Wang, H.A. Lu, Electrospinning of polyacrylonitrile solutions at elevated temperatures, Macromolecules 40 (2007) 7973-7983.

[106] T. Uyar, F. Besenbacher, Electrospinning of uniform polystyrene fibers: The effect of solvent conductivity, Polymer 49 (2008) 5336-5343.

[107] C.L. Pai, M.C. Boyce, G.C. Rutledge, Morphology of Porous and Wrinkled Fibers of Polystyrene Electrospun from Dimethylformamide, Macromolecules 42 (2009) 2102-2114.

[108] D. Li, Y. Xia, Electrospinning of nanofibers: reinventing the wheel?, Advanced materials 16 (2004) 1151-1170.

[109] A.E. Deniz, A. Celebioglu, F. Kayaci, T. Uyar, Electrospun polymeric nanofibrous composites containing TiO_2 short nanofibers, Materials Chemistry and Physics 129 (2011) 701-704.

[110] B. Ortaç, F. Kayaci, H.A. Vural, A.E. Deniz, T. Uyar, Photoluminescent electrospun polymeric nanofibers incorporating germanium nanocrystals, Reactive and Functional Polymers 73 (2013) 1262-1267.

[111] J. Andrew, D. Clarke, Enhanced ferroelectric phase content of polyvinylidene difluoride fibers with the addition of magnetic nanoparticles, Langmuir 24 (2008) 8435-8438.

[112] S. Anitha, B. Brabu, D.J. Thiruvadigal, C. Gopalakrishnan, T. Natarajan, Optical, bactericidal and water repellent properties of electrospun nano-composite membranes of cellulose acetate and ZnO, Carbohydrate Polymers 87 (2012) 1065-1072.

[113] H. Dong, D. Wang, G. Sun, J.P. Hinestroza, Assembly of metal nanoparticles on electrospun nylon 6 nanofibers by control of interfacial hydrogen-bonding interactions, Chemistry of Materials 20 (2008) 6627-6632.

[114] D. He, B. Hu, Q.-F. Yao, K. Wang, S.-H. Yu, Large-scale synthesis of flexible free-standing SERS substrates with high sensitivity: electrospun PVA nanofibers embedded with controlled alignment of silver nanoparticles, ACS nano 3 (2009) 3993-4002.

[115] M. Roso, S. Sundarrajan, D. Pliszka, S. Ramakrishna, M. Modesti, Multifunctional membranes based on spinning technologies: the synergy of nanofibers and nanoparticles, Nanotechnology 19 (2008) 285707.

[116] P. Zhang, C. Shao, Z. Zhang, M. Zhang, J. Mu, Z. Guo, Y. Liu, In situ assembly of well-dispersed Ag nanoparticles (AgNPs) on electrospun carbon nanofibers (CNFs) for catalytic reduction of 4-nitrophenol, Nanoscale 3 (2011) 3357-3363.

[117] F. Kayaci, T. Uyar, Encapsulation of vanillin/cyclodextrin inclusion complex in electrospun polyvinyl alcohol (PVA) nanowebs: prolonged shelf-life and high temperature stability of vanillin, Food chemistry 133 (2012) 641-649.

[118] J.M. Lagaron, Multifunctional and nanoreinforced polymers for food packaging. 2011: Elsevier.

[119] E. Mascheroni, C.A. Fuenmayor, M.S. Cosio, G. Di Silvestro, L. Piergiovanni, S. Mannino, A. Schiraldi, Encapsulation of volatiles in nanofibrous polysaccharide membranes for humidity-triggered release, Carbohydrate polymers 98 (2013) 17-25.

[120] A.C. Stijnman, I. Bodnar, R. Hans Tromp, Electrospinning of food-grade polysaccharides, Food Hydrocolloids 25 (2011) 1393-1398.

[121] A.-C. Vega-Lugo, L.-T. Lim, Controlled release of allyl isothiocyanate using soy protein and poly (lactic acid) electrospun fibers, Food Research International 42 (2009) 933-940.

[122] F. Kayaci, Y. Ertas, T. Uyar, Enhanced thermal stability of eugenol by cyclodextrin inclusion complex encapsulated in electrospun polymeric nanofibers, Journal of agricultural and food chemistry 61 (2013) 8156-8165.

[123] F. Kayaci, H.S. Sen, E. Durgun, T. Uyar, Functional electrospun polymeric nanofibers incorporating geraniol–cyclodextrin inclusion complexes: High thermal stability and enhanced durability of geraniol, Food Research International 62 (2014) 424-431.

[124] F. Kayaci, O.C. Umu, T. Tekinay, T. Uyar, Antibacterial electrospun poly (lactic acid)(PLA) nanofibrous webs incorporating triclosan/cyclodextrin inclusion complexes, Journal of agricultural and food chemistry 61 (2013) 3901-3908.

[125] Z. Aytac, S.Y. Dogan, T. Tekinay, T. Uyar, Release and antibacterial activity of allyl isothiocyanate/β-cyclodextrin complex encapsulated in electrospun nanofibers, Colloids and Surfaces B: Biointerfaces (2014).

[126] T. Dvir, B.P. Timko, D.S. Kohane, R. Langer, Nanotechnological strategies for engineering complex tissues, Nature nanotechnology 6 (2011) 13-22.

[127] M.F. Canbolat, A. Celebioglu, T. Uyar, Drug delivery system based on cyclodextrin-naproxen inclusion complex incorporated in electrospun polycaprolactone nanofibers, Colloids and Surfaces B: Biointerfaces 115 (2014) 15-21.

[128] G. Ma, D. Fang, Y. Liu, X. Zhu, J. Nie, Electrospun sodium alginate/poly (ethylene oxide) core–shell nanofibers scaffolds potential for tissue engineering applications, Carbohydrate polymers 87 (2012) 737-743.

[129] C. Burger, B. Chu, Functional nanofibrous scaffolds for bone reconstruction, Colloids and Surfaces B: Biointerfaces 56 (2007) 134-141.

[130] S. Chakraborty, I. Liao, A. Adler, K.W. Leong, Electrohydrodynamics: a facile technique to fabricate drug delivery systems, Advanced drug delivery reviews 61 (2009) 1043-1054.

[131] S. Agarwal, A. Greiner, J.H. Wendorff, Electrospinning of manmade and biopolymer nanofibers—Progress in techniques, materials, and applications, Advanced functional materials 19 (2009) 2863-2879.

[132] J. Xie, X. Li, Y. Xia, Putting electrospun nanofibers to work for biomedical research, Macromolecular rapid communications 29 (2008) 1775-1792.

[133] J. Xie, M.R. MacEwan, A.G. Schwartz, Y. Xia, Electrospun nanofibers for neural tissue engineering, Nanoscale 2 (2010) 35-44.

[134] A. Hasan, A. Memic, N. Annabi, M. Hossain, A. Paul, M.R. Dokmeci, F. Dehghani, A. Khademhosseini, Electrospun scaffolds for tissue engineering of vascular grafts, Acta biomaterialia 10 (2014) 11-25.

[135] K. Yoon, B.S. Hsiao, B. Chu, Functional nanofibers for environmental applications, Journal of Materials Chemistry 18 (2008) 5326-5334.

[136] T. Uyar, R. Havelund, J. Hacaloglu, F. Besenbacher, P. Kingshott, Functional electrospun polystyrene nanofibers incorporating α-, β-, and γ-cyclodextrins: comparison of molecular filter performance, ACS nano 4 (2010) 5121-5130.

[137] C. Shin, Filtration application from recycled expanded polystyrene, Journal of colloid and interface science 302 (2006) 267-271.

[138] S. Ramakrishna, R. Jose, P. Archana, A. Nair, R. Balamurugan, J. Venugopal, W. Teo, Science and engineering of electrospun nanofibers for advances in clean

energy, water filtration, and regenerative medicine, Journal of materials science 45 (2010) 6283-6312.

[139] R. Barhate, S. Ramakrishna, Nanofibrous filtering media: filtration problems and solutions from tiny materials, Journal of membrane science 296 (2007) 1-8.

[140] H.R. Pant, B. Pant, P. Pokharel, H.J. Kim, L.D. Tijing, C.H. Park, D.S. Lee, H.Y. Kim, C.S. Kim, Photocatalytic TiO< sub> 2</sub>–RGO/nylon-6 spider-wave-like nano-nets via electrospinning and hydrothermal treatment, Journal of membrane science 429 (2013) 225-234.

[141] D. Aussawasathien, C. Teerawattananon, A. Vongachariya, Separation of micron to sub-micron particles from water: electrospun nylon-6 nanofibrous membranes as pre-filters, Journal of membrane science 315 (2008) 11-19.

[142] F. Kayaci, Z. Aytac, T. Uyar, Surface modification of electrospun polyester nanofibers with cyclodextrin polymer for the removal of phenanthrene from aqueous solution, Journal of hazardous materials 261 (2013) 286-294.

[143] F. Kayaci, T. Uyar, Electrospun polyester/cyclodextrin nanofibers for entrapment of volatile organic compounds, Polymer Engineering & Science (2014).

[144] T. Uyar, R. Havelund, Y. Nur, A. Balan, J. Hacaloglu, L. Toppare, F. Besenbacher, P. Kingshott, Cyclodextrin functionalized poly (methyl methacrylate)(PMMA) electrospun nanofibers for organic vapors waste treatment, Journal of membrane science 365 (2010) 409-417.

[145] T. Uyar, R. Havelund, Y. Nur, J. Hacaloglu, F. Besenbacher, P. Kingshott, Molecular filters based on cyclodextrin functionalized electrospun fibers, Journal of membrane science 332 (2009) 129-137.

[146] V. Thavasi, G. Singh, S. Ramakrishna, Electrospun nanofibers in energy and environmental applications, Energy & Environmental Science 1 (2008) 205-221.

[147] L. Yang, A. Raza, Y. Si, X. Mao, Y. Shang, B. Ding, J. Yu, S.S. Al-Deyab, Synthesis of superhydrophobic silica nanofibrous membranes with robust

thermal stability and flexibility via in situ polymerization, Nanoscale 4 (2012) 6581-6587.

[148] S. Kundu, R.S. Gill, R.F. Saraf, Electrospinning of PAH nanofiber and deposition of Au NPs for nanodevice fabrication, The Journal of Physical Chemistry C 115 (2011) 15845-15852.

[149] Y.-Z. Long, M. Yu, B. Sun, C.-Z. Gu, Z. Fan, Recent advances in large-scale assembly of semiconducting inorganic nanowires and nanofibers for electronics, sensors and photovoltaics, Chemical Society Reviews 41 (2012) 4560-4580.

[150] J.B.-H. Tok, Z. Bao, Recent advances in flexible and stretchable electronics, sensors and power sources, Science China Chemistry 55 (2012) 718-725.

[151] P. Gomathi, D. Ragupathy, J.H. Choi, J.H. Yeum, S.C. Lee, J.C. Kim, S.H. Lee, H.D. Ghim, Fabrication of novel chitosan nanofiber/gold nanoparticles composite towards improved performance for a cholesterol sensor, Sensors and Actuators B: Chemical 153 (2011) 44-49.

[152] L. Matlock-Colangelo, A.J. Baeumner, Recent progress in the design of nanofiber-based biosensing devices, Lab on a Chip 12 (2012) 2612-2620.

[153] A. Senthamizhan, A. Celebioglu, T. Uyar, Ultrafast on-site selective visual detection of TNT at Sub ppt level using fluorescent gold cluster incorporated single nanofiber, Chemical Communications (2014).

[154] A. Senthamizhan, A. Celebioglu, T. Uyar, Flexible and highly stable electrospun nanofibrous membrane incorporating gold nanocluster as a efficient probe for visual colorimetric detection of Hg (II), Journal of Materials Chemistry A (2014).

[155] B. Ding, M. Wang, X. Wang, J. Yu, G. Sun, Electrospun nanomaterials for ultrasensitive sensors, Materials Today 13 (2010) 16-27.

[156] S. Demirci Uzun, F. Kayaci, T. Uyar, S. Timur, L. Toppare, Bioactive Surface Design Based on Functional Composite Electrospun Nanofibers for Biomolecule

Immobilization and Biosensor Applications, ACS applied materials & interfaces 6 (2014) 5235-5243.

[157] Z. Zhang, C. Shao, P. Zou, P. Zhang, M. Zhang, J. Mu, Z. Guo, X. Li, C. Wang, Y. Liu, In situ assembly of well-dispersed gold nanoparticles on electrospun silica nanotubes for catalytic reduction of 4-nitrophenol, Chem. Commun. 47 (2011) 3906-3908.

[158] C. Su, C. Shao, Y. Liu, Electrospun nanofibers of TiO< sub> 2</sub>/CdS heteroarchitectures with enhanced photocatalytic activity by visible light, Journal of colloid and interface science 359 (2011) 220-227.

[159] F. Kayaci, C. Ozgit-Akgun, I. Donmez, N. Biyikli, T. Uyar, Polymer–inorganic core–shell nanofibers by electrospinning and atomic layer deposition: Flexible nylon–ZnO core–shell nanofiber mats and their photocatalytic activity, ACS applied materials & interfaces 4 (2012) 6185-6194.

[160] F. Kayaci, C. Ozgit-Akgun, N. Biyikli, T. Uyar, Surface-decorated ZnO nanoparticles and ZnO nanocoating on electrospun polymeric nanofibers by atomic layer deposition for flexible photocatalytic nanofibrous membranes, RSC Advances 3 (2013) 6817-6820.

[161] F. Kayaci, S. Vempati, C. Ozgit-Akgun, N. Biyikli, T. Uyar, Enhanced photocatalytic activity of homoassembled ZnO nanostructures on electrospun polymeric nanofibers: A combination of atomic layer deposition and hydrothermal growth, Applied Catalysis B: Environmental 156 (2014) 173-183.

[162] F. Kayaci, S. Vempati, I. Donmez, N. Biyikli, T. Uyar, Role of zinc interstitials and oxygen vacancies of ZnO in photocatalysis: A bottom-up approach to control the defect density, Nanoscale (2014).

[163] Z.-G. Wang, L.-S. Wan, Z.-M. Liu, X.-J. Huang, Z.-K. Xu, Enzyme immobilization on electrospun polymer nanofibers: an overview, Journal of Molecular Catalysis B: Enzymatic 56 (2009) 189-195.

[164] H. Li, W. Zhang, S. Huang, W. Pan, Enhanced visible-light-driven photocatalysis of surface nitrided electrospun TiO2 nanofibers, Nanoscale 4 (2012) 801-806.

[165] R. Sahay, P.S. Kumar, R. Sridhar, J. Sundaramurthy, J. Venugopal, S.G. Mhaisalkar, S. Ramakrishna, Electrospun composite nanofibers and their multifaceted applications, Journal of Materials Chemistry 22 (2012) 12953-12971.

[166] W.-E. Teo, S. Ramakrishna, Electrospun nanofibers as a platform for multifunctional, hierarchically organized nanocomposite, Composites Science and Technology 69 (2009) 1804-1817.

[167] J. Sun, W. Wei, Y. Xu, J. Qu, X. Liu, T. Endo, A curing system of benzoxazine with amine: reactivity, reaction mechanism and material properties, RSC Advances 5 (2015) 19048-19057.

[168] C. Li, Q. Ran, R. Zhu, Y. Gu, Study on thermal degradation mechanism of a cured aldehyde-functional benzoxazine, RSC Advances 5 (2015) 22593-22600.

[169] H. Zhang, W. Gu, R. Zhu, Q. Ran, Y. Gu, Study on the thermal degradation behavior of sulfone-containing polybenzoxazines via Py-GC-MS, Polymer Degradation and Stability 111 (2015) 38-45.

[170] P. Yang, X. Wang, H. Fan, Y. Gu, Effect of hydrogen bonds on the modulus of bulk polybenzoxazines in the glassy state, Physical Chemistry Chemical Physics 15 (2013) 15333-15338.

[171] W.-K. Kim, W.L. Mattice, Molecular modeling of a thin film of polybenzoxazine, Langmuir 14 (1998) 6588-6593.

[172] T. Feng, J. Wang, H. Wang, N. Ramdani, L. Zu, W. Liu, X. Xu, Copolymerization of fluorene-based main-chain benzoxazine and their high performance thermosets, Polymers for Advanced Technologies (2015).

[173] C.H. Lin, Y.S. Shih, M.W. Wang, C.Y. Tseng, T.Y. Juang, C.F. Wang, Emission and surface properties of main-chain type polybenzoxazine with pyridinyl moieties, RSC Advances 4 (2014) 8692-8698.

[174] B. Kiskan, Y. Yagci, Self-healing of poly (propylene oxide)-polybenzoxazine thermosets by photoinduced coumarine dimerization, Journal of Polymer Science Part A: Polymer Chemistry 52 (2014) 2911-2918.

[175] J. Shi, X. Zheng, L. Xie, F. Cao, Y. Wu, W. Liu, Film-forming characteristics and thermal stability of low viscosity benzoxazines derived from melamine, European Polymer Journal 49 (2013) 4054-4061.

[176] J. Liu, X. Lu, Z. Xin, C. Zhou, Synthesis and surface properties of low surface free energy silane-functional polybenzoxazine films, Langmuir 29 (2012) 411-416.

[177] A.D. Baranek, L.L. Kendrick, J. Narayanan, G.E. Tyson, S. Wand, D.L. Patton, Flexible aliphatic-bridged bisphenol-based polybenzoxazines, Polymer Chemistry 3 (2012) 2892-2900.

[178] C.H. Lin, S.L. Chang, T.Y. Shen, Y.S. Shih, H.T. Lin, C.F. Wang, Flexible polybenzoxazine thermosets with high glass transition temperatures and low surface free energies, Polymer Chemistry 3 (2012) 935-945.

[179] A. Tuzun, B. Kiskan, N. Alemdar, A.T. Erciyes, Y. Yagci, Benzoxazine containing polyester thermosets with improved adhesion and flexibility, Journal of Polymer Science Part A: Polymer Chemistry 48 (2010) 4279-4284.

[180] M. Nakamura, H. Ishida, Synthesis and properties of new crosslinkable telechelics with benzoxazine moiety at the chain end, Polymer 50 (2009) 2688-2695.

[181] B. Kiskan, Y. Yagci, H. Ishida, Synthesis, characterization, and properties of new thermally curable polyetheresters containing benzoxazine moieties in the main chain, Journal of Polymer Science Part A: Polymer Chemistry 46 (2008) 414-420.

[182] T. Takeichi, T. Kano, T. Agag, Synthesis and thermal cure of high molecular weight polybenzoxazine precursors and the properties of the thermosets, Polymer 46 (2005) 12172-12180.

[183] P. Lorjai, S. Wongkasemjit, T. Chaisuwan, A.M. Jamieson, Significant enhancement of thermal stability in the non-oxidative thermal degradation of bisphenol-A/aniline based polybenzoxazine aerogel, Polymer Degradation and Stability 96 (2011) 708-718.

[184] S. Mahadik-Khanolkar, S. Donthula, A. Bang, C. Wisner, C. Sotiriou-Leventis, N. Leventis, Polybenzoxazine Aerogels. 2. Interpenetrating Networks with Iron Oxide and the Carbothermal Synthesis of Highly Porous Monolithic Pure Iron (0) Aerogels as Energetic Materials, Chemistry of Materials 26 (2014) 1318-1331.

[185] D.A. Rubenstein, H. Lu, S.S. Mahadik, N. Leventis, W. Yin, Characterization of the physical properties and biocompatibility of polybenzoxazine-based aerogels for use as a novel hard-tissue scaffold, Journal of Biomaterials Science, Polymer Edition 23 (2012) 1171-1184.

[186] T. Chaisuwan, T. Komalwanich, S. Luangsukrerk, S. Wongkasemjit, Removal of heavy metals from model wastewater by using polybenzoxazine aerogel, Desalination 256 (2010) 108-114.

[187] P. Katanyoota, T. Chaisuwan, A. Wongchaisuwat, S. Wongkasemjit, Novel polybenzoxazine-based carbon aerogel electrode for supercapacitors, Materials Science and Engineering: B 167 (2010) 36-42.

[188] P. Lorjai, T. Chaisuwan, S. Wongkasemjit, Porous structure of polybenzoxazine-based organic aerogel prepared by sol–gel process and their carbon aerogels, Journal of sol-gel science and technology 52 (2009) 56-64.

[189] O.S. Taskin, B. Kiskan, A. Aksu, N. Balkis, J. Weber, Y. Yagci, Polybenzoxazine: A Powerful Tool for Removal of Mercury Salts from Water, Chemistry-A European Journal 20 (2014) 10953-10958.

[190] K. Pakkethati, N. Tungsattabutrat, T. Chaisuwan, S. Wongkasemjit, High performance of polybenzoxazine membranes for ethanol-water separation via pervaporation technique, Materials Research Innovations 16 (2012) 243-248.

[191] Y. Ertas, T. Uyar, Main-chain polybenzoxazine nanofibers via electrospinning, Polymer 55 (2014) 556-564.

[192] V.A. Ganesh, H.K. Raut, A.S. Nair, S. Ramakrishna, A review on self-cleaning coatings, Journal of Materials Chemistry 21 (2011) 16304-16322.

[193] J. Lin, Y. Cai, X. Wang, B. Ding, J. Yu, M. Wang, Fabrication of biomimetic superhydrophobic surfaces inspired by lotus leaf and silver ragwort leaf, Nanoscale 3 (2011) 1258-1262.

[194] X. Liu, Y. Liang, F. Zhou, W. Liu, Extreme wettability and tunable adhesion: biomimicking beyond nature?, Soft Matter 8 (2012) 2070-2086.

[195] X. Wang, B. Ding, J. Yu, M. Wang, Engineering biomimetic superhydrophobic surfaces of electrospun nanomaterials, Nano today 6 (2011) 510-530.

[196] J. Lin, X. Wang, B. Ding, J. Yu, G. Sun, M. Wang, Biomimicry via electrospinning, Critical Reviews in Solid State and Materials Sciences 37 (2012) 94-114.

[197] N. Ghosh, B. Kiskan, Y. Yagci, Polybenzoxazines—new high performance thermosetting resins: synthesis and properties, Progress in polymer Science 32 (2007) 1344-1391.

[198] H.-C. Liu, W.-C. Su, Y.-L. Liu, Self-assembled benzoxazine-bridged polysilsesquioxanes exhibiting ultralow-dielectric constants and yellow-light photoluminescent emission, Journal of Materials Chemistry 21 (2011) 7182-7187.

[199] C.F. Wang, Y.C. Su, S.W. Kuo, C.F. Huang, Y.C. Sheen, F.C. Chang, Low-Surface-Free-Energy Materials Based on Polybenzoxazines, Angewandte Chemie International Edition 45 (2006) 2248-2251.

[200] X. Tang, Y. Si, J. Ge, B. Ding, L. Liu, G. Zheng, W. Luo, J. Yu, In situ polymerized superhydrophobic and superoleophilic nanofibrous membranes for gravity driven oil–water separation, Nanoscale 5 (2013) 11657-11664.

[201] Y. Shang, Y. Si, A. Raza, L. Yang, X. Mao, B. Ding, J. Yu, An in situ polymerization approach for the synthesis of superhydrophobic and superoleophilic nanofibrous membranes for oil–water separation, Nanoscale 4 (2012) 7847-7854.

[202] B. Li, B. Jiang, D.J. Fauth, M.L. Gray, H.W. Pennline, G.A. Richards, Innovative nano-layered solid sorbents for CO 2 capture, Chemical Communications 47 (2011) 1719-1721.

[203] Y. Li, W. Xiao, K. Xiao, L. Berti, J. Luo, H.P. Tseng, G. Fung, K.S. Lam, Well-Defined, Reversible Boronate Crosslinked Nanocarriers for Targeted Drug Delivery in Response to Acidic pH Values and cis-Diols, Angewandte Chemie 124 (2012) 2918-2923.

[204] J. Yuan, X. Liu, O. Akbulut, J. Hu, S.L. Suib, J. Kong, F. Stellacci, Superwetting nanowire membranes for selective absorption, Nature Nanotechnology 3 (2008) 332-336.

[205] R.N. Wenzel, Resistance of solid surfaces to wetting by water, Industrial & Engineering Chemistry 28 (1936) 988-994.

[206] A. Cassie, S. Baxter, Wettability of porous surfaces, Transactions of the Faraday Society 40 (1944) 546-551.

[207] G. McHale, N. Shirtcliffe, M. Newton, Contact-angle hysteresis on super-hydrophobic surfaces, Langmuir 20 (2004) 10146-10149.

[208] L. Zhang, Z. Zhang, P. Wang, Smart surfaces with switchable superoleophilicity and superoleophobicity in aqueous media: toward controllable oil/water separation, NPG Asia Materials 4 (2012) e8.

[209] M. Huang, Y. Si, X. Tang, Z. Zhu, B. Ding, L. Liu, G. Zheng, W. Luo, J. Yu, Gravity driven separation of emulsified oil–water mixtures utilizing in situ

polymerized superhydrophobic and superoleophilic nanofibrous membranes, Journal of Materials Chemistry A 1 (2013) 14071-14074.

[210] W. Zhang, X. Lu, Z. Xin, C. Zhou, A self-cleaning polybenzoxazine/TiO 2 surface with superhydrophobicity and superoleophilicity for oil/water separation, Nanoscale 7 (2015) 19476-19483.

[211] T.-H. Kao, J.-K. Chen, C.-C. Cheng, C.-I. Su, F.-C. Chang, Low-surface-free-energy polybenzoxazine/polyacrylonitrile fibers for biononfouling membrane, Polymer 54 (2013) 258-268.

[212] H.-Y. Li, Y.-L. Liu, Polyelectrolyte composite membranes of polybenzimidazole and crosslinked polybenzimidazole-polybenzoxazine electrospun nanofibers for proton exchange membrane fuel cells, Journal of Materials Chemistry A 1 (2013) 1171-1178.

[213] C.K. Liu, K. Lai, W. Liu, M. Yao, R.J. Sun, Preparation of carbon nanofibres through electrospinning and thermal treatment, Polymer International 58 (2009) 1341-1349.

[214] E.J. Ra, T.H. Kim, W.J. Yu, K.H. An, Y.H. Lee, Ultramicropore formation in PAN/camphor-based carbon nanofiber paper, Chemical Communications 46 (2010) 1320-1322.

[215] S.N. Arshad, M. Naraghi, I. Chasiotis, Strong carbon nanofibers from electrospun polyacrylonitrile, Carbon 49 (2011) 1710-1719.

[216] K. Chakrabarti, P. Nambissan, C. Mukherjee, K. Bardhan, C. Kim, K. Yang, Positron annihilation spectroscopy of polyacrylonitrile-based carbon fibers embedded with multi-wall carbon nanotubes, Carbon 44 (2006) 948-953.

[217] H. Niu, J. Zhang, Z. Xie, X. Wang, T. Lin, Preparation, structure and supercapacitance of bonded carbon nanofiber electrode materials, Carbon 49 (2011) 2380-2388.

[218] K.K.H. Wong, M. Zinke-Allmang, J.L. Hutter, S. Hrapovic, J.H. Luong, W. Wan, The effect of carbon nanotube aspect ratio and loading on the elastic

modulus of electrospun poly (vinyl alcohol)-carbon nanotube hybrid fibers, Carbon 47 (2009) 2571-2578.

[219] Y. Yang, A. Centrone, L. Chen, F. Simeon, T.A. Hatton, G.C. Rutledge, Highly porous electrospun polyvinylidene fluoride (PVDF)-based carbon fiber, Carbon 49 (2011) 3395-3403.

[220] C.R. Nair, Advances in addition-cure phenolic resins, Progress in polymer Science 29 (2004) 401-498.

[221] H.Y. Li, Y.Y. Lee, Y. Chang, C.H. Lin, Y.L. Liu, Fiber Mats: Robustly Blood-Inert and Shape-Reproducible Electrospun Polymeric Mats (Adv. Mater. Interfaces 9/2015), Advanced Materials Interfaces 2 (2015).

[222] F. Kasapoglu, I. Cianga, Y. Yagci, T. Takeichi, Photoinitiated cationic polymerization of monofunctional benzoxazine, Journal of Polymer Science Part A: Polymer Chemistry 41 (2003) 3320-3328.

[223] Y. Yagci. Photoinitiated cationic polymerization of unconventional monomers. in Macromolecular symposia. 2006: Wiley Online Library.

[224] J. Bai, Z. Shi, J. Yin, A novel main chain benzoxazine polymer with the ability of UV-induced self-surface modification, Polymer 54 (2013) 2498-2505.

[225] J. Shi, P. Chen, K. Wang, J. Lu, J. Nie, A novel high efficiency benzophenone based polymeric photoinitiator from ring-opening polymerization of benzoxazine, Polymer Science Series B 56 (2014) 632-638.

[226] J. Bai, Z. Shi, Novel benzoxazine resins as photoinitiator comprising benzophenone and coinitiator amine for photopolymerization, Journal of Applied Polymer Science 128 (2013) 1785-1791.

[227] G. Temel, D.S. Esen, N. Arsu, One-component benzoxazine type photoinitiator for free radical polymerization, Polymer Engineering & Science 52 (2012) 133-138.

[228] Y. Ertas, T. Uyar, Cross-linked main-chain polybenzoxazine nanofibers by photo and thermal curing; stable at high temperatures and harsh acidic conditions, Polymer 84 (2016) 72-80.

[229] G. Lligadas, A. Tuzun, J.C. Ronda, M. Galia, V. Cadiz, Polybenzoxazines: new players in the bio-based polymer arena, Polymer Chemistry 5 (2014) 6636-6644.

[230] C.F. Wang, J.Q. Sun, X.D. Liu, A. Sudo, T. Endo, Synthesis and copolymerization of fully bio-based benzoxazines from guaiacol, furfurylamine and stearylamine, Green Chemistry 14 (2012) 2799-2806.

[231] P. Thirukumaran, A. Shakila, S. Muthusamy, Synthesis and characterization of novel bio-based benzoxazines from eugenol, Rsc Advances 4 (2014) 7959-7966.

[232] P. Thirukumaran, A.S. Parveen, M. Sarojadevi, Synthesis and Copolymerization of Fully Biobased Benzoxazines from Renewable Resources, Acs Sustainable Chemistry & Engineering 2 (2014) 2790-2801.

[233] L. Dumas, L. Bonnaud, M. Olivier, M. Poorteman, P. Dubois, Eugenol-based benzoxazine: from straight synthesis to taming of the network properties, Journal of Materials Chemistry A 3 (2015) 6012-6018.

[234] T. Periyasamy, S.P. Asrafali, S. Muthusamy, New benzoxazines containing polyhedral oligomeric silsesquioxane from eugenol, guaiacol and vanillin, New Journal of Chemistry 39 (2015) 1691-1702.

[235] P. Thirukumaran, A.S. Parveen, K. Kumudha, M. Sarojadevi, Synthesis and Characterization of New Polybenzoxazines From Renewable Resources for Bio-Composite Applications, Polymer Composites 37 (2016) 1821-1829.

[236] B.S. Rao, A. Palanisamy, Monofunctional benzoxazine from cardanol for bio-composite applications, Reactive & Functional Polymers 71 (2011) 148-154.

[237] L. Dumas, L. Bonnaud, M. Olivier, M. Poorteman, P. Dubois, Bio-based high performance thermosets: Stabilization and reinforcement of eugenol-based

benzoxazine networks with BMI and CNT, European Polymer Journal 67 (2015) 494-502.

[238] R. Ambrozic, U. Sebenik, M. Krajnc, Synthesis, curing kinetics, thermal and mechanical behavior of novel cardanol-based benzoxazines, Polymer 76 (2015) 203-212.

[239] P. Thirukumaran, R. Sathiyamoorthi, A.S. Parveen, M. Sarojadevi, New Benzoxazines From Renewable Resources for Green Composite Applications, Polymer Composites 37 (2016) 573-582.

[240] S.R. Mir, M. Ali, R. Kapoor, Chemical composition of essential oil of Cinnamomum tamala Nees et Eberm. leaves, Flavour and fragrance journal 19 (2004) 112-114.

[241] G.R. Mallavarapu, S. Ramesh, R. Chandrasekhara, B. Rajeswara Rao, P. Kaul, A. Bhattacharya, Investigation of the essential oil of cinnamon leaf grown at Bangalore and Hyderabad, Flavour and fragrance journal 10 (1995) 239-242.

[242] M.N.I. Bhuiyan, J. Begum, F. Akter, Constituents of the essential oil from leaves and buds of clove (Syzigium caryophyllatum (L.) Alston), African Journal of Plant Science 4 (2010) 451-454.

[243] H. Ishida, Process for preparation of benzoxazine compounds in solventless systems. 1996, Google Patents.

[244] H. Ishida, D.J. Allen, Physical and mechanical characterization of near-zero shrinkage polybenzoxazines, Journal of Polymer Science Part B: Polymer Physics 34 (1996) 1019-1030.

[245] H.-D. Kim, H. Ishida, A study on hydrogen-bonded network structure of polybenzoxazines, The Journal of Physical Chemistry A 106 (2002) 3271-3280.

[246] P. Thirukumaran, A.S. Parveen, M. Sarojadevi, Synthesis of eugenol-based polybenzoxazine-POSS nanocomposites for low dielectric applications, Polymer Composites 36 (2015) 1973-1982.

[247] E. Nour-Eddine, Q.L. Yuan, F.R. Huang, Investigation of curing and thermal behavior of benzoxazine and lignin mixtures, Journal of Applied Polymer Science 125 (2012) 1773-1781.

[248] C. Yan, X.Y. Fan, J. Li, S.Z. Shen, Synthesis and Characterization of Bisphenol A Diphthalimide Bisbenzoxazine Monomers and the Properties of Their Polybenzoxazines, Journal of Applied Polymer Science 121 (2011) 2778-2787.

[249] T. Uyar, R. Havelund, J. Hacaloglu, X.F. Zhou, F. Besenbacher, P. Kingshott, The formation and characterization of cyclodextrin functionalized polystyrene nanofibers produced by electrospinning, Nanotechnology 20 (2009).

[250] R. Liska, Photoinitiators with functional groups. V. New water-soluble photoinitiators containing carbohydrate residues and copolymerizable derivatives thereof, Journal of Polymer Science Part A: Polymer Chemistry 40 (2002) 1504-1518.

[251] R. Gopal, S. Kaur, Z. Ma, C. Chan, S. Ramakrishna, T. Matsuura, Electrospun nanofibrous filtration membrane, Journal of Membrane Science 281 (2006) 581-586.

[252] Y. Tian, M. Wu, R. Liu, Y. Li, D. Wang, J. Tan, R. Wu, Y. Huang, Electrospun membrane of cellulose acetate for heavy metal ion adsorption in water treatment, Carbohydrate polymers 83 (2011) 743-748.

[253] F. Ji, C. Li, B. Tang, J. Xu, G. Lu, P. Liu, Preparation of cellulose acetate/zeolite composite fiber and its adsorption behavior for heavy metal ions in aqueous solution, Chemical engineering journal 209 (2012) 325-333.

[254] R. Saliba, H. Gauthier, R. Gauthier, M. Petit-Ramel, Adsorption of copper (II) and chromium (III) ions onto amidoximated cellulose, Journal of Applied Polymer Science 75 (2000) 1624-1631.

[255] A.A. Taha, Y.-n. Wu, H. Wang, F. Li, Preparation and application of functionalized cellulose acetate/silica composite nanofibrous membrane via

electrospinning for Cr (VI) ion removal from aqueous solution, Journal of environmental management 112 (2012) 10-16.

[256] S.-L. Chen, X.-J. Huang, Z.-K. Xu, Functionalization of cellulose nanofiber mats with phthalocyanine for decoloration of reactive dye wastewater, Cellulose 18 (2011) 1295-1303.

[257] Y. Wang, X. Zhang, X. He, W. Zhang, X. Zhang, C. Lu, In situ synthesis of MnO 2 coated cellulose nanofibers hybrid for effective removal of methylene blue, Carbohydrate polymers 110 (2014) 302-308.

[258] A. Celebioglu, S. Demirci, T. Uyar, Cyclodextrin-grafted electrospun cellulose acetate nanofibers via “Click” reaction for removal of phenanthrene, Applied Surface Science 305 (2014) 581-588.

[259] C.Q. Yang, X. Wang, I.-S. Kang, Ester crosslinking of cotton fabric by polymeric carboxylic acids and citric acid, Textile Research Journal 67 (1997) 334-342.

[260] H.S. Barud, A.M. de Araújo Júnior, D.B. Santos, R.M. de Assunção, C.S. Meireles, D.A. Cerqueira, G. Rodrigues Filho, C.A. Ribeiro, Y. Messaddeq, S.J. Ribeiro, Thermal behavior of cellulose acetate produced from homogeneous acetylation of bacterial cellulose, Thermochimica acta 471 (2008) 61-69.

[261] T. Wu, X. Cai, S. Tan, H. Li, J. Liu, W. Yang, Adsorption characteristics of acrylonitrile, p-toluenesulfonic acid, 1-naphthalenesulfonic acid and methyl blue on graphene in aqueous solutions, Chemical engineering journal 173 (2011) 144-149.

[262] T. Takeichi, Y. Guo, T. Agag, Synthesis and characterization of poly (urethane-benzoxazine) films as novel type of polyurethane/phenolic resin composites, Journal of Polymer Science Part A: Polymer Chemistry 38 (2000) 4165-4176.

[263] H. Ishida, Y.H. Lee, Infrared and thermal analyses of polybenzoxazine and polycarbonate blends, Journal of Applied Polymer Science 81 (2001) 1021-1034.

[264] H. Ishida, Y.-H. Lee, Synergism observed in polybenzoxazine and poly (ε-caprolactone) blends by dynamic mechanical and thermogravimetric analysis, Polymer 42 (2001) 6971-6979.

[265] H. Ishida, Y.H. Lee, Study of hydrogen bonding and thermal properties of polybenzoxazine and poly-(ε-caprolactone) blends, Journal of Polymer Science Part B: Polymer Physics 39 (2001) 736-749.

[266] Y.-C. Su, S.-W. Kuo, D.-R. Yei, H. Xu, F.-C. Chang, Thermal properties and hydrogen bonding in polymer blend of polybenzoxazine/poly (N-vinyl-2-pyrrolidone), Polymer 44 (2003) 2187-2191.

[267] J. Szejtli, Cyclodextrin technology. Vol. 1. 1988: Springer.

[268] J. Szejtli, Introduction and general overview of cyclodextrin chemistry, Chemical reviews 98 (1998) 1743-1754.

[269] E.M. Del Valle, Cyclodextrins and their uses: a review, Process biochemistry 39 (2004) 1033-1046.

[270] W. Saenger, J. Jacob, K. Gessler, T. Steiner, D. Hoffmann, H. Sanbe, K. Koizumi, S.M. Smith, T. Takaha, Structures of the common cyclodextrins and their larger analogues beyond the doughnut, Chemical reviews 98 (1998) 1787-1802.

[271] A. Celebioglu, T. Uyar, Cyclodextrin nanofibers by electrospinning, Chemical Communications 46 (2010) 6903-6905.

[272] A.R. Hedges, Industrial applications of cyclodextrins, Chemical reviews 98 (1998) 2035-2044.

[273] S.L. Shenoy, W.D. Bates, H.L. Frisch, G.E. Wnek, Role of chain entanglements on fiber formation during electrospinning of polymer solutions: good solvent, non-specific polymer–polymer interaction limit, Polymer 46 (2005) 3372-3384.

[274] P. Gupta, C. Elkins, T.E. Long, G.L. Wilkes, Electrospinning of linear homopolymers of poly (methyl methacrylate): exploring relationships between fiber formation, viscosity, molecular weight and concentration in a good solvent, Polymer 46 (2005) 4799-4810.